Investigations of Intraday Variable Blazar Cores and the Connected Interstellar Medium

Dissertation

zur

Erlangung des Doktorgrades (Dr. rer. nat.)

der

Mathematisch-Naturwissenschaftlichen Fakultät

der

Rheinischen Friedrich-Wilhelms-Universität Bonn

vorgelegt von

Lars Fuhrmann

aus

Duisburg

Juni 2004

Angefertigt mit Genehmigung der Mathematisch-Naturwissenschaftlichen Fakultät der
Rheinischen Friedrich-Wilhelms-Universität Bonn

Diese Dissertation ist auf dem Hochschulschriftenserver der ULB Bonn
http://hss.ulb.uni-bonn.de/diss_online elektronisch publiziert.
Erscheinungsjahr 2006

1. Referent: **Prof. Dr. Ulrich Klein**
2. Referent: **Priv.-Doz. Dr. Walter K. Huchtmeier**

Tag der Promotion: 27. August 2004

Preamble

Since the early history of man, the sky and its celestial objects always attracted attention and fascination to the human eye and it became a great task for mankind to explore and understand their secrets over ages. This task is not over - rather the opposite is true. The first optical instruments made it possible to explore the sky and to investigate its objects in more detail. This smoothed the way for systematic studies of the optical sky and, as result, the beginning awareness of the great variety of its physical phenomena.

In the thirties, Karl Jansky established the possibility to study the sky beyond the visible light and thus opened the view of astronomy to the whole electromagnetic spectrum. It soon turned out, that early optical astronomy is only one step towards the even more complicated, mysterious and fascinating task to obtain an overall picture of the universe as nowadays observed across the whole electromagnetic spectrum.

A class of objects, which today are classified as 'active galaxies' or more generally called *Active Galactic Nuclei* (hereafter AGN) form one part of this overall picture. This kind of discrete astronomical objects were the first to be observed outside the visible part of the spectrum - strong extragalactic radio sources. Nowadays, a whole 'zoo' of different types of objects are known to be active galaxies, which exhibit very peculiar and often extreme properties compared to their 'non-active' counterparts. These properties involve extreme energetic phenomena in the innermost core regions of these galaxies, which can not be linked to a stellar (i.e. fusion powered) origin. A common characteristic is their broad spectral energy distribution (SED): they usually exhibit extremely high luminosities across all wavelengths (from radio up to γ-ray). A further characteristic is the often observed strong variability in their intensity across the whole electromagnetic spectrum. The work done in the framework of this thesis is dedicated to an extreme form of this variability frequently observed in a subclass of AGN: *IntraDay Variability* (hereafter IDV) of compact Blazar cores in the radio regime. Although discovered about 15 years ago, radio IDV is still under hot and controversial discussion, since a complete and consistent explanation has yet to be found. The work presented here shall provide a further contribution to shed light upon the mechanism in operation.

Contents

1

Introduction

1.1 Active Galactic Nuclei and Compact Blazar Cores

In 1943, Carl Seyfert observed a new class of optical galaxies with the host galaxy still visible (mostly spirals), but with an unusual bright nucleus and strong emission features in their optical spectra. According to the appearance of broad ($\sim 1000\,\mathrm{km\,s^{-1}}$) and/or narrow ($\sim 100\,\mathrm{km\,s^{-1}}$) emission lines these objects are known today as Seyfert type I or Seyfert type II galaxies (Sey I, Sey II), respectively. This was the starting point for the discovery of several classes of such active objects. Hey et al. (1946) discovered the first discrete radio source, the radio galaxy Cygnus A, and together with improved instrumentation and large radio surveys soon more radio galaxies were found. With a better knowledge of their positions, these sources could subsequently be identified with their optical counterparts (mostly elliptical galaxies) and thus were found to be extragalactic (e.g. Bolton et al. 1949). This implied already huge energy densities in these objects due to the high luminosities and distances involved. The physical origin of the radio emission was soon found to be (non-thermal) synchrotron emission of relativistic electrons, which gyrate along magnetic field lines.

In the late fifties, a new class of strong radio sources was found to be apparently connected with bright and compact stellar objects on optical plates and was called quasars (quasi-stellar radio sources). The subsequent detection of highly redshifted optical emission lines proved their origin to be extragalactic as well (e.g. Schmidt 1963). Up to now, many quasars have been detected of which only a small part exhibits a strong counterpart in the radio regime. This led to the distinction between radio-loud and radio-quiet objects. 3C273 is a typical example for a radio-loud quasar. While its brightness in the radio regime is comparable to what was already known from radio galaxies (e.g. Cyg A), its luminosity in the optical band ($\sim 10^{46}\,\mathrm{erg\,s^{-1}}$) exceeds that of a whole, normal galaxy by a factor $\sim 10^4$.

Today, a whole 'zoo' of active extragalactic objects has been found (e.g. Sey I and II, Fanaroff-Riley type I and type II radio galaxies (FR I and FR II), steep- and flat-spectrum quasars, BL Lacs, LINERs etc.), all showing somehow different properties and types of activity. The enormous energy requirement ($\sim 10^{60}\,\mathrm{erg}$ for radio sources like Cyg A) and small dimensions of the emitting regions (constrained by variability studies to several light weeks) opened controversial discussions about the cause of its origin. Today it is generally accepted that the only capable physical mechanism behind such energies is the release of potential gravitational energy caused by the accretion of matter onto an extremely massive and compact object. In the standard model the whole 'zoo' of active objects is believed to be powered by an active galactic nuclei consisting of a supermassive black hole of mass 10^7–$10^9 M_\odot$ accreting matter. Figure 1.1 gives a schematic view of the prevailing picture of an AGN and its basic ingredients. The accretion flow forms an accretion disk (AD), where

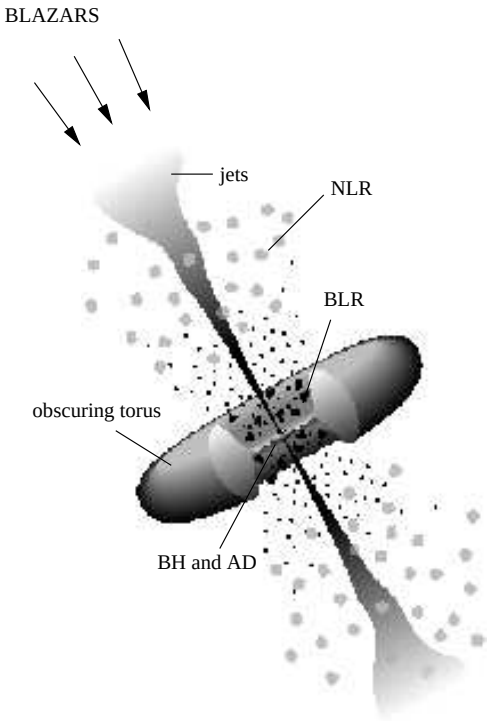

FIGURE 1.1— A sketch of the physical structure of an AGN. Basic ingredients are: a supermassive black hole (BH) and an accretion disk (AD) at the center. Two relativistic plasma jets emerge from the nucleus perpendicular to the disk and penetrate through the broad line region (BLR), narrow line region (NLR) and can travel deep into the intergalactic medium. A molecular dust torus obscures the inner part. Depending on the viewing angle, the appearance and thus classification of an AGN depends strongly on its orientation to our line of sight. In this framework, jets of Blazars are pointing close towards the observer.

angular momentum is transported outwards by viscous friction and matter transported inwards. Further components of an AGN and its surrounding are two kinds of gas clouds. The broad line region (BLR) consists of clouds in the local vicinity of the black hole, which move extremely fast in its gravitational potential and produce broad emission lines in the optical spectra of AGN (as mentioned earlier). The narrow line region (NLR) is the extension of the BLR towards larger distances (50–100 pc) with slower gas clouds and is the origin of the narrow emission lines. A molecular dust torus (possibly the outer region of the accretion disk) obscures the central system and is inferred by the presence of an infrared-bump in the SED of several AGN. Along the spin-axis of the black hole, the acceleration and ejection of material occurs (most likely by the existence of a toroidal magnetic field frozen in the rotating disk) perpendicular to the disk forming a relativistic twin jet. Here, the synchrotron emitting plasma travels with relativistic speeds outwards from the core along two opposite channels through the BLR, NLR and the interstellar medium of the host galaxy. The beams finally terminate often deep in the intergalactic medium (up to mega-parsec distances in the most extreme cases) and form large radio structures (lobes and hot spots). The earlier mentioned radio galaxy Cygnus A is a prototype for such (powerful) AGN seen edge-on.

Within the relativistic jet model, an important feature is relativistic Doppler boosting of synchrotron emission into the direction of motion. Together with the presence of a torus, which obscures the nucleus (BLR and AD) for certain viewing angles, the appearance and thus identification of an AGN is consequently expected to depend strongly on its orientation relative to our line of sight. Therefore unification schemes try to explain the variety of AGN types with a few intrinsic "host populations" seen at different angles (e.g. Urry & Padovani 1995). The basic parameters in modern unification schemes are luminosity, viewing angle, radio loudness and age.

This thesis concentrates on two types of radio-loud AGN: flat-spectrum (core dominated) radio quasars and BL Lacs, often collectively addressed to *blazars*. Within the unification scheme, blazars are the sources, where the relativistic jet is pointing towards the observer, thus we see the jet almost face on (see Figure 1.1). Their host populations are most likely the lower luminosity FR I (BL Lacs) and powerful FR II radio galaxies (quasars). The overall SED of blazars is usually non-thermal and consists of two spectral components, the first peaking in the IR through X-ray band and the second in the γ-ray domain. The

latter extends sometimes even into the TeV band. While the first peak is produced via synchrotron emission of the relativistic particles, the second peak is likely caused by inverse Compton scattering of soft photons by the same electron population responsible for the synchrotron emission. Among other characteristic features (flat or inverted radio spectrum; unusual emission lines etc.), blazars are extremely compact on milli-arcsecond (mas) scale with a morphology dominated by the strongly boosted and compact core emission. Observed with Very Long Baseline Interferometry (VLBI), blazars usually appear unresolved, slightly resolved or show a core-(bent) jet structure. Important characteristics are their outstanding activity/variability across the whole electromagnetic spectrum and superluminal motion in their jets.

1.2 Variability of AGN

Since the discovery of quasars, variability studies have proven to be an important tool to investigate the emission process in AGN[1]. Matthews & Sandage (1963) made the first size estimates of the emitting regions applying causality arguments to the time scales of variable optical intensities. Time scales (known at that time) of weeks led directly to small source sizes of only several light weeks and immediately discarded a stellar origin of the optical emission. The subsequent discovery of month to year time scale variations in the radio regime by Dent (1965) and Sholomitskii (1965) suggested similar small source structures in radio sources and therefore high brightness temperatures and photon densities - higher than allowed by catastrophic cooling beyond the inverse Compton limit. This led to the idea of bulk relativistic motion in the jets of AGN (Rees 1967). The subsequent development of VLBI could confirm both, relativistic speeds in the jets due to the detection of apparent superluminal motion, and compact source structures. As a result, the 'brightness temperature problem' could be solved in the framework of relativistic Doppler boosting and the variability proved to be intrinsic. Furthermore, long-term VLBI studies revealed a close relation between structural changes in AGN (on pc-scale) and the observed changes in their measured intensities.

Early observations in other regimes (e.g. optical, X-ray, γ-ray) already revealed even more rapid (days to hours) variability in AGNs. This can be usually attributed to an source-intrinsic origin. Heeschen (1984) undertook very systematic studies to search for short-term variations also at radio wavelengths. Low amplitude changes on time scales of weeks (7–21 days) at 3.3 GHz were detected in about 50 % of a large sample of sources. This variability was found to be limited to flat-spectrum sources, whereas steep-spectrum sources did not show what was called *flickering*. The conclusion was drawn that sources with a flat spectrum are more compact than those exhibiting a steep spectrum. In subsequent studies the origin of the variations could be proven to be source-extrinsic (Heeschen & Rickett 1987): due to its galactic latitude dependence flickering is most likely to be produced by scattering of the radio emission in the galactic, interstellar medium (ISM).

Intensive studies with the Effelsberg 100 m telescope in the mid-eighties (and later with the Very Large Array, VLA) by A. Witzel, D. Heeschen and their collaborators established the discovery of radio variability in blazars on even shorter time scales of about one day (Witzel et al. 1986, Heeschen et al. 1987). Such intraday variability was found to be present in about 30 % of these objects (Quirrenbach et al. 1992, Kraus et al. 2003) and revealed extremely tiny dimensions of the emitting core regions. If the rapid variability is intrinsic to the source, causality implies physical sizes of light days. With the recent detection of even faster sources (~ 0.5 hours, e.g. Kedziora-Chudczer et al. 1997), intrinsic IDV

[1] Interestingly, the first radio source Cygnus A was recognized by Hey et al. (1946) due to its radio variability. Later, this variability could be attributed to scintillation in the Earth's atmosphere.

reveals even light hour physical sizes or nano-arcsecond angular sizes. For that reason, IDV poses fundamental problems to any theoretical interpretation due to excessive brightness temperatures. Hence, the cause of the variations seen in IDV sources (hereafter IDVs) is still controversial with major claims being made for either (i) a source intrinsic or (ii) extrinsic origin due to scattering in the ISM similar to the phenomenon of flickering or pulsar scintillation.

1.3 Scope of this Thesis

Although radio IDV was already discovered about 15 years ago and intensive observational and theoretical studies were performed to provide a complete description of the phenomenon, it still asks for a final explanation. The present situation suggests a complicated mixture of both, source intrinsic and extrinsic effects. However, there is increasing evidence for *interstellar scintillation* (ISS) to play the major role at least in the "extreme" IDV sources. One has to note, that the involved sizes of blazar cores are sufficiently small to scintillate in the ISM. For this reason scattering can be expected to be always present. Hence, the main questions in the context of radio IDV can be summarized as: (i) is there an intrinsic contribution to radio IDV at all ? (ii) can we clearly identify ISS in all IDV sources and thus confirm the extrinsic origin and model all features of IDV with ISS ? (iii) if IDV is indeed a mixture of both effects, can we disentangle those and find a consistent combination of both to fully explain the observed phenomenae ?

The work presented here should be regarded as a further contribution to shed some light on the physical mechanism in operation. In order to find (to some extent) answers to the questions above, a few new approaches have been followed in this work.

The first part of this thesis is dedicated to a new phenomenon in IDV studies. In the most extreme IDVs, the annual modulation of the radio variability has attracted a lot of attention. A scattering model, which takes the Earth's motion with respect to the scattering medium into account, can nicely explain this feature and clearly identifies ISS as origin of the IDV seen in these sources. In order to detect such seasonal cycles also in "normal" IDV sources, a new Effelsberg monitoring program over a period of about two years was carried out. Three sources were examined for this purpose, while our studies concentrated on the quasar 0917+624 where such effect was already suggested earlier (Rickett et al. 2001, Jauncey & Marquart 2001). Parallel to the Effelsberg observations, a VLBI monitoring of this source was performed aiming the investigation of intrinsic structural changes and their influence on the IDV behavior.

The search for an intrinsic contribution to the IDV pattern is a further subject of this thesis. Here, high frequency observations are of particular importance. Due to its frequency dependence, ISS should vanish with increasing frequency and an intrinsic contribution (if present) should show up in the mm- and sub-mm regime. In September 1998, the BL Lac 0716+714 showed 20 % peak-to-peak variations during 48 hours of observations with Effelsberg at 32 GHz (Krichbaum et al. 2002, Kraus et al. 2003). This was the first detection of IDV at mm-wavelengths. Motivated by these findings, a new project has been started to search for IDV at 32 and 345 GHz in a small sample of IDV sources. In this framework, the multi-frequency results for one particular source, J1819+3845, are investigated in view of ISS.

A totally new approach is the attempt to directly detect the required scattering material in front of intraday variables. The presence of a screen of ionized material in the ISM of our Galaxy responsible for ISS had been suggested many years ago. Until now, only indirect hints do exist and no attempts were performed to directly detect the medium along the line of sight. The possibility of a direct search for the required material is introduced. Along with the investigation of a possible connection between source positions and particular ISM features, first spectral line observations towards

IDV sources are presented.

This thesis is structured as follows. The subsequent chapter gives an introduction to IDV and the theoretical models proposed to explain the phenomenon. It shall provide a short summary of the present situation. The following chapters are organized in three major parts: Chapters 3 to 5 are dedicated to our annual modulation studies containing a description of the model, our long-term IDV monitoring with Effelsberg and the parallel VLBI-monitoring of the main target 0917+624. In Chapter 6, the high-frequency approach is presented. The attempt to search for the scattering medium in the local ISM is the subject of Chapter 7. Along with suggestions for future work, Chapter 8 summarizes the results and the conclusions.

1.4 Conventions

The following conventions were followed throughout this thesis:
(i) A spatially flat universe was assumed with the cosmological parameters measured by the Wilkinson Microwave Anisotropy Probe (WMAP) of $H_0 = 71\,\mathrm{km\,s^{-1}\,Mpc^{-1}}$, $\Omega_m = 0.27$, and $\Omega_\Lambda = 0.73$ (e.g. Bennett et al. 2003).
(ii) The spectral index α is defined as $S \propto \nu^{-\alpha}$.

2

Introduction to IDV - Theory versus Observations

In the radio regime, the flickering of extragalactic radio sources on time scales of weeks was addressed to interstellar scattering in our Galaxy (Heeschen & Rickett 1987). In contrast, flux density outbursts on time scales of months to years have been observed in the radio as well as other regimes (e.g. mm, optical) since decades. Such flares are often clearly accompanied by the ejection of new VLBI components in the innermost regions of these sources. Shock-propagation in the jets emerging from the nucleus is generally believed to be the origin of such activity (e.g. Valtaoja et al. 1992).

The situation for the observed rapid intraday variations is somehow more complicated and still under debate (see Wagner & Witzel 1995 for a review). Here, intrinsic as well as extrinsic explanations were proposed, whereas the observational situation suggests a complicated mixture of both effects. The following chapter shall provide a short introduction to intraday variability in the radio regime. The observational properties of the IDV phenomenon will be presented in comparison with the theoretical models trying to explain IDV.

2.1 Observational Appearance of Intraday Variability

Radio intraday variations could be established as a frequent phenomenon in compact radio cores through independent observations with different telescopes or truly simultaneous observations of constant calibrators. These observations have clearly demonstrated the reliability of IDV, showing changes in amplitude and polarization on time scales of hours to two days (e.g. Witzel et al. 1990). More detailed investigations revealed two types of IDV. They are classified by the so-called first-order structure function $SF(\tau)$ of the observed light curves (Heeschen et al. 1987). Such time series analysis led to the distinction between changes on scales significantly longer than ~ 50 hours (type I - IDV) and variability with time scales less than ~ 50 hours (type II - IDV). Observations of a larger sample of sources deduced from the S5-radio catalog (Kühr et al. 1981a, 1981b) led to the statistical conclusion that about 30 % of compact blazar cores can be expected to exhibit the faster type II - IDV (Quirrenbach et al. 1992, Krichbaum et al. 1992, Quirrenbach et al. 2000, Kraus et al. 2003).

The type of the observed object is important for the occurrence of IDV. Nearly without exception, intraday variations appear only in compact, flat-spectrum BL Lacs and core-dominated quasars containing at least ~ 80 % of their source total flux in the central region. The more extended, typical core-jet, steep-spectrum sources do not show such rapid variations. Due to the small viewing angles towards these objects this indicates that compactness plays an important role in the IDV phenomenon.

The appearance of IDV in the observed light curves can be summarized as follows: radio

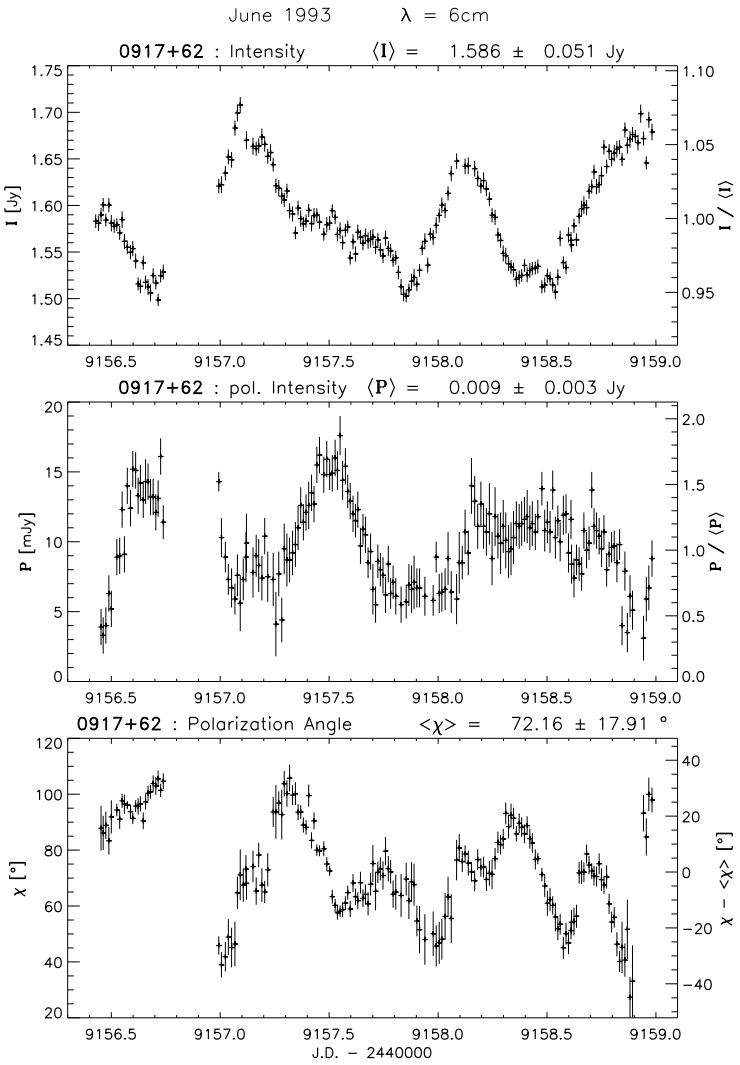

FIGURE 2.1— A typical example: IDV in the quasar 0917+624 at 5 GHz (Kraus 1997). From top to bottom are shown total and polarized intensity and polarization angle. Note the short time scale of 0.3 days of the variations and the anti-correlation of total and polarized flux density (top, center). In polarized light the variability amplitude exceeds a factor of 2, whereas in total intensity the relative variability is $10-15\,\%$. The polarization angle displays strong variations on scales of up to 80°.

IDV reveals rapid flux density variability as well as strong variations in the polarization of the emission. An important quantity is the modulation or variability index $m_{I,P}$ of total power I and polarized flux P

$$m_{I,P}\,[\%] = 100 \times \frac{\sigma_S}{< S_{I,P} >}\ , \qquad (2.1)$$

which can be directly derived from the observed light curves. σ_S is the rms flux density variation and $< S_{I,P} >$ the average of the total flux density I or polarized flux density P over time, respectively. The variability amplitudes appear to differ from source to source. While m_I typically ranges between $5-10\,\%$ (e.g. Quirrenbach et al. 2000, and references therein), the variability index m_P in polarized light is more pronounced and can exceed $100\,\%$. The polarization angles typically vary by up to a few ten degrees, but occasionally can show 'flips' by 180°. For most known IDV sources, the intensity and polarization variations are correlated and appear as 'quasi-periodic' oscillations. A typical example for a source showing pronounced IDV is displayed in Figure 2.1. During this period in June 1993, the light curves of the quasar 0917+624

showed variability on time scales of 0.3 days and amplitudes of 10−15 %, while also higher values were observed at other epochs. The variations of total power and polarization plotted in Figure 2.1, however, appear to be anti-correlated. The largest amplitudes in the S5-radio sample were found in 0804+499. Here, Quirrenbach et al. (1992) reported variations on a 35 %-level at 6 cm wavelength.

An important observational result in view of theoretical interpretations is the fact that m_I varies over a broad range of radio frequencies. Figure 2.2 displays multi-frequency observations of 0917+624 in May 1989 during a coordinated campaign with the Effelsberg 100 m and the participation of the Very Large Array (VLA) (Witzel et al. 1990). The data measured between 2 and 20 cm wavelengths reveal strong variations in all wave bands. Individual maxima and minima are visible throughout all frequencies without substantial time lag. In addition, changes in variability amplitude are clearly seen. Here, m_I peaks at λ11 cm and decreases systematically towards both, higher and lower frequencies. The smallest amplitude appears at λ2 cm and is reduced by a factor of $\sim$3. At these shorter wavelengths more fine structure is seen. Such behavior (also with different peak-frequencies at different epochs) was observed in other sources and sometimes with an additional increase of the variability amplitude towards higher frequencies. This behavior is of particular interest in order to discriminate between different theoretical models trying to explain IDV.

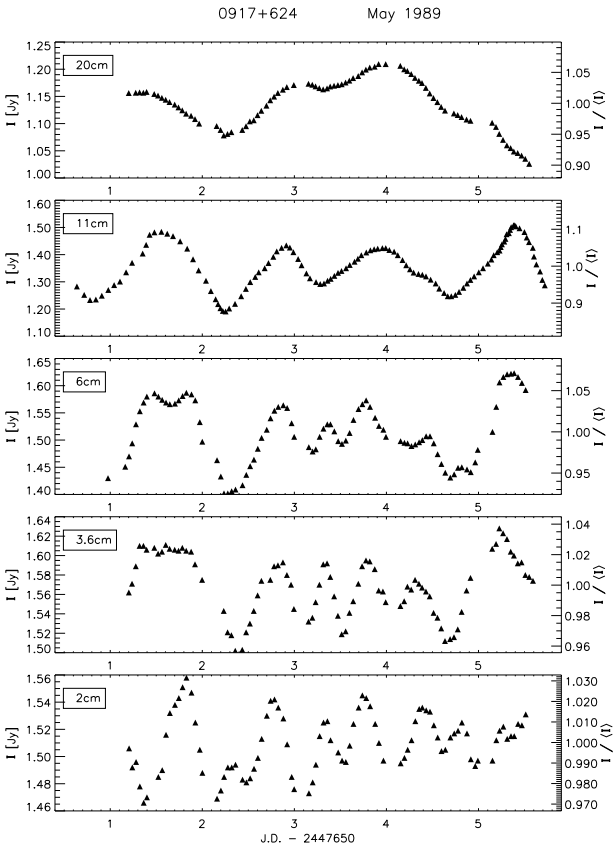

FIGURE 2.2— Multi-frequency observations of the quasar 0917+624 during a coordinated campaign with the Effelsberg 100 m RT and the VLA (plot by A. Kraus, priv. comm.). From top to bottom (note the different scale): total power at 20 cm (VLA), 11 cm (Effelsberg), 6 cm (Effelsberg), 3.6 cm (VLA) and 2 cm (VLA). All bands show marked variability with no indication of substantial time lags between the individual extrema at different wavelengths. Note the pronounced variability amplitude at λ11 cm and the decrease of m_I towards both, higher and lower frequencies.

Examples of sources with the highest amplitudes found today are the "extreme" IDV sources PKS 0405−385, PKS 1257−326 and J1819+3845 (e.g. Kedziora-Chudczer et al. 1997, Bignall et al. 2003, Dennett-Thorpe & de Bruyn 2000). Variations by a factor of three or more on time scales of only $\sim$0.5 hours are common in these extremely compact (point-like) quasars. Due to such extraordinary properties they may form a new, the most extreme class of IDV- type objects.

Not only the strength of variability varies depending on source, observing date and frequency. Also the variability time scale t_{var} appears to vary. Transitions between different IDV modes at the same observing frequency and between different wavebands were observed: in the case of the BL Lac object 0716+714, a transition from a mode of daily to weekly variations ($\Delta t = 1 \rightarrow 5$ days) occurred simultaneously in the radio and optical regime (Quirrenbach et al. 1991, Wagner et al. 1993). Furthermore a strong correlation between radio spectral index and optical flux is observed. Figure 2.3 displays the mentioned observing campaign. In the 4.8 GHz light curve a four

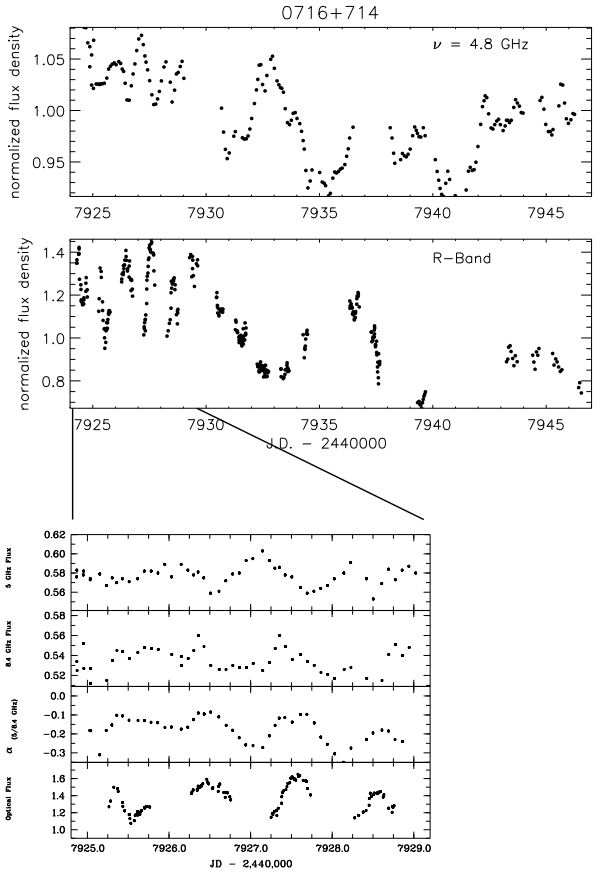

FIGURE 2.3— Correlated radio-optical IDV in the BL Lac object 0716+714 (taken from Wagner & Witzel 1995). **Top:** Variations at 5 GHz are shown, below at R-band. Note the increase of the variability amplitude from about 10 % in the radio to 40 % in the optical and the mutual transition from a fast quasi-periodic variability mode to slower variations after J.D. 2447929. **Bottom:** The fast variability mode in 0716+714 during TJD=7925-7929. This is an enlargement of the previous figure. From top to bottom the variations at 5 GHz, 8 GHz, of the spectral index $\alpha_{5/8\,GHz}$ and the optical R-band are shown. The good correlation of radio spectral index with optical flux density is evident.

day period of daily quasi-periodic variability is accompanied by a jump to slower variations after J.D. 2447929. Similar changes in the time scale were observed also in other sources. For example, the fast and rapid variations of the quasar PKS 0405−385 were observed to be episodic (Kedziora-Chudczer et al. 1997). In 0917+624, variability (time scale 0.8−1.6 days) was seen at cm-wavelengths over many years (1986−1998). The variations suddenly slowed down in September 1998, but the previous fast variability mode was recovered in February 1999 (Kraus et al. 1999)[1].

Also in the most extreme IDV sources, PKS 1257−326 and J1819+3845, similar changes of t_{var} are seen during the last years. Here, the variability time scale shows a modulation with the observing day throughout a year. More detailed investigations of such 'seasonal cycles' are part of this thesis and will be presented in Chapters 3−5.

Attempts to directly relate flux density variations with structural variations in the source itself on VLBI-scales were performed in a few cases. While total intensity maps of IDV sources do not show evidence for convincing changes on such short time scales, polarization IDV seems to be more common: Gabuzda et al. (2000a, 2000b) reported daily polarization variations (polarized flux and polarization angle) in the VLBI structure of 0716+714, 0917+624 and 0954+658. Here, the locations of the polarization variations in the sources are different, either in the VLBI-core itself or in the innermost VLBI jet. However, up to now only structural position variations of VLBI components on time scales of weeks have been observed. New space-VLBI observations of the type I IDV source 2007+77 by Krichbaum et al. (2000) show structural changes on a two weeks time scale. This leads to apparent velocities in the innermost region of up to 21 c (see Figure 2.4). In the framework of intraday variability the detection of such high or even higher velocities are of particular importance to relax the intrinsic 'high brightness temperature problem' discussed later.

Further observational constraints on the different interpretations for IDV come from correlated or anti-correlated rapid variations in the images of gravitational lens systems. Here, Biggs et al. (2001) detected flux changes on a time scale of a few days correlated in both images of the lens system B0218+357.

The detection of time delays between the variability patterns observed simultaneously

[1]More recently (in the framework of this thesis), even a stop of strong IDV was observed in this source (Fuhrmann et al. 2002, see Chapter 4).

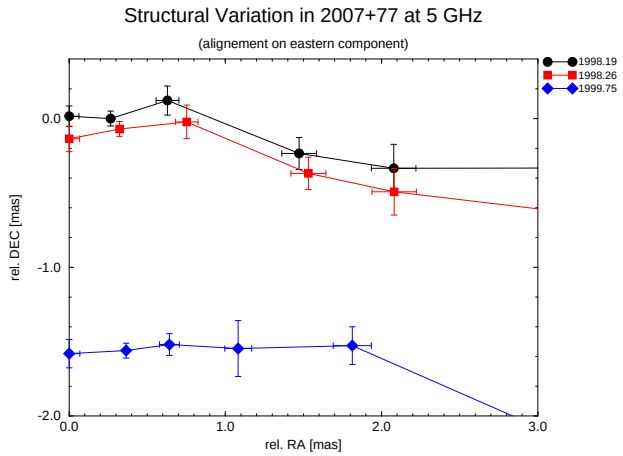

FIGURE 2.4— Structural variation in 2007+77 at 5 GHz. Displayed are 3 different epochs observed with VSOP (Krichbaum et al. 2000). The first two epochs are separated by two weeks, the last two by 1.5 years. Depending on the identification of the components the derived apparent velocity is given within $7\mathrm{c} \leq \beta_{app} \leq 21\mathrm{c}$

at different telescopes has proven to be an important tool to investigate the ISS origin of IDV. For the highly variable sources PKS 0405−385 and J1819+3845 (Jauncey et al. 2000a, Dennett-Thorpe & de Bruyn 2002) significant time lags were found which were used to determine the transverse velocity of the scattering medium.

The appearance of IDV at higher radio frequencies plays a key role in IDV studies in order to discriminate between the different theoretical models. Owing to the difficulty of obtaining well enough calibrated flux measurements in the mm-regime, the attempts to search for IDV at these wavelengths are sparse. Here, the main aim is to trace the modulation index m_I towards higher frequencies, which holds the potential to exclude an extrinsic origin as sole explanation for IDV. In 1998, Wagner et al. suggested the existence of mm-IDV for PKS 0405−385 using the Swedish ESO Submillimeter Telescope (SEST) in Chile. Figure 2.5 shows the detection of flux density variations with amplitudes of more than 50 % at 230 GHz. New evidence for the presence of mm-IDV comes from flux density measurements of 0716+714 performed by Kraus et al. (2003) (see also Krichbaum et al. 2002) using the Effelsberg 100 m telescope. The first clear detection of significant IDV at 32 GHz in September 1998 suggests variations with time scales of ∼12 hours on a 20 %-peak-to-peak level (see Figure 6.2 in Chapter 6). In order to confirm such mm-IDV, new observations with Effelsberg (32 GHz) and the Heinrich Hertz Telescope (HHT) (345 GHz) were performed in the framework of this thesis and will be presented in Chapter 6.

Finally, important in the context with the observational appearance of IDV are the so-called Extreme Scattering Events (hereafter ESEs). They show up as dramatic flux density variations at Gigahertz frequencies and were first detected by Fiedler et al. (1987) for the IDV-BL Lac 0954+658. Such events usually occur on time scales of weeks to months and are characterized by a deep flux minimum in the light curve often accompanied by surrounding maxima. Fiedler et al. explained such events as due to strong scattering of the emission from the extragalactic object by isolated structures (plasma inhomogeneities,"plasma lenses") in the interstellar medium along the line of sight. In March 2000, an even faster ESE appeared in the light curves of 0954+658 during an IDV monitoring project at the 100 m telescope. Here, however, it occurred extremely rapid on a time scale of less than two days (Cimó et al. 2002a) and led to a related size of the refracting structure of ~ 0.04 AU.

2.2 Theoretical Problems of IDV

Nowadays, intraday variations are observed throughout the whole electromagnetic spectrum (see Wagner & Witzel 1995 for a review). In the optical to γ-ray bands, variations on time scales ≤ 1 day pose no severe problem within a source intrinsic interpretation. In the radio bands, however, these short time scales imply a violation of the inverse Compton limit as described in the following.

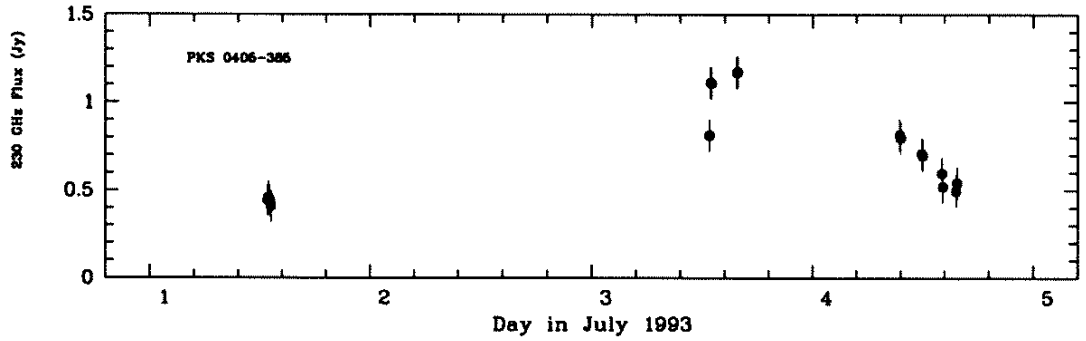

FIGURE 2.5— 230 GHz flux density variations of PKS 0405-385 in July 1993 observed with SEST. Wagner et al. 1998 suggested high frequency IDV on a time scale of two days.

2.2.1 Variability and Source Size: The Causality Argument

The main problem in understanding the physical cause of IDV comes from the short time scales of the variations itself. Using causality arguments, these fast variations imply extremely small source sizes: If the variations are intrinsic to the source, an upper limit for the size of the emitting region follows from the light-travel-time argument. An intrinsic process (illumination) propagates through a region with diameter d introducing a maximum in the light curve lasting for the time Δt. Following the theory of relativity nothing can travel faster than the speed of light c and the linear size of the emitting region d is limited to

$$d \leq c\,\Delta t\,. \tag{2.2}$$

Taking into account the relation between the linear size d and the angular extend θ

$$d = D_A\,\theta = \frac{D_L}{(1+z)^2}\,\theta\,, \tag{2.3}$$

the maximum angular extend of a variable component can be estimated using the measured time scale. Here, z is the redshift of the source and D_A the cosmological angular diameter distance. For a flat universe ($\Omega_m + \Omega_\Lambda = 1$), the cosmological luminosity distance D_L can be approximated by (Pen 1999):

$$D_L = \frac{c}{H_0}[z + (1 - \frac{3}{4}\Omega_\mathrm{m})z^2 + (9\Omega_\mathrm{m} - 10)\frac{\Omega_\mathrm{m}}{8}z^3 + \ldots]\,. \tag{2.4}$$

Using equations 2.2 and 2.3 leads to

$$\theta \leq \frac{(1+z)^2}{D_L}\,c\,\Delta t \tag{2.5}$$

and the maximum angular size of a variable component (with the observed time scale Δt) in useful units is given by

$$\theta_\mathrm{max} = 0.173\,[\mathrm{mas}]\frac{(1+z)^2\,\Delta t\,[d]}{D_L\,[Mpc]}\,. \tag{2.6}$$

Here, the angular size θ_max, the time scale Δt and the luminosity distance D_L is given in milli-arcseconds [mas], days [d] and megaparsec [Mpc], respectively.

The light curve of 0917+624 shown in Figure 2.1 provides a typical example. Using the cosmological parameters measured by WMAP of $H_0 = 71\,\mathrm{km\,s^{-1}\,Mpc^{-1}}$ and $\Omega_m = 0.27$, the observed time scale $\Delta t = 0.3$ days yields a maximum angular size of only $0.03\,\mu$as at a redshift of $z = 1.446$. Thus, IDV studies in principle provide an angular resolution much higher than achieved with present radio telescopes[2], including Space- and mm-VLBI. While present resolutions are accessible on scales $\sim 50-300$ micro-arcsecond, variability studies nowadays offer nano-arcsecond structures for the most IDVs, in particular, for the extreme IDV sources. Note that even if the variations are not intrinsic and the causality

[2] About 40 years ago, the discovery of variable structures on time scales of months to years and related physical sizes of light months to light years (using the causality argument) led directly to the development of VLBI.

argument does not apply, angular sizes derived from interstellar scintillation must be smaller than a few tens of micro-arcseconds.

2.2.2 The Brightness Temperature of a Variable Component

The maximum angular sizes can be used to estimate the brightness temperature of the emitting region. Taking into account an emitting component with Gaussian brightness distribution and angular diameter θ, the brightness temperature can be expressed as (e.g. Kraus 1997):

$$T_B = 1.22 \cdot 10^{12} \frac{S}{\theta^2 \nu^2} \ . \qquad (2.7)$$

Together with equation 2.6 for the maximum angular size of a variable component, equation 2.7 yields a 'variability brightness temperature' in Kelvin [K] for a variable source structure with variability amplitude ΔS,

$$T_B = 4.5 \cdot 10^{10} \Delta S \left(\frac{\lambda D_L}{\Delta t (1+z)^2} \right)^2 \ , \quad (2.8)$$

expressed in useful units of flux density S [Jy], wavelength λ [cm], luminosity distance D_L [Mpc] and time scale Δt [d]. It immediately becomes clear that IDV time scales reveal apparent brightness temperatures as high as 10^{21} K for the most extreme variable sources. Taking the previous example of 0917+624, equation 2.8 yields a brightness temperature of $T_B = 7.79 \times 10^{18}$ K for the variations seen in Figure 2.1 (ΔS = 0.14 Jy).

2.2.3 The Inverse Compton Problem

Such high values of T_B observed in IDV blazar cores imply a violation of the inverse Compton (IC) limit. The involved mechanism is the catastrophic cooling of the relativistic electrons due to IC scattering beyond a maximum brightness temperature limit of 10^{12} K (Kellermann & Pauliny-Toth, 1969): IC scattering of the synchrotron radiation field from radio into the X-ray regime by the emitting electrons leads to dramatic energy losses. This effect is strongly temperature dependent and limits the brightness temperature of observed radio sources to a certain value $T_{\rm max}$. This becomes clear by taking the ratio of inverse Compton radiation L_C to synchrotron radiation L_S into consideration. L_C/L_S consists of a first order ($\sim (T_{\rm max}/10^{12})^5$) and a second order scattering term ($\sim (T_{\rm max}/10^{12})^{10}$). For temperatures of $T_{\rm max} < 10^{11}$ K, the ratio L_C/L_S becomes <1. When the temperature exceeds 10^{12} K, so $T_{\rm max} > 10^{12}$ K, the second order scattering term becomes important and

$$L_C/L_S \sim (T_{\rm max}/10^{11})^{10} \ . \qquad (2.9)$$

In such conditions, brightness temperatures in excess of 10^{12} K lead to catastrophic IC cooling and the brightness temperature decreases to a value below 10^{12} K, where IC and synchrotron losses are of the same order. For a maximum brightness temperature of $\sim 10^{11}$ K at 1 GHz, the half-life of the emitting electrons is about 10^4 years. In contrast, an increase of $T_{\rm max}$ towards 10^{12} K leads to a half-life of about 1 day and decreases with the -7^{th} power of $T_{\rm max}$.

The strong dependence of Compton scattering on $T_{\rm max}$ implies that T_B can not be dramatically higher than 10^{12} K except for very short periods after an observed radio outburst (where IC is expected to provide a significant contribution to the X-ray flux). Here, Slysh (1992) discussed the possibility of transient periods with T_B's greatly exceeding the IC limit ($\sim 10^{15}$ K) due to non-stationary processes and particle acceleration (compensation of the IC losses). In any case, the violation of the IC limit by several orders of magnitudes poses substantial problems for any theoretical interpretation. Each theoretical model trying to explain IDV has to overcome this 'high brightness temperature problem'. The different approaches will be introduced in the forthcoming sections with particular emphasis on the observational situation.

2.3 Intrinsic Explanations

All attempts to explain IDV and the connected high brightness temperatures intrinsic

to the source rely mainly upon the relativistic jet model introduced in the first chapter. The different explanations can be divided into two classes related to the involved radiation process, each containing "subclasses" with different physical assumptions.

2.3.1 Beaming in relativistic Jets

Early variability studies indicated already a violation of the IC limit due to the high T_B's deduced from the months- to years variability discovered in compact radio sources. In addition, early VLBI observations have shown that the compact radio emission can be resolved into a series of discrete "knots" moving in an often only one-sided jet on pc-scales. These knots were found to separate from an apparently stationary, synchrotron self-absorbed core with speeds greater than the speed of light. This apparent superluminal motion as well as the observed high T_B's could successfully be explained within the (today generally accepted) relativistic jet model. Here, the knots are relativistically moving features in a collimated flow of synchrotron emitting plasma at small angles to the line of sight (e.g. Blandford, McKee, and Rees 1977, Blandford & Königl 1979). An important consequence is that relativistic effects are involved which change the appearance of important parameters of the source. For example, the synchrotron radiation pointing towards the observer gets Doppler boosted, while receding radiation gets de-boosted. The Doppler factor

$$D = \frac{1}{\Gamma(1 - \beta \cos\theta)} \ , \qquad (2.10)$$

with the bulk Lorentz factor $\Gamma = 1/\sqrt{1-\beta^2}$, the angle θ between the direction of motion and the line of sight, and the velocity in units of c, $\beta = v/c$, relates the quantities in the observers frame with those in the comoving frame (e.g. Rybicki & Lightman 1979):

$$\begin{aligned} S_{obs} &= \left(\frac{D}{1+z}\right)^{3-\alpha} \cdot S \qquad (2.11) \\ \nu_{obs} &= \frac{D}{1+z} \cdot \nu \\ t_{obs} &= \left(\frac{D}{1+z}\right)^{-1} \cdot t \end{aligned}$$

The factor $D^{3-\alpha}$ with spectral index α is strictly valid for an isotropically emitting blob moving in the jet flow. This dependence is reduced to $D^{2-\alpha}$ for a continuous jet. The resulting amplification (reduction) of an approaching (receding) synchrotron jet close to the line of sight can be dramatic and naturally explain the one-sidness of compact radio sources. Other quantities become Doppler shifted as well. The frequency in the observers frame appears higher and the observed time scale is shortened.

Together with equation 2.8 for T_B of a variable component, the transformation of the flux density given in equation 2.11 yields the relation between the observed and intrinsic brightness temperature. For flat-spectrum sources ($\alpha \simeq 0$), it follows

$$T_B^{obs} \simeq \left(\frac{D}{1+z}\right)^3 \cdot T_B \ . \qquad (2.12)$$

Thus, in order to explain the excessive brightness temperatures of up to 10^{21} K deduced from IDV, Doppler factors as high as 100–1000 are required to bring the apparent values down to the IC limit of 10^{12} K. Taking as example 0917+714, a Doppler factor of $D = 267$ is needed to reduce the observed $T_B = 7.79 \times 10^{18}$ K to the required 10^{12} K. In contrast, the superluminal speeds usually observed in the jets of compact radio sources allow for Doppler boosting of the order 10–20 (e.g. Witzel et al. 1988, Kellermann et al. 2000). Even the most extreme speeds observed with VLBI so far, $v_{app} \approx 40\,c$ (Marscher et al. 2000), can only explain moderate values of D.

The situation becomes even more extreme, when following the arguments of Begelmann, Rees & Sikora (1994). Relativistic jets emitting with a surface brightness of 10^{12} K are radiatively inefficient. They should carry their high energy as bulk motion over long distances which is not observed. Therefore, Readhead (1994) suggested that incoherent synchrotron jets emit at a brightness temperature where

magnetic energy and particle energy are in equipartition: $T_E \sim 2 \times 10^{11}$ K. This conditions would even enlarge the values for D given earlier by a further factor 2–3. In addition, the maximum synchrotron emissivity of relativistic jets radiating at the inverse Compton limit sets an upper limit for the Doppler factor: $D \sim T_B^{-1/4} U^{7/16}$ (Begelmann, Rees & Sikora 1994). Here, the kinetic energy flux requirement U becomes uncomfortably high - comparable to the total power of the source for Doppler factors > 100 (for $T_B^{obs} \sim 10^{18}$ K).

In summary, relativistic Doppler boosting alone is not able to explain IDV intrinsically. Several models based upon relativistic jets with additional physical assumptions were developed in order to overcome the afore mentioned problems. These models will be shortly introduced in the following sections.

2.3.2 Shock-in-Jet- and Geometrical Models

The earlier mentioned discrete "knots" found in the jets of quasars and BL Lacs are usually interpreted as shocks propagating down the jet. In this picture, the knots are supposed to be the "hot downstream regions" of these shocks along the jet. The often observed month- to years variability ("outbursts") in the cm- and mm light curves of these sources could successfully be explained within such shock-in-jet models (Marscher & Gear 1985, Valtaoja et al. 1988, Hughes et al. 1989a, 1989b). The latter authors show that both, the appearance of VLBI maps of superluminal sources (and their components) and the characteristics of total and polarized flux outbursts are likely be associated with the propagation of one or a series of closely spaced shocks. In this framework, the adiabatic compression of particles and fields can lead to a strong increase in flux density. Its spectral and temporal evolution is characterized by three stages, the Compton, synchrotron and adiabatic phase. Its maximum (at the turnover frequency) propagates from high to low frequencies, whereas its amplitude increases in the first two stages and finally decreases in the third phase. A great success of this model is the "natural" explanation of polarization variations. While on kpc-scales the magnetic fields in these jets are suggested to be slightly ordered along the jet flow (e.g. Roberts et al. 1990), its orientation is mostly random inside the jet. A strong compression due to a passing shock front tends to order these magnetic fields perpendicular to the flow direction. In addition to an outburst in synchrotron radiation (and therefore in total flux density), the compression will produce a substantial increase of the polarized emission. In this framework, multi-component models (two or more close shock fronts) have been invoked to explain the often larger and more rapid variability in polarization compared to total intensity. Furthermore, rapid polarization angle variations can be expected for a shock changing its orientation with respect to the jet direction when moving in a helical jet structure (e.g. Königl & Choudhuri 1985).

Owing to the success of these models for long-term radio variability, it was natural to apply them to IDV time scales. Many theoretical efforts have been made to fine-tune the above (or similar) models and to account for particular features seen in IDV light curves (e.g. quasi-periodicity, (anti-) correlations between S and P, spectral changes). Different physical assumptions led to different kinds of jet-based models trying to explain IDV, such as:

(i) Interaction between relativistic shocks and small scale inhomogeneities or turbulences in the jet (Qian et al. 1991, Marscher 1992),
(ii) Small changes (due to a swinging or oscillating jet) in the viewing angle of shocks inside a relativistic jet (Gopal-Krishna & Wiita, 1992),
(iii) Modified shock-in-jet model, where a shock moves in a magnetically confined jet with oscillating jet width (Qian et al. 1996),
(iv) Lighthouse effect: helical motion of superluminal knots in highly collimated jets (Camenzind & Krockenberger 1992),
(v) Electron-sheets propagating through

oblique standing shocks in jets (Spada et al. 1999),
(vi) Relativistic aberration due to anisotropic radiation of a shock moving in a slightly curved jet (Qian et al. 2000).

In the model of Qian et al. (1991), the time scale, t_{var}, of variability produced in a shock-in-jet model is directly related to the distance traveled by the relativistic shock along the jet between two extrema in the light curve. In order to scale the usually longer time scales down to IDV time scales, this corresponds to spacial scales of less than $\sim 0.2\,\mathrm{pc}$ in the jet (for reasonable values of Γ and D of the shock). This may reflect the inhomogeneities in the electron density and/or magnetic field distribution along the jet. Consequently, Qian et al. (1991, model (i)) proposed a two component model: a moving thin shock component which illuminates these inhomogeneities in the underlying, stable jet component close to the line of sight. Using this assumption, all characteristic features in the multi-frequency IDV of 0917+624 could be explained (total and polarized flux variability, anti-correlation and polarization angle swing, spectral evolution). In particular, the T_B-problem is solved. The size of the emitting region is now determined by the shock thickness and the jet radius and can be much larger than the source size determined by causality arguments. Thus, boosting factors matching the observed values are sufficient to reach $10^{12}\,\mathrm{K}$.

Other characteristic features seen in IDV-light curves require modifications and/or additional assumptions. In order to explain the particular features seen during the correlated radio-optical variations in 0716+714, (e.g. the behavior of radio spectral index and optical variations), Qian et al. (1996, model (iii)) proposed a modified shock-in-jet model with a special geometry. Here, the shock propagates through a magnetically confined jet with oscillating jet width. The authors find for small angles to the line of sight a D^5 scaling rather than the usual D^3 for T_B.

Other models include modifications due to geometrical effects (e.g. models (ii), (iv) and (vi)). In addition to intrinsic changes of the flux as assumed in the previous cases, intrinsic IDV can be produced by temporal changes of the viewing angle for $\theta \lesssim 1/\Gamma$. If, for example, the shock (or knot) moves along a curved, helical or swinging jet close to the line of sight, θ is time dependent and the Doppler factor changes with time:

$$D(t) = \frac{1}{\Gamma(1 - \beta\cos\theta(t))} \ . \qquad (2.13)$$

This leads to temporal changes of the flux density in the observers frame ("lighthouse effect"). Taking into account equation 2.11, changes of $\Delta\theta$ result in changes of the observed flux density of the order (Kraus 1997):

$$\frac{\Delta S}{S} \leq m\,\Gamma\,\Delta\theta \ , \qquad (2.14)$$

where m denotes the exponent of the Doppler factor in equation 2.11. Thus, small changes of $\Delta\theta \sim 0.5^\circ$ can produce variability of a few 10 % for reasonable values of Γ.

Due to relativistic aberration, radiation emitted in the plane of the shock with a viewing angle $\theta(t)$ would then appear to arrive at the observer at a time dependent angle $\theta'(t)$:

$$\theta'(t) = \frac{\cos\theta(t) - \beta}{1 - \beta\cos\theta(t)} \ . \qquad (2.15)$$

In addition to the changes introduced by the Doppler factor $D(t)$, changes in the aberration angle θ' can produce strong variations, especially in the polarized emission.

In summary, small swings of the jet or minor changes in the trajectories of shocks can lead to substantial changes in total flux, polarization, polarization degree and polarization angle on IDV time scales. By fine-tuning the changes in θ, correlations and anti-correlations between these quantities and even polarization angle swings can be explained (models (ii) and (vi)).

2.3.3 Theory vs. Observations: Pros and Cons

The discrepancy between observed and required Doppler factors of about two orders

of magnitude poses substantial problems for any intrinsic interpretation. Even if a Doppler factor of $\sim$ 100 would be theoretically possible, we are still left with a gap of two or three orders of magnitude between the observed and allowed T_B after correcting for Doppler boosting. For this reason, Doppler boosting alone is not able to explain sources radiating with apparent brightness temperatures of $\sim 10^{18} - 10^{21}$ K.

Although shock-in-jet models allow to relax the T_B problem, the short time scales require very thin shocks. At radio frequencies, however, radiative losses are unlikely to provide such thin emission layers (Marscher 1992). It is furthermore unclear, whether thin shocks can travel long distances along a turbulent relativistic flow and produce the high duty cycle and often self-similar variability pattern. In addition, the opacity in the shocked material is expected to vary due to the scanned inhomogeneities in the jet. This should result in time lags between light curves at different frequencies which are observed only occasionally. Finally, the proposed special source geometries and required strong alignments to the line of sight make such shock-in-jet explanations unlikely to be observed in about 30 % of all flat-spectrum sources (see also the discussion in Beckert et al. 2002b).

However, intrinsic jet-models are able to explain IDV in a more complete and consistent manner (with reasonable model parameters) for particularly well studied cases (e.g. 0917+624). Even if there is increasing evidence for interstellar scintillation (see below), several observational peculiarities support the idea that IDV is maybe a complicated mixture of intrinsic and extrinsic effects (see also Krichbaum et al. 2002). The observed radio-optical correlation in 0716+714, the observed increasing strength of the variability towards higher frequencies (and the mm-IDV seen in 0716+714 in particular), the daily polarization variations in VLBI images and the correlated intraday variations in the images of the gravitational lens system B0218+357 are examples which are hard to reconcile with extrinsic interpretations.

2.3.4 Coherent Emission

A more "revolutionary" approach to overcome the high brightness temperatures in IDVs is a scenario where coherent emission processes play an important role in incoherent synchrotron jets (or even replace this paradigm). However, coherent emission is a completely new process, which was not observed in any AGN so far.

Coherent emission can easily produce an extremely high T_B, since its intensity is due to collective emission of all particles within a coherent volume. The basic ingredient is a beam of relativistic electrons moving in an outflow away from the central source. When the beam meets a "low-plasma density zone", where the beam density reaches 0.1 times the turbulent background plasma density, collective emission arises due to scattering of the relativistic electrons in the beam. The electrons scatter coherently from concentrations of intense electric field strength (electrostatic plasma waves). The latter evolves from strong turbulence in such low-density zone generated by the passage of the beam (e.g. Benford 1985, 1992; Baker et al. 1988). Lesch & Pohl (1992) suggested reconnecting magnetic fields in the inner part of the accretion disk and its coronal environment as formation mechanism of the electron beam. The resulting emission is broad-band with a bremsstrahlung-like spectrum and could be investigated in several laboratory experiments. Although the coherent radiation spectrum is expected to exceed the synchrotron emission strongly and therefore would reduce the energy requirements of the central engine, several theoretical problems remain. It is not clear up to now, if the mechanism can explain all characteristics of IDV. The recent detections of circular polarization (CP) in radio sources (e.g. Wardle et al. 1998, Macquart et al. 2000) have rekindled discussions as to its origin. Since CP is predicted for a coherent mechanism, future work has to show if a new radiation process, as coherent emission, is responsible.

2.4 Extrinsic Explanations I: Interstellar Scintillation

The small angular extend of a star (compared to the larger extend of a planet) leads to optical twinkling due to our turbulent atmosphere in front of the star. In the same way, the radio emission of compact astronomical objects is expected to scatter through the turbulent interstellar plasma in our Galaxy. A basic feature in this context is the dispersion of electromagnetic waves due to the index of refraction in an electron-ion plasma (see e.g. Quirrenbach 1989 for details). The latter depends on the electron density n_e in the medium and the observing frequency. The dispersive medium causes an excess propagation path length by introducing a phase shift to the electromagnetic wave. Assuming the scattering plasma exhibits irregularities (spatial and/or temporal fluctuations) in the electron density driven by turbulence in the ISM, the index of refraction and the additional path length will show fluctuations as well. This introduces random phase fluctuations into the wavefront and leads to distortions of the incoming wave producing spatial variations in its amplitude.

Using this approach, the phenomenon of interstellar scintillation could successfully be established as explanation for long-term as well as short-term variations of pulsar signals (e.g. Sieber 1982; Rickett, Coles, and Bourgois 1984). Nowadays, several kinds of long-term (months to weeks) variability found in compact extragalactic radio sources are known to be connected with ISS as well (e.g. Ryle et al. 1978; Fanti et al. 1983; Codes, Ananthakrishnan, and Dennison 1984; Heeschen 1984; Rickett 1986).

In order to produce scintillations responsible for IDV, a few conditions have to be satisfied. Firstly, the scattering plasma should be located at a distance of only $\sim 10-300\,\mathrm{pc}$, constrained by the observed range of variability time scales. Secondly, the IDV source has to exhibit sufficient compact components and the observer has to move with respect to the medium in order to see the variations.

As shown in Section 2.2.1, IDV blazar cores are expected to exhibit micro- or even nanoarcsecond angular sizes. Objects of such small angular extend must scintillate through the interstellar plasma. For that reason ISS must play an important rule also in IDV sources. Indeed, the present situation suggests that the discussion about the origin of IDV can be reduced to the question, if IDV can entirely be explained by ISS.

2.4.1 Models for ISM-Irregularities

In order to describe the phenomenon and give a full prediction of scintillation observables, the knowledge of (i) the spatial density spectrum of the electron density fluctuations and (ii) the distribution of the scattering material in our Galaxy and/or local ISM is essential. The "standard" model is based on a wide-spread distribution of turbulence. Here, the spatial power spectrum of electron density fluctuations in the ISM along the line of sight $\tilde{z}$ at wave number q is described by a power law,

$$\Phi(\tilde{z}, q) = C_n^2(\tilde{z}) q^{-\beta} \tag{2.16}$$

with a large range between a lower cut-off q_{min} (outer scale) and an upper cut-off q_{max} (inner scale). C_n^2 is a measure for the strength of turbulence in the direction of $\tilde{z}$ and can be assumed to be proportional to n_e^2 (Rickett 1970). One has to note, that also other models have been suggested. "Single-scale" models attribute the ISM irregularities to discrete, large/small-scale structures in the Galaxy, e.g. radio loops or single cloud structures (e.g. Shapirovskaya, 1978; Wambsganss et al. 1989), similar to those refracting structures postulated to explain extreme scattering events. In this framework, Qian et al. (submitted) considered a specific cloud-plasma-lens scenario in front of the quasar 1150+812. The observed polarization angle swing in this source can then be explained in terms of refractive focusing/defocusing caused by a small cloud located in the Galactic Loop III at a distance of $\sim 130\,\mathrm{pc}$. They point out that a combination of clouds with different size and

structure could account not only for specific "events", but also produce normal intraday variability.

Usually, "normal" ISS is used and the power law index in equation 2.16 is assumed to be of Kolmogorov form, $\beta = 11/3$ (e.g. Rickett 1986). However, pulsar scintillation studies show evidence that a Kolmogorov spectrum is too simple and ask for an enhancement on the larger spatial scales ($10^{13} - 10^{14}$ cm) relative to the smaller ($10^9 - 10^{10}$ cm) scales (Lambert & Rickett 2000). For this reason, e.g. a $\beta = 4$ model was discussed by the latter authors (see also Armstrong, Rickett & Spangler 1995) which then would physically include also a clumpy ISM consisting of discrete, discontinuous structures (e.g. clouds with sharp boundaries or supernova shock fronts). Recent structure function modeling by Beckert et al. (2002a, 2002b) suggests even steeper spectra with $\beta \sim 4.3 - 4.6$ for the IDV in 0917+624.

It has been argued that the interstellar density fluctuations are highly anisotropic and elongated along the local magnetic field configuration in the medium (Desai, Gwinn, & Diamond 1994). Thus, Chandran & Backer (2002) discussed an anisotropic Goldreich-Sridhar power spectrum for the ISM density fluctuations.

For the distribution of scattering material in the Galaxy, the models of e.g. Taylor & Cordes (1993) and Bhat, Gupta, & Rao (1998) provide the scattering strength C_n^2 along the line of sight. Based upon pulsar scintillation measurements, the former authors modeled its distribution with a two component model: (i) a locally uniform galactic disk with $\sim$700 pc scale height and (ii) a more clumpy component (spiral arms) superimposed. The model of Bhat et al. provides details for the local ISM with enhanced scattering material in a shell at $\sim 50{-}150$ pc around the Sun.

2.4.2 Scattering Regimes

The earlier mentioned phase change introduced by the medium at distance L and the resulting change in amplitude of an incoming wavefront at wavelength λ can be described by the Fresnel-Kirchhof integral (Narayan 1992, Born & Wolf 1980). Let $\varphi(x, y)$ be the phase change introduced by a scattering screen at transverse position (x,y), then the amplitude of the wavefront observed at position (X,Y) in the observers plane is

$$\Psi(X,Y) = \frac{e^{-i\pi/2}}{2\pi r_F^2} \int\int \exp\left(i\,\varphi(x,y) + i\frac{(x-X)^2 + (y-Y)^2}{2r_F^2} \right) dx\,dy \quad (2.17)$$

with the Fresnel scale

$$r_F = \sqrt{\frac{\lambda L}{2\pi}}\ . \quad (2.18)$$

The second term in the integral reflects the contribution to the phase due to the excess path length from position (x,y) to (X,Y). For the absence of any scattering, $\varphi(x, y) = 0$, the phase is stationary at $(x, y) = (X, Y)$ and we end up with a circular, coherent patch of radius $\sqrt{2r_F}$ at this position, the first Fresnel zone. In addition to the Fresnel scale, a further characteristic length scale is the diffractive scale r_{diff}. This scale denotes the transverse separation over which the phase fluctuation (rms phase difference) is coherent and considered to be constant to within a specified limit of 1 rad[3]. It is this length scale, which defines the two different regimes of scattering: (i) strong scattering at low frequencies and (ii) weak scattering above a characteristic transition frequency.

Weak Scintillation

This regime is characterized by the condition $r_{diff} \gg r_F$. Here, the random phase fluctuations introduced by the screen over the first Fresnel zone are small and the Fresnel scale keeps the relevant scale in this regime. Thus, the amplitude $\Psi(X, Y)$ in equation 2.17 varies weakly around its unscattered value of unity resulting in only small flux variations (given by $F(X, Y) = |\Psi(X, Y)|^2$).

The changes in flux can be attributed to the effect of weak focusing and defocusing caused

[3] A more detailed definition can be obtained using the "phase structure function", see Narayan 1992.

by the phase fluctuations with length scale $\sim r_F$ producing a scintillation pattern ("scintels") onto the Earth's orbital plane (see Figure 3.3, Chapter 3). An observer aligned with a focusing region of phase fluctuation will see the flux $F(X,Y) > 1$, consequently an observer aligned with a defocusing region will see $F(X,Y) < 1$. For the presence of a transverse velocity v between scattering screen (scintillation pattern respectively) and observer, temporal scintillations will be observed with a time scale given by the Fresnel time scale:

$$t_{scint} \sim t_F = \frac{r_F}{v} \ . \tag{2.19}$$

The strength of the variations described by the modulation index m (compare equation 2.1) is weak and is given by

$$m \sim \left(\frac{r_F}{r_{diff}}\right)^{5/6} < 1 \ . \tag{2.20}$$

The discussion given here is strictly valid for scattering of a point source as long as its angular size θ_S is smaller than the angular size determined by the Fresnel scale:

$$\theta_F = \frac{r_F}{L} = \sqrt{\frac{\lambda}{2\pi L}} \tag{2.21}$$

and thus $\theta_S < \theta_F$. The influence of larger source sizes will be discussed later.

Strong Scintillation

The modulation index for weak scattering in equation 2.20 increases with wavelength and distance. Hence, as we go from weak scattering to greater λ or L, the modulation index will reach about unity[4]. This happens, when the diffractive and Fresnel scales are approximately equal and defines the transition from weak to strong scattering. For extragalactic radio sources this transition is expected between 1 and 5 GHz (e.g. Walker 1998). When r_{diff} becomes smaller than r_F ($r_{diff} \ll r_F$), we enter the regime of strong scattering and the spatial scale splits into two scales (see below). Here, the random phase fluctuations introduced by the scattering medium are much stronger and change by many radians over the Fresnel scale. Thus, the diffractive scale takes over as the relevant scale in this regime and displays the characteristic size of a coherent patch with approximately constant phase within 1 rad.

In the strong scattering regime one distinguishes between two branches[5], since a further length scale becomes important, the refractive scale

$$r_{ref} = \frac{r_F^2}{r_{diff}} \gg r_{diff} \ . \tag{2.22}$$

The latter has its origin in the large scale density fluctuations on length scales $\sim 10^{13}-10^{14}$ cm and is referred to as the branch of 'refractive scintillation'. The diffractive scale r_{diff} is connected with the small scale fluctuations on length scales $\sim 10^{9}-10^{10}$ cm and displays the branch of 'diffractive scintillation'.

Diffractive Scintillation (DISS): This branch of strong scattering produces narrowband, high amplitude, short time scale variations and can be understood as multi-path propagation. Each point in the observers plane receives rays from a large number of points on the scattering plane: a large number of coherent patches of size $\sim r_{diff}$ on the screen scatters radiation into a cone of angle:

$$\theta_{scatt} \sim \frac{\lambda}{r_{diff}} \sim \frac{r_{ref}}{L} \ . \tag{2.23}$$

As result, each point in the observers plane becomes illuminated by many rays (of different patches) with random, uncorrelated phases which interfere and produce a random interference pattern.

The critical angular size for a source to show diffractive effects is given by the diffractive

[4] More precisely, m increases until it saturates at a value greater than unity and when the scattering becomes even stronger it decreases asymptotically towards unity.

[5] This becomes clear using the "spatial intensity power spectrum", which has two peaks at widely separated length scales. See e.g. Rickett 1990 and Narayan 1992.

scale:

$$\theta_{diff} = \frac{r_{diff}}{L} = \left(\frac{r_{diff}}{r_{ref}}\right)^2 \theta_{scatt} \ . \quad (2.24)$$

Thus, for a screen at distance $\sim 100\,\mathrm{pc}$ and $r_{diff} \sim 10^9\,\mathrm{cm}$, a source as small as $\sim 0.7\,\mu\mathrm{as}$ is required. This is the reason, why only galactic pulsars are so far detected to show diffractive scintillations. For a point source with $\theta_S < \theta_{diff}$ the modulation index for diffractive scattering is of order unity (100 % modulations) and the diffractive variability time scale is given by

$$t_{scint} \sim t_{diff} = \frac{r_{diff}}{v} \ . \quad (2.25)$$

Refractive Scintillation (RISS): This branch is characterized by broadband, relatively weak and slow variations due to electron density fluctuations on the much larger length scales $\sim r_{ref}$. Refractive effects can be described as the focusing-defocusing action of phase fluctuations: all cones (with θ_{scatt}) of the coherent patches with size r_{diff} on the screen are focused/defocused towards the observer. Consequently, the radiation of a larger number of coherent patches reaches the observer and the flux is increased. The reverse is true for a defocusing action. The requirement on the source angular size for this regime is much less stringent. The relevant angular size is $\theta_{scatt} = r_{ref}/L$ (equation 2.23). For a point source with $\theta_S < \theta_{scatt}$ the time scale for refractive scintillations is

$$t_{scint} \sim t_{ref} = \frac{r_{ref}}{v} \gg t_{diff} \ , \quad (2.26)$$

and for the strength of the variations follows

$$m \sim \left(\frac{r_{diff}}{r_F}\right)^{1/3} < 1 \ . \quad (2.27)$$

Quenched Scintillation

The previous discussion is only valid for sources (or source components) smaller or approximately equal than the relevant scales in the turbulent medium. The angular size of an extragalactic self-absorbed, incoherent synchrotron source at redshift z is given as (Beckert et al. 2002a)

$$\theta = 2.1\mathrm{mas}\frac{(1+z)}{D}\left[\frac{\nu}{\mathrm{GHz}}\right]^{-1}\left[\frac{S_\nu}{\mathrm{Jy}}\cdot\frac{10^{11}\,\mathrm{K}}{T_B}\right]^{0.5} .$$

It is usually larger than the Fresnel, refractive and in particular, diffractive angular scale for a screen beyond the solar system and at frequencies of a few GHz. For example, the Fresnel angular size at a distance of 5 pc is of the order $50\,\mu$as for an observing frequency of 5 GHz and becomes even more stringent with increasing distance (100 pc: $\sim 10\,\mu$as). Consequently, the amplitude of the variations in weak and refractive strong scattering is mostly quenched by the source size and diffractive effects even disappear entirely by averaging over the large source size. The extended source acts as a spatial filter of size $L\theta_S$ and the scintillation time scale increases while the modulation index decreases. The scalings are as follows (Narayan 1992):

weak scattering ($\theta_S > \theta_F$):

$$t_{scint} \sim t_F\left(\frac{\theta_S}{\theta_F}\right) > t_F \quad (2.28)$$
$$m \sim m_P\left(\frac{\theta_F}{\theta_S}\right)^{7/6} < m_P < 1 \ .$$

refractive strong scattering ($\theta_S > \theta_{scatt}$):

$$t_{scint} \sim t_{ref}\left(\frac{\theta_S}{\theta_{scatt}}\right) > t_{ref} \quad (2.29)$$
$$m \sim m_P\left(\frac{\theta_{scatt}}{\theta_S}\right)^{7/6} < m_P < 1 \ ,$$

whereas the index P denotes the quantity for the case of a point source (equations 2.19−2.20 and 2.26−2.27).

2.4.3 Theory vs. Observations: Pros and Cons

There is increasing evidence for ISS to play an important role in the IDV phenomenon. On the one hand, due to the involved small source sizes, IDV sources must scintillate and therefore ISS should at least partly contribute to

the observed variations. On the other hand, recent observations clearly suggest that ISS is the sole origin for the extreme rapid IDV seen in the sources PKS 0405−385, PKS 1257−326 and J1819+3845. Here, the detected time lags between the simultaneous light curves observed at two distant telescopes can not be of intrinsic origin. The same is true for the detection of an annual modulation in the variability time scale which can nicely be explained within an ISS interpretation.

The flickering of radio sources could be established as ISS due to its galactic latitude dependence (stronger variability towards the enhanced scattering material in the galactic disk). For IDV, such dependence is not observed and often cited as argument against an ISS explanation for IDV. However, such dependence is not necessarily to be expected, since IDV probes more local ($\sim 15 - 100\,\mathrm{pc}$) regions of enhanced scattering material in contrast to the former sources. Such local, concrete features and components of the ISM in front of IDVs should not reflect a galactic latitude dependence.

The observed frequency dependence of the modulation index and the variability time scale (compare Figure 2.2), where, for example, m is often strongest around 5 GHz and weaker towards both lower and higher frequencies, is expected for the transition between strong and weak ISS. Although this applies to several sources, it is not generally observed and intrinsic "source evolution" has probably to be taken into account. The episodic variations in PKS 0405−385, for example, complicate the situation, since the screen is not expected to "vary" on such time scales (Kedziora-Chudczer et al. 1998).

Scintillation induced, anti-correlated polarization and in particular, polarization angle variations can only be explained taking two or more component models into account. The observed variability in polarization is then the result of the vector sum of the polarized components which can produce anti-correlations and polarization angle variations. Although such source models can fit the observations quantitatively very well (e.g. Rickett et al. 1995, Rickett et al. 2002), the complicated polarization and polarization angle variations have not been fully reproduced by ISS until now.

In addition, the observed brightness temperature derived from ISS scales only linearly with the Doppler factor. Although already strongly reduced, the often high values of $T_B \sim 10^{13} - 10^{14}\,\mathrm{K}$ still require quite high Doppler boosting ($\sim 10-100$) depending on the assumed screen distance. Similar to the argument given earlier against an intrinsic origin, even for ISS this provides problems. It implies an uncomfortable large fraction of sources which are beamed extremely close towards us. In particular, de Bruyn (priv. comm.) recently reported the discovery of diffractive scintillation in J1819+3845. If confirmed, the size of the scintillating component is as small as $\lesssim 1\,\mu$as. This immediately suggests brightness temperatures of order $10^{16}\,\mathrm{K}$ and again, boosting factors of $D \gtrsim 10^4$ are needed.

Moreover, the observed features presented in Section 2.3.3, e.g. the radio-optical correlation and the increase of m towards higher frequencies are hard to reconcile with ISS. Towards higher frequencies m should vanish: in the weak scattering regime, both a point source (equation 2.20) and an extended source (equation 2.28, here depending on the frequency behavior of the source size) should show decreasing scintillations. This is the reason why ISS can not explain variability at high frequencies and in particular in the optical regime.

2.5 Extrinsic Explanations II: Microlensing

For this type of propagation effect trying to explain IDV, more "cons" than "pros" do exist. Already in the sixties, Barnothy (1965) suggested the possibility of variability in the flux density of a background source due to the presence of a large mass distribution (intervening galaxy or single stars) along the line of sight. Here, relative velocities between ob-

server, source and lens system lead to a variable magnification with time and thus to variability in the observed flux.

Several observational findings suggest that microlensing can be excluded as general explanation for IDV (e.g. "special geometry" not observed, absence of a redshift dependence, similar problems with T_B and high Doppler factors, frequency dependence of IDV not in agreement with such achromatic effect). For this reason, the effect of microlensing as origin of IDV will not be discussed in further detail here (see e.g. Quirrenbach 1989, Gopal-Krishna & Subramania 1991 and Kraus 1997 for a detailed discussion).

Part I: Seasonal Cycles due to the orbital Motion of the Earth

3

Annual Modulations in Intraday Variable Blazar Cores

The first major part of this thesis is dedicated to a pretty new phenomenon in the field. In 2000, Dennett-Thorpe & de Bruyn reported a dependence of the variability time scale on the day of the year in the quasar J1819+3845. In order to explain this behavior, they suggested an ISS scenario, where the changing relative velocity between Earth and scattering screen over the course of a year produces a seasonal cycle in the variability time scale of the scintillations.

In view of ISS this idea is not new and was suggested already for the low-frequency variability of extragalactic radio sources by Bondi et al. (1992). The new point is its application to IDVs and the possibility to use its detection as further proof for ISS being responsible also for intraday variability. Consequently, the confirmation of such seasonal cycles in IDV sources holds the potential to disentangle between an intrinsic or extrinsic origin of IDV. As by-product, it will constrain both, properties of the interstellar medium (e.g. distance, velocity dispersion and anisotropy) and source parameters (e.g. source structure and size of the scintillating compact component).

3.1 Introduction

In the ISS model described in the previous chapter no special consideration was given to a possible influence of the change in the Earth's velocity vector relative to the screen.

Bondi et al. (1992, 1994) observed a large sample of low frequency variable sources at 408 MHz and reported the discovery of an annual variability in the time scales for these slowly variable sources. They interpreted this effect as due to the changing Earth's velocity vector along its orbit around the Sun throughout a year. Such explanation is based on the standard ISS model (e.g. Rickett et al. 1995), but takes into account the difference between the motion of the observer and the scattering medium. It turns out that, if these velocities are comparable in magnitude, the relative velocity will change as the Earth moves parallel with, and six months later, against the motion of the scintillation pattern projected onto the solar system. In the former case the relative velocity is low, in the latter, high. The ISS time scale depends on the observers motion through the spatial scintillation pattern. Consequently, in the first case the variability time scale will be lengthened, in the latter it will be shortened.

At present, such seasonal cycles have been clearly detected only in the two most extreme IDV sources: J1819+3845 (Dennett-Thorpe & de Bruyn 2000, 2003) and more recently in PKS 1257−326 (Bignall et al. 2003). In the framework of this thesis, new observations were performed in order to identify seasonal cycles also in "normal" IDV sources. Hence, the first part of the thesis (Chapter 3 to 5) is dedicated to a deeper investigation of this effect: Chapter 3 will give an overview and develop model predictions for the variability time scale with emphasis on three particular

sources. Chapter 4 will present our new Effelsberg flux-density-monitoring program of a small IDV sample performed during 2000 and 2003 in order to (i) confirm a similar effect also in other IDV sources and (ii) to investigate the predictions of such annual modulation model in more detail. Finally, Chapter 5 will focus on the VLBI monitoring of 0917+624 performed in parallel to the flux density monitoring. This part will try to connect intrinsic structural changes in the source with the outcome of a possible seasonal effect in our data.

3.2 Annual Modulations in IDV

Westerbork observations of the quasar J1819+3845 during a period of 12 months have clearly demonstrated a variation of the IDV time scale. In particular, a slow-down of the variability near day 280 was detected. Figures 3.1 and 3.2 display the situation. While the variability remains almost constant and extremely fast over the course of the year, between July and December (days $\sim 200-350$) a prolongation of the variability time scale by up to a factor of ~ 10 becomes visible. In the following year this prolongation was observed again (Dennett-Thorpe & de Bruyn 2003, Figure 3.1) strongly supporting ISS as cause of the intraday variations in this source. In addition to the Earth's motion with respect to the Local Standard of Rest (LSR), the best fit with an ISS model requires a medium velocity of $\sim 25\,\mathrm{km\,s^{-1}}$ at a distance of about 20 pc (see Figure 3.2). For quasar PKS 1257−326, the best reproduction of the data yields a LSR velocity of $\sim 5\,\mathrm{km\,s^{-1}}$ for a screen at a distance of $\sim 10-15$ pc (Bignall et al. 2003).

In the standard ISS model, the Earth - and by this, the observer - moves through a scintillation pattern projected onto the Earth's orbital plane. The variability time scale is then determined by two quantities: the spatial scale of the "scintles" and the observers velocity projected onto the scintillation pattern. In order to explain the seasonal cycles of the variability time scale in terms of ISS, the relative motion of the Earth with respect

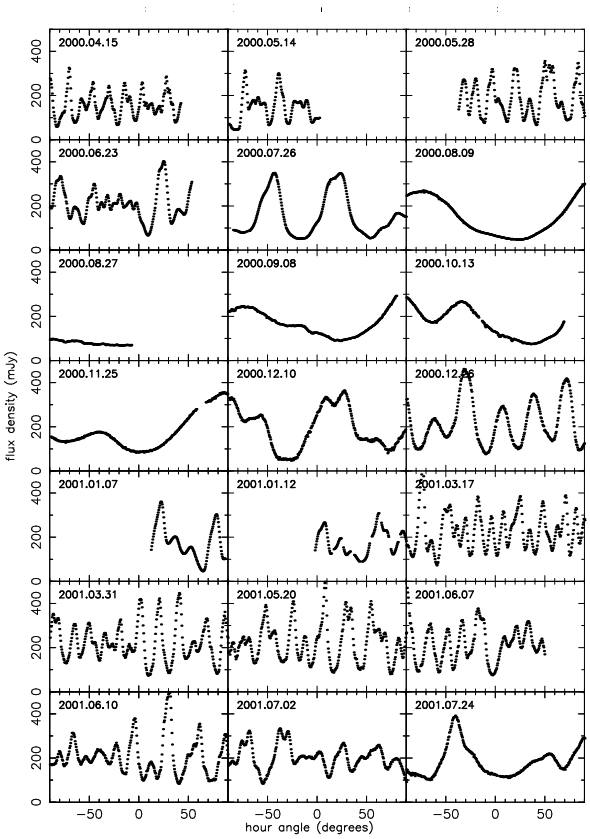

FIGURE 3.1— Light curves of J1819+3845 over a 15 months period between 2000 and 2001 observed with Westerbork at 4.9 GHz (taken from Denneth-Thorpe & de Bruyn 2003). Note the high amplitudes and often sinosoidial variability pattern. While the variability is usually extremely fast (~ 15 minutes), a 'slow down' period between July and December with much longer time scales (~ 120 minutes) is clearly visible.

to the scattering medium (and its change in particular) has to be taken into account[1]. This relative motion is composed of three different velocities[2]:

1. the velocity of the Earth's orbital motion around the Sun: $\mathbf{V}_\oplus$
2. the velocity of the Sun in the LSR frame: $\mathbf{V}_\odot$
3. the velocity of the scattering medium with respect to the LSR: $\mathbf{V}_\wr$

Figure 3.3 shows an illustration of the situation. The Earth and the solar system moves

[1]The proper motion of the extragalactic radio source itself is negligible.

[2]In the following, boldface letters denote vectors.

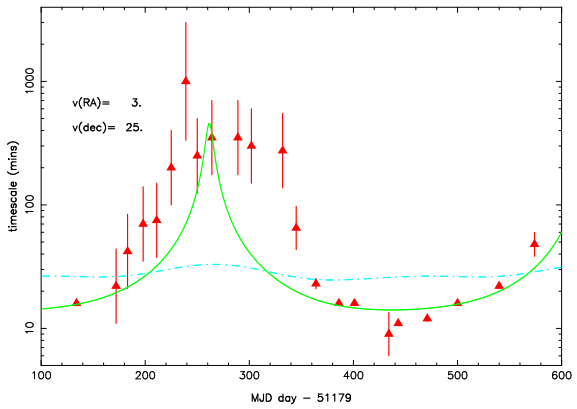

FIGURE 3.2— Scintillation time scales of J1819+3845 throughout one year deduced from the Westerbork observations between May 1999 and May 2000 (taken from Dennett-Thorpe & de Bruyn 2000). The highly variable quasar J1819+3845 shows a clear prolongation of the variability around day 280. The solid line displays the best χ^2-fit to the data for a screen velocity of $v(RA) = -5\,\mathrm{km\,s^{-1}}$ and $v(Dec) = 25\,\mathrm{km\,s^{-1}}$. The dash-dotted line represents the predictions for a screen moving at rest in the LSR.

through the pattern produced by a galactic screen in front of an IDV source. The different velocities involved are indicated by different vectors. These velocity vectors have to be combined to the total velocity $\mathbf{V}$ giving the "true" relative velocity vector between Earth and scattering screen:

$$\mathbf{V} = \mathbf{V}_\odot + \mathbf{V}_\oplus - \mathbf{V}_\wr \,. \tag{3.1}$$

In order to make predictions for the ISS time scale, which then can be tested directly by observations, each velocity component has to be calculated and subsequently combined through equation 3.1. This will be done in the following using the known relations from spherical trigonometry:

$$\cos a = \cos b \cos c + \sin b \sin c \cos A \tag{3.2}$$

and

$$\frac{\sin a}{\sin A} = \frac{\sin b}{\sin B} = \frac{\sin c}{\sin C} \tag{3.3}$$

for a nautical triangle with angles A, B, C and sides a, b, c.

3.2.1 Earth's Motion around the Sun

We first have to define an appropriate reference frame. Following Qian & Zhang (2001), we assume an equatorial coordinate system with its zero-point fixed at the center of the Sun. The x-axis points towards the equinox, the y-axis towards the terrestrial equator at right ascension 6^h and the z-axis in direction to the north pole. In this case, the relations between the coordinates x, y, z and the equatorial coordinates of a source, α, δ, are given by

$$\begin{aligned} \cos x &= \cos\alpha \cos\delta \\ \cos y &= \cos\delta \sin\alpha \\ \cos z &= \sin\delta \end{aligned} \tag{3.4}$$

using the trigonometrical relations given in equations 3.2 and 3.3. In such a reference frame, the right ascension and declination of the Earth ($\alpha_\oplus$, $\delta_\oplus$) are:

$$\begin{aligned} \alpha_\oplus &= \alpha^*_\odot + 180^\circ \\ \delta_\oplus &= -\delta^*_\odot \,, \end{aligned} \tag{3.5}$$

where $\alpha^*_\odot$ and $\delta^*_\odot$ denote the Sun's right ascension and declination in the usual geocentric equatorial coordinate system. Taking the Astronomical Almanac (1999) and defining the relations

$$k = 180^\circ/\pi \tag{3.6}$$

$$t = \tan^2(0.5\epsilon) \tag{3.7}$$

we are able to calculate the Sun's coordinates

$$\begin{aligned} \alpha^*_\odot &= \lambda - ft\sin 2\lambda + \\ &\quad + 0.5ft^2 \sin 4\lambda \,, \\ \delta^*_\odot &= \arcsin(\sin\epsilon \sin\lambda) \end{aligned} \tag{3.8}$$

throughout a year using the following relations:

$$L = 280.46^\circ + 0.985647\,n \tag{3.9}$$

$$g = 357.528^\circ + 0.9856003\,n \tag{3.10}$$

$$n = \text{day of year} - 1.5 \tag{3.11}$$

$$\begin{aligned} \lambda &= L + 1.915^\circ \sin g + \\ &\quad + 0.02^\circ \sin 2g \end{aligned} \tag{3.12}$$

$$\epsilon = 23.439^\circ \,. \tag{3.13}$$

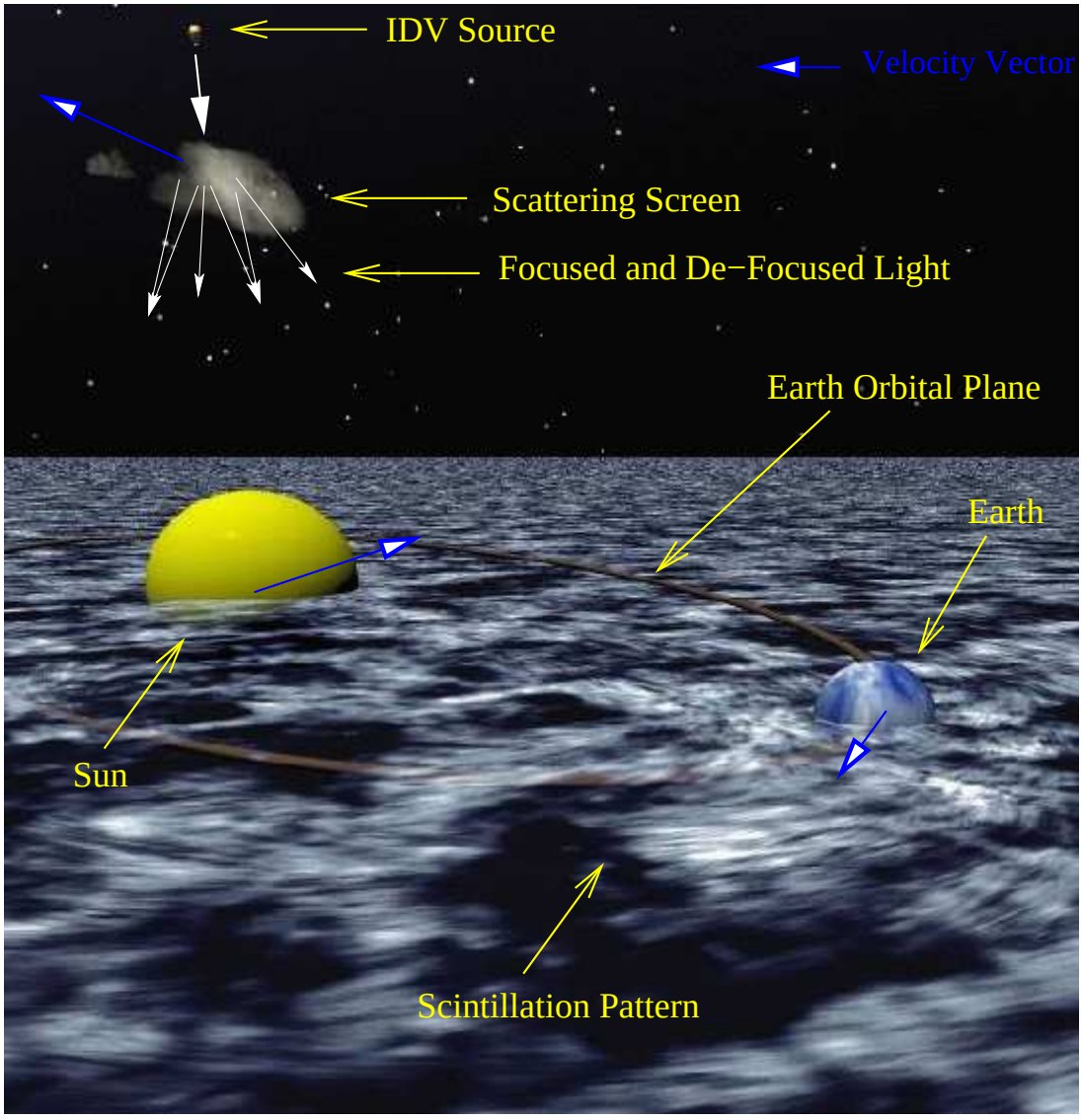

FIGURE 3.3— A sketch of the annual modulation model: the screen produces bright and dark patches onto the earth orbital plane by focusing and de-focusing the light from the IDV source. The Earth and the solar system moves through this spacial scintillation pattern producing the observed flux density variations. The time scale of the scintillations depends upon the relative velocity of the Earth with respect to the scattering screen. Hence, all velocity vectors (Sun, Earth and screen; blue vectors) have to be taken into account.

Here, L is the longitude of the Sun, g the anomaly, λ the ecliptic longitude and ϵ the angle of the ecliptic with respect to the Sun's plane, respectively. The spatial velocity of the Earth's orbital motion around the Sun can then be calculated by

$$\begin{aligned} \mathbf{V}_\oplus &= -V_\oplus \frac{\sin\delta_\oplus}{\sin\epsilon} \cdot \mathbf{X}_0 \\ &\quad + V_\oplus \cos\alpha_\oplus \cos\delta_\oplus \cos\epsilon \cdot \mathbf{Y}_0 \\ &\quad + V_\oplus \cos\alpha_\oplus \cos\delta_\oplus \sin\epsilon \cdot \mathbf{Z}_0 \ , \end{aligned} \tag{3.14}$$

where $\mathbf{X}_0$, $\mathbf{X}_0$ and $\mathbf{Z}_0$ correspond to the unit vectors of the coordinate system X,Y,Z. The velocity of the Earth is given by $V_\oplus = 29.8\,\mathrm{km\,s^{-1}}$.

3.2.2 Sun's Motion in the LSR Frame

The second velocity component involved is the Sun's motion with respect to the LSR. The so-

lar system is known to move in the LSR frame with a velocity of $V_\odot = 16.6\,\mathrm{km\,s^{-1}}$ in the direction towards the solar apex (Gilmore & Zeilik 2000). The equatorial coordinates (B 1950) of this direction are

$$\begin{aligned} \alpha_{apex} &= 267.0^\circ \\ \delta_{apex} &= 28.0^\circ \ . \end{aligned} \tag{3.15}$$

Using equations 3.4 and the coordinates 3.15 of the solar apex direction, the Sun's velocity in the LSR frame can be expressed as

$$\begin{aligned} \mathbf{V}_\odot &= V_\odot \cos\alpha_{apex}\cos\delta_{apex}\cdot\mathbf{X}_0 \\ &\quad + V_\odot \sin\alpha_{apex}\cos\delta_{apex}\cdot\mathbf{Y}_0 \\ &\quad + V_\odot \sin\delta_{apex}\cdot\mathbf{Z}_0 \ . \end{aligned} \tag{3.16}$$

3.2.3 The Screen Velocity

The third velocity component required to calculate the total velocity in equation 3.1 is the LSR velocity of the scattering screen in front of the scintillating source. Neglecting the possibility that the scintillations are produced by multiple layers with different velocities at different distances, we assume the scattering to occur in one single screen. As result, the entire scattering medium can be described by one distinguished velocity at a certain distance. Since the important quantity in the ISS model is the observer's transverse velocity through the scintillation pattern, the motion of the screen along the line of sight can be neglected. The velocity components of the scattering material can then be assumed to be a composition of its motion in right ascension $V_{\alpha_\wr}$ and declination $V_{\delta_\wr}$ along the source position. We can write

$$\mathbf{V}_\wr = \mathbf{V}_{\alpha_\wr} + \mathbf{V}_{\delta_\wr} \ . \tag{3.17}$$

The two components can be calculated to be

$$\begin{aligned} \mathbf{V}_{\alpha_\wr} &= -V_{\alpha_\wr}\sin\alpha_\wr\cdot\mathbf{X}_0 + V_{\alpha_\wr}\cos\alpha_\wr\cdot\mathbf{Y}_0 \ , \\ \mathbf{V}_{\delta_\wr} &= -V_{\delta_\wr}\cos\alpha_\wr\sin\delta_\wr\cdot\mathbf{X}_0 \\ &\quad - V_{\delta_\wr}\sin\alpha_\wr\sin\delta_\wr\cdot\mathbf{Y}_0 \\ &\quad + V_{\delta_\wr}\cos\delta_\wr\cdot\mathbf{Z}_0 \ , \end{aligned} \tag{3.18}$$

where $\alpha_\wr$ and $\delta_\wr$ denote the position of the screen in front of the source (usually the position of the IDV source).

3.2.4 The Earth's transverse Velocity through the Scintillation Pattern

Finally, all velocity components (equations 3.14, 3.16 and 3.18) have to be combined to determine the total velocity using equation 3.1. The components (V_x, V_y, V_z) of this relative Earth speed with respect to the scattering medium are then given by

$$\begin{aligned} V_x &= -V_\oplus\frac{\sin\delta_\oplus}{\sin\epsilon} + V_\odot\cos\alpha_{apex}\cos\delta_{apex} \\ &\quad + V_{\alpha_\wr}\sin\alpha_\wr + V_{\delta_\wr}\cos\alpha_\wr\sin\delta_\wr \ , \\ V_y &= V_\oplus\cos\alpha_\oplus\cos\delta_\oplus\cos\epsilon \\ &\quad + V_\odot\sin\alpha_{apex}\cos\delta_{apex} - V_{\alpha_\wr}\cos\alpha_\wr \\ &\quad + V_{\delta_\wr}\sin\alpha_\wr\sin\delta_\wr \ , \\ V_z &= V_\oplus\cos\alpha_\oplus\cos\delta_\oplus\sin\epsilon V_\odot\sin\delta_{apex} \\ &\quad - V_{\delta_\wr}\cos\delta_\wr \ . \end{aligned} \tag{3.19}$$

The relevant velocity for the ISS model is the transverse motion of the Earth through the scintillation pattern. For this reason the relative velocity projected perpendicular to the source direction has to be calculated using equations 3.19. Assuming θ to be the angle between the total velocity $\mathbf{V}$ and the line of sight towards the IDV source, the transverse speed through the pattern is

$$V_\perp = V\cdot\sin\theta \tag{3.20}$$

with

$$V = \sqrt{V_x^2 + V_y^2 + V_z^2} \ . \tag{3.21}$$

The term $\sin\theta$ is equal $(1-\cos^2\theta)^{\frac{1}{2}}$ and $\cos\theta$ can be expressed as

$$\begin{aligned} \cos\theta &= \frac{V_x}{V}\cos\alpha_\wr\cos\delta_\wr + \frac{V_y}{V}\sin\alpha_\wr\cos\delta_\wr \\ &\quad + \frac{V_z}{V}\sin\delta_\wr \ . \end{aligned} \tag{3.22}$$

Using the known values of (i) the source coordinates, (ii) the velocities $V_\odot$, $V_\oplus$ of Sun and Earth, respectively and (iii) the Earth's coordinates given in 3.5 (using the Sun's coordinates defined in 3.8), we are able to calculate the relative velocity between Earth and scintillation pattern projected perpendicular to each

individual source direction. This can be done for any assumed screen LSR velocity $(V_{\alpha_l}, V_{\delta_l})$ at any day of the year. It turns out that, for sources like 0917+624, the velocity due to the Earth's orbital motion around the Sun nearly cancels the projected velocity of the Sun relative to the LSR near day 280. As a result, the predicted relative velocity projected perpendicular to the source direction shows a large annual modulation throughout the year from a maximum of $\sim 40\,\mathrm{km\,s^{-1}}$ to a deep minimum of only a few $\mathrm{km\,s^{-1}}$. If the medium is assumed to exhibit a velocity with respect to the LSR, then the time for minimum velocity can change substantially. Examples of our results will be given in the forthcoming sections (e.g. Figure 3.6).

3.2.5 Predictions for the Variability Time Scale

On its path around the Sun, the Earth "scans" the bright and dark patches (scintles) produced by the scattering screen. As result we observe intensity fluctuations in our light curves. As described in Chapter 2, the variability time scale for ISS is proportional to the length scale of the scintillation pattern s_0 divided by the relative motion of the observer through the pattern transverse to the line of sight, $t_{ISS} = s_0/V_\perp$. Consequently, an annual modulation is expected also in this parameter. It is important to note, that in principle not only the amplitude of the velocity contributes to changes in the variability time scale. The length scale of the pattern may change with orientation due to either an elongated source structure or anisotropy in the scattering plasma. Such configuration results in an asymmetric (elliptical) scintillation pattern and the length scale in t_{ISS} depends on the direction of V as the Earth revolves around the Sun.

Anisotropy in the scattering medium is supported by e.g. the elongations found in scatter-broadened images of radio sources and the ISS modeling of the variability/annual modulation seen in the intra-hour variables (e.g. Desai & Fey 2001; Rickett, Kedziora-Chudczer & Jauncey 2002; Bignall et al. 2003). In the quenched scattering regime effects due to anisotropy become negligible, since the scale of the pattern is then dominated by the angular size of the source itself. In order to produce first predictions for the variability time scale we make the simplification of an isotropic medium and neglect any possible asymmetry in the source structure (Gaussian source).

The length scale of the pattern, s_0, depends on the distance D to the screen and the angular size of the scintillating source. Following Goodman (1997), the characteristic time scale for interstellar scintillation can be written as

$$t_{ISS} = 0.58 \cdot \theta_{eff} \cdot D/V_\perp \qquad (3.23)$$

in units of t_{ISS} - day, D - kpc, θ_{eff} - $10\,\mu$as and $V_\perp$ - $30\,\mathrm{km\,s^{-1}}$. The angular scale, θ_{eff}, depends on the true angular size of the source θ_S, the angular scale of the first Fresnel zone θ_F and the scattering angle θ_d at frequency ν:

$$\theta_{eff} = [\theta_S^2 + (0.71\theta_d)^2 + (0.85\theta_F)^2]^{\frac{1}{2}}\,, \qquad (3.24)$$

where

$$\theta_F = 0.257\nu^{-0.5} D^{-0.5} \qquad (3.25)$$

and

$$\theta_d = 0.293\nu^{-2.2}\mathrm{SM}^{0.6}\ . \qquad (3.26)$$

The exponent -2.2 results from the assumption that the inhomogeneities in the medium follow a Kolmogorov scaling (e.g. Armstrong, Rickett & Spangler 1995). The scattering measure SM describes the cumulative effect of these irregularities along the line of sight l:

$$\mathrm{SM} = \int_0^l C_n^2 dl \approx < C_n^2 > \cdot l\ . \qquad (3.27)$$

The structure constant C_n^2 measures the local scattering properties of the ISM. In order to produce first predictions of the variability time scale the assumption $l = 0.5 \cdot D$ will be used.

3.3 A possible Candidate: The Case of 0917+624

The quasar 0917+624 is one of the sources in the original IDV sample, which showed variability on time scales shorter than one day

(Heeschen et al. 1987). Since then, the source was regularly monitored over the last 15 years and generally was found to be strongly variable with amplitude variations of $10 - 20\,\%$ on time scales of $0.8 - 1.6$ days. Furthermore, faster variability was detected in the polarized flux and the polarization angle. Here, larger amplitude variations (up to a factor of 2) are common and once a 180°-swing in the polarization angle was observed (Quirrenbach et al. 1989). The pronounced IDV in this source seems to be directly correlated in the wavelength range $2 \leq \lambda \leq 11$ cm (compare Figure 2.2). The polarized flux density is observed to be usually anti-correlated with the total flux density (Kraus et al. 2003, compare Figure 2.1). On milliarcsecond-scales (Standke et al. 1996), the source is dominated by a compact core with a jet pointing in north-south direction (see Figure 3.4). The latter exhibits a more compact feature out to 10 mas, but seems to extend outwards up to 30 mas as diffuse, extended structure. As origin of the rapid variations both, intrinsic (e.g. Qian et al. 1991) as well as scintillation effects (e.g. Rickett et al. 1995) were suggested.

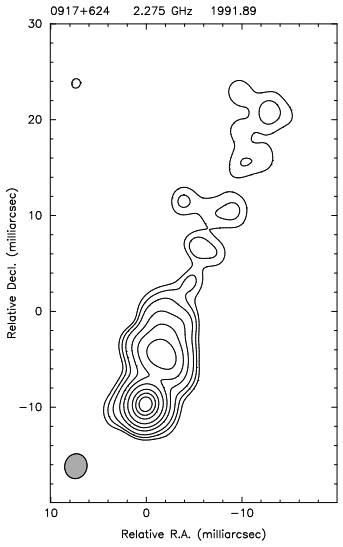

FIGURE 3.4— The quasar 0917+624 on mas-scale observed with VLBI at 2 GHz (Standke et al. 1996). The source exhibits the typical core-jet structure with a bright, compact core component and a jet oriented towards north-south direction. Diffuse, extended jet emission is visible out to 30 mas from the core.

In September 1998, Kraus et al. (1999) detected a remarkable change in the variability properties: the rapid variability stopped and only a slow, monotonic increase of 7 % in flux density over the 5 day observing session was observed (Figure 3.5). Observations in February 1999 then showed 0917+624 to be variable again on a time scale of 1.3 days. Kraus et al. (1999) interpreted the slow-down in September as probably due to either a disappearance of the scintillating compact component or an increase in its angular size: the ejection of a new jet component temporarily could lead to a core size much larger than the scattering size (set by the ISM) and a reduction of the observed interstellar scintillation (quenched ISS, Chapter 2).

An alternative possibility to explain the behavior of 0917+624 within an ISS model was given by Rickett et al. 2001 (see also Jauncey and Macquart 2001). They suggested that the observed change in the variability time scale depends on the time of the year and thus reflects the orbital motion of the Earth relative to the ISM. Hence, using an ISS model for 0917+624 (Rickett et al. 1995) together with the orbital motion scenario presented in Section 3.2, the prolongation in September 1998 could be explained.

In order to investigate this idea in more detail, we will use the results of our calculations presented in Section 3.2. In Figure 3.6 (left) the velocity of the Earth relative to the LSR projected perpendicular to the direction of 0917+624 is displayed versus day of the year. Near day number 285 the velocity of the Earth's orbital motion nearly cancels versus the projected velocity of the Sun relative to the LSR. Consequently, the predicted time scales in Figure 3.6 (right) remain nearly constant over a large fraction of the year and show a substantial prolongation in September and October (days 250−330).

In Figure 3.6 (right) we overplot the predicted and observed time scales and find a general agreement between the observations and

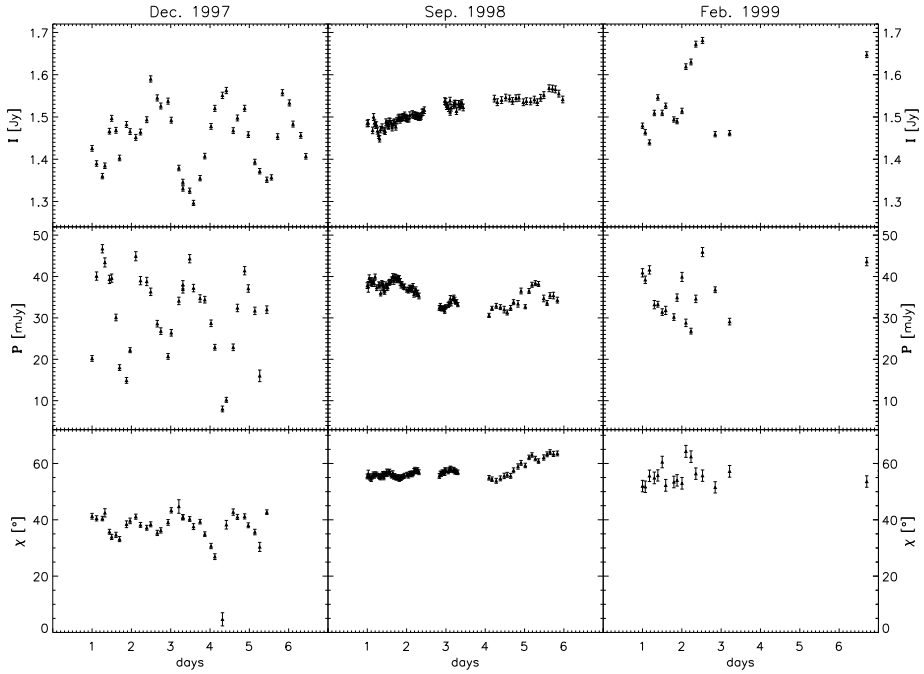

FIGURE 3.5— Flux density measurements at $\lambda 6$ cm of 0917+624 by Kraus et al. (1999) between December 1997 and February 1999. From **top** to **bottom**: total flux density I, polarized flux density P and polarization angle χ plotted against time. Note the remarkable prolongation of the variability time scale in September 1998 and the return to fast variability in February 1999.

the predictions. The data point in September from Kraus et al. (1999) lies in the period of the predicted increase. The other data points come from observations performed during 1989−2000 with the Effelsberg telescope and the VLA at 6 cm wavelength (Quirrenbach 1989, Kraus 1999, Quirrenbach et al. 2000, Cimó 2003, Kraus et al. 2003). We use the 6 cm data as the wavelength most commonly observed. The time scales were estimated using a structure function analysis on each time series (Heeschen et al. 1987). The errors of the obtained time scales are usually high ($\sim 50\%$) due to the often low number of observed variability cycles per epoch. A detailed discussion of the time scale analysis and the connected errors will be given in the context of our new observing campaigns (Chapter 4).

The model predictions were calculated for suitable values of (i) the distance D to the screen, (ii) the source size θ_S and (iii) the strength of scattering $< C_n^2 >$ (Rickett et al. 1995, Rickett et al. 2001, Qian et al. 2001). The parameters which were used are summarized in Table 3.3.

Since we have only one data point during the highly interesting time period (September and October), a new monitoring program was required in order to confirm the annual modulation in this source. These new observations will be presented in Chapter 4.

3.4 Applications to the Medium and the Source Structure

As in the case of J1819+3845 (Figure 3.2), a good sampling of the variability time scale throughout a year allows us to detect a clear presence of the annual cycle and the short-term variations can be identified as due to interstellar scintillation. In turn, this constrains important parameters of both the source structure and the screen properties. In general, a large difficulty in modeling the observed IDV parameters (variability strength and time scale) via ISS is the inaccurate knowledge of (i) the distance D to the screen,

Source	α_{J2000} [hh mm ss.ss]	δ_{J2000} [±dd mm ss.s]	D [kpc]	θ_S [μas]	$< C_n^2 >$ [$10^{-3.5} m^{-20/3}$ kpc]
0716+714	07 21 53.45	+71 20 36.4	0.35	70	0.5
0917+624	09 21 36.23	+62 15 52.2	0.15	70	0.5
0954+658	09 58 47.25	+65 33 54.8	0.15	70	0.5

TABLE 3.1— Coordinates and ISM parameters for each source direction used in the calculations of the relative velocity and variability time scale.

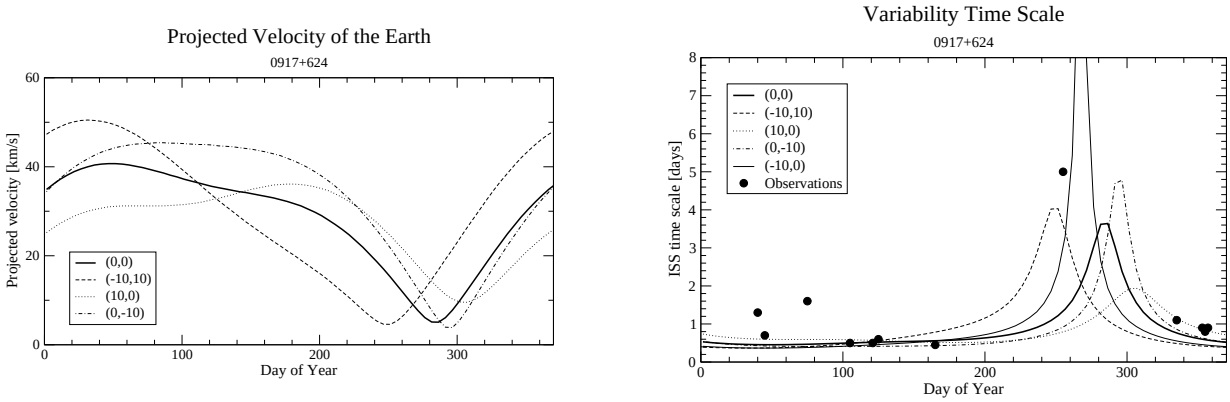

FIGURE 3.6— **Left:** the velocity of the Earth relative to the LSR projected perpendicular to the direction of 0917+624 versus day of the year for 4 different velocities of the screen (V_α, V_δ). Note the strong decrease near day 285. **Right:** resulting prolongation in the predictions of the variability time scale. We overplot the predicted and the observed time scales and find a good agreement (see text).

(ii) the source size and (iii) the relative velocity V to the scattering material.

The observed time scales throughout the year together with the better model for the relative velocity (as given in Section 3.2) thus jointly constrain both size of the scintillating component and screen distance – a larger source size requires a smaller distance and vice versa (distance-diameter constraint).

The scattering medium exhibits a few additional free parameters which have to be taken into account when modeling the annual cycle. As shown earlier, an offset of the screen velocity from the LSR introduces two additional parameters (the screen LSR velocities in RA and Dec). As can be seen from Figure 3.6 for 0917+624, the velocity of the medium is not expected to exhibit a large offset from the LSR, since the prolongation in September 1998 occurred close to the prediction based on the assumption that the medium is stationary in the LSR ($V_\alpha, V_\delta = 0, 0$). This suggests an upper bound on the range of velocities in the ISM of about $10\,\mathrm{km\,s^{-1}}$ (thin lines in Figure 3.6). Future observations of the full annual cycle will help us to determine the velocity distribution in the scattering medium more precisely.

In addition, the detection of seasonal cycles opens the possibility to explore anisotropy in both the source structure and the scattering medium. Two additional model parameters occur: (i) the axial ratio of the elliptical scintles and (ii) the orientation of the anisotropy. In such a scenario the orientation of the velocity vector relative to the major axis of the scattering ellipse varies throughout a year producing an additional variation in the spatial scale over 6 months. Together with the changing Earth's velocity, the latter can produce multiple periods of prolongation in the time scale plots. Figure 3.7 displays an example for

0917+624 (B. Rickett, priv. comm.). The different predictions are calculated for the same source and ISS model: a screen at rest in the LSR with Kolmogorov spectrum at a distance of 200 pc and a Gaussian source of 0.05 mas (FWHM) in size. An anisotropic scintillation pattern with axial ratio 0.25:1 has been assumed. The different curves correspond to different orientations of the scattering ellipse (from 0° to 150° as labeled). For example, an orientation of 150°(dashed curve) creates two periods with slower variations near day 120 and day 290.

In summary, a good sampled annual cycle over the course of a year allows to (i) confirm the ISS origin of the variations and (ii) model the ISS and constrain various ISS parameters. For e.g. PKS 1257−326, the best fit to the annual cycle yields a scattering distance of $\sim 10-15$ pc, an anisotropic pattern with axial ratios < 0.5, screen velocities of $v(RA) = 5\,\mathrm{km\,s^{-1}}$, $v(Dec) = 0\,\mathrm{km\,s^{-1}}$ and a source size of $30-37\,\mu$as (Bignall et al. 2003). In particular, a time offset (which itself shows an annual cycle) is observed between the IDV

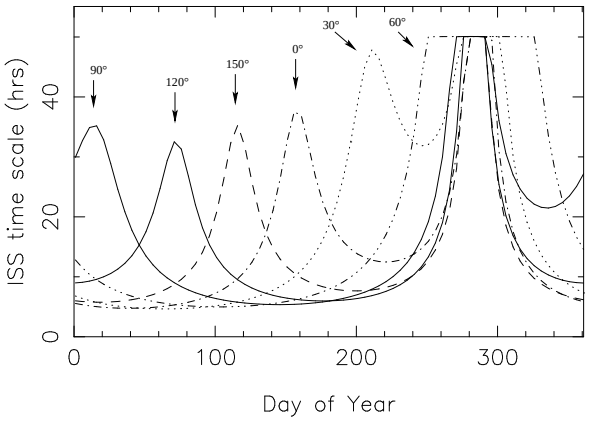

FIGURE 3.7— Model predictions of the variability time scale for 0917+624 adopting an anisotropic medium scenario (B. Rickett, priv. comm.). All curves are calculated for a Kolmogorov screen at 200 pc at rest in the LSR and a single Gaussian source with FWHM of 0.05 mas. The axial ratio of the scattering ellipse is assumed to be 0.25:1 for all curves and the orientation of the ellipse is varied for each plot between 0°and 150°as labeled. The predicted time scales are only plotted up to ~ 50 hours for better illustration.

patterns at each observing frequency (4.8 and 8.6 GHz). The authors interpreted this as an offset between the scintillating components at each frequency due to opacity effects within the source on a scale of $\sim 10\,\mu$as [3].

3.5 Model Predictions vs. Observations for two other IDVs

Until now, only two sources were found to show a clear seasonal dependence of the variability time scale: J1819+3845 and PKS 1257−326. Besides a confirmation for 0917+624, the detection of an annual variability in more sources is indispensable to establish the effect as a common feature in cm-radio IDV.

In the following we will apply the results of our calculations presented in Section 3.2 to two other IDV sources and compare the predictions with the observations. The individual parameters used for the modeling are given in Table 3.3. The variability time scales were deduced from observations of the earlier mentioned authors.

3.5.1 0716+714

This source was discovered in the late seventies as the optical counterpart of an extragalactic radio source (Kühr et al. 1981) and later identified as a BL Lac due to its featureless optical spectrum and high linear polarization (Biermann et al. 1981). Various attempts to find its redshift failed and only a lower limit of $z \geq 0.3$ was suggested from its starlike appearance and the absence of a host galaxy (Stickel et al. 1993, Wagner et al. 1996).

Nowadays 0716+714 is known to be one of the most variable radio sources in the sky. Variability throughout the whole electromagnetic spectrum on long as well as extremely short ($\sim$ hours) time scales is reported. The optical and radio investigation of its long-term behavior reveals several outbursts in both regimes over decades, but with quite different

[3] Again, variability studies in principle provide an angular resolution much higher than achieved today with any other instrumentation.

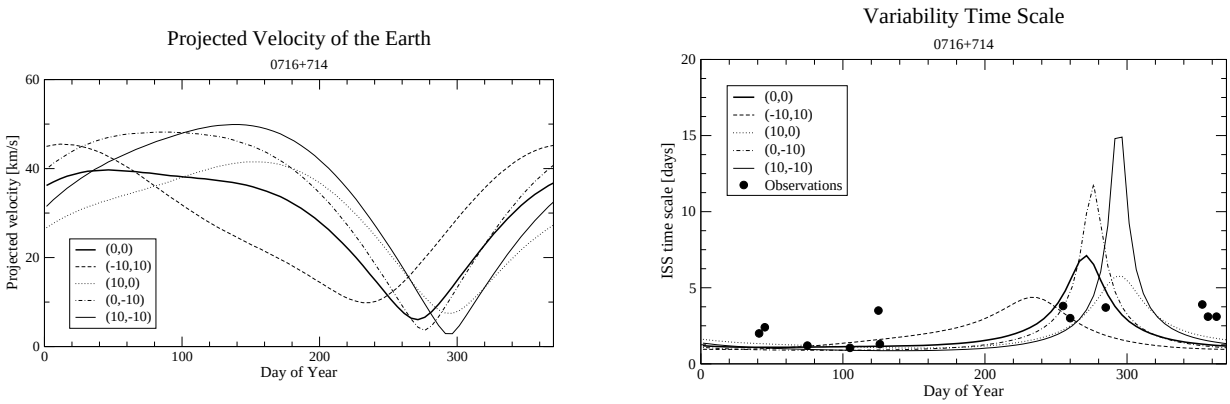

FIGURE 3.8— **Left:** the velocity of the Earth relative to the LSR projected perpendicular to the direction of 0716+710 versus day of the year for 4 different velocities of the screen (V_α, V_δ). Note the strong decrease near day 285. **Right:** resulting 'slow-down-peak' in the predictions of the variability time scale. Superimposed are the observed time scales resulting from IDV sessions at $\lambda 6$ cm between 1989−2000. A clear agreement is not visible (see text).

appearance and without any clear correlation (Raiteri et al. 2003). On shorter time scales, the source has shown pronounced variations in both total intensity and polarization at all radio bands (e.g. Wagner et al. 1993). Often extremely fast variations (~ 2 hours) are observed to be accompanied with variations on longer time scales ($\sim 1-3$ days) indicating the presence of more than one discrete time scale in the light curves (Kraus et al. 2003).

Claims are being made for both an intrinsic origin of the IDV in this source (e.g. due to the observed radio-optical correlation, Qian et al. 1996) as well as an origin due to interstellar scintillation (e.g. Qian 1995). The detection of a seasonal cycle in this source would be of particular importance to clarify the situation.

0716+714 is one of the most frequently observed IDV sources and therefore makes it suitable to test the annual modulation model. Figure 3.8 shows the outcome of our calculations for the Earth's relative velocity and the variability time scale for different screen velocities with respect to the LSR. The distance to the screen has been assumed to be 0.35 kpc to account for the often observed longer time scales (> 1 day) compared to e.g. 0954+658. As can be seen in Figure 3.8, the projected velocities and time scales can vary by a factor ~ 10 throughout a year. The slowest variations are predicted to occur around September and October.

Even though a total of 12 measurements of the variability time scale at 6 cm wavelength are available, it happens that only three of them lie in the predicted period of slow ISS. Although these points represent variations with longer time scales - 3.8 days (around day 255), 3.0 days (around day 260) and 3.7 days (around day 285) - further 6 data points with slower variations are distributed over the whole one year period (around days 45, 125, and 360). This contradicts the model predictions, since only three data points show the predicted shorter time scales (near day 100). An anisotropic scenario could produce "multiple peaks" in the time scale over the year, whereas even in this case a sudden decrease by a factor of ~ 3 within a few days (near day 125) seems not very reasonable (compare Figure 3.7).

3.5.2 0954+658

Another frequently observed IDV source is the BL Lac 0954+658 with a redshift of $z = 0.367$. It is one of the few IDV sources in which variability has been seen whenever it was observed, here however, with weaker amplitudes of only a few percent ($Y \sim 4\,\%$, e.g. Kraus et al. 2003). Also for this source different expla-

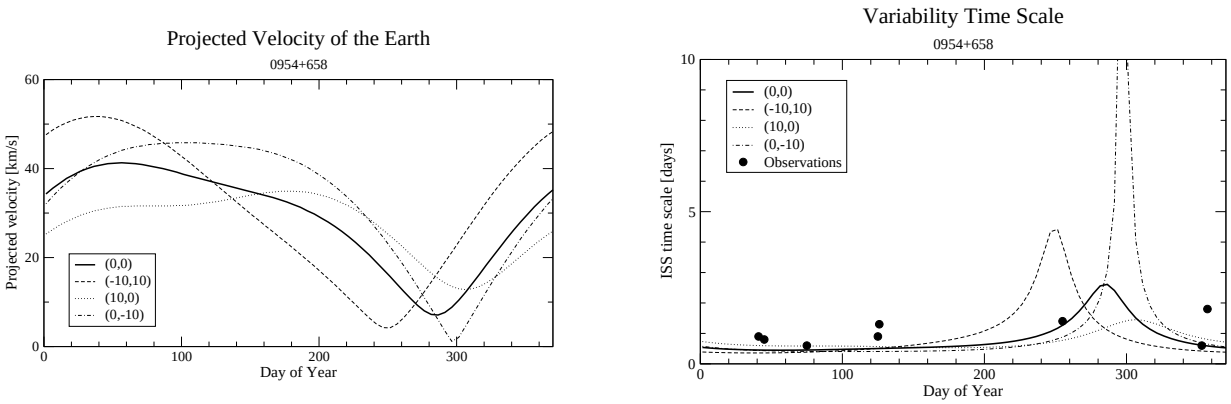

FIGURE 3.9— **Left:** the velocity of the Earth relative to the LSR projected perpendicular to the direction of 0954+658 versus day of the year for 4 different velocities of the screen (V_α, V_δ). Note the strong decrease near day 280. **Right:** resulting 'slow-down-peak' in the predictions of the variability time scale. Superimposed are 8 measurements of the variability time scale deduced from data obtained between 1989−2000. Only one data point is available in the period of the predicted increase, but does not show an unusual slower variability time scale (see text).

nations for its IDV were suggested. Among an intrinsic origin due to the tentative detection of a radio-optical correlation (Wagner et al. 1993), a sole extrinsic origin can not be ruled out. In this context, 0954+658 is of particular interest, since extreme scattering events were observed in this source several times indicating the presence of an extremely turbulent and clumpy interstellar medium along the line of sight (e.g. Fiedler et al. 1987). The detection of an annual cycle in its variability time scale would strongly support this idea and favor interstellar scintillation as origin of the intraday variations.

Figure 3.9 shows the outcome of our calculations towards the direction of 0954+658. Low relative velocities are again expected around day 280 resulting in a prolongation of ISS during the same time period. Depending on the screen LSR velocities, the parameters can vary by a factor of about 10 throughout a year.

A total of 8 measurements of the variability time scale at 6 cm wavelength are superimposed in Figure 3.9. Unfortunately, only one data point lies in the period of predicted increase (day 255), but does not show a pronounced prolongation ($t = 1.4$ days). Other points with comparable time scales are distributed over the rest of the year, where the variations are predicted to be fast (e.g. day 357). Similar to 0716+714, time scales measured during the same period of the year (only a few days apart) but in different years can be very different. For example, the variations of 0954+658 in December 1991 (around day 357) appeared to be slower than the model predictions. In contrast, observations in December 1989 (around day 353) revealed faster variability by a factor of ~ 3. Such deviations from the model predictions can be explained in the following ways: (i) Long-term changes (over month and years) in the inner structure of the source strongly influence its scintillation behavior. As result, a seasonal effect is washed out over the years. (ii) Taking into account an anisotropic medium, a multi-peak structure in the time scale over the year could be explained, but the observed sudden drop from faster to slower variations within a few days is hard to reconcile. Finally (iii), the variations seen in 0716+714 and 0954+658 are not caused by interstellar scintillation and thus an annual modulation is not observed.

3.6 A new Monitoring Project

In summary, the results presented here do not show evidence for an annual cycle in the IDV patterns of 0716+714 and 0954+658.

In contrast, the remarkable slow-down in September 1998 supports the existence of a seasonal cycle in the variability time scale of 0917+624. Although the case of 0917+624 (together with J1819+3845 and PKS 1257−326) was already cited as "compelling evidence for ISS as the principle cause of IDV at cm wavelength" (Bignall et al. 2003), such interpretation depends only on one data point. A more frequent sampling of the variability time scale throughout the year is essential to verify the slow ISS scenario and thus the ISS origin of IDV for this source.

Based on these findings, we started a new monitoring project with the Effelsberg telescope at 6 cm wavelength in order to test the annual modulation model in these "normal" IDV sources. Parallel to the Effelsberg campaign, a new VLBI monitoring experiment for 0917+624 has been started to investigate the connection between structural changes in the compact VLBI structure of the source and its IDV behavior. These Effelsberg as well as VLBI observations will be presented in the following (Chapter 4 and 5).

4

Effelsberg 4.85 GHz Flux Density Monitoring

The new flux density monitoring program at 6 cm wavelength covers the time period from September 2000 to October 2002 and was carried out with the Effelsberg 100 m telescope of the MPIfR. This chapter presents the observations, data reduction and results in view of the annual modulation model presented in the previous chapter. The simultaneous VLBI-monitoring of the main target source 0917+624 will be presented in Chapter 5.

4.1 Observations and Data Reduction

During a time interval of about two years, 28 single observing sessions with a duration of a few hours up to three days were performed whenever a small gap in the Effelsberg observing schedule was available. In this experiment, the main candidate for the presence of an annual cycle, 0917+624, was observed with a dense duty cycle of about 2 measurements every 1.5 hours. In addition, two non-IDV sources, 0951+699 and 0836+710, were always included as secondary calibrators. Together with 0917+624, the two further candidates, 0716+714 and 0954+658, were observed in order to test the reliability of the annual modulation model for "normal" IDV sources. The monitoring program was used also to search for new IDV as well as calibrator sources. The IDV candidates were selected mainly according to their compactness (flat radio spectrum and/or compact VLBI structure) and brightness (≥ 0.5 Jy) from the 1 Jy catalog (Kühr et al. 1981). A few sources were taken on the basis of exhibiting an interesting behavior in earlier observations (e.g. Quirrenbach et al. 1992, Kraus et al. 2003). Hence, a total of 22 individual sources were observed at least once during the overall 28 sessions. All observed sources and their basic parameters are summarized in Table 4.1. Details of each observing run are given in Table 6.2 (page 67).

Since all measured sources are point-like and sufficiently strong at $\lambda 6$ cm, we were able to measure the flux densities with cross-scans in azimuth and elevation (e.g. Heeschen et al. 1987, Quirrenbach et al. 1992, Kraus 1997). We observed strong standard flux density calibrators like 3C286, 3C295, 3C48 and NGC7027 frequently to be able to link the measured fluxes to the standard flux density scale and to adjust the focus of the telescope between day and night time.

The standard procedures were used to reduce continuum multi-feed IDV data acquired with the Effelsberg 100 m telescope. This reduction procedure is described in more detail elsewhere (e.g. Quirrenbach 1989, Quirrenbach et al. 1992 and Kraus 1997) and only a shorter, step-by-step version will be presented here.

4.1.1 The 4.85 GHz Multi-Feed System

All observing runs were performed with the 4.85 GHz double-horn receiver mounted in the secondary focus of the 100 m telescope (compare Figure 6.4 in Chapter 6). The system consists of two horns with a feed separation of $8\farcm1$ along the azimuth axis. Each horn is

All sources observed between 2000 and 2002					
Source	α_{1950} [hh mm ss.ss]	δ_{1950} [± dd mm ss.s]	$S_{5\,\mathrm{GHz}}$ [Jy]	N	IDV
0346+800*	03 46 49.41	+80 00 33.5	0.3	2	+
0403+765*	04 03 59.20	+76 48 52.5	2.9	2	−
J0422+535*	04 18 29.10	+53 38 52.0	0.4	1	+
0454+844	04 54 57.02	+84 27 53.1	0.3	1	+
0602+673	06 02 38.89	+67 21 18.3	1.0	1	+
0604+728*	06 04 39.19	+72 49 27.1	0.6	18	−
0615+820	06 15 32.71	+82 03 56.5	0.8	2	−
0718+793*	07 18 08.81	+79 17 22.7	0.8	18	−
0716+714	07 16 13.01	+71 26 15.3	0.8	26	+
0804+499	08 04 58.39	+49 59 23.1	0.7	2	+
0828+493	08 28 47.97	+49 23 33.1	0.4	2	+
J0834+551*	08 30 51.00	+55 24 18.0	5.4	1	+
0835+580*	08 35 09.99	+58 04 51.6	0.6	3	−
0917+624	09 17 40.30	+62 28 38.5	1.4	28	−
J0949+661*	09 45 14.84	+66 28 58.1	1.2	1	+
0954+658	09 54 57.84	+65 48 15.7	0.5	25	+
J0957+552	09 54 14.35	+55 37 16.5	2.0	1	+
1003+830*	10 03 25.73	+83 04 56.7	0.6	2	+
1031+567*	10 31 55.97	+56 44 18.1	1.2	1	−
J1814+411*	18 12 47.33	+41 12 06.2	0.6	1	+
J1819+385	18 17 46.80	+38 43 47.0	0.2	1	+
J1852+402*	18 50 51.79	+40 15 22.5	0.8	1	+

TABLE 4.1— A total of 22 compact sources were part of the IDV monitoring between 2000 and 2002. Their coordinates (B 1950) as well as flux densities are given (column 2–4). N in column 5 denotes the total number of observing epochs for the given source. The last column indicates if significant IDV was detected (results of the χ^2-test, Section 4.2). All sources labeled with a star (*) were examined for IDV for the first time.

followed by an equal 'first stage' unit containing a circular polarization transducer and two **H**igh **E**lectron **M**obility **T**ransistor (HEMT) - amplifiers. Within this unit, the Superheterodyne principle is realized: the high frequency signal is converted down to an intermediate frequency using a mixer connected with a local oscillator. After this first stage processing, each horn tree is followed by a separate backend consisting of a ZF-polarimeter providing total power as well as full polarization information of the received signal. The great advantage of such a multi-feed configuration is its usage as 'software-beam-switching' system. During an observation the 'main' horn is centered on the source position, while the second horn (weather horn) points towards a position 8.′1 away. In contrast to a hardware-beam-switching system (e.g. the 32 GHz Effelsberg receiver, Chapter 6), the two independent signals are recorded separately and subtracted in the subsequent data reduction process. This enables to reduce the influence of the atmosphere on the astronomical signal.

4.1.2 Cross-Scan Analysis

According to the "traditional" procedure for IDV observations with the Effelsberg telescope, all measurements were done using cross-scans. This method proved to be suc-

cessful over years for point-like and moderately strong sources. It represents the ideal compromise between sufficient accuracy and a high enough duty cycle (time between two adjacent scans on the same source) compared to other possible methods (mapping or on-off-measurements). As a by-product, the pointing deviation of the telescope, which influences precise flux density measurements[1], can be determined and corrected simultaneously during the observations. One cross-scan consists of sub-scans in two perpendicular directions (azimuth and elevation) across the source position with the number of subscans matched to the source brightness at the given frequency. In our case, a maximum of 12 sub-scans per scan was sufficient for the weakest sources in the sample, while usually eight sub-scans were used for the stronger sources (~ 1 Jy). Each subscan has a length of 4−5 times the Half-Power-Beam-Width (HPBW) of the telescope in order to determine the noise level (baseline) at the left and right side of the source position. With a HPBW of $143''$ at 4.85 GHz this yields an overall scan duration of $\sim 4-6$ minutes.

The measured source brightness is a convolution of the point-like brightness distribution of the source with the antenna beam. Hence, as first step in the data reduction (after subtraction of main and weather horn), a Gaussian profile is fitted to each sub-scan using the program CONT2 within the MPIfR software package TOOLBOX. The amplitude of these Gaussians is a measure of the flux density of the source. The fitting yields the following parameters: flux density proportional to the amplitude of the Gaussian fit, pointing offset from the center position and the HPBW. Figure 4.1 shows an example of a cross-scan observation on 0917+624 and the subsequent Gauss-fit analysis.

As next step, obviously bad sub-scans are flagged. The cross-scans are usually influenced by e.g. changing weather conditions (clouds or rain on the line of sight), temperature gradients (which often are accompanied with telescope distortions), wind or interference. The flagging procedure for each sub-scan of one scan is done on the basis of the following criteria:

(i) flux $> \pm 5\,\%$ of the average
(ii) pointing error $> \pm 10\,\%$ of the HPBW
(iii) HPBW $> \pm 10\,\%$ of the average

Taking the example in Figure 4.1, this procedure yields the flagging of sub-scan eight due to the strong pointing offset of more than $15''$.

4.1.3 Pointing Correction

The cross-scan method enables to control the pointing behavior of the telescope directly during the observations. After each scan, the pointing offset with respect to the center position is given (in the same way as described above) by a Gaussian fit to the averaged sub-scans in azimuth and elevation, respectively. The pointing in both directions is subsequently corrected using these offsets. However, remaining pointing offsets (after moving the telescope to a new source position) and the connected underestimation of the true flux density can be corrected in the subsequent data reduction process.

Here, a comparison of the two cross-scan directions allows the correction of the deviation from the true position (and the connected underestimation of the amplitude) by assuming a two dimensional Gaussian profile. The correction of the measured amplitude S for the deviation in one direction by using the pointing offset in the other direction is given by

$$S_{Azi}^{corr} = S_{Azi} \cdot \exp\left(4 \cdot \ln 2 \cdot \frac{x_{Elv}^2}{\theta_{Elv}^2}\right) . \qquad (4.1)$$

Here, as an example, the correction of the Azimuth scan using the pointing offset x_{Elv} and the HPBW θ_{Elv} of the Elevation scan is given. As a first step, the mean pointing offset and HPBW in one direction is calculated. The subsequent estimation of a correction factor for each sub-scan in one direction is followed by the correction of the amplitude value of each sub-scan using equation 4.1. After this pointing correction, all sub-scans are averaged.

[1] Details are presented in Chapter 6 in the context of our 32 GHz observations

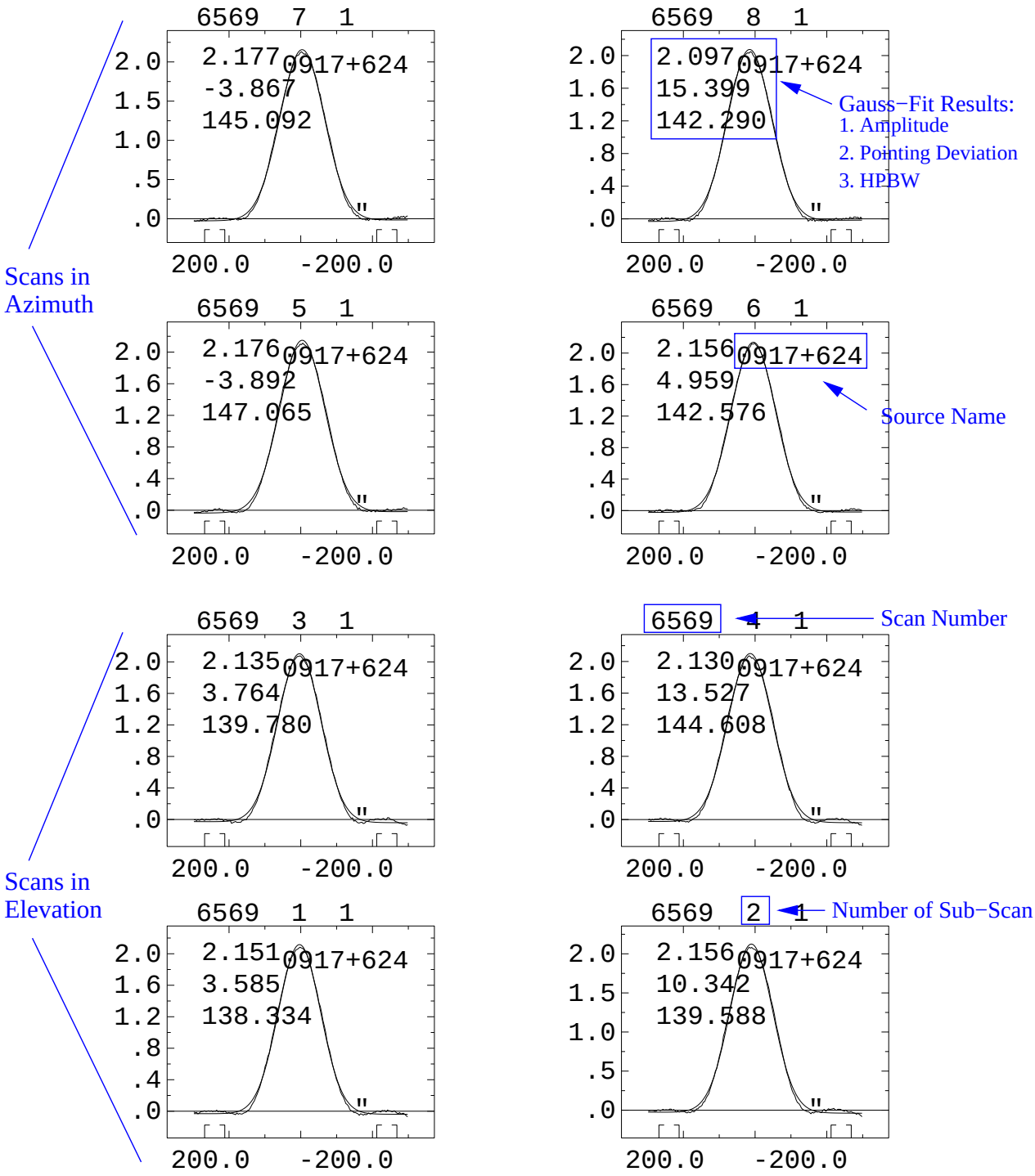

FIGURE 4.1— Example of a cross-scan observation on the main target source 0917+624: The scan consist of four sub-scans in azimuth and elevation, respectively. The parameters shown in the plots are labeled. The flux value is given by the amplitude of a Gaussian fit (straight line) to the data. Due to its strong pointing deviation of more than 10 % of the beam size, sub-scan 8 was flagged during the data reduction process.

As final result of the cross scan analysis, we end up with one value for the amplitude per scan plus statistical error. The subsequent data reduction steps will be described in the following and are summarized in Figure 4.2. They consist mainly of the final flux density calibration and the correction for systematic sources of error in order to achieve the highest possible accuracy. The latter is based on the frequent observation of the usually constant, secondary calibrators.

4.1.4 Gain Correction

Due to the large diameter of the Effelsberg telescope, the huge weight of its construction leads to gravitational distortions in the 100 m dish surface. As a result, the focus position as well as the surface accuracy (and thus sensitivity) varies with changing elevation. The Effelsberg telescope construction is based on the so-called 'principle of homological distortion'. Here, a controlled deformation of the dish into a paraboloid is always realized. An adjustment of the focus with changing elevation thus ensures the receivers and secondary mirror to be always in the focal plane. In contrast, the influence of the changing surface accuracy has to be corrected after the observations: the dish surface is optimized for elevations around 35° and the sensitivity decreases towards both, higher and lower elevations. Frequent measurements of secondary calibrators (ideally along the whole elevation range) allow to correct for this effect by plotting their normalized amplitude versus elevation (gain curve). A quadratic fit

$$G = A_0 + A_1 \cdot \mathrm{Elv} + \mathrm{A}_2 \cdot \mathrm{Elv}^2 \qquad (4.2)$$

yields the constants A_0, A_1 and A_2 for each observing run and is used to remove these systematics from the whole data set at the given epoch. Such 'gain correction' is the first step in the reduction process and an example is given in Figure 4.2.

4.1.5 Time-dependent Correction

The secondary calibrators were always observed with similar duty cycles as the program sources. This allows the correction of remaining, systematic time-dependent effects in the measured flux densities. Those consist mainly of changing weather conditions, drifts in the receiver system and thermal expansion of the telescope due to temperature gradients during the run (e.g. thermal loading from the Sun). The light curves of the normally constant calibrators display these effects. Figure 4.2 gives an example of the normalized flux vs. time for the two secondary calibrators 0836+710 and 0951+699 (second panel on the right). A comparison of the light curves shows that both sources exhibit mainly the same systematic amplitude changes. This happens on short time scales (up to a few hours in the first part) as well as on time scales of ~ 0.5 days (monotonic increase in the second part). In the case of the data shown in Figure 4.2, such effects occur on a 0.5–1 %-level, but can occasionally reach a few percent during bad weather conditions. Since the amplitudes of our target sources are also affected by these time-dependent systematics, the latter have to be removed in order to achieve a better level of accuracy (≤ 1 %) and detect the lowest level of variability. The data of the secondary calibrators were used to remove the time-dependent effects from the whole data set by constructing a mean correction curve over the observing period. This has been done for each epoch using the densely sampled light curves of 0836+710 and 0951+699 (see Figure 4.2).

Finally, the measured amplitudes of all sources of one epoch have to be linked to the absolute flux density scale (Baars et al. 1977, Ott et al. 1994)[2]. This is done using the frequent observations of primary calibrators (e.g. 3C286, 3C48 and 3C295) at the given epoch.

4.1.6 The final Measurement-Errors

The single measurement errors (the statistical error from the Gauss fit analysis) is usually smaller than the error suggested by the residual scatter in the final secondary calibra-

[2] In addition, these fluxes are monitored frequently throughout a year in order to account for long-term changes.

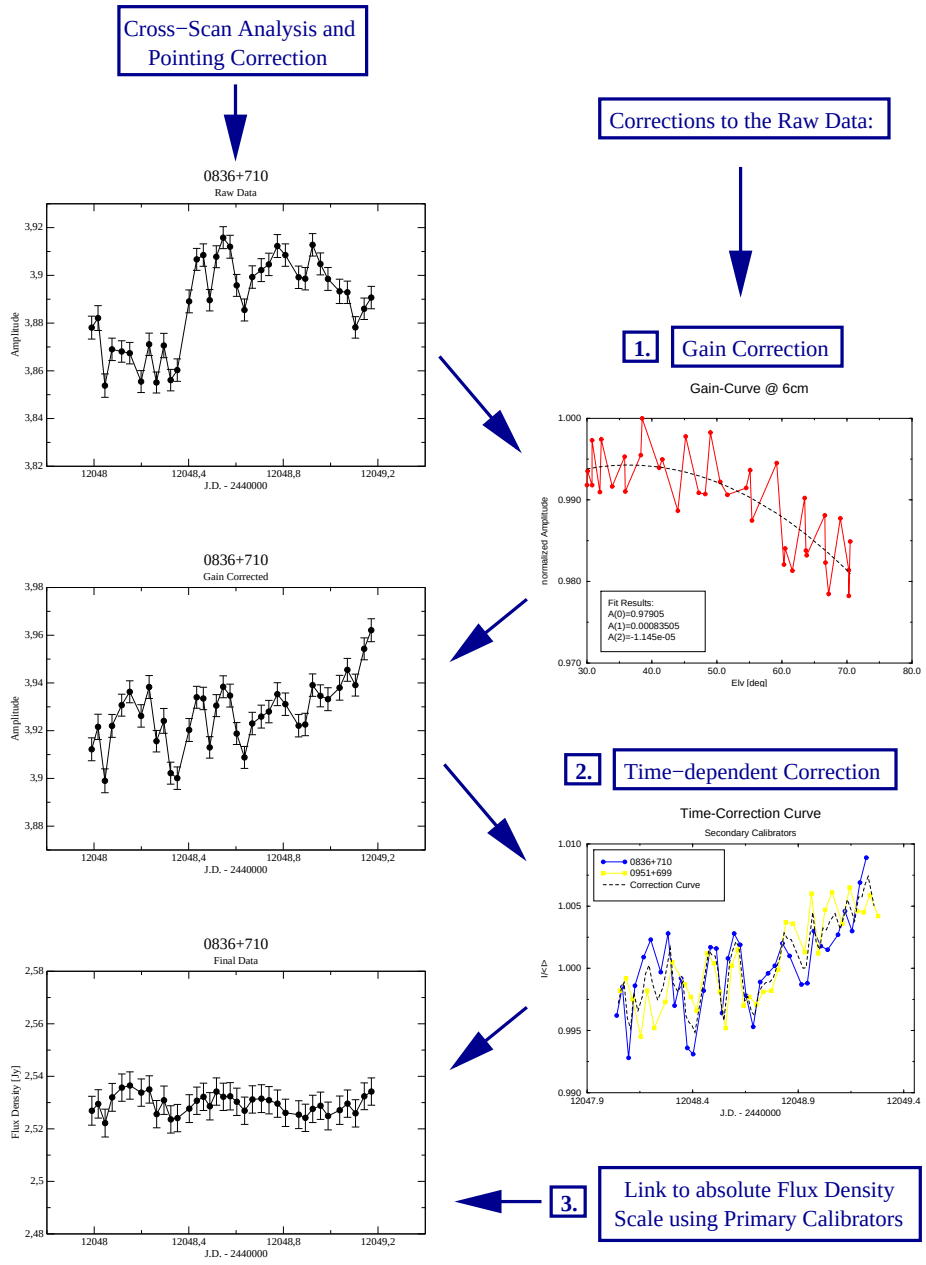

FIGURE 4.2— Sketch of the data reduction procedure for flux density measurements with the Effelsberg telescope at 4.85 GHz. After the cross-scan analysis, the raw data undergoes mainly three additional corrections: (i) elevation-dependent correction, (ii) time-dependent correction and (iii) scaling to the absolute flux density (see text). The corrections are plotted on the right side of the tree, while their outputs are shown on the left.

tor light curves. Since the latter defines the level (1σ) on which we are able to detect variability and thus represents our final observing accuracy, an additional error has been applied to each data point. This error was deduced from the averaged scatter of the secondary calibrators 0836+710 and 0951+699 around their mean values at each given epoch.

Consequently, the final flux density errors are composed of the statistical errors from the reduction process (Gaussian fits of averaged sub-scans) and a contribution from the sys-

tematics as seen in the secondary calibrators (weather and system conditions). The final errors lie in the range of $\leq 0.5 - 1\,\%$. In the cases of good up to ideal weather conditions, these values are lowered to $\sim 0.3\,\%$.

4.2 IDV Analysis

After the data reduction process each light curve is investigated by a standard variability analysis based on the following steps: (i) test for the presence of IDV (χ^2-test), (ii) identification of the variability strength (modulation index and variability amplitude) and (iii) determination of a characteristic time scale of the variations.

4.2.1 χ^2-Test

In order to search for the existence of short term variations, each light curve undergoes the following procedure. As a criterion for the source variability, the hypothesis of a constant function (non-variable source) is examined and the light curve is fitted by a χ^2-test of the kind

$$\chi^2 = \sum_{i=1}^{N} \left(\frac{S_i - < S >}{\Delta S_i} \right)^2 , \qquad (4.3)$$

with the reduced χ^2

$$\chi^2_r = \frac{1}{N-1} \sum_{i=1}^{N} \left(\frac{S_i - < S >}{\Delta S_i} \right)^2 . \qquad (4.4)$$

Here, S_i denotes the individual flux densities, $< S >$ their average in time, ΔS_i their errors and N the number of measurements (e.g. Taylor 1982, Bevington & Robertson 1992). The factor $1/(N-1)$ in the reduced χ^2 corresponds to the division of χ^2 by the degree of freedom. In the case of a constant function, this is equal to the number of measurements minus one. Values of $\chi^2_r \sim 1$ represent a good fit of the data with a constant function, while values significantly larger than 1 correspond to light curves with a low probability of being constant.

Finally, only those sources for which the probability that they can be modeled by a constant function was found to be $\leq 0.1\,\%$ are considered as IDV sources.

4.2.2 Modulation Index and Variability Amplitude

An important parameter to quantify a light curve is the modulation index m. It is related to the mean flux density $< S >$ and the rms flux density variations σ_S in the time series by

$$m[\%] = 100 \cdot \frac{\sigma_S}{< S >} \qquad (4.5)$$

and yields a measure for the strength of the observed variations. Epoch-dependent effects (e.g. weather and receiver instabilities) can systematically influence the rms variations in the data. Therefore it is useful to compare the modulation index of a variable source with those of the secondary calibrators observed at the same epoch. This gives rise to the definition of a variability amplitude given by

$$Y[\%] = 3\sqrt{m^2 - m_0^2} \, . \qquad (4.6)$$

The obtained quantity is noise-bias corrected using the mean modulation index m_0 calculated from the secondary calibrators[3]. This allows the comparison of the strengths of the variability at different epochs.

One should note, that the error of the modulation index critically depends on the observing duration and the sampling interval. The reliability of parameters quantifying the variations in a time series depends on the type of variations observed. In the case of IDV, the observed flux densities can be assumed to be part of a stochastic process with a characteristic time scale. The basic statistical uncertainty due to the finite, small number of points sampled within a limited observing period has then to be taken into account. Following Cimó (2003), we define three quantities for the contribution to the final error in m:

[3] The factor three is used according to the definition in Heeschen et al. (1987). It is calculated empirically to reach a good agreement between Y and the true amplitude.

- the error due to the limited measurement accuracy can be absorbed into the mean flux density error $\Delta < S >$

- the number n of independent variability cycles (and hence the accuracy of m) is limited by the finite observing duration T_{obs}. In addition, the observing period could be shorter than the time scale of the variations leading to an underestimation of m. The hereby related errors can be described as

$$\Delta n = 0.85 \frac{1}{\sqrt{n}} \ , \tag{4.7}$$

  where n denotes the number of variability cycles (with time scale t_{var}) observed within T_{obs}:

$$n = \frac{T_{obs}}{t_{var}} \tag{4.8}$$

- a third contribution is related to the finite sampling of the stochastic variations. Variations could occur on time scales shorter than the typical sampling interval (under-sampling). Assuming that significant variations could be present within at least three data points, this error can be expressed as

$$\Delta N = \frac{1}{N} \ , \tag{4.9}$$

  where N is given by

$$N = \frac{T_{obs}}{3 < t_s >} \tag{4.10}$$

  taking into account the mean sampling interval $< t_s >$.

Thus, the final uncertainty of m can be lowered by (i) a high number of independent samples of the variability pattern observed and (ii) a densely sampled duty cycle. The same is true for the derived time scales of the variations. In our case, the basic statistical uncertainty of m typically lies in the range of 30–50 %.

4.2.3 Time scale analysis

To further quantify the observed variations, a characteristic variability time scale t_{IDV} has to be extracted from our time series. This time scale can then be compared with the predictions of the annual modulation model presented in the previous chapter. Here, various methods are available and different kinds of t_{IDV} with different definitions are used in the literature. Besides a direct estimation from the light curve itself (e.g. mean peak-to-peak time), the time series are best analyzed by first order structure functions (SF) or autocorrelation functions (ACF). Following Simonetti et al. (1985), the discrete first order structure function SF(τ) for a time series $S(t_i)$ of flux measurements at time t_i is given as

$$SF(\tau) = < (S(t) - S(t+\tau))^2 >_t \ , \tag{4.11}$$

where $< \ . \ >_t$ denotes the average over time (for samples with equal τ). For small time lags, $\tau \rightarrow 0$, the SF displays the noise level present in the time series. For increasing time lags the SF is characterized by a power law, $SF \propto \tau^{\beta}$, with a slope of $\beta \lesssim 2$. Finally, the SF reaches a first maximum and a 'plateau-level' for long time lags. The first maximum displays the characteristic time scale for decorrelation, t_{IDV}, while at the plateau the SF becomes proportional to the modulation index m: $SF_{plateau} = 2m^2$ (see Figure 4.3 for an example). In the past, the SF was used to define different types of IDV sources. According to Heeschen et al. (1987), an IDV type II source reaches a maximum in the SF within the observing period. By definition, this period has been arbitrarily fixed to two days (Wagner & Witzel 1995). Consequently, a type I IDV source exhibits a monotonically increasing SF over the observing period without clear maximum/plateau and displays variability on longer time scales. The SF of a type 0 (non-variable) source is dominated by noise and hence appears to be constant over the observing period.

The autocorrelation function $\rho(\tau)$ of a time series $S(t_i)$ is defined as (Edelson & Krolik

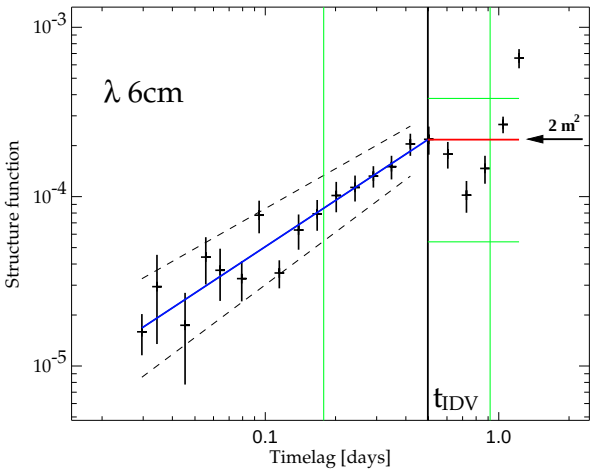

FIGURE 4.3— Example of a SF analysis for the light curve of 0716+714 obtained in May 2001. The time where the power law fit reaches the first maximum/fitted plateau level is taken as characteristic time scale t_{IDV} (see text).

1988)

$$\rho(\tau) =< (S(t) \cdot S(t-\tau)) >_t \ , \qquad (4.12)$$

with its relation to the structure function given by

$$SF(\tau) = 2[\rho(0) - \rho(\tau)] \ . \qquad (4.13)$$

In the same way as for the SF, the ACF yields information on both characteristic time scales and periodicities in the time series. In the investigation of pulsar scintillation, the usual way is to define the "decorrelation" time scale as the time lag during which the ACF falls to $1/e$ of its maximum (e.g. Cordes 1986). Other authors refer to the time scale as the half-width at half maximum (HWHM) of the ACF (e.g. Rickett et al. 1995). In IDV studies, the usage of both, SF and ACF is common. Dennett-Thorpe & de Bruyn (2000) make use of the SF, while their definition of t_{IDV} corresponds to the full-width of the ACF at $1/e$ of its maximum. Because the definition of the variability time scale is a matter of convention, it is only important to use a consistent method to be able to compare the observations with theoretical calculations. In this work, the following SF procedure was used and applied to each data set in order to obtain a characteristic time scale t_{IDV} (see Beckert et al. 2002a). For each data set $f(t_i)$, the discrete structure function

$$SF(\tau_j) = N_{ij}^{-1} \sum_{i=1}^{n} w(i)w(i+j)[f(t_i) - f(t_i+\tau_j)]^2 \qquad (4.14)$$

was calculated. Here, N_{ij} is the normalization and $w(i)$ are weighting functions with $w(i)w(i+j) > 0$, if a measurement at time t_i and another at $t_i + \tau_j$ was obtained. In addition, the weighting function accounts for binning of an unevenly sampled time series. Subsequently, two linear fits are performed to estimate the slope of the SF ($SF = a \cdot \tau^{\beta}$) and the plateau level ($\rho_0 = 2m^2$). A typical example is shown in Figure 4.3. The plateau level is obtained by the mean of the SF after the first maximum (the saturation level, red line) and the connected error by its variance (green, horizontal lines). As can be seen from Figure 4.3, the plateau level is often not well pronounced (see below). The error of the power law fit to the SF consists of the variance of the fit parameters a and β and the envelops in Figure 4.3 (dashed lines) result from a linear fit to these errors. The characteristic time scale is then determined by the crossing point of the power law and the fitted saturation level, $\rho_0 = a \cdot t^{\beta}$, and is given by

$$t_{IDV} = \left(\frac{\rho_0}{a}\right)^{1/\beta} \ , \qquad (4.15)$$

(black vertical line) and its error

$$\Delta t_{IDV} = \left(\frac{\rho_0 \pm \Delta\rho_0/\sqrt{3}}{a \pm \Delta a/\sqrt{3}}\right)^{\frac{1}{\beta \pm \Delta\beta/\sqrt{3}}} \qquad (4.16)$$

(green, vertical lines). Finally, the modulation index m is derived from the plateau level and its related error according to $m = (0.5 \cdot \rho_0)^{1/2}$.

This procedure is straightforward for regular light curves with a large number of variability cycles (and thus long observing duration), since the SF then shows a clear maximum and saturation level. However, this is often

not the case in our (often shorter) epochs and shows the difficulties connected with the observation of "normal" IDV sources compared to their "extreme" counterparts. Sources like J1819+3845 exhibit a pronounced and regular variability pattern with time scales of about 0.5 hours or even less. In these cases, observing runs as short as 12 hours are sufficient to obtain a large number of individual variability cycles. Consequently, the SFs show their "ideal" shape and the statistical errors of t_{IDV} and m are small. The situation for normal IDV sources with time scales of 0.5–1 day is different. Here, a large amount of observing time (ideally 5 or more days) is essential to obtain a similar accuracy of the derived values. The situation becomes even more stringent when the detection of a prolongation in the time scale (of a few days) is aspired. Within the monitoring program presented here, only a few cycles are observed and not even complete ones in the shorter epochs. Furthermore, the light curves obtained from normal IDV sources often show an irregular pattern with multiple structures and several superimposed time scales (see below). This complicates the situation, since the SFs (and also ACFs) deviate from there "ideal" shape for these cases (several maxima, no clear plateau level etc.).

In order to obtain reliable values, a SF analysis was performed only for epochs with a duration of at least 24 hours. However, the errors are still high - up to 100 % in the most extreme cases. A cross-check was done using the ACFs and the light curves itself. Here, the time scales were estimated as the time between subsequent maxima and minima in the time series and the modulation index as defined in equation 4.5. In all cases, the results are in good agreement with the values obtained from the SF analysis.

4.3 Results

In the following sections, the results for our three main target sources will be summarized and discussed in view of the annual modulation model presented in Chapter 3, together with a few notes on other interesting sources. The whole set of light curves and detailed results of the IDV analysis for all sources and epochs can be found in Appendix A and B.

4.3.1 0917+624

In Figure 4.4 and Table 4.2, we summarize our results for 0917+624 at 6 cm wavelength. Since September 2000, all 28 individual light curves show a very inactive source with only a few percent amplitude variations. At the top of Figure 4.4, the long-term light curve of 0917+624 over the full monitoring period (Sept. 2000 – Oct. 2002) is displayed. During this time interval, we detected a long-term trend with a nearly monotonic, $\sim$25%-decrease in total flux from 1.5 Jy down to 1.2 Jy since September 2000. In a short period from August to December 2001, a small two-folded increase in flux (around J.D. 2452200) is visible. Such long-term behavior is typical for compact radio sources (e.g. 3C345, 0836+710, 0716+714 see below) and is often accompanied by the ejection of new jet components in the innermost core-region on VLBI-scales (e.g. Otterbein et al. 1998). A more detailed investigation of this effect will be presented in Chapter 5.

In addition, Figure 4.4 shows 10 individual light curves measured between September 2000 and April 2002. All curves of 0917+624 show only extremely low amplitude variations of $Y \leq 0.5 - 2.2$ % ("ripples") on very short time scales of $\sim 0.3 - 0.4$ days. These values of Y are dramatically lower than those observed in the past between 1989 and 1999 ($Y \leq 4.2 - 16.2$ %). In addition, the variations are often comparable to or not much stronger than those seen in the secondary calibrator light curves (m_0 in Table 4.2). The same is true for the χ^2-test results. Since September 2000, no significant, strong IDV was seen in 0917+624 and the pronounced IDV seen at earlier times is completely missing. As a result, the structure functions of the time series often appear similar to those obtained from non-variable sources and a detailed SF analysis for 0917+624 (t_{IDV}, m) was not possible. For this reason, Table 4.2 summarizes the re-

TABLE 4.2— Results of the IDV analysis.

0917+624							
Date	Day	Duration [hours]	Flux [Jy]	m [%]	m_0 [%]	Y [%]	χ^2_r
16/09/2000	260	24	1.51	0.43	0.37	0.46	1.22
03/12/2000	338	43	1.50	0.48	0.20	1.30	5.13
17/12/2000	352	36	1.50	0.71	0.23	2.02	9.24
09/02/2001	40	27	1.44	0.42	0.19	1.10	3.13
24/03/2001	83	43	1.41	0.77	0.24	2.21	7.24
09/04/2001	99	22	1.40	0.68	0.20	1.96	10.17
04/05/2001	124	65	1.38	0.46	0.23	1.19	4.55
18/05/2001	138	34	1.38	0.31	0.15	0.81	1.99
03/08/2001	215	67	1.43	0.47	0.28	1.08	1.52
20/10/2001	294	49	1.41	0.48	0.03	1.44	9.85
25/12/2001	359	23	1.43	0.50	0.50	0.00	0.72
12/04/2002	102	37	1.31	0.39	0.34	0.57	1.39

sults obtained directly from the light curves using equations 4.5 and 4.6 (for epochs with a duration of at least one day).

4.3.2 0716+714

In contrast to 0917+624, the BL Lac 0716+714 often shows the variability pattern expected from previous observations. Figure 4.5 displays several individual light curves obtained between September 2000 and October 2002. The long-term light curve at the top shows strong long-term activity and a first flare around J.D. 2451895 with a peak-to-peak amplitude of 40 %. Here, a steep increase lasting for about two months and a subsequent, flatter decrease is clearly visible. A second, broader flare develops during the second half of the observing period reaching a comparable amplitude as the former in the last observing session (October 2002). This long-term activity of 0716+714 (similar to 0917+624, but much more pronounced) has been well known from decades of radio, mm and optical observations and studied in great detail. Raiteri et al. (2003) performed a statistical analysis by means of cross-correlations and found a periodicity in the optical oscillations of ~ 3.3 years. Here, a variation of the Doppler factor (by ~ 1.3) due to either energetic (noticeable change of the Lorentz factor) or geometrical changes (a few degrees in the viewing angle) is the most likely explanation. In the radio regime their study indicates a variability time scale of 5.5−6 years with only weak correlations to the optical behavior.

Turning back to variability on intraday time scales, several individual light curves are displayed in Figure 4.5. As can be seen, often slower and more pronounced variations are observed together with faster and lower amplitude variations superimposed on the same light curve (e.g. December 2000, May 2001). Such substructure has already been observed in the past (e.g. Quirrenbach 1989, Kraus et al. 2003) and seems to be a typical characteristic of the "slower" IDV sources compared to the extreme IDVs with their regular, sinusoidal variability pattern.

The results of the IDV analysis by means of structure functions are given in Table 4.3 for each single session with a duration of at least one day. In addition, the modulation index m_0 as well as the χ^2_r are given. The overall modulation index m varies strongly over the whole observing period of about two years. Several light curves show only low amplitude variations (e.g. September 2000, February 2001),

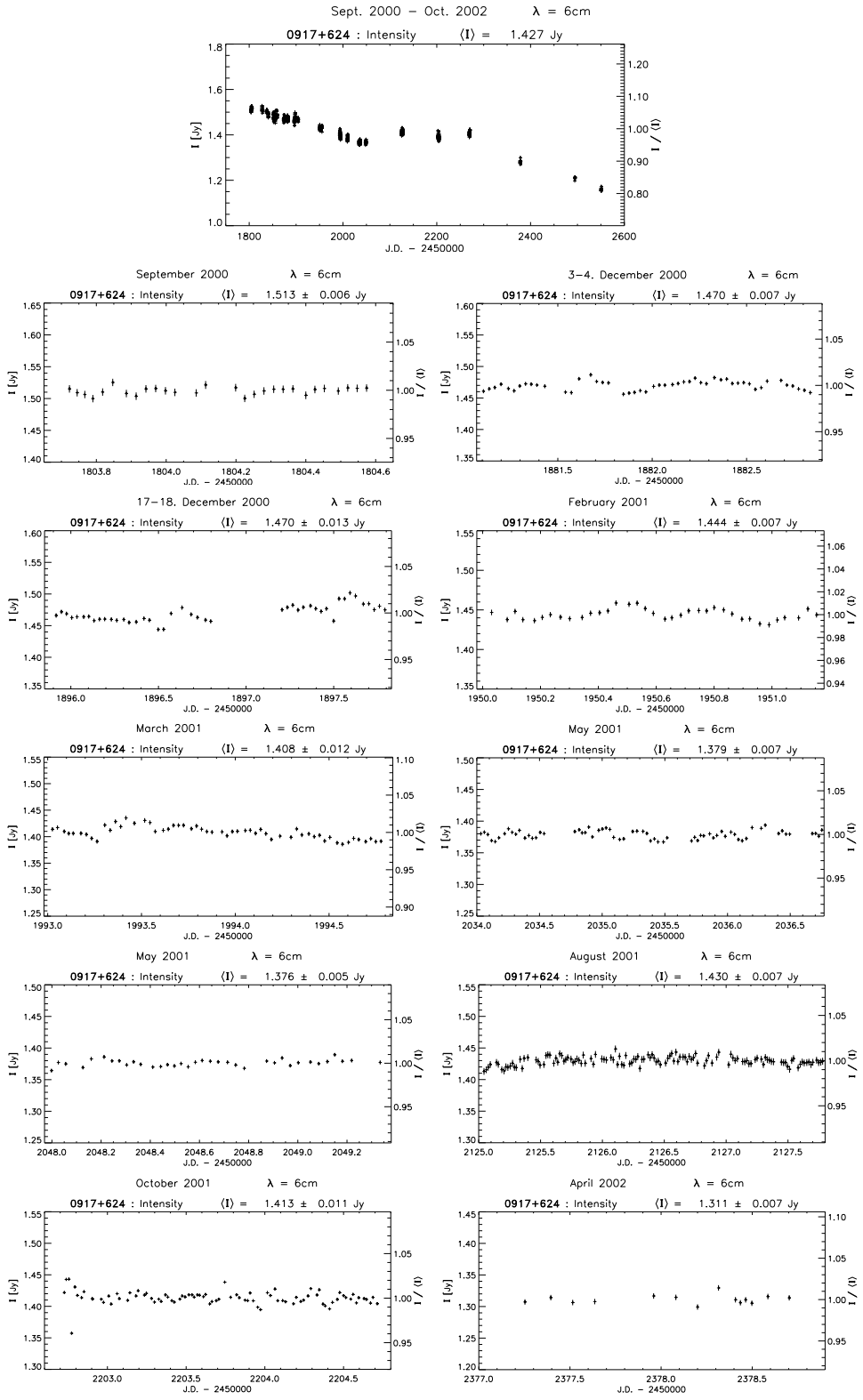

FIGURE 4.4— Summary of our observations between September 2000 and October 2002 for 0917+624: at the top, the long-term light curve with a trend of a $\sim$25%-decrease is displayed. In addition, several individual light curves are plotted. All curves show only low amplitude variations (see text).

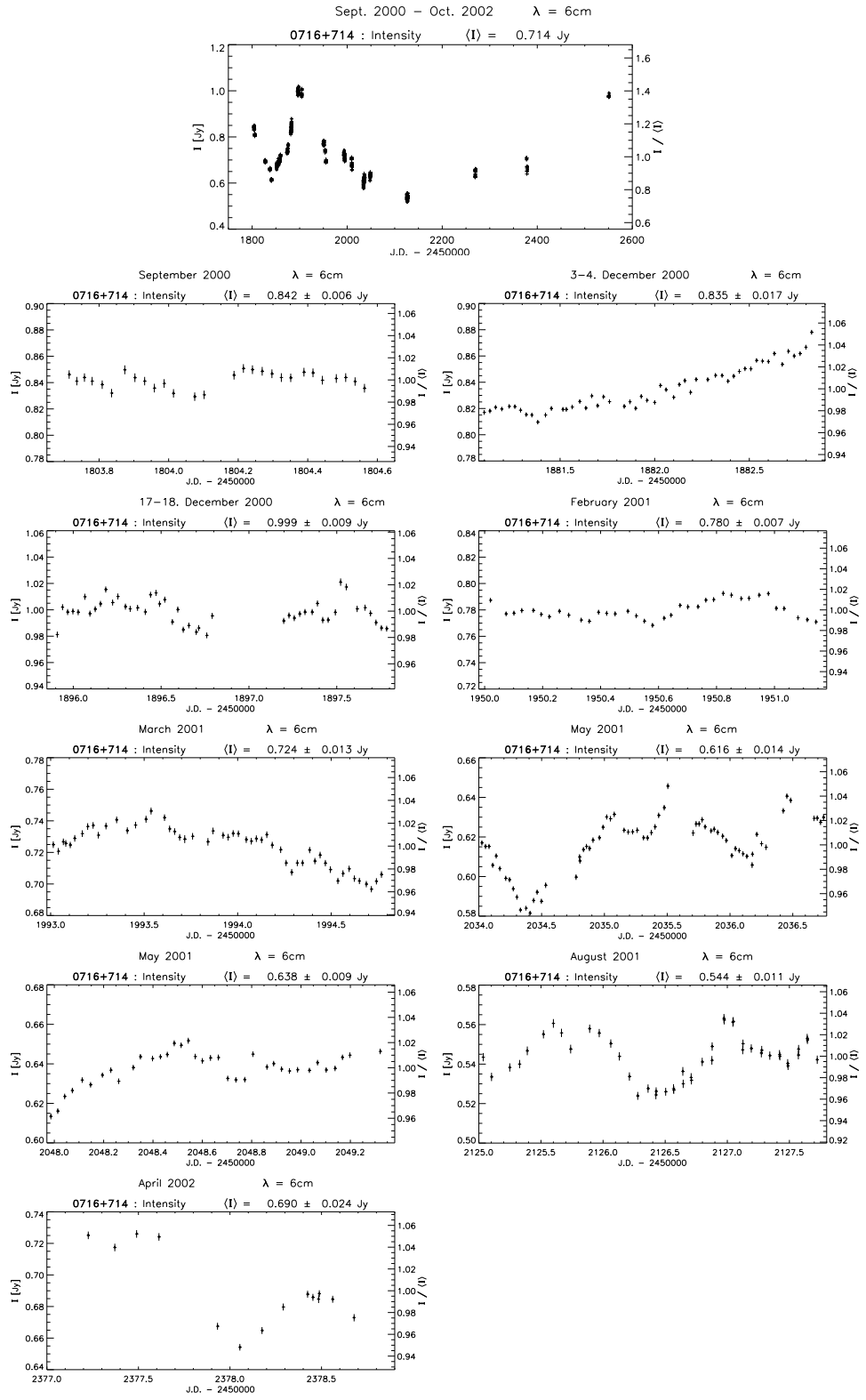

FIGURE 4.5— Summary of our observations between September 2000 and October 2002: at the top, the long-term light curve of 0716+714 with pronounced long-term activity is displayed. In addition, several individual light curves are plotted (see text).

TABLE 4.3— Results of the structure function analysis.

0716+714							
Date	Day	Duration [hours]	Flux [Jy]	Time scale [days]	Mod. index m [%]	m_0 [%]	χ^2_r
16/09/2000	260	24	0.84 ± 0.01	$0.17^{+0.18}_{-0.11}$	0.75 ± 0.17	0.37	3.45
03/12/2000	338	43	0.84 ± 0.02	$\gtrsim 1.79$	$\gtrsim 2.10$	0.20	90.34
17/12/2000	352	36	1.00 ± 0.01	$0.35^{+0.44}_{-0.26}$	0.98 ± 0.11	0.23	16.37
09/02/2001	40	27	0.78 ± 0.01	$0.24^{+0.16}_{-0.12}$	0.93 ± 0.11	0.19	13.52
24/03/2001	83	43	0.72 ± 0.01	$1.04^{+0.20}_{-0.19}$	2.24 ± 0.27	0.24	36.86
09/04/2001	99	22	0.69 ± 0.02	$\gtrsim 0.92$	$\gtrsim 2.52$	0.20	133.15
04/05/2001	124	65	0.62 ± 0.01	$0.55^{+0.22}_{-0.20}$	2.13 ± 0.55	0.23	120.98
18/05/2001	138	34	0.64 ± 0.01	$0.50^{+0.42}_{-0.32}$	1.63 ± 0.61	0.15	35.15
03/08/2001	215	67	0.54 ± 0.01	$0.35^{+0.19}_{-0.16}$	2.13 ± 0.52	0.28	26.80
25/12/2001	359	23	0.66 ± 0.01	$0.59^{+0.25}_{-0.23}$	2.54 ± 0.49	0.50	11.74
12/04/2002	102	37	0.69 ± 0.02	$0.68^{+0.21}_{-0.20}$	4.30 ± 0.62	0.34	107.10

whereas others exhibit a pronounced variability pattern (e.g. May 2001, August 2001). Values of m as low as 0.75 % are observed together with values higher by a factor of ~ 5. A similar behavior is seen for the time scale of the variability. Fast periods with time scales between 0.2 to 0.4 days (e.g. September 2000, February 2001, August 2001) are accompanied by slower variations. Two epochs were found where the structure function did not saturate within the observing period. In these cases (December 2000 and April 2001), only a lower limit for the modulation index and the variability time scale could be obtained. These two epochs, together with the observations in March 2001, display the periods with the slowest variability time scales ($\gtrsim 1.8$, $\gtrsim 0.9$ and 1.0 days respectively) – in the most extreme case a factor $\gtrsim 9$ slower with regard to the remaining epochs. A more detailed analysis in view of the annual modulation model will be given in Section 4.4. In particular, a possible dependence of the derived quantities on the mean flux density (and thus intrinsic source evolution) will be examined. As expected, the formal errors in both time scale and modulation index are high due to the usually low number of variability cycles observed. However, the changes of both quantities over the whole observing period appear to be statistically significant.

4.3.3 0954+658

In Figure 4.6 and Table 4.4 we summarize our results for 0954+658. The long-term light curve shows a similar activity as 0716+714. After a 5 months period of nearly constant flux density, two flares were observed with their maxima around May 2001 and December 2001. This long-term behavior is similar to what has been observed in the past, where 0954+658 was always active with changes in amplitude by a factor of up to 4 over months and years.

The individual curves displayed at the bottom of Figure 4.6 show almost always strong variability with peak-to-peak amplitudes of $\sim 5-7$ %. The light curves appear often as a strongly irregular pattern with short, sawtoothed peaks superimposed (e.g. December 2000a, March 2001, May 2001). This is similar to what was already seen in the light curves of 0716+714 (e.g. May 2001), but here it appears to be more frequent and much more pronounced. The existence of variability with such multiple structure (several distinct time scales and amplitudes) is, again, in contrast to the quasi-oscillatory variability seen in the most extreme IDVs. In the framework of ISS, this could be explained by a different scat-

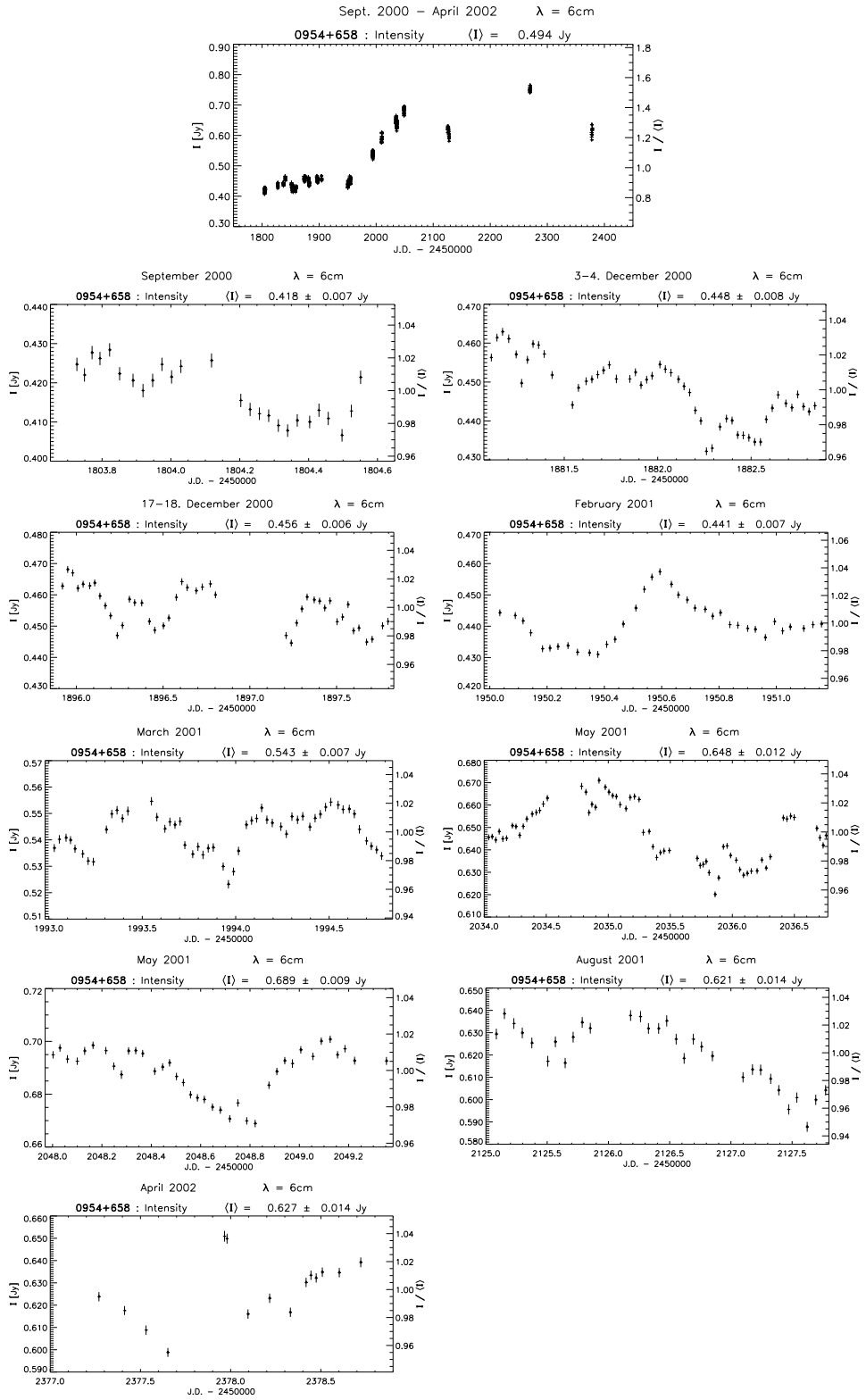

FIGURE 4.6— Summary of our observations between September 2000 and October 2002: at the top, the long-term light curve of 0954+658 with pronounced flares is displayed. In addition, several individual light curves are plotted (see text).

TABLE 4.4— Results of the structure function analysis.

0954+658							
Date	Day	Duration [hours]	Flux [Jy]	Time scale [days]	Mod. index m [%]	m_0 [%]	χ^2_{red}
16/09/2000	260	24	0.42 ± 0.01	$0.33^{+0.18}_{-0.15}$	1.73 ± 0.43	0.37	16.77
03/12/2000	338	43	0.45 ± 0.01	$0.58^{+0.39}_{-0.32}$	1.90 ± 0.56	0.20	62.52
17/12/2000	352	36	0.46 ± 0.01	$0.30^{+0.29}_{-0.19}$	1.53 ± 0.39	0.23	32.96
09/02/2001	40	27	0.44 ± 0.01	$0.19^{+0.12}_{-0.09}$	1.63 ± 0.47	0.19	38.43
24/03/2001	83	43	0.54 ± 0.01	$0.25^{+0.17}_{-0.13}$	1.38 ± 0.27	0.24	22.91
09/04/2001	99	22	0.60 ± 0.01	$0.31^{+0.19}_{-0.15}$	2.35 ± 0.38	0.20	95.75
04/05/2001	124	65	0.65 ± 0.01	$0.63^{+0.22}_{-0.21}$	2.06 ± 0.45	0.23	84.94
18/05/2001	138	34	0.69 ± 0.01	$0.25^{+0.15}_{-0.13}$	1.35 ± 0.50	0.15	41.85
03/08/2001	215	67	0.62 ± 0.01	$1.20^{+0.61}_{-0.60}$	2.41 ± 0.80	0.28	34.92
25/12/2001	359	23	0.77 ± 0.01	$0.36^{+0.23}_{-0.18}$	1.08 ± 0.25	0.50	2.38
12/04/2002	102	37	0.63 ± 0.01	$0.27^{+0.16}_{-0.13}$	2.38 ± 0.69	0.34	45.45

tering medium (e.g. a different turbulence spectrum and/or several sheets of material at different distances) or a different brightness distribution of the scintillating region in the source.

The results of the structure function analysis are given in Table 4.4 for all epochs with a duration $\gtrsim 24$ hours. Although the epoch in December 2001 shows a somehow lower value of $m = 1.1\,\%$ with respect to the mean value of $m = 1.8\,\%$, the scatter of m throughout the whole observing period is much lower compared to 0716+714. The same is true for the estimated variability time scales. The source is usually fast with time scales of ~ 0.3 days. Two epochs, December 2000a and May 2001, are found to exhibit slower variability by a factor of ~ 2, whereas the period with the most prolongated time scale is seen in August 2001. Here, the SF analysis yields a variability time scale of 1.2 days, a factor of about 4 slower compared to most of the remaining epochs.

4.3.4 Final epoch in April 2003

A last observing epoch was performed in April 2003. While 0716+714 and 0954+658 showed their 'normal' variability pattern, no restart of the variability in 0917+624 could be detected. The source still exhibits an extremely low level of variations. Thus, up to now, 0917+624 has stopped its pronounced variability for more than 2.5 years.

4.4 Discussion

4.4.1 Extremely quenched Scintillations in 0917+624

It can be seen from Figure 4.4 that 0917+624 passed through a dramatic change of its variability properties when compared to the past. The change can clearly be seen by plotting light curves of our new campaign on the same scale with data from earlier observations. This is realized in Figure 4.7. While in June 1993 0917+624 showed its normal, strong variability pattern with 15 %-amplitude variations ($m = 3.3\,\%$) on a time scale of ~ 0.5 days, the variations between March and October 2001 appear dramatically low. The modulation indices obtained from all light curves between 2000 and 2003 have always been low: $m \leq 0.8\,\%$. In the most extreme case, this is a factor ~ 15 lower than the variations observed in the past between 1988−1999 ($m = 4{-}5\,\%$). In order to explain the behavior of 0917+624 in the context of the annual modulation model, however, three main problems appear: i) Other IDV sources in the same region of the sky (e.g. 0716+714, 0954+658) do not show the expected clear

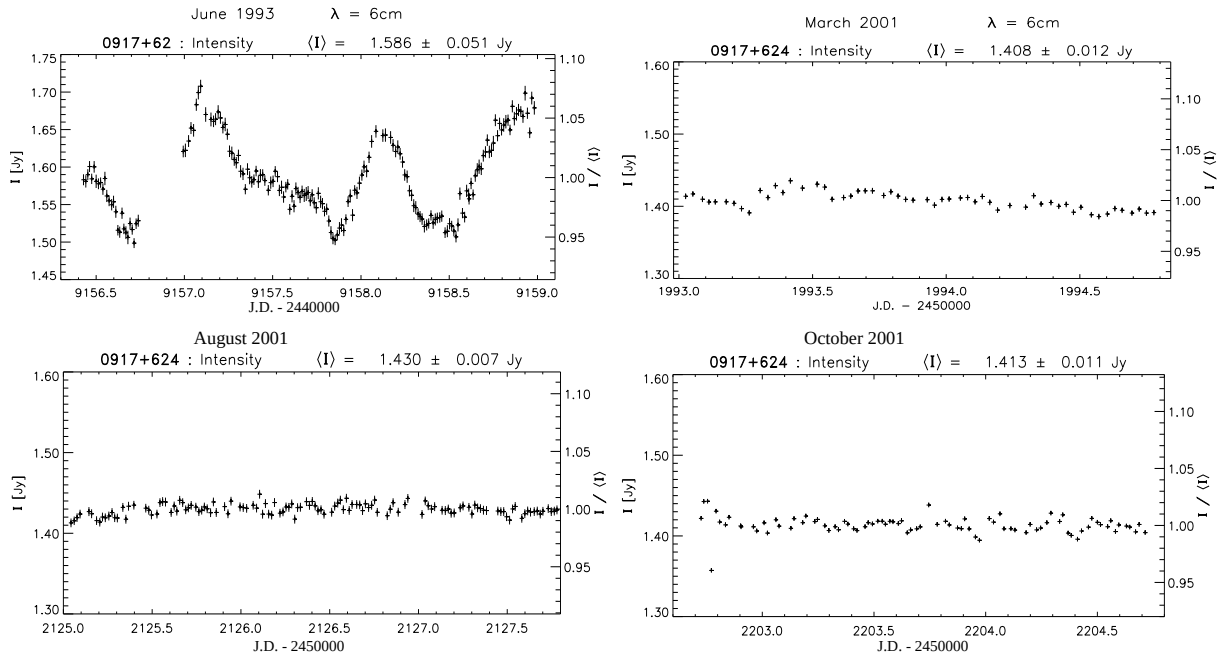

FIGURE 4.7— Comparison of epochs with different variability pattern: the upper left curve shows 0917+624 in June 1993 with its normal, strong variability pattern ($m = 3.3\,\%$). Three additional light curves from March, April and October 2001 (plotted on the same scale) are displayed ($m \lesssim 0.8\,\%$). Note the low variations compared to the past.

seasonal dependence of the variability time scale (see below). ii) The orbital motion of the Earth should affect the time scale, but not the modulation index m (Rickett et al. 2001). The strength of the variations is independent of the velocity vector and its orientation throughout a year (even in the presence of any anisotropy). However, m now appears to be strongly variable. iii) Our monitoring program presented here has not yet revealed a restart of the strong, pronounced and fast variability in 0917+624 since September 2000. This contradicts the model predictions presented in Chapter 3, which claimed recovery to the "normal" variability already at the end of year 2000 (see Figure 3.6). We suggest two possible scenarios in order to explain the present anomalous behavior of 0917+624:

(i) Changes in the scattering medium

The interstellar medium could be far more complex than presently assumed. A change in the scattering properties of the screen might explain the change of the variability mode in 0917+624. If the spatial scale of the scintillation pattern decreased, then the source size could quench the ISS as extremely as now observed. For weak ISS or RISS this would imply either a decrease in the strength of turbulence in small, localized regions of the ISM or an increase in the distance to such a region. In turn this would require a very inhomogeneous ISM with moving 'clouds' or 'layers' at different distances. The inhomogeneities would then have to occur on angular scales of less than the angular separation from 0917+624 to other sources ($\leq 5 - 10°$), the latter still showing pronounced IDV.

Beckert et al. (2002) published an analytical solution for the modulation index in the

weak, quenched scattering regime. Using this expression, the required changes in the scattering properties of the medium can be constrained (see Chapter 6[4]). Here, a slab model for the screen of 1 pc thickness with a uniform distribution for the strength of turbulence C_n^2, and a Kolmogorov spectrum with $\beta = 11/3$ is assumed. First, the distance to the ionized material can be constrained using equation 2.28 (Chapter 2) for the variability time scale in the weak, quenched scattering regime. The typical variability time scale of 0.5 days at $\lambda 6$ cm seen in the past and relative velocities not larger than 40 km s^{-1} require a screen distance of $\sim$100–150 pc for reasonable source sizes (0.08–0.12 mas). A further unknown in the modeling of ISS is the amount of total flux density contained in the scintillating component and the non-scintillating "base-level". Using the values 150 pc and 0.08 mas for the slab model leads to a modulation index of 7.3 % at $\lambda 6$ cm assuming all flux to be in the scintillating component. This value is higher than the observed value of $m \sim 5-6$ % seen between 1988−1999. This discrepancy indicates that the variable component most likely contains only about 80 % of the source total flux. However, since this is rather unknown, in the following we will use the simplification of 100 % of the source total flux in the scintillating component.

The typical, already quenched variability of $m \sim 5-6$ % seen in the past can then be explained by one $\sim$0.1 mas component scintillating behind a screen at a distance of 150 pc. Here, C_n^2 is assumed to be of the order 0.1 m$^{-20/3}$ as deduced from pulsar studies for enhanced turbulence in the local ISM (Local Bubble wall). In order to quench the scintillations further down to the now observed $m \sim 0.5$ %, changes in the scattering properties of the medium are related to changes in the distance D to the screen or the strength of turbulence. Here, m scales as

$$m^2 \sim D^{-0.3} < C_n^2 > \quad . \qquad (4.17)$$

[4]In Chapter 6 this model is presented in more detail and investigated in the context of multi-frequency observations of J1819+3845.

Taking only a change in the mean strength of turbulence $< C_n^2 >$ into account requires a decrease by a factor of $\sim$130 within a time period of about one year (1999−2000). A sole increase in distance to the material (and thus decrease in the Fresnel angular scale) requires unrealistic high values of D ($\sim$kpc) due to the weak dependence of m^2 on D. Thus, in this context, the present situation of 0917+624 is most likely explained by either a "hole" in the screen or a moving foreground layer or clump, which was present during the last 15 years and has suddenly disappeared between 1999−2000 (both leading to the required strong and sudden decrease in $< C_n^2 >$). In this case the velocity in the scattering medium can be constrained to at least 0.1 mas per year or 1.2 m s^{-1} at a screen distance of 150 pc.

(ii) Intrinsic changes in the source structure

An alternative interpretation could be based on intrinsic variations in the inner source structure on scales which are of the order of the scattering size. The dominant components, which in the past were responsible for ISS, could have either disappeared or they increased their intrinsic size to values much larger than the Fresnel angular size. As result, only extremely quenched scintillations are observed. Adopting the above model, the required enlargement can be estimated. In order to quench m at $\lambda 6$ cm from 5−6 % down to 0.5 % by a sole increase in source size, the component has to increase its size to 0.7−0.8 mas (assuming a screen at 100–200 pc distance). Consequently, the $\sim$0.1 mas component, which was responsible for the ISS seen in the past, should have increased in size by a factor of 7−8 to produce the present, extremely quenched scintillations. These values appear extremely high and such a dramatic increase in component size should become visible in new VLBI observations of the source (see Chapter 5).

4.4.2 Evidence for Changes in the Scintillating Core Region of 0917+624

Support for the latter idea comes from multi-frequency IDV observations of 0917+624 performed in March 2000 (Cimó 2003). This epoch can be treated as an intermediate case between the typical, strong variability seen in the past (until February 1999) and the extremely quenched variability presented here (since September 2000). During this run in March 2000, 0917+624 was observed at 11, 6 and 2.8 cm wavelengths over a period of one week. Already at this time its variability at 6 cm wavelength was strongly reduced ($m = 0.7\,\%$, Figure 4.8) compared to observations in February 1999 ($m = 5.1\,\%$). Interestingly, the λ11 cm-light curve from March 2000 still showed stronger variability ($m = 1.3\,\%$), but the variations were also already quenched compared to earlier observations at this wavelength. Here, m was usually in the range of 3−5 % (Quirrenbach 1989, Kraus et al. 2003; Figure 4.8). Taking, as described above, an increase in size of one scintillating component between February 1999 and September 2000 into account, the reduced variability index at λ 6 cm in March 2000 can be reproduced by a component of size $\sim$0.6 mas behind a 100−200 pc distant screen.

Assuming we are still in the weak scattering regime at λ 11 cm, the scintillation behavior at this wavelength can be examined with the same model. This is supported by the fact that the variability in 0917+624 peaks somewhere close to this wavelength (Quirrenbach 1989, see Figure 2.2 in Chapter 2). By scaling the 0.6 mas component at λ 6 cm linear in frequency yields a component size of $\sim$1 mas at 11 cm wavelength. Such component would produce quenched variability with $m \sim 1.2\,\%$ at λ11 cm for a screen at 100−200 pc. This is close to the value of 1.3 % observed in March 2000, where the variations were already reduced, but, as expected, still not entirely quenched. This provides evidence that the scintillating component steadily increased in size after February 1999 from $\sim$0.1 mas to

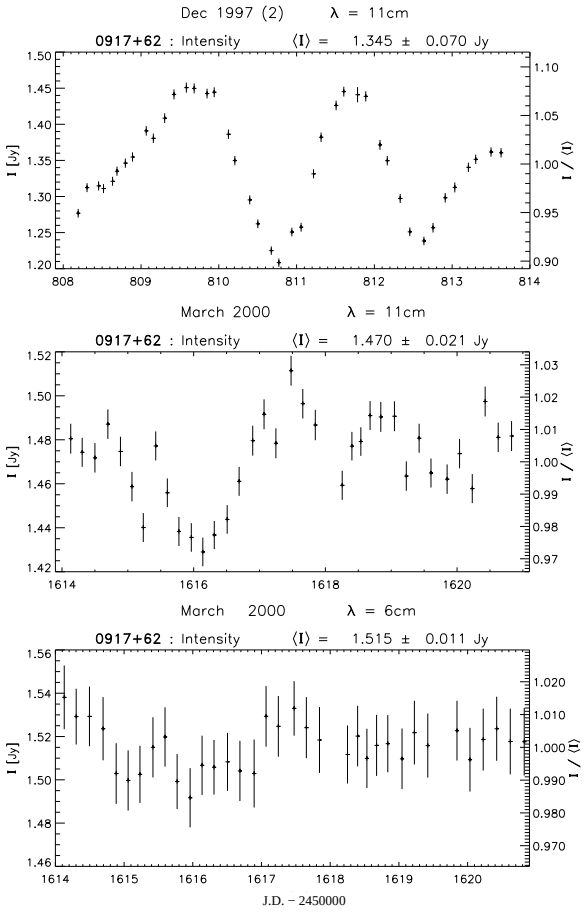

FIGURE 4.8— The intermediate case between strong (until February 1999) and extremely quenched variability (since September 2000) in 0917+624: The λ11 cm-light curve from March 2000 (middle) shows by a factor of 4 reduced variability compared to earlier λ11 cm-observations (here December 1997, top). The light curve at λ6 cm from March 2000 (bottom) exhibits an already strongly quenched modulation index (0.7 %), but slightly higher as usually observed since September 2000 (0.5 %).

$\sim$0.6 mas at λ6 cm in March 2000 and up to 0.7−0.8 mas in September 2000. As a result, the variability strength steadily decreased to the reduced value at λ11 cm and the strongly reduced value at λ6 cm in March 2000 to finally terminate in the extremely (nearly entirely) quenched λ6 cm-variations seen since September 2000 ($\sim$0.5 %). New Effelsberg observations at a wavelength of 11 cm could support this idea, but are presently not possible due to technical reasons.

One has to note that the previous description with one scintillating component in

0917+624 is probably too simple. This is supported by the often rapid and complicated variations in polarization and polarization angle and its anti-correlation with total intensity (compare Figure 2.1 in Chapter 2). This behavior can only be modeled by ISS when a multi-component model with at least two polarized sub-components of sizes 0.05−0.07 mas is taken into account (e.g. Rickett et al. 1995). However, it appears as if the strong and compact source component, which was responsible for the deep flux density modulations in the past, has increased in size and thus ceased varying (e.g. due to a blending of the VLBI core with a newly ejected jet component) .

Direct evidence for an increase in size of the inner, scintillating region of 0917+624 is coming from VLBI observations performed between 1999 and 2000 (Krichbaum et al. 2002). These findings will be presented in Chapter 5 together with our new VLBI epochs.

4.4.3 Annual Modulation and long-term Behavior of 0716+714 and 0954+658

0716+714

In order to compare the results of 0716+714 with the predictions of the annual modulation model presented in Chapter 3, Figure 4.9 displays the measured modulation indices and time scales versus day of the year. The distribution of the variability time scale (bottom of Figure 4.9) shows two periods of slower variations separated by about 250 days. While in between the time scales are observed to be shorter ($\lesssim 0.5$ days), the first period of slower variations occurs around days 80−100 and consist of a few epochs with a time scale of up to one day. The second period is characterized by only one data point (with the slowest variability observed in December 2000, day 338), where the SF have not been saturated after 1.8 days. This "double peak" structure in the time scale over the year appears to fit nicely with the expectation for annual modulations in an anisotropic screen scenario (compare Figure 3.7 in Chapter 3). Here, e.g. an orientation of the scattering ellipse of

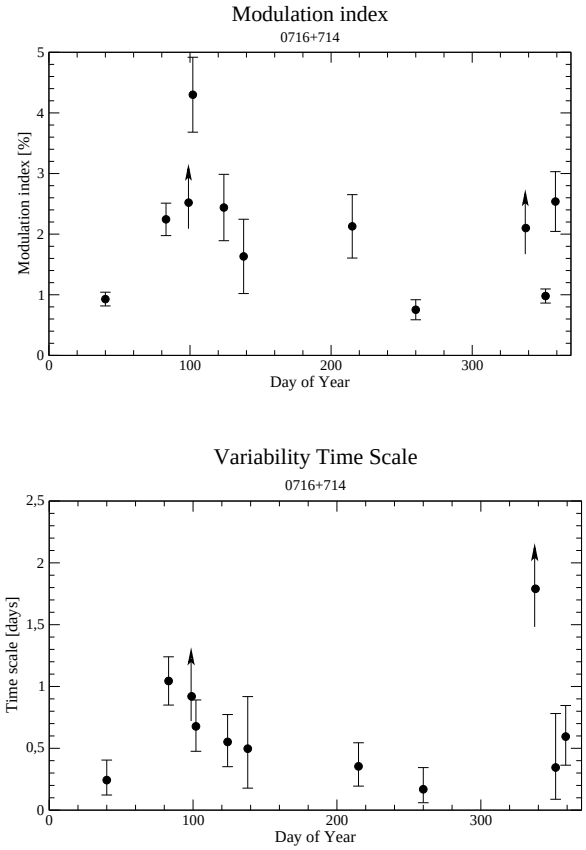

FIGURE 4.9— Results of the SF analysis for 0716+714 plotted versus day of the year. **Top:** modulation index. **Bottom:** variability time scale.

150° would produce a secondary peak close to day 70 and a primary peak near day 290 in this part of the sky (depending on axial ratio, source size and screen velocity). The question remains, whether the observed prolongations reflect a real annual modulation effect caused by the changing relative velocity or if other mechanisms are in operation. Evidence for the latter possibility comes from the behavior of the modulation index over the year. As outlined earlier, this quantity should be independent of the orientation of the velocity vector and thus should be approximately constant over the year. In contrast, Figure 4.9 shows a large scatter, where at least four points (out of 11) deviate more than a factor of two from the average of $m = 2\,\%$. This appears to be statistically significant and shows that m is not as constant as predicted. In particular, the first

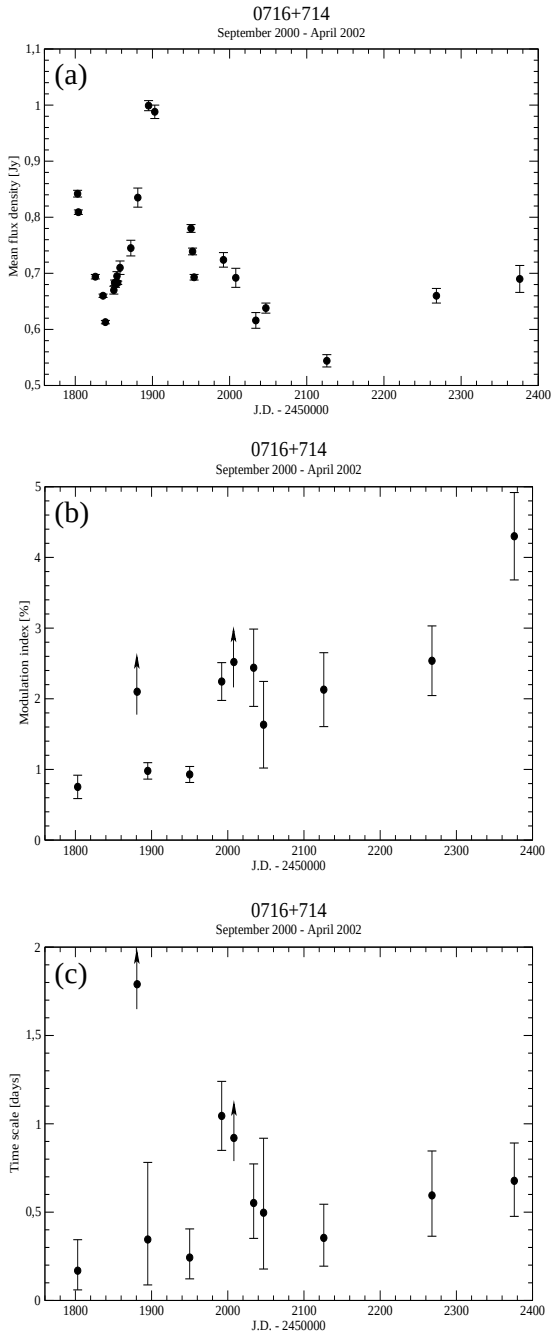

FIGURE 4.10— Long-term behavior of 0716+714: (a) source total flux, (b) modulation index, (c) variability time scale over the full monitoring period. Note the similar behavior close to J.D. 2452000 (see text).

peak in the variability time scale plot seems to be correlated with an increase of m around the same day number ($\sim$ day 100). A comparison of the long-term behavior of the two quantities supports this idea. Figure 4.10 shows the long-term distribution of the total flux density (a), the modulation index (b) and the variability time scale (c) over the full monitoring period between September 2000 and April 2002. It turns out, that the modulation index exhibits a steady increase over this 19-month period with its maximum in the last epoch. A similar trend is visible in the diagram showing the variability time scale, but here less pronounced and statistically less significant due to the larger error bars. Superimposed we find a local maximum in the m-distribution near J.D. 2452020, which coincides with a period of slower variability and lower total flux densities around the same time. When examining the behavior of m in dependence of time scale and flux density, it appears as if m is indeed correlated with both quantities. Figure 4.11 displays m versus time scale and total flux density. A linear least-square fit reveals a dependence in a fashion, that m increases with t_{IDV}. The data point with the slowest time scale (1.8 days), however, deviates from this distribution. Furthermore, m seems to be correlated with flux density as well. Although the degree of correlation is poorer, a trend is seen: stronger variability towards lower flux densities. A similar behavior was found in a more general statistical analysis of IDV (Cimó 2003). In particular, examining the behavior of 0716+714 in the past (1989−2000) reveals often stronger variability at epochs of lower total flux density. This might be interpreted as structural changes in the core region (e.g. new jet-components and thus larger core size), which influence the overall variability characteristics (similar to the scenario proposed for 0917+624).

The previous discussion indicates that at least the first period of slower variations around days 80−100 does not reflect a true seasonal cycle predicted by the anisotropic screen scenario. Intrinsic source evolution (as evident in the large outbursts in Figure 4.10) is more likely to be responsible. Consequently, this period will be excluded from the subsequent discussion.

The situation is less clear in the second pe-

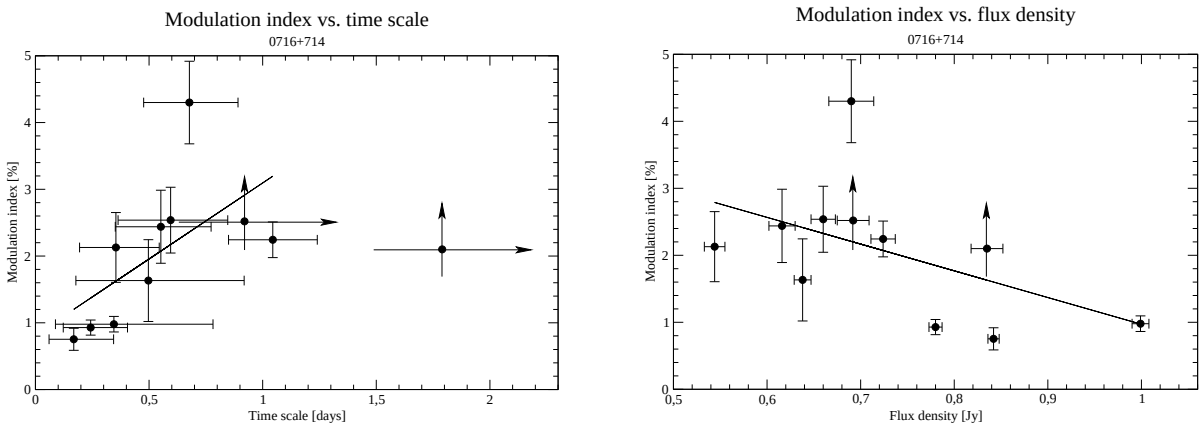

FIGURE 4.11— **Left:** modulation index versus time scale. **Right:** modulation index versus total flux density. In both cases a trend of correlation is visible (linear fit). The data point with slowest variability observed deviates from the strong linear trend seen on the left and has been excluded from the fit analysis in this case.

riod of slower variations (around day 338), since only one data point is available. Here, however, the corresponding modulation index is close to its mean value and deviates from the dependence seen in Figure 4.11. Assuming (i) that the prolongation in this part of the year is indeed caused by the slower relative velocity between Earth and screen and (ii) that the slower variability around days 80−100 is due to an intrinsic origin as argued above (and hence negligible), our results can be compared with the model calculations presented in Chapter 3. A detailed least-square-fit analysis as done in the cases of J1819+3845 and PKS 1257−326 is not possible due to the lack of additional measurements between days 300–360. However, in order to produce a 'slow-down period' so close to the end of the year, a large offset of the screen velocity with respect to the LSR has to be assumed. In Figure 4.12 we overplot our model predictions for different LSR velocities of the scattering medium. The model parameters (source size θ_S and screen distance D) are chosen as follows. Assuming we are in the weak quenched scattering regime, the usually shorter variability time scale throughout the year can be used to constrain both the source size and the screen distance in a fashion that a larger source size requires a smaller distance and vice versa. According to Chapter 2, the scintillation time scale in this regime is given by $t = \theta_S \cdot D/v$. In order to obtain time scales of $\lesssim 0.3-0.4$ days, a reasonable parameter range for both quantities is $70-200$ pc for D and $50-100\,\mu$as for θ_S with relative velocities not much larger than $40\,\mathrm{km\,s^{-1}}$. For the model calculations in Figure 4.12, a screen distance of 100 pc and a source size of $70\,\mu$as was used.

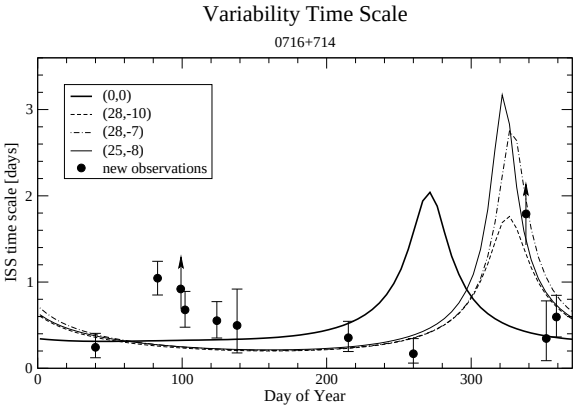

FIGURE 4.12— Variability time scales of 0716+714 versus day of the year with model calculations superimposed. Different LSR velocities for the screen (V_α, V_δ) are assumed as indicated. Ignoring the first peak (around day 90) the model can qualitatively explain the second slow-down near day 340 (see text).

A screen at rest (in the LSR) produces a minimum in the transverse velocity at days

near 270 for sources in this part of the sky (thick solid curve). The prolongation around day 338 can then be fitted only, when offsets in the range of $V_\alpha = 25\,\mathrm{km\,s^{-1}}$ and $V_\delta = -10\,\mathrm{km\,s^{-1}}$ are assumed. Although high when compared with the values found for PKS 1257−326, they are in good agreement with the velocities coming from the delay experiment and annual modulation studies in J1819+3845 (e.g. Dennett-Thorpe & de Bruyn 2003). In addition, the periods of fast variability are in good agreement. The sharp drop by a factor of 5 from slow (day 338) to fast variability (day 352) within two weeks, however, is difficult to reconcile with the model. This deviation is relaxed taking the large error of the observed values into account. In general, the annual modulation model can qualitatively explain the slower variability observed in December 2000.

New observations with better time sampling during the period October to December will have to show, if a real seasonal dependence and thus ISS is present.

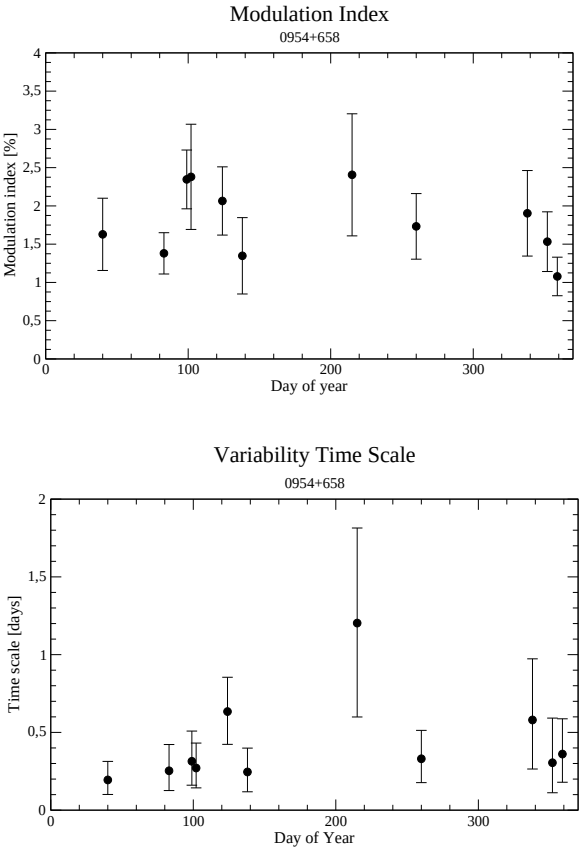

FIGURE 4.13— Results of the SF analysis for 0954+658 plotted versus day of the year. **Top:** modulation index. **Bottom:** variability time scale.

0954+658

The situation appears different for 0954+658. Figure 4.13 displays m and t versus day of the year. The top panel shows the scatter of m to be much less pronounced as seen in the case of 0716+714. The variability time scale plotted at the bottom reveals usually fast variations throughout the year (~ 0.3 days) and the scatter of t is much lower when compared to 0716+714. The two data points around days 124 and 338 display slower time scales, but appear not significant within the errors. The most interesting period in the second half of the year, where an prolongation is expected, is characterized by the slowest variability time scale observed (day 215). Here, the variations slowed down by a factor of 4. However, the error is larger due to the low number of variability cycles observed (~ 2). The long-term distribution of total flux density, modulation index and time scale are shown in Figure 4.14, which shows no obvious similar trend in contrast to what was seen in 0716+714. Furthermore, no significant correlation is evident, when plotting m versus flux density and time scale. This provides evidence, that intrinsic source evolution plays a minor role with regard to the IDV behavior of the source. Consequently, we may have detected the predicted seasonal dependence.

A comparison with the orbital motion model shows, that a prolongation so early in the year can be reproduced only with screen LSR-velocities in the range of $V_\alpha = -25\,\mathrm{km\,s^{-1}}$ and $V_\delta = 20\,\mathrm{km\,s^{-1}}$. Figure 4.15 displays the data with model calculations for different screen velocities superimposed. Similar to 0716+714, the screen distance and the source size have been constrained to 100 pc and 70 μas respectively, again using the observed fast variability throughout the year (~ 0.3 days). The agreement between data and model is obvious. The screen LSR-velocities

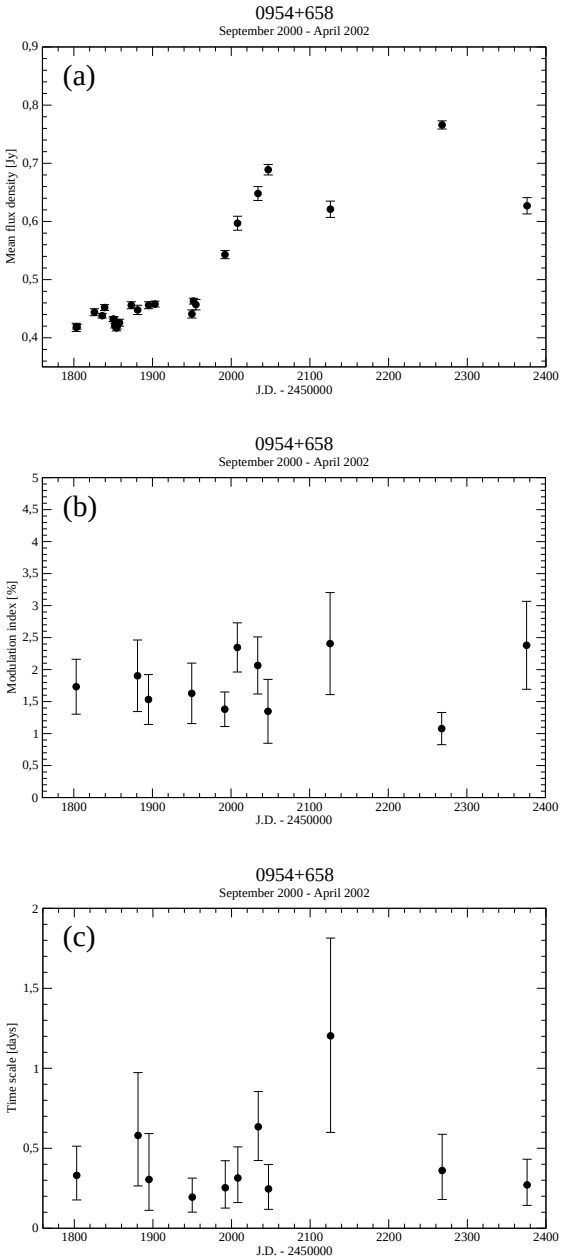

FIGURE 4.14— Long-term behavior of 0954+658 over the full monitoring period: (a) source total flux, (b) modulation index, (c) variability time scale. A similar behavior as seen in 0716+714 is not visible (see text).

differ strongly from those required to reproduce the data of 0716+714 (Figure 4.12) and the old data of 0917+624 (Figure 3.6, Chapter 3). If indeed ISS is in operation and the prolongations observed here reflect only seasonal cycles, the interstellar medium must exhibit a

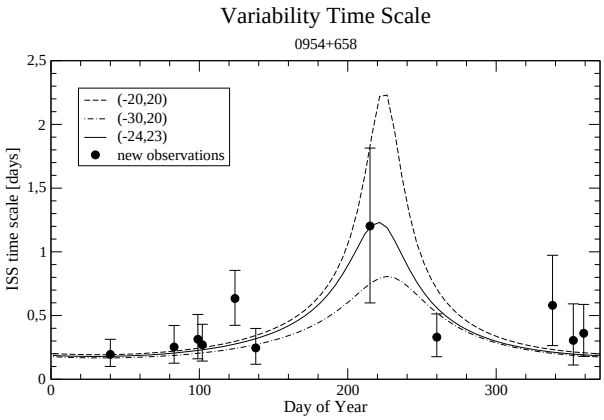

FIGURE 4.15— Variability time scales of 0954+658 versus day of the year with model calculations superimposed. Different LSR velocities for the screen (V_α, V_δ) are assumed as indicated. The model can explain the slower variability at day 215 and the faster variability throughout the year.

large velocity dispersion on angular scales of a few square degrees on the sky.

Once more, only one data point is available in the predicted slow-down period. More observations, in particular between May and October, are essential to confirm the seasonal cycle in 0954+658 proposed here.

4.5 Notes on other sources

A total of 19 additional sources were observed at least once during the 28 observing sessions (compare Table 4.1). From this, 12 were found to exhibit variations on short time scales. Both, the χ^2-test and modulation index of these sources differ significantly from those of the secondary calibrators and thus they were identified as IDV sources. The remaining 6 objects did not show significant variability. In the following, a few individual sources will be briefly presented.

J0422+535: This quasar was examined for IDV for the first time. The light curve from October 2001 exhibits fast variations with a peak-to-peak amplitude of $\sim 5\,\%$ ($Y = 3.55\,\%$, $\chi^2_r = 42.1$), Consequently, J0422+535 is identified as new IDV source.

0454+844: A BL Lac object which was observed already twice in the past. In both sessions IDV was detected (Kraus et al. 2003) and the variability amplitude at $\lambda 6\,\mathrm{cm}$ increased by a factor of ~ 3 between the two runs in December 1997 (from $Y = 3.19\,\%$ to $Y = 8.75\,\%$). Such change of the variability pattern within two weeks seems implausible for an ISS explanation unless one takes into account strong and fast changes of the intrinsic source properties (e.g. size of the scintillating components). However, the new observations in August 2001 again reveal weaker variations with $Y = 3.95\,\%$.

0718+792: This radio source has no optical counterpart and thus its redshift is unknown. As a possible secondary calibrator candidate it was investigated for variability several times. The flux density usually scattered around its mean value by $\sim 1\,\%$ - slightly more compared to 0836+710 and 0951+699. Although the χ^2_r reveals often values close to one and thus low probability for a variable light curve, sometimes much higher values are evident. Its usage as 'standard' secondary calibrator is therefore questionable.

0828+493: Already identified as IDV type II (Kraus 1997), this BL Lac object at $z = 0.55$ shows IDV in the light curve from May 2001. Here, the variations are not so dramatic as in the past: variability with an amplitude of $Y = 5.27\,\%$ and a time scale of $\sim 12\,\mathrm{hours}$ is visible compared to much faster ($\sim 5\,\mathrm{hours}$) and stronger ($Y = 7.04\,\%$) variations observed in the highly under-sampled light curve from December 1991.

J1814+4113: Located close to J1819+3845 (see below) on the sky, this compact core-jet source with $z = 1.56$ is the most promising new IDV candidate. Although observed with low sampling, the first light curve shows already fast variations on time scales of ~ 4 hours and a peak-to-peak amplitude of $5\,\%$ ($Y = 3.64\,\%$, $\chi^2_r = 69.5$, see Figure 4.16).

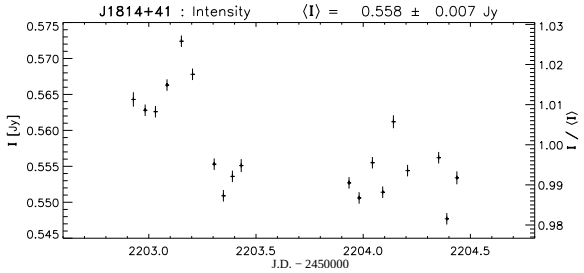

FIGURE 4.16— A new IDV candidate: J1814+4113 in October 2001 with peak-to-peak variations of 5%. Note the period around J.D. 2452203.2, where extremely fast variations with a time scale of $\sim 4\,\mathrm{hours}$ are clearly visible.

J1819+3845: This well known ISS candidate was observed in October 2001 and probably shows the most rapid variations observed with the Effelsberg telescope so far. Although highly undersampled, the light curve exhibits dramatic peak-to-peak variations of $90\,\%$ as expected from the Westerbork observations (e.g. Denneth-Thorpe & de Bruyn 2000). The "longer" time scales of $\sim 4\,\mathrm{hours}$ are in good agreement with the prolongation predicted by the annual modulation model during this time of the year (compare Figure 3.2 in Chapter 3).

Most of the remaining sources exhibit relatively low amplitude variations. In order to identify whether they are IDV sources or not the χ^2-test was used and the results are given in Table 4.1. Finally, seven of the 12 new IDV candidates turned out to exhibit variability on intraday time scales. The light curves and more detailed results for each source (S, m, Y and χ^2_r) are given in the Appendix.

4.6 Summary and Conclusions

The monitoring program presented here has shown, that the detection of annual modulations (and thus the presence of ISS) in "normal" type II IDV sources is a difficult

task. On the one hand, the longer time scales (compared to the extreme sources) require extended observing runs (5 days or more) in order to reach a sufficient high accuracy of m and t. Together with the need for a good sampling throughout the year (at least monthly), the amount of observing time is extremely high. On the other hand, the slower IDV sources show usually a more complex (core-jet) structure (in contrast to the point-like appearance of the extreme IDVs) and are dominated by long-term activity in their core regions. The latter appears to strongly influence the IDV characteristics of these sources and thus a seasonal effect is easily washed out. As seen in the episodic variability of PKS 0405−385, also extreme IDV sources can be affected by such long-term changes (Kedziora-Chudczer et al. 1998).

The most promising new candidate for the presence of a seasonal cycle is the BL Lac 0954+658. The data is in overall agreement with the model and a prolongation of the variability time scale was observed around day 215. Consequently, we propose the existence of an annual cycle in this source. Again, only one data point in the highly interesting period is available. For this reason, a detailed analysis of the effect and its implications for the ISM (e.g. anisotropy) and the source structure was not possible.

The situation appears more complicated in the BL Lac object 0716+714. We suggest that probably two effects are blended. The variable modulation index over the year and its correlation with other source parameters imply a strong influence of intrinsic source evolution on the IDV characteristics. This strongly influences the unambiguous detection of a seasonal cycle in the variability time scale. The latter, however, is suggested by the slower variability observed around day 338.

The annual modulation effect in 0917+624 proposed earlier could not be confirmed. Instead, the source shows a dramatic change in its IDV properties and ceased varying for more than 2.5 years. The seasonal cycle may at present not be visible due to structural changes in the central region. As a result, only extremely quenched scattering could be observed. We propose several scenarios in order to explain this behavior. Besides changes in the scattering properties of the screen itself, the most likely explanation is due to changes in the VLBI core of the source.

All sessions between 2000 and 2002					
Date	T_{obs} [hrs]	J.D[a] - 2450000	Epoch	Day of Year	Target Sources [b]
16.09.00	24	1803	2000.70	260	0604+728, 0716+714, 0718+793, 0917+624, 0954+658
17-18.09.00	10	1804	2000.71	261	0604+728, 0716+714, 0718+793, 0917+624, 0954+658
09.10.00	15	1826	2000.77	283	0604+728, 0716+714, 0718+793, 0917+624, 0954+658
19.10.00	15	1836	2000.79	293	0604+728, 0716+714, 0718+793, 0804+499, 0835+580, 0917+624, 0954+658
22.10.00	10	1839	2000.81	296	0604+728, 0716+714, 0718+793, 0917+624, 0954+658
02.11.00	15	1850	2000.84	307	0604+728, 0716+714, 0718+793, 0917+624, 0954+658
03.11.00	14	1851	2000.84	308	0604+728, 0716+714, 0718+793, 0917+624, 0954+658
04.11.00	10	1852	2000.84	309	0604+728, 0716+714, 0718+793, 0917+624, 0954+658
06.11.00	5	1854	2000.85	311	0604+728, 0716+714, 0718+793, 0917+624, 0954+658
07.11.00	5	1855	2000.85	312	0604+728, 0716+714, 0718+793, 0917+624, 0954+658
10-11.11.00	10	1858	2000.86	315	0604+728, 0716+714, 0718+793, 0917+624, 0954+658
24-27.11.00	24	1872	2000.90	329	0604+728, 0716+714, 0718+793, 0917+624, 0954+658
3-4.12.00	43	1881	2000.92	338	0346+800, 0615+820, 0716+714, 0917+624, 0954+658
17-18.12.00	36	1895	2000.96	352	0346+800, 0615+820, 0716+714, 0917+624, 0954+658
25.12.00	8	1903	2000.98	360	0604+728, 0716+714, 0718+793, 0917+624, 0954+658
09-10.2.01	27	1949	2001.11	40	0604+728, 0716+714, 0718+793, 0917+624, 0954+658
12.2.01	5	1952	2001.12	43	0604+728, 0716+714, 0718+793, 0917+624, 0954+658
14.2.01	7	1954	2001.12	45	0604+728, 0716+714, 0718+793, 0917+624, 0954+658
24-26.3.01	43	1992	2001.23	83	0403+765, 0604+728, 0716+714, 0718+793, 0917+624, 0954+658, 1003+830
09-10.4.01	22	2008	2001.27	99	0604+728, 0716+714, 0718+793, 0917+624, 0954+658
04-07.5.01	65	2033	2001.34	124	0403+765, 0716+714, 0828+439, 0917+624, 0954+658, 1003+830
18-21.5.01	34	2047	2001.38	138	0602+673, 0716+714, 0804+499, 0917+624, 0954+658
03-06.8.01	67	2124	2001.59	215	0454+844, 0602+673, 0716+714, 0835+580, 0917+624, 0954+658
20-22.10.01	49	2202	2001.80	293	J0422+53, J0834+55, 0917+624, J0949+66, J0957+55, J1814+41, J1819+385, J1852+40
25-26.12.01	23	2268	2001.98	359	0716+714, 0835+580, 0917+624, 0954+658, 1031+567
12-14.04.02 [c]	37	2376	2002.28	102	0716+714, 0917+624, 0954+658
07-08.8.02	14	2493	2002.60	219	0917+624
03.10.02	7	2550	2002.75	276	0716+714, 0917+624

TABLE 4.5— Summary of the Effelsberg monitoring program between 2000 and 2002.

[a] J.D., Epoch and Day are given for the beginning of the observing run

[b] The secondary calibrators 0836+765 and 0951+699 are not given here, but were always observed.

[c] This epoch has been part of an larger session with extension towards higher frequencies (see Chapter 7)

5

VLBI Observations of the Quasar 0917+624 at 15 GHz

Based on the results shown in the previous chapter it appears as if 0917+624 has stopped to be intraday variable since at least the last 2.5 years ($m \sim 0.5\,\%$). This strongly contradicts the model predictions for annual modulations presented in Chapter 3, which claimed recovery to the fast variability mode already at the end of year 2000. The observed non-variability of 0917+624 on daily time scales is at present not at all understood, particularly in view of the past 15 years, during which the source always was one of the most prominent examples of an IDV source.

As outlined in the previous chapter, one of the possible explanations for the present quiescence of 0917+624 is that the intrinsic structure of the source has considerably changed. The dominant structure components, which were responsible for rapid interstellar scintillation in the past, either must have disappeared or must have increased their intrinsic size. A sudden increase of the size of the core due to the formation of a new component at the footpoint of the jet could explain the IDV observations. Such a scenario would lead to a size of the scintillating component temporary larger than the scattering size of the medium, then producing only strongly quenched scintillations. After the ejection, the new component moves further down the jet and subsequently separates from the core region. This should lead after some time to a decreasing size of the scintillating component and the variations should re-appear. If this scenario is realized in 0917+624, new VLBI observations should reveal (i) a new component ejected shortly before 0917+624 ceased varying for the first time in September 1998 (as already suggested by Krichbaum et al. 2002, see below), (ii) one or more new components ejected during the last three years causing the present, 2.5 years-quiescence of the source and (iii) changes in the flux density of the VLBI core.

In order to test this scenario, new VLBI observations of 0917+624 at 15 GHz were performed. The VLBI monitoring covers the time period between December 2001 and July 2002. After a short discussion of previous VLBI observations of this source, we present the analysis and results of our new epochs.

5.1 Previous VLBI observations

At present, investigations of 0917+624 on VLBI scales were done in 1988–1993 (Standke et al. 1996), 1997–1998 (Alberdi et al. priv. comm.), and 1999–2000 (Krichbaum et al. 2002).

5.1.1 First VLBI study of 0917+624

The most intensive VLBI observations of the source were performed by Standke et al. (1996). Their observations were carried out with the European and US VLBI networks in 10 sessions between September 1988 and November 1993. The source was observed in the frequency range of 1.7 to 22.2 GHz.

0917+624 was found to be morphologically similar to the well known core-jet sources (e.g.

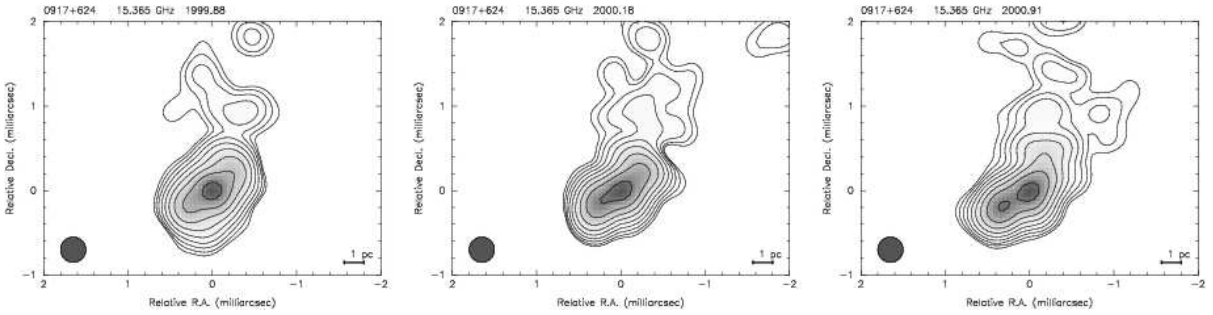

FIGURE 5.1— The first three 15 GHz VLBI epochs of 0917+624 observed between 1999.9 and 2000.9 by Krichbaum et al. (2002).

0836+710), but with a core-to-jet brightness ratio higher by a factor of 2. In all maps an unresolved component (their component A) is visible at the southern "end" of the source containing more than 70 % of the total source flux. Due to its compactness, variability and spectral shape this component has been identified with the VLBI core. Their modelfits reveal limits to its size of the order ≤ 0.2 mas at 3.6 cm and ≤ 0.4 mas at 6 cm. Further down the jet, several components are seen up to a distance of 26 mas from the core. In comparison to the latter, the position angle of these jet components is different by $\sim 20°$. These findings indicate that the innermost milliarcseconds of the source exhibit a bent morphology, while on larger scales the jet forms a relatively straight structure. The jet component B seen in the 15 and 22 GHz maps shows an increasing elongation over the three epochs and thus suggests an ejection and outward motion, while for components C and D proper motion of 0.15 and 0.23 mas yr^{-1} could be detected. From the latter, the authors deduced apparent superluminal motion of $\beta_{app} = 7.8$, a minimum Lorentz factor, $\Gamma_{min} = 7.9$ and a maximum angle to the line of sight of $\theta_{max} = 7.4°$ ($H_0 = 100\,\mathrm{km\,s^{-1}\,Mpc^{-1}}$, $q_0 = 0.5$).

5.1.2 0917+624 at 15 GHz between 1999–2000

Direct evidence for an increase in size of the inner, scintillation region of 0917+624 is coming from VLBI observations at 15 GHz performed by Krichbaum et al. (2002) during 1999–2000 (Figure 5.1). The VLBI maps reveal a considerably bent core-jet morphology, with the brightest two central components separating at a rate of about ~ 0.17 mas/yr ($\beta_{app} = 5.8$, see Figure 5.2). The easternmost of the two components exhibits an inverted spectrum ($\alpha_{5/15GHz} \simeq +1$) and indicates that this is probably the core. Extrapolating the motion of the two components backwards in time, leads to a time of ejection near 1998.6, shortly before the date, when 0917+624 ceased varying for the first time (September 1998). Strongly quenched scattering can be expected, when the relative separation between two or more components is less or equal than the scattering size defined by the ISM. From the observed speed and a typical scattering size of $\sim$ 0.05–0.07 mas for this source (Rickett et al. 1995), one expects a period of reduced (or no) variability of at least 0.3–0.5 years after component ejection. Again, this is consistent with the observed restart of the variability in February 1999 (Kraus et al. 1999). These findings suggest, that the prolongation of the variability time scale observed in September 1998 is due to extremely quenched scattering and does not reflect a seasonal cycle as proposed earlier (Chapter 3).

It is therefore very tempting to assume that the present quiescence (since year 2000) in the variability of 0917+624 once more is caused

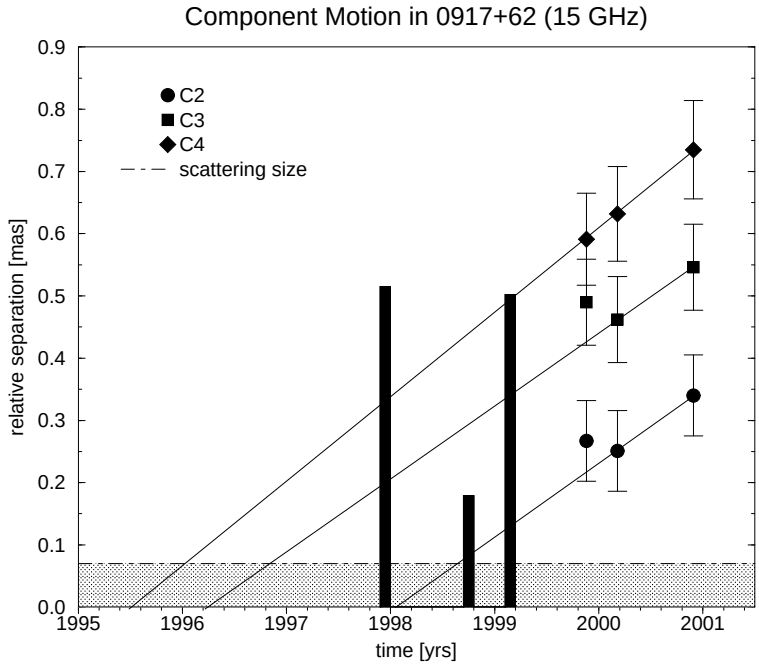

FIGURE 5.2— Relative separation of the inner components C2, C3 and C4 from the core. Back-extrapolation of components is shown as well as strength of variability at given IDV epochs (see text).

by a blending effect of the core with a newly ejected component. This component probably was ejected during the first half of the year 2000 and should become visible in new VLBI observations. First evidence for such a component ejection comes from the two most recent 15 GHz maps (compare Figure 5.1), which already show a 30 % increase of the core flux density between March and November 2000.

5.2 New VLBI Monitoring between 2001 and 2003

We therefore continued the multi-frequency VLBI monitoring of 0917+624. The VLBI imaging was done in parallel to the ongoing flux density monitoring with the Effelsberg telescope.

5.2.1 Observations and Data Reduction

The observations were carried out with the 10 antennas of the VLBA (Very Long Baseline Array) plus Effelsberg in three Epochs between December 2001 and July 2002. Data were obtained at frequencies 5, 15 and 22 GHz with full polarization information for 0917+624 and two other (calibrator) sources. A brief summary of the epochs presented here is given in Table 5.1.

In order to investigate the recent findings of Krichbaum et al. (2002), a subset of these new epochs was extracted consisting of the 15 GHz data. The reduction and analysis of the latter was performed in the framework of this thesis and will be presented here.

After correlation at the Array Operation Center of the VLBA in Socorro (NM, USA), the data ran through a standard calibration procedure to permit the averaging of the visibilities over both, frequency and time. The pre-calibration data processing was performed within the software package *AIPS* (Astronomical Image Processing System, Fomalont 1981). Here, the *a-priori* amplitude calibration was done using telescope gain curves and T_{sys}-measurements, while phase-cal information was used in the *a-priori* phase calibration in order to remove instrumental phase offsets and slopes (single-band delays) between and within the different bands (two

ν_{ref} [MHz]	Epoch	Date	Stations	Mode	$\Delta\nu$ [MHz]	Time [hrs]	Comments
15.365	2001.98	26 Dec. 01	VLBA+EB	128-4-2	2×16	12	MK down
15.365	2002.23	27 Mar. 02	VLBA+EB	128-4-2	2×16	12	
15.365	2002.53	13 Jul. 02	VLBA+EB	128-4-2	2×16	12	1 hrs no data at EB+FD

TABLE 5.1— **Summary of the VLBI observations.** The table gives the reference frequency ν_{ref}, observing epoch, date, antennas involved in the observations, recording mode, observing bandwidth $\Delta\nu$ and observing duration. The station codes mentioned here are: EB Effelsberg, FD Fort Davis and MK Mauna Kea. The observations were performed with the whole VLBA-array plus Effelsberg at 5, 15 and 22 GHz. In the framework of this work, only the 15 GHZ data was used.

IFs). Residual phase errors due to the atmosphere and the "not-perfect" correlator model (multi-band delays) as well as residual single-band delays were corrected by fring fitting the data. To obtain the brightness distribution of the source, hybrid mapping was done within the software package DIFMAP (Shepherd et al. 1994) using clean and self-calibration techniques. Finally, Gaussian models were fitted to the data, which yield a parameterization of the source components and allow the cross-identification of components over all epochs between 1999 and 2002.

5.2.2 Source Morphology

The final clean maps of all three epochs are displayed in Figure 5.3 and show a similar morphology compared to the earlier 15 GHz observations. All maps exhibit an unresolved central region which contains more than 70 % of the source total flux within about 0.5 mas. More extended structure is visible at distances between 0.6 and 2.5 mas pointing towards the north. Here, a change in position angle of about 40° occurs up to a distance of 2 mas, thus the source forms a bent core-jet like structure. Structural changes in the innermost core region are visible within the three epochs as well as in comparison to the earlier epochs of Krichbaum et al. (2002).

The measured positions, geometries and parameters of the various components along the source are given in Table 5.2. The maps obtained from the model fitting are shown in Figure 5.4. The values given in Table 5.2 represent the "best" source model obtained from a larger number of fits per epoch. From comparison between these various model fits, the errors were determined empirically from the scatter in the different fits. The fitting procedure was straightforward for the first two epochs, where the most stable model with the best value of χ^2_{red} ($\lesssim 1$) was obtained using seven Gaussian components. However, the situation for the last epoch was different. Here, the χ^2_{red} could be strongly reduced only by considering an additional source component.

5.2.3 Component Motion in 0917+624

In order to test the "component ejection" scenario proposed to explain the unusual IDV behavior of the source, the maps of Krichbaum et al. (2002) were combined with the new data (epochs 4–6). The cross-identification of components between all epochs allows to examine the source kinematics (e.g. component speeds and ejection times).

Since the identification of the core with the most southern component C1 in epochs 4–6 can not be verified by its spectral shape so far, various identification scenarios were tested to find the most reliable identification scheme across all six epochs, in particular with regard to the additional modelfit component of epoch 6. The most reliable identification scenario is shown in Figure 5.5, which is suggested by the good agreement/cross-identification of the components between epochs 1–5 (taking flux density, position and FWHM of the individual components into account). Here, the south-

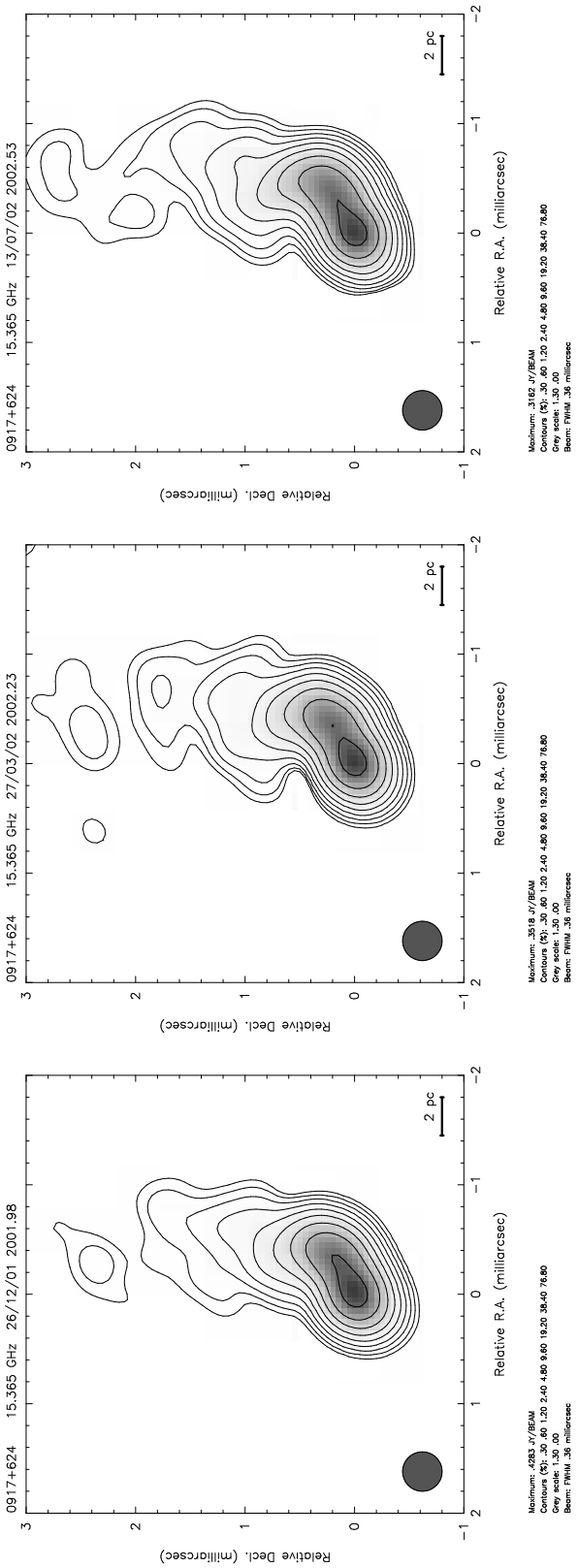

FIGURE 5.3— Final maps of the new VLBI epochs obtained between December 2001 and July 2002.

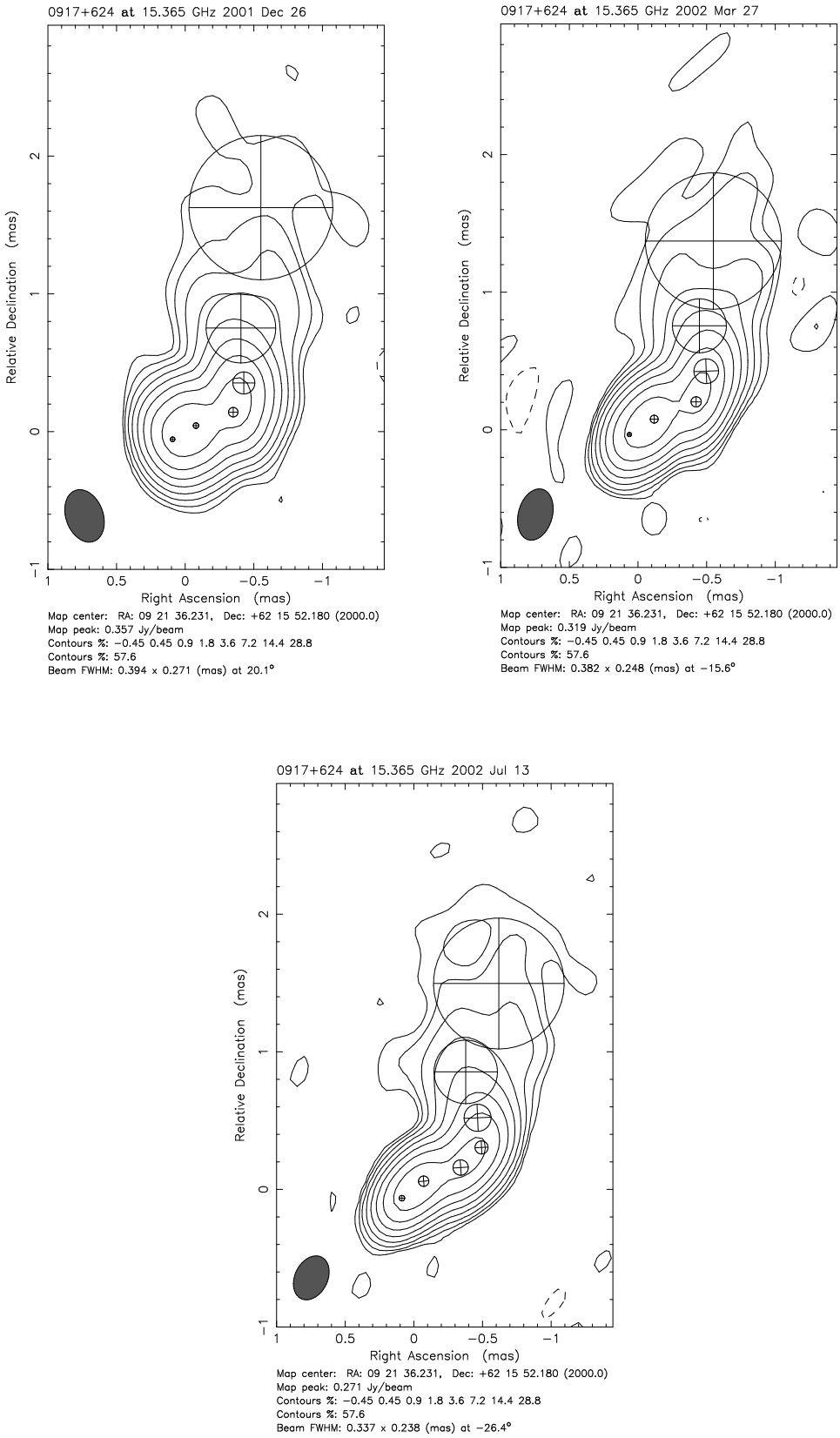

FIGURE 5.4— Final modelfit maps of epochs 4–6 are displayed with model fit components superimposed.

TABLE 5.2— VLBI model components of epochs 4–6

Comp.	Epoch	S [Jy]	ΔS [Jy]	r [mas]	Δr [mas]	p.a. [°]	Δp.a. [°]	FWHM [mas]	ΔFWHM [mas]
C1	2001.98	0.22	0.03	–	–	–	–	0.03	0.02
	2002.23	0.15	0.05	–	–	–	–	0.03	0.04
	2002.53	0.15	0.01	–	–	–	–	0.04	0.02
C2a	2001.98	0.29	0.04	0.20	0.03	–59.8	3.5	0.04	0.02
	2002.23	0.28	0.04	0.21	0.04	–58.2	1.3	0.06	0.02
	2002.53	0.22	0.01	0.20	0.01	–52.0	0.5	0.08	0.01
C2b	2001.98	0.22	0.02	0.48	0.04	–66.0	1.1	0.07	0.01
	2002.23	0.18	0.01	0.54	0.03	–64.0	1.9	0.07	0.04
*	2002.53	0.16	0.05	0.48	0.03	–62.5	2.4	0.11	0.05
C3	2001.98	0.19	0.01	0.66	0.05	–51.8	0.9	0.16	0.01
	2002.23	0.15	0.01	0.73	0.02	–50.6	3.0	0.18	0.02
*	2002.53	0.08	0.01	0.80	0.02	–43.3	1.5	0.20	0.04
C4	2001.98	0.08	0.01	0.95	0.06	–31.7	1.8	0.51	0.03
	2002.23	0.05	0.02	0.94	0.08	–32.8	5.9	0.39	0.04
*	2002.53	0.06	0.01	1.03	0.04	–26.8	1.4	0.46	0.09
C5	2001.98	0.03	0.01	1.80	0.15	–20.9	2.2	1.05	0.05
	2002.23	0.05	0.01	1.53	0.10	–23.5	1.4	0.99	0.03
	2002.53	0.04	0.01	1.71	0.14	–24.3	1.4	0.95	0.11
C6	2001.98	0.04	0.01	6.30	0.01	–21.3	0.2	2.00	0.03
	2002.23	0.04	0.01	6.29	0.02	–21.7	0.2	2.11	0.06
	2002.53	0.03	0.01	6.27	0.01	–21.8	0.1	1.97	0.16

* Epoch 6 was found to fit less into the identification scheme of epochs 1–5, since a clear cross-identification of components C2b, C3 and C4 have not been possible. Thus, epoch 6 was neglected in the subsequent analysis.

ern most component C1 of the new epochs was identified with the core of epochs 1–3. Component C2 of epochs 1–3 was identified with component C2b, whereas the subsequent components C3–C4 correspond to components C3–C4 in epochs 1–3. Epoch 6, however, does not fit well into this scheme due to the afore mentioned problems and thus was neglected in the subsequent analysis. New VLBI epochs have to verify the reliability of the model fitting of epoch 6. The relative separation of the innermost components C2a–C4 is shown in Figure 5.5, which now can be traced over a period of about two years. A linear fit to the data of each component gives a proper motion of $\mu^{\mathrm{C2b}} = 0.12\,\mathrm{mas\,yr^{-1}}$, $\mu^{\mathrm{C3}} = 0.10\,\mathrm{mas\,yr^{-1}}$ and $\mu^{\mathrm{C4}} = 0.16\,\mathrm{mas\,yr^{-1}}$, respectively. This yields apparent superluminal velocities of $\beta_{app}^{\mathrm{C2b}} = 4.2$, $\beta_{app}^{\mathrm{C3}} = 3.6$ and $\beta_{app}^{\mathrm{C4}} = 5.5$, respectively. This is in agreement with the previous findings.

5.2.4 Component Ejection and Variability Characteristics

The first jet component of epochs 4–5 (labeled C2a), as seen in Figure 5.5, has no counterpart in the previous epochs (1–3) and thus can be identified as newly ejected component. This is in agreement with the proposed quenched scattering scenario, where at least one new component is expected to explain the present non-variability of the source.

As seen from Figure 5.5, extrapolating the motion of the components backwards in time yields their approximate ejection times of $\sim$1995.6 (C4), $\sim$1996.0 (C3) and $\sim$1998.3 (C2b), respectively. The strength of intra-day variations (modulation indices) deduced from IDV observations between 1998 and 2002 are shown as black bars in Figure 5.5. Unfortunately, 0917+624 was not examined for IDV between 1993 and 1997 and thus a direct comparison of its IDV behavior and the

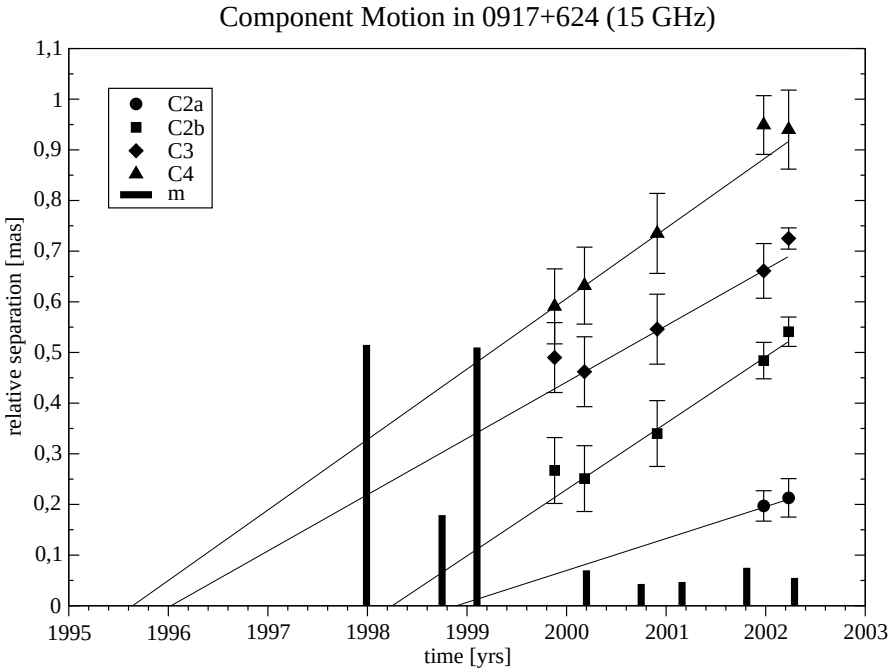

FIGURE 5.5— Component Motion in 0917+624: The inner components identified by Krichbaum et al. (2002) are shown with the new epochs 4–5 superimposed. The extrapolated ejection dates are indicated. The black bars belong to the strength of variability at the given time. A new jet component (C2a) is visible with an approximate ejection date about one year before 0917+624 ceased varying for the second time (see text).

ejection of components C3 and C4 is not possible. However, the ejection of component C2b around 1998.3 occurred shortly before the source stopped its variability (September 1998) and therefore confirms the previous findings of Krichbaum et al. (2002). At this time of strongly reduced variations, the relative separation of C2b from the core was about 0.07 mas. The onset of IDV in February 1999 occurred at a separation of about 0.1 mas. We will now consider the ISS model of weak scattering introduced in Chapter 4 (Beckert et al. 2002, see also Chapter 6) with the same screen parameters and assume that the quenched variability of $m_{6\mathrm{cm}} = 1.8\,\%$ in September 1998 was produced by a blend of the core with component C2b. Scaling the angular scale of 0.07 mas at 15 GHz linear in frequency yields a component size of 0.22 mas at 4.85 GHz. Such component would produce quenched variability of the order 2.3 % at 4.85 GHz for a screen distance of 150 pc, in good agreement with the observed value of 1.8 %. For a scintillating component of such size and a relative velocity of $15\,\mathrm{km\,s^{-1}}$ between Earth and screen during this time of the year (compare Chapter 3), a variability time scale of about 7 days would be expected. Again, this in good agreement with the prolongated time scale of > 5 days observed at that time. Thus, the rough estimations given here strongly support the extremely quenched scattering scenario proposed earlier.

Although no significant motion of component C2a could be detected within the errors, a linear interpolation suggests an ejection time around 1999.0, about one year before the source was observed to exhibit again strongly quenched variations. Although a similar scenario appears likely, a core separation

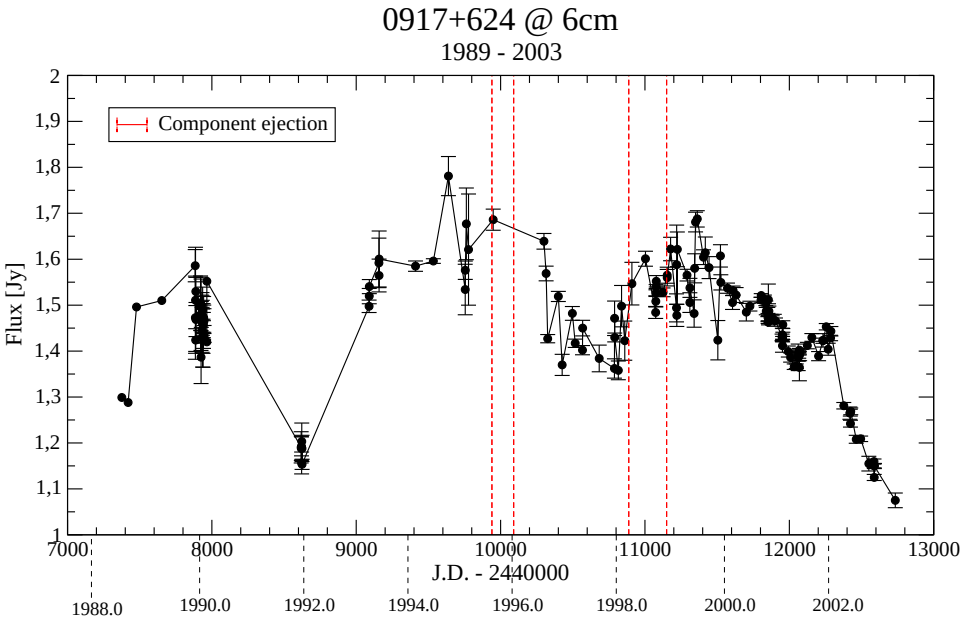

FIGURE 5.6— Flux density of 0917+624 at 6 cm wavelength observed with Effelsberg between 1989 and 2003. The ejection of components C2a, C2b, C3 and C4 (red, dashed lines) occurred during periods of larger flux density outbursts. The smaller flares near Epoch 2000.5 and 2002.0 may indicate the ejection of new jet features.

of 0.2 mas in March 2002 indicates that C2a can not produce quenched scintillations over the continuous period of about 2.5 years as observed. Additional components ejected somewhere between 1999 and 2002 are thus required to explain the ongoing inactivity of the source. A comparison of long-term flux density evolution with component ejection times reveals that the ejection of new components occurs mainly during larger flux density outbursts (Figure 5.6). Although the flux density strongly decreased over the last years, two smaller flares between 2000 and 2002 may indicate the occurrence of additional components.

However, the present situation appears different when compared to the first period of quenched variability in September 1998. It is important to note that within the previous scenario longer variability time scales are expected due to the increase in source size. This is not observed as seen e.g. in Figure 4.7. Here, the remaining low-level variations since September 2000 appear to be fast ($\lesssim 0.3-0.4$ days). In addition, the modulation index is even smaller by a factor of about three compared to September 1998. This may indicate that a further effect is important. The only possible mechanism in view of ISS is a strong decrease of the amount of source total flux contained in the scintillating component(s) between 2000 and 2003. In this scenario, the ratio between total flux density in the scintillating component and non-scintillating components ($S_{tot} = S_{scint} + S_{ext}$) should have changed considerably. The strong decrease in total flux density at $\lambda 6$ cm as well as the strong flux density decrease of the core and component C2b of more than 50 % over the five VLBI epochs supports this idea.

5.3 Conclusions

The results presented here outline the importance of the mas/μas structure of an IDV source at the time of observation. In particular, a connection was found between strongly reduced IDV (lower m, longer time scales) and the appearance of a newly ejected jet component on sub-mas scale. The latter appear to strongly influence the IDV characteristics of these sources (strength of variability, IDV time scales) and can be explained by extremely quenched scattering due to a temporary larger angular size of the scintillating component in the source. Here, the ejection of new components at higher frequencies (and subsequent increase in component size) occurs during periods of strong flux density outbursts. This is in agreement with the results of Chapter 4, where 0716+714 was observed to be less strong variable during epochs of higher total flux density. In addition, a similar tendency is seen also in statistical investigations of IDV sources (e.g. Cimò 2003). However, the situation in 0917+624 appears more complicated during the second period of inactivity, where the expected longer time scales were not observed. We propose a further effect to be important: changes in the amount (here decrease) of total flux density contained in the scintillating component.

All this indicates that intrinsic source evolution on time scales of weeks to months and on sub-mas scales plays an important role: IDV is not a "steady state" situation. New monitoring projects (total flux density, IDV and VLBI) are essential to investigate these effects in more detail. For example, a better knowledge of the source kinematics (more accurate component speeds and ejection times) and the exact time between component ejection and absent/onset of the fast variability mode is important. This will allow us to estimate the scattering size of the ISM towards 0917+624 without assumptions on the physical properties of the ISM.

Part II: High Frequency Observations of IDVs

6

High Frequency IDV: Search for an Intrinsic Contribution

Rapid flux density variability in blazars is nowadays observed over the whole electromagnetic spectrum: from gamma-rays to the cm-radio regime. Such multi-frequency investigations are very important, since they can help to disentangle source intrinsic and extrinsic effects. Bridging the gap between the cm-radio and IR-optical regime, systematic observations in the mm- and sub-mm regime are required, but are not yet done frequently. New observations at high radio frequencies (32 GHz and 345 GHz) were performed during the time of this thesis and are presented in the following. In the first part of Chapter 6 we discuss the scientific motivation and relevance of such high frequency observations of IDVs. The subsequent sections present the 32 GHz observations and results in detail. In addition, the multi-frequency observations of one particular source, J1819+3845, are discussed in view of a specific model for interstellar scintillation.

6.1 Scientific Background and Motivation

Owing to the high brightness temperatures and small source sizes of AGN, it is nearly unavoidable that IDV sources scintillate. Consequently, ISS must play an important role in the IDV phenomenon. As already mentioned in previous chapters, at least in three sources the evidence for interstellar scintillation as the main cause for their rapid variability has recently become very strong: PKS 0405−385, J1819+3845 and PKS 1257−326 (Jauncey et al. 2000a, Dennett-Thorpe & de Bruyn 2002 and Bignall et al. 2003). In addition, the variations of 0917+624 in total intensity can be explained via ISS (Rickett et al. 1995). The polarization variations in PKS 0405-385 can nicely be modeled by interstellar scintillation using a correlation analysis (Rickett et al. 2002). However, there is also still room for an intrinsic contribution to the IDV pattern, since ISS is not able to fully explain the observational appearance of IDV, e.g. (see also the discussion in Chapter 2):

- the complicated polarization and, in particular, polarization angle variations cannot yet be completely reproduced by the standard model of ISS (Rickett et al. 1995, Qian et al. 2001). The current modeling indicates that a mixture of ISS and source intrinsic variability could explain the observations.

- it was also shown that the frequency dependence of the variability amplitude in a few sources does not decrease with increasing frequency as expected for weak interstellar scintillation (Krichbaum et al. 2002, Cimò 2003). Figure 6.1 displays the noise-bias corrected variability amplitude Y for 0716+714 versus frequency for 5 different epochs. Although this quantity (and hence its error) is effected by observational parameters (compare Chapter 4), time variability of Y and a few cases with a clear trend of Y increasing

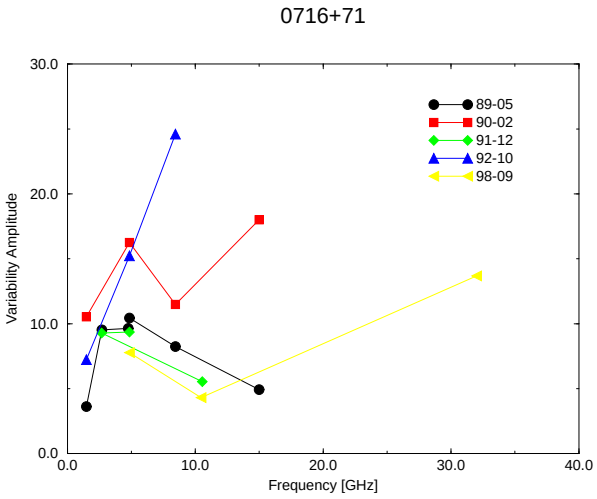

FIGURE 6.1— The variability amplitude Y (in %) of 0716+714 plotted versus frequency for 5 different epochs between 1989 and 1998. Note the time variability and the increase of Y towards shorter wavelength ("intrinsic up-turn") in a few cases, which is not in agreement with ISS (Krichbaum et al. 2002).

with frequency is seen. Such behavior is not expected for a standard ISS scenario unless one takes a source intrinsic and time variable contribution into account which increasingly dominates towards higher frequencies ("intrinsic up-turn").

The arguments above indicate that IDV is maybe not caused by a single physical process, but must be seen as a complicated mixture of two effects. An intrinsic contribution appears to be present since some additional possibilities are not yet ruled out: (i) the inverse Compton limit might be not such a hard limit as presently assumed. The latter could be violated and inverse Compton catastrophes occur for brief periods of time (leading to IC avalanches and associated short-term flashes of second order IC scattering) (ii) the radiation could be coherent. Also the fact that with only moderate Lorentz factors apparent brightness temperatures of the order 10^{16}K can be reached indicate that maybe not only one physical process is at work.

If IDV indeed is a source and frequency dependent mixture of intrinsic and propagation effects, then multi-frequency and polarization observations will help to disentangle both effects. Here, high frequency observations are of particular importance: in the weak, quenched scattering regime, the autocorrelation $\rho(x)$ of light curves can be calculated as integral along the line of sight through the scattering screen (see Section 6.4 for details). The square of the modulation index $m^2 = lim_{\tau\to 0}\rho(\tau)$ of the variations can then be calculated (Beckert et al. 2002). This yields the following frequency-dependents of m:

$$\rho(0) = m^2 \sim \lambda^4\theta^{-2.3}\,. \qquad (6.1)$$

Depending on the frequency behavior of the source size θ, the strength of total power variations explained by ISS should thus decrease strongly towards higher frequencies. This fact provides the most direct observational test for interstellar scattering. ISS should vanish at frequencies much higher than the critical frequency, where the transition between strong and weak scintillation occurs (usually between 1−5 GHz) and the intrinsic contribution (if present) should show up as up-turn in the mm- and sub-mm regime.

This fact and the strong argument for the presence of IDV in this regime coming from the correlated variability over the whole spectrum in a few sources (e.g. 0716+714, see Chapter 2) was taken as motivation for high frequency observations in a few cases up to now: Wagner et al. (1993) suggested the existence of mm-IDV for PKS 0405−385 based on data from the Swedish ESO Submillimeter Telescope (SEST) in Chile. Figure 5 in Chapter 2 shows significant variations on a time scale of 2 days at 230 GHz in July 1993. Results from previous mm-observations performed with the IRAM 30-m telescope on Pico Veleta and the mm-interferometer on Plateau de Bure are still inconclusive. Bolometer-measurements at Pico were affected by beam dilution and bad weather, which limits the calibration accuracy to $10-15\,\%$. Test experiments at Plateau de Bure are effected by its linear receiver feeds, which make it impossible to disentangle intrinsic flux density variations from the response of source polarization and parallactic rotation of the E-vector. In

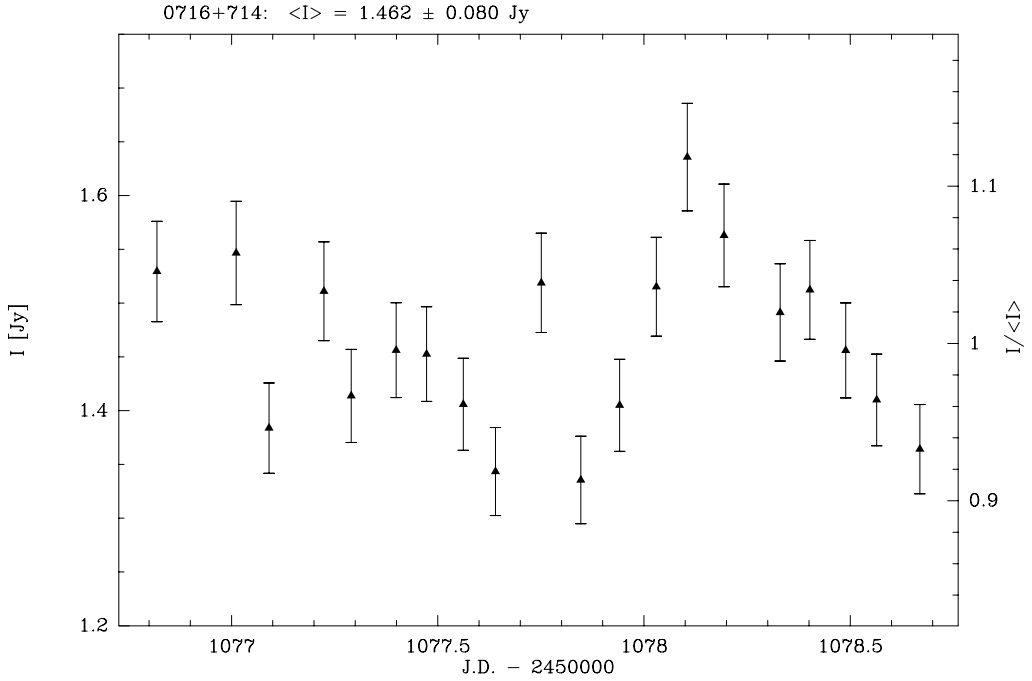

FIGURE 6.2— High frequency IDV in 0716+714: Kraus et al. (2003) (see also Krichbaum et al. 2002) found significant variations at 32 GHz in September 1998 with 20 % peak-to-peak variations. The time scale of the variability is ∼ 12 hours. The observations were performed with the first module of the 9 mm-receiver mounted in the secondary focus of the Effelsberg telescope.

all cases the weather was not optimal to detect (or rule out) IDV in the mm-band for our high declination sources.

The most promising evidence for the presence of mm-IDV comes from flux density measurements performed with Effelsberg at 9 mm wavelength. Figure 6.2 displays this flux density variability of 0716+714, which shows rapid variations with a peak-to-peak amplitude of 20 % during 48 hours of observation in September 1998 (Krichbaum et al. 2002, Kraus et al. 2003). The measurement error achieved during the observing period is 7 %. This is the first time that IDV is directly detected also at mm-wavelengths.

Since so far little is known about the variability characteristics in the mm- and sub-mm regime, we took these results as motivation for new high frequency observations. A systematic study of the frequency dependence of IDV and, in particular, the detection of an intrinsic contribution would rule out ISS as sole explanation for rapid intraday variations.

Two projects were proposed during 2002: (i) observations with the Heinrich Hertz Sub-Millimeter Telescope (HHT) at 345 GHz to bridge the gap between the millimeter and optical band and search for sub-millimeter variability in the most promising candidate 0716+714 (ii) new Effelsberg observations at 32 GHz with the aim to confirm the presence of mm-IDV in 0716+714 and other IDV sources.

HHT Observations at 345 GHz

The 345 GHz observations were performed during a three week radio-sub-mm-optical campaign in April/May 2002. A detailed presentation of this project (observations, data reduction and results) is given in the thesis of G. Cimò (2003). Hence, only a short summary will be presented here, while our new Effelsberg 32 GHz observations will be discussed in detail in Section 6.2.

Our main target, 0716+714, was observed with a duty cycle of two measurements per hour using the 19-channel bolometer array.

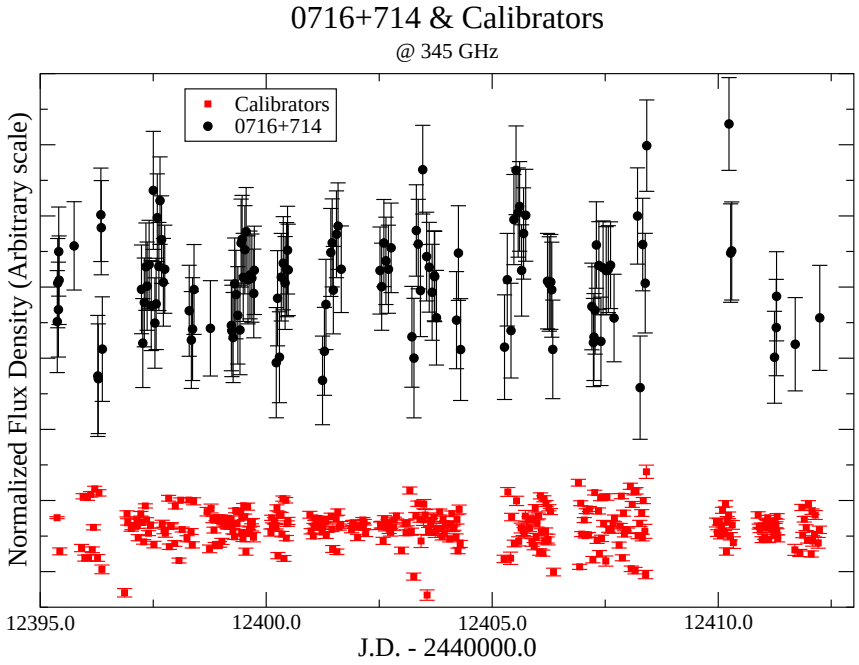

FIGURE 6.3— Final 345 GHz light curves obtained with the HHT over a three week period. 0716+714 (black) and all calibrator scans (red) are shown. Compared to the scatter of the calibrators, 0716+714 shows 3σ-variability with a time scale of ~ 0.5 days.

The system consists of 19 individual broadband continuum receivers and is sensitive around a wavelength of 0.87 mm (345 GHz). We observed in the on-source-off-source observing mode with the number of on-off subscans matched to the source brightness at the given frequency. Sky-dip scans as well as observations of primary and secondary calibrators (Ultra Compact HII regions, planetary nebula and planets) were done with a densely time sampled duty cycle.

After the subtraction of atmospheric contributions using the off horns, corrections for the atmosphere opacity and a final time-dependent correction, we obtained the light curves plotted in Figure 6.3. For better comparison, the normalized fluxes of both target and (combined) calibrator sources are shown (Cimò 2003). The peak-to-peak variations of 0716+714 and the remaining variations seen in the combined calibrator light curve indicate a (weak) $3\,\sigma$-detection of variability on time scales of ~ 12 hours. The performed IDV analysis yields a χ^2_r of 1.07 providing a 87 % probability for the consistency with the hypothesis of a variable source.

If real, the observations presented in Figure 6.3 show for the first time intraday variability in the sub-mm regime. Due to the frequency dependence of ISS, these variations should be attributed to an intrinsic origin. Assuming a lower limit for the redshift of 0.3, the variations seen in Figure 6.3 imply a brightness temperature of $T_B \gtrsim 2 \times 10^{14}$ K. A moderate Doppler factor of $D \gtrsim 6$ allows to reduce the temperature down to the inverse Compton limit of 10^{12} K. This value is in good agreement with the results of recent component-motion studies performed by Bach et al. (2002) for this source.

6.2 Effelsberg Observations at 32 GHz

The light curve shown in Figure 6.2 from September 1998 was obtained with the old Module 1 of the Effelsberg 32 GHz receiver mounted in the secondary focus (Figure 6.4). Our new observing runs in April and Septem-

Year of manufacturing	1999
Type	HEMT cooled
Number of Horns	3
Channels	12 total, 3 x Correlation
System Temp. (zenith)	60 K
Center frequency	32 GHz
IF-Bandwidth	2-4 GHz
RF-Bandwidth	31-33 GHz
local Oscillator	29 GHz
max. V/F Frequency	5 MHz
Polarization	LHC and RHC
Ellipticity	max. 0.3 db
Feed	3 Secondary focus horns
Feed Distances	horn1-2: 486,3 mm
	horn2-3: 225,1 mm
Calibration	Noise diodes
Cool-down duration	24 hrs

TABLE 6.1— A few technical parameters of the new module 2 correlation receiver in Effelsberg.

ber 2002 were performed with the new Module 2, which has better stability and system characteristics (T_{sys}) than module 1. A few technical parameters are given in Table 6.1.

6.2.1 The new Module 2 Correlation Receiver

The original setup of the 32 GHz multi-feed system was planned as an symmetrical array consisting of three identical, independent modules with three horns each (3×3 matrix). Up to now, two modules are installed. The module 1 was designed as software beam switching total power system with two amplifiers and one polarimeter per feed. First test experiments (Testbericht 1997, W. Reich & E. Fürst) revealed sufficient sensitivity for polarized emission. In contrast, the sensitivity for total power measurements suffered strongly from stability problems of the HEMT amplifiers. For this reason, the second module was constructed as a hardware beam switching correlation receiver. Here, the three horns are connected with wave guides allowing for sensitive total power measurements through a correlation of the difference signals. The disadvantage of such configuration is the missing polarization information since only one stable channel per horn remains. In addition, the long wave guide connections between the horns are not without risk for the required high stability. However, first lab and astronomical test experiments of the system confirmed its good and sufficient performance in practical life (Testbericht 1999, U. Teuber and MPIfR Memo 2000/1, W. Reich).

The whole system is mainly divided into two parts: the correlation frontend and the ZF-correlation processor. Within the first unit, each feed is followed by a circular polarization transducer separating the received signal into left- and right hand circular polarization (LCP, RCP). Two adjacent horn signals are then joined by wave guides and a magic tee. Horn 5 has the closest position to the optical axis of the telescope and is used as main horn, while horns 4 and 6 are used as "weather horns" (sensitive to the atmospheric contribution close to the source position). With the help of the magic tees, the subtraction of the weather from the astronomical signal takes place ("hardware beam switching"). Each magic tee produces a sum and a difference signal of the two adjacent horn signals (e.g. horn

5 and 6: LCP of source plus weather and LCP of source minus weather) which then are further processed separately. Each of the three magic tees is then followed by an independent path of first stage amplification and conversion down to an intermediate frequency (IF). Here, the two signals per magic tee are separately feed into a cooled HEMT amplifier followed by a bandpass filter (31−33 GHz). Subsequently, the signals are mixed with the signal of a local oscillator working at 29 GHz. This gives an intermediate frequency of 2−4 GHz as input for the second unit, the ZF-correlation processor. This unit performs the real correlation of the two signals (of each horn combination). After a further bandpass filter (2−4 GHz) and second stage amplification, the signals are each divided by a power-divider onto the correlation and total power output. The correlation in the correlation tree is done through a phase discriminator operating as correlator. Here, one signal enters the discriminator always with a phase shift of 180°, while a switch (S5) allows to introduce a phase shift of 0° or 180° to the other signal. As result, the correlation takes place as phase-dependent multiplication of the two signal trees, where instabilities of non-correlated sources (receiver instabilities and weather) cancel out. We end up with four output channels per magic tee: two total power sum/difference signals as well as the stabilized sine and cosine signals of the correlator total power combination.

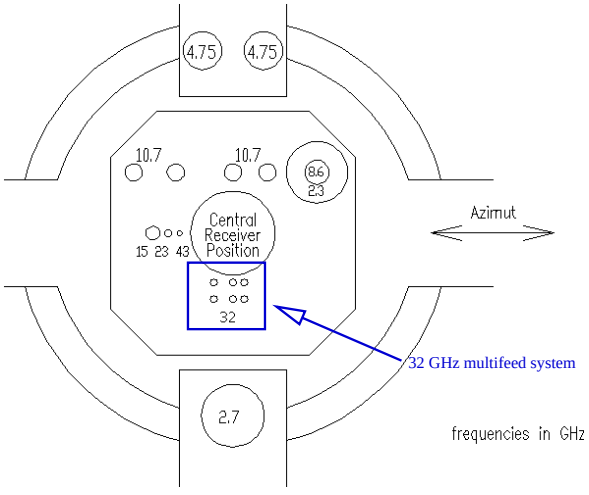

FIGURE 6.4— Arrangement of the receiver systems mounted in the secondary focus of the 100 m telescope. The position of the 32 GHz multi-feed system is marked with a box. Up to now, 2 modules consisting of 3 horns each are installed.

For our purpose of observing flux densities with cross scans (see next section), the astronomical interesting signals are the stabilized correlator outputs of those two magic tees which combine horns 4-5 and horns 5-6. Because the signal in the sine channels should vanish up to a few percent of the cosine signal, the two remaining important channels are the cosine outputs of horn 4/5 and horn 5/6. They provide the stabilized, weather-subtracted astronomical signal. In order to gain sensitivity, a combination of both cosine signals was used in the subsequent data reduction.

6.2.2 Observing Runs

Two observing sessions were performed with the new 32 GHz receiver: in April and September 2002. Our main target source, the BL Lac 0716+714, was observed in both sessions together with a sufficient number of secondary calibrators. Two additional IDV sources, 0917+624 and 0954+658, were investigated for short-term variations in the first run. A short summary of both observing sessions is given in Tables 6.2.

As already mentioned in Chapter 4, the frequent measurement of secondary calibrators (nearby, non-IDV sources) is of great importance. This is particularly true for observations in the mm- and sub-mm regime in order to reduce the increasing influence of systematic time dependent effects. They usually are of different origin: e.g. (short-term) gain fluctuations introduced by changes in the atmospheric conditions, changes in the receiver parameters or thermal expansion of the telescope (defocusing). Thus, a densely time sampled duty cycle of target sources and secondary calibrators ensures to trace these contributions. This could be sufficiently realized in the second run, where three secondary calibrators were observed with a highly time sampled cycle together with the target source 0716+714.

Date	Duration [hrs]	Scans	Duty Cycle [hrs]	Weather
12-14.04.02	42	399	2	faint up to thick clouds, periods of rain
24-25.09.02	18	179	0.3	mostly clear, stronger wind, later clouds

Session I in April 2002:					
Source	α [hh mm ss.ss]	δ [±dd mm ss.s]	S_{9mm} [Jy]	IDV Source	Secondary Calibrator
0716+714	07 16 13.0	+71 26 15.3	1.6	x	
0836+710	08 36 21.5	+71 04 22.5	1.5		x
0917+624	09 17 40.3	+62 28 38.5	0.7	x	
0954+658	09 54 57.8	+65 48 15.4	1.0	x	
W3OH	02 23 16.8	+61 38 57.0	3.5		x

Session II in September 2002:					
Source	α [hh mm ss.ss]	δ [±dd mm ss.s]	S_{9mm} [Jy]	IDV Source	Secondary Calibrator
0716+714	07 16 13.0	+71 26 15.3	1.6	x	
0802+733	08 02 32.2	+73 23 53.4	0.3		x
0831+554	08 31 04.4	+55 44 41.4	0.6		x
0836+710	08 36 21.5	+71 04 22.5	1.5		x

TABLE 6.2— **Top:** Summary of the two observing sessions in April and September 2000 with the new module of the 32 GHz receiver in Effelsberg. The first run has been performed together with observations at 4.85 GHz, hence the duty cycle is much lower (∼1 scan @ 32 GHz every two hours). **Middle:** The first run in April 2002: source list plus coordinates (B1950), flux density at 32 GHz and classification. **Bottom:** The second run in September 2002.

The first run in April 2002 was part of a larger observing session with extension to lower frequencies (4.85 GHz, Chapter 3). Due to the large amount of scans per cycle, the number of secondary calibrators was limited to only two (0836+710 and W3OH). However, the duty cycle was still reduced by a factor of ~ 6 compared to the second epoch.

We observed using the method of cross scans with the number of subscans matched to the source brightness at the given frequency (compare Chapter 4). Depending on the source and session, the number of subscans was in the range of 12−20. In order to estimate the noise level (baseline), each subscan had a length of 4−5 HPBW of the telescope beam. With an Effelsberg beam of $25''$ at 32 GHz, this yields an overall scan duration of ~ 12 minutes. Observations of standard flux density calibrators like 3C286, NGC7027

and 3C309.1 were done frequently. At such frequencies the focus and pointing accuracy is of particular importance (see next section). For example, small changes in the temperature conditions of different parts of the instrument can cause small defocusing effects of the sub-reflector (normally up to ± 5 mm/day). Since these effects can be important at higher frequencies, we performed focus-scans every 2-3 hours to adjust the axial focus position.

6.2.3 Data Reduction

The data reduction is mainly done as described in Chapter 4 for the 4.85 GHz data. Along with fixed instrumentation/system based difficulties (less aperture efficiency, higher T_{sys} etc.), the two main problems at higher frequencies (compared to the cm-regime) are related to the pointing inaccuracy and the increasing influence of the atmosphere. In order to minimize these contributions to our final measurement error, special attention paid to the reduction process as well as additional corrections are required.

1. Pointing:

The HPBW of an antenna beam decreases with increasing frequency. As a result, the pointing accuracy becomes more and more important towards higher frequencies. In contrast to the more than $2'$ beam at 4.85 GHz, pointing deviations of a few arcseconds can already influence precise flux density measurements with a beam size of only $25''$. While the Effelsberg driving control allows a pointing accuracy of $\leq 1''$, the pointing of an azimuth-elevation mounted radio telescope depends on various additional, systematic factors: e.g. inclination of the main axis, collimation of the axis, collimation of the telescope, gravitational distortion and refractive effects. The latter, produced by the neutral component of the atmosphere, depends on the refraction index of the atmosphere and the elevation. Usually the above mentioned pointing effects are of little consequence with regard to the observer, since they are implemented in the so-called 'pointing model'

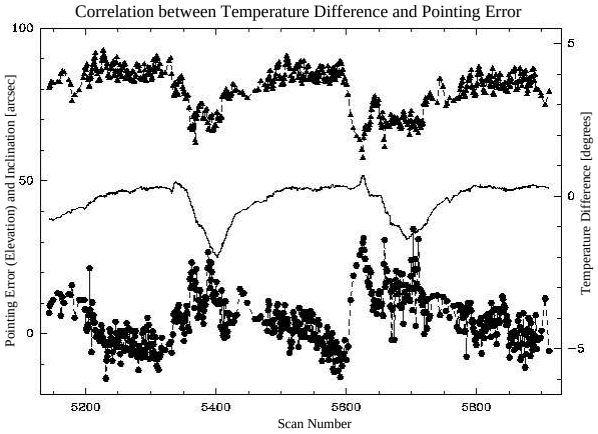

FIGURE 6.5— Influence of temperature differences in the telescope structure on the pointing accuracy: output of the inclination device (triangles), pointing error in elevation (circles) (both in arcseconds) as well as temperature differences (line) (in degrees) between front- and back side of a carrier in the telescope structure versus scan number (period of ~ 60 hrs). Correlations between the parameters are obvious (taken from http://www.mpifr-bonn.mpg.de/akraus).

of the telescope. The (long-term variable) correction parameters/constants in Effelsberg are derived frequently throughout a year. This usually allows a pointing accuracy of about $3''$ over the whole sky[1]. However, there are additional, mostly random effects on much shorter time scales (seconds to hours) which have to be taken into account, in particular at higher observing frequencies. Distortions in the telescope structure (caused by e.g. wind or temperature gradients between different parts of the telescope) can have large influence on the pointing accuracy: deviations of up to $30''$ were seen. Figure 6.5 gives an impression of the pointing response to changes in temperature and telescope inclination over a period of ~ 60 hours. Small changes in temperature of only one degree can already cause strong pointing errors of the order $> 20''$ with strong impact on observations with a beam size of only $25''$.

In addition, the pointing model corrects only for the normal refraction using the weather data. At frequencies higher than

[1] see http://www.mpifr-bonn.mpg.de/akraus for more details.

10 GHz, the rapid time variable anomalous refraction can occur (Altenhoff et al. 1987). If anomalous refraction is important, the apparent source positions appear to move away from their actual positions (in azimuth and elevation) by up to 40″ for time periods of several ten seconds. It is caused by small variations in the H_2O content, perhaps by single cells of moist air. In particular, due to the local weather conditions in Effelsberg, which is embedded into a valley, such random effect is probably important. However, anomalous refraction appears to be extremely difficult to be taken into account.

Moving the 100 m telescope from one source position to another, the above mentioned problems show often their strongest effects. Figure 6.6 displays such situation. The two upper panels show the average of two subscans in elevation and azimuth, respectively, after moving the telescope to the new source position of 0716+714. The pointing offsets from the center position are quite high, more than 7″ in elevation. Such offset would lead to an underestimation of the flux density of the order 20 %. In order to minimize the above mentioned pointing effects (which are not covered by the pointing model), we performed a short pointing scan before each measurement scan. As result, the pointing behavior of the following scan could often be improved by a factor of 3 or more. The two lower panels in Figure 6.5 show the averaged subscans in azimuth and elevation of a measurement scan after a short pointing scan. The maximum pointing deviation is reduced to $\sim 2''$and consequently, the amplitude is higher by a about 15 %.

After the cross-scan analysis (Chapter 4), first inspection of each subscan "by eye" leads to the flagging of obviously bad scans (e.g. corrupted data with bad Gaussian fits or strong deviations in amplitude, pointing or HPBW from their mean values). According to the 4.85 GHz-procedure, in a second run each subscan was analyzed with an awk-script to determine the quality of the Gaussian fit. Subscans matching the following criteria were subsequently flagged:

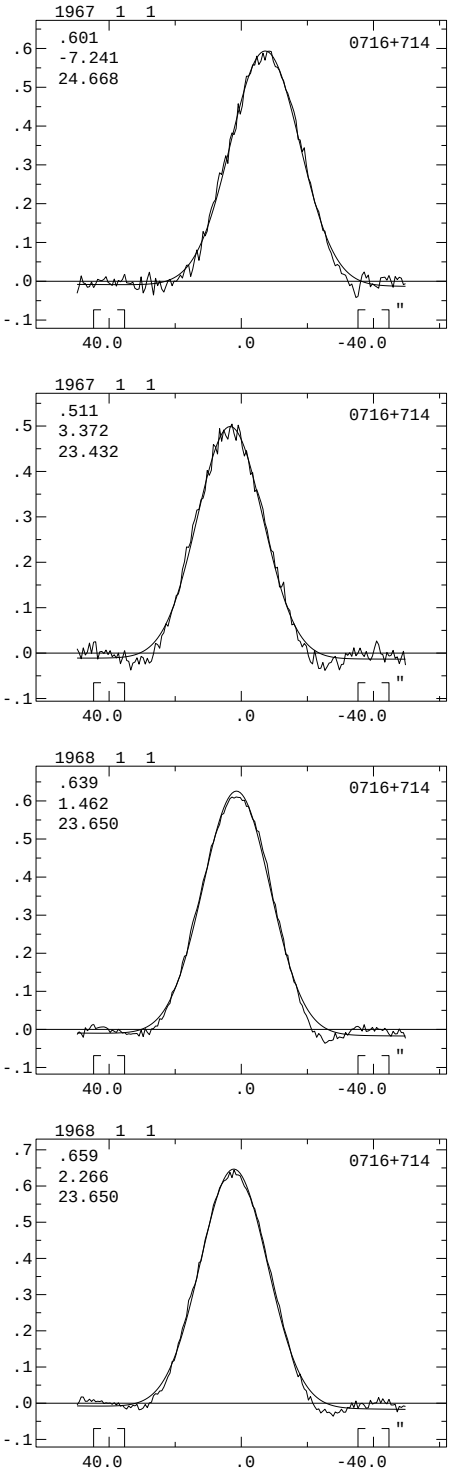

FIGURE 6.6— **Upper panels:** averaged subscans in elevation and azimuth of a pointing scan at a new position. **Lower panels:** the following scan shows a much better pointing behavior (second fit value) and the amplitude is higher by 15 %.

(i) amplitude $> \pm$ 10 % of the average
(ii) pointing deviation $> \pm$ 15 % of the HPBW
(iii) HPBW $> \pm$ 15 % of the average
The remaining pointing errors of each subscan are then corrected using the method described in Chapter 4 followed by a weighted average of all subscans.

2. Opacity Correction:
The atmosphere causes additional disturbance of the radio astronomical signal. In the meter-wavelengths range ionospheric contributions (scintillation, Faraday rotation) are important, but do not play a significant rule at higher frequencies due to their λ^2-dependence. In contrast, the tropospheric absorption and thus attenuation of the astronomical signal is of particular importance in the mm- and sub-mm regime. Here, the different constituents of the atmosphere absorb by different amounts. Most important of these is water vapor. Its concentration varies quite strongly with the local weather conditions. While at clear sky conditions the attenuation is of the order 0.1 dB ($\sim$2 %), a large rain cloud can cause values as high as 1.5 dB ($\sim$30 %) (e.g. Rohlfs & Wilson 1986). The different constituents are also radio emitters, since the atmosphere can be considered to be in local thermal equilibrium (LTE). Consequently, the emission of the atmosphere has to be taken into account as well. The absorption can be described by knowledge of the path length along the line of sight through the atmosphere and the optical depth (or opacity) τ of the latter: $e^{-\tau_0 \cdot A}$. Here, τ_0 denotes the opacity at the zenith and A the air mass along the line of sight. The latter is given by $A = 1/\sin(\mathrm{Elv})$. The emission of the atmosphere can be described as noise temperature T_{Atm} depending on the physical temperature of the atmosphere T_0 ($\sim$300 K) and the opacity $\tau = \tau_0 \cdot A$:

$$T_{Atm} = T_0 \cdot (1 - e^{-\tau}) \,. \qquad (6.2)$$

The system temperature T_{sys} measured off-source can be used to correct our data for the atmospheric contributions. T_{sys} consists mainly of two components, a receiver-dependent term T_{RX} plus the atmospheric contribution T_{Atm}. Neglecting other possible components (e.g. spill-over, cosmic microwave background) the system temperature is given by

$$T_{sys} = T_{RX} + T_{Atm} \cdot (1 - e^{-\tau_0 A}) \,. \qquad (6.3)$$

Using the expression for the mean brightness temperature of the atmosphere in [K] given by Altschuler et al. (1968) and Falcone et al. (1971),

$$T_{Atm} = 1.12 \cdot T_0 - 50 \,, \qquad (6.4)$$

the optical depth τ_0 can be estimated[2]. This is usually done by frequent and fast T_{sys}-measurements as function of telescope elevation in elevation-steps of $\sim$5-10°, so-called 'Sky-Dips': Taking into account the approximation $e^{-x} \simeq (1 - x)$, we obtain

$$\begin{aligned} T_{sys} &= T_{RX} + T_{Atm} \cdot \tau_0 \cdot A \qquad (6.5) \\ &= T_{RX} + T_{Atm} \cdot \tau_0 \cdot \frac{1}{\sin(\mathrm{Elv})} \quad . \end{aligned}$$

Using equation 6.4 for T_{Atm} we end up with an equation for a straight line. Its slope yields an estimate of τ_0 and the constant term T_{RX}. Since a Sky-Dip procedure of frequent τ-measurements is not possible within a densely time-sampled IDV experiment, we used the following method to perform a τ-correction: The overall optical depth was estimated as temporal average over the whole observing period extracting T_{sys} from each individual cross-scan. The upper panels of Figure 6.7 display our results for both sessions. The fit of a straight line to this data yields $\tau_0 = 0.06$ and $\tau_0 = 0.03$ for Session I and II, respectively.

These values allow the subsequent correction of the atmospheric absorption towards lower elevations in the case of bad, but stable weather conditions (constant τ). However,

[2]Here, T_0 denotes the (air-) temperature measured at the Earth's surface in [K].

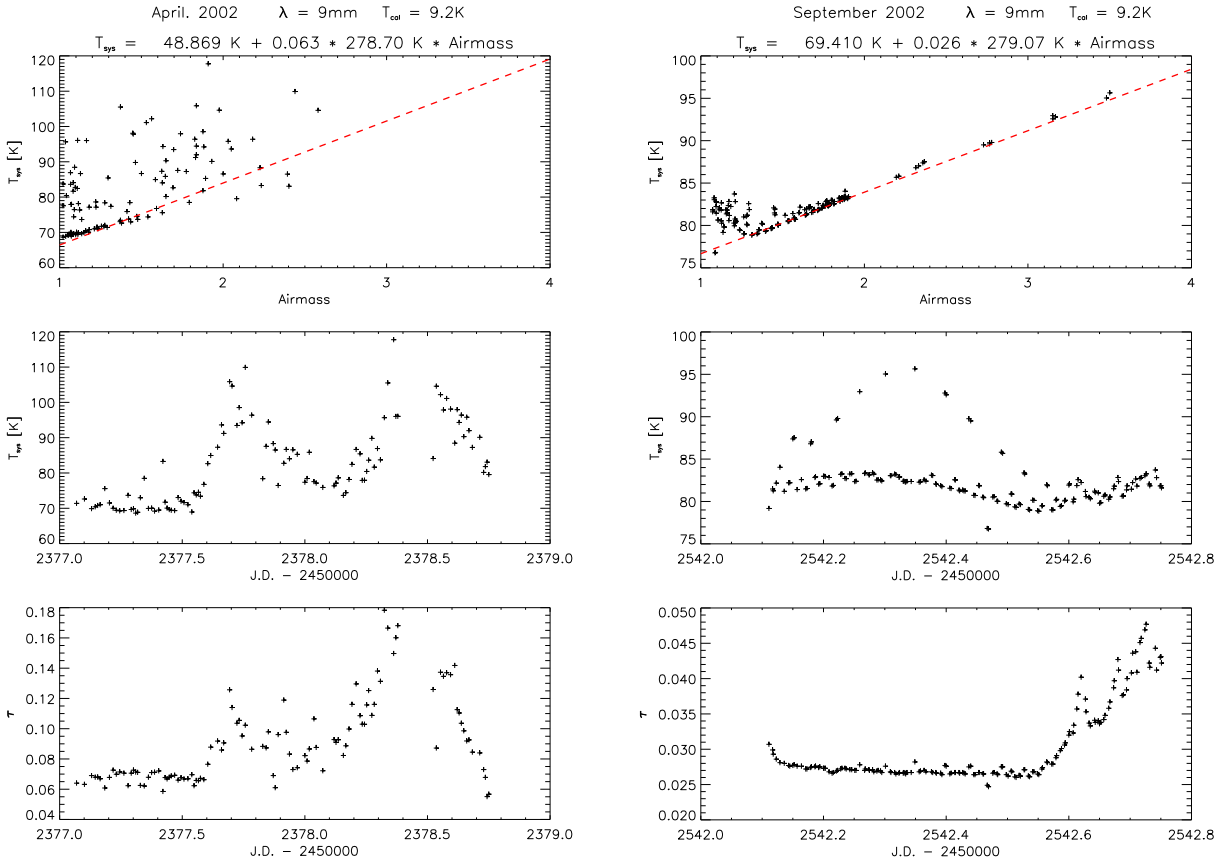

FIGURE 6.7— τ-correction using the T_{sys}-values from each scan over the whole observing period. **Left:** Session I in April 2002, **Right:** Session II in September 2002. A linear regression (red) of T_{sys} vs. Airmass gives the mean opacity at the zenith and the (receiver dependent) constant term T_{RX} (top). The system temperature over time is displayed in the middle, showing often strong variations due to changing weather conditions (plus changing elevation). An interpolation between T_{RX} and each individual system temperature yields a τ-value for each flux density measurement (bottom).

the situation is usually different as seen in Figure 6.7 (middle). Strong variations (e.g. two peaks at J.D. 2452377.7 and J.D. 2452378.4) of T_{sys} over time are seen indicating unstable, changing atmospheric conditions (thick clouds, periods of rain). An increase of 50 K corresponds to changes in τ by a factor of three (up to 0.18) and results in flux density changes of the order $\sim 20\,\%$.

In order to minimize these effects, an interpolation between T_{RX} (obtained from the first fit) and T_{sys} of each individual cross-scan was done. This procedure yields the opacity at each given time of a flux density measurement (Figure 6.7, bottom). Using these τ-values, the observed flux density $S_{observed}$ of each cross-scan was finally corrected according to

$$S_{source}(t) = S_{observed}(t) \cdot e^{\frac{\tau(t)}{\sin(\mathrm{Elv})}}\,, \qquad (6.6)$$

where S_{source} denotes the true flux density of the source.

3. Gain- and Time Correction:

In order to correct for the elevation dependence of the antenna sensitivity, a gain correction was done according to the procedure described in Chapter 4. The opacity corrected, normalized amplitudes of the secondary calibrators were used to construct a gain curve at 32 GHz (Figure 6.8).

Subsequently, a time-dependent correction was performed as described in Chapter 4. Here, remaining time-dependent systematics

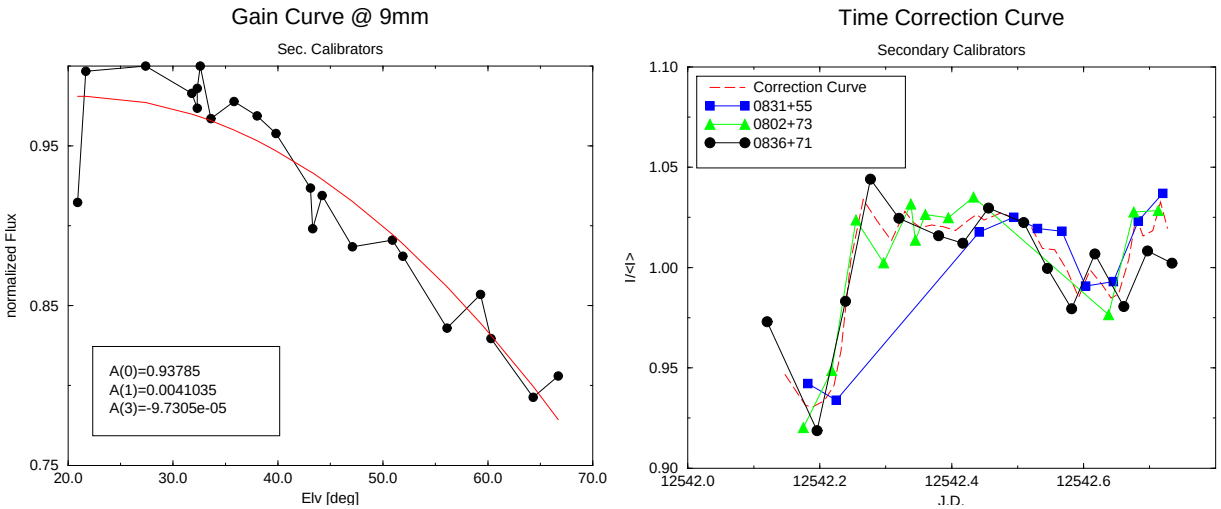

FIGURE 6.8— **Left:** Gain curve at 32 GHz constructed using the secondary calibrators. A quadratic regression gives the fit values displayed in the plot. These are used to correct the data for elevation dependent effects. **Right:** A final time dependent correction is done using the light curves of the secondary calibrators, which behave similar over the observing period (as example, Session II is shown). The averaged correction curve is displayed as red, dashed line.

(remaining (long-term) changes in the atmosphere, thermal drifts, instabilities in the receiver and electronics etc.), which at this stage are not yet corrected, are traced by the frequently observed secondary calibrators. For example, Figure 6.8 shows their light curves obtained during Session II. All three sources behave in a similar way throughout the observing period indicating the same origin of the remaining variations. A mean correction curve was obtained for each session by averaging the data of all secondary calibrators (red dashed line in Figure 6.8).

Finally, the flux density scale was linked to the standard scale of Baars et al. (1977) and Ott et al. (1994) using the primary calibrator measurements of 3C286, 3C48 and NGC7027.

6.2.4 Results

All final light curves are displayed in Figure 6.9. The resulting flux density error of each cross-scan is composed of the statistical error from the reduction process (Gaussian fit of averaged subscans) and a contribution from the residual scatter seen in the secondary calibrators light curves (see also Chapter 4). The individual values lie in the range of $\lesssim 4\,\%$. In all light curves only weak variability is present compared to the secondary calibrators. The maximum peak-to-peak variations are of the order $\sim 15\,\%$, while a maximum value as high as $\sim 8\,\%$ is seen in the case of the secondary calibrators.

The standard variability analysis[3] was done and the results (modulation indices, variability amplitudes and χ^2-tests) are presented in Table 6.3. In the following, the light curves and results of the variability analysis for each IDV source are discussed. For better illustration and comparison, Figures 6.10 and 6.11 display the (normalized) light curves of each individual IDV source together with the data of all secondary calibrators.

0716+714

Both sessions in Figure 6.10 show an somehow larger scatter in 0716+714 (with sometimes stochastic appearance) compared to the secondary calibrator light curve ($Y = 8.1\,\%$ and $Y = 4.5\%$). The overall situation is best characterized using the χ^2-test. The first session in April 2002 yields a χ^2_r-value of 3.26, higher

[3]The standard variability analysis was done in accordance to Chapter 4. See this Chapter for more details.

Session I in April 2002									$m_0 = 2.3$
Source	Scans	$< S >$ [Jy]	σ [Jy]	m [%]	Y [%]	χ^2	χ^2_r	$\chi^2_{0.1\%}$	variable
0716+714	23	0.96	0.03	3.5	8.1	45.94	2.18	2.20	–
0836+710	21	1.47	0.03	1.7	0.0	15.15	0.76	2.27	–
0917+624	19	0.69	0.03	3.7	8.6	35.95	2.12	2.40	–
0954+658	20	0.98	0.03	3.3	7.2	40.05	2.23	2.35	–
W3OH	16	3.47	0.08	2.2	0.0	20.21	1.35	2.51	–

Session II in September 2002									$m_0 = 1.2$
Source	Scans	$< S >$ [Jy]	σ [Jy]	m [%]	Y [%]	χ^2	χ^2_r	$\chi^2_{0.1\%}$	variable
0716+714	29	2.21	0.04	1.9	4.5	54.349	1.941	2.03	–
0802+73	14	0.29	0.01	1.9	4.6	21.856	1.681	2.66	–
0831+55	10	0.56	0.01	0.9	0.0	3.675	0.408	3.10	–
0836+71	15	1.56	0.02	1.1	0.0	9.468	0.676	2.58	–

TABLE 6.3— Results of the variability analysis for all sources observed in April (top) and September (bottom) 2002. The mean flux density, the modulation index m, variability amplitude Y and the results of the χ^2-test are given. $\chi^2_{0.1\%}$ gives the value of χ^2_r for a 0.1% significance level (IDV detection). The modulation index m_0 was 2.3 % and 1.2 %, respectively.

than the value for the 0.1% significance level of variability ($\chi^2_{0.1\%}$ in Table 6.3) and thus IDV was formally detected. However, this result depends strongly on the first, low flux density value in the light curve. Flagging this scan yields a χ^2_r-value of 2.12, which now is lower than $\chi^2_{0.1\%}$ (in this case 2.21). A direct comparison of the peak-to-peak amplitudes seen in the light curves of target and calibrator sources yields a similar result: no 3σ-variability is present.

The situation appears similar during the second session. Again, no significant variability is detected (χ^2_r, peak-to-peak amplitudes). However, the mean flux density of 0716+714 increased by more than a factor of 2 between the two observing sessions.

0917+624

This source shows the largest variations of all sources observed during the two runs (top of Figure 6.11). The peak-to-peak variations are on a 14 %-level ($Y = 8.6\%$) and the χ^2-test suggests the detection of variability. Again, this result depends on one data point only (around J.D. 2452378.0), which seems to coincide with the raise of the second peak in the system temperature and opacity (Figure 6.7). Flagging also this scan yields a χ^2_r of 2.12 ($\chi^2_{0.1\%} = 2.40$). Consequently, no significant variability is present.

0954+658

As seen in the previous cases, the light curve of 0954+658 shows an somehow larger scatter than the combined calibrator light curve (bottom of Figure 6.11). The peak-to-peak variations of 0954+658 reach about 13 % ($Y = 7.2\%$) and the χ^2-test indicates the presence of variability. Again, the most variable part of the light curve coincides with the bad weather period, whereas at almost stable conditions

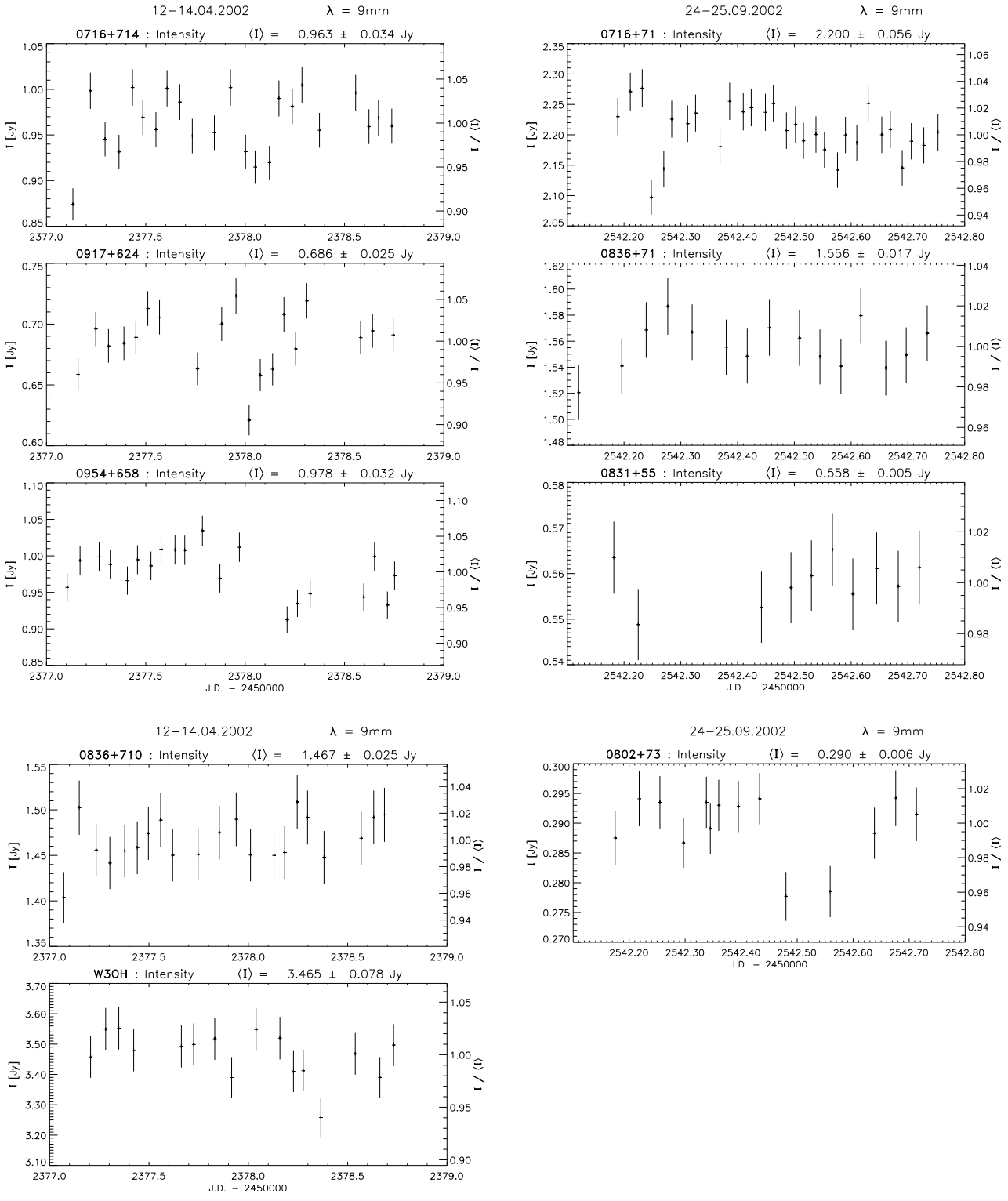

FIGURE 6.9— Final light curves of IDVs and secondary calibrators at 32 GHz. **Left:** Session I in April 2002. **Right:** Session II in September 2002. The left scale of each light curve displays the total flux density, while the right scale corresponds to the normalized flux density.

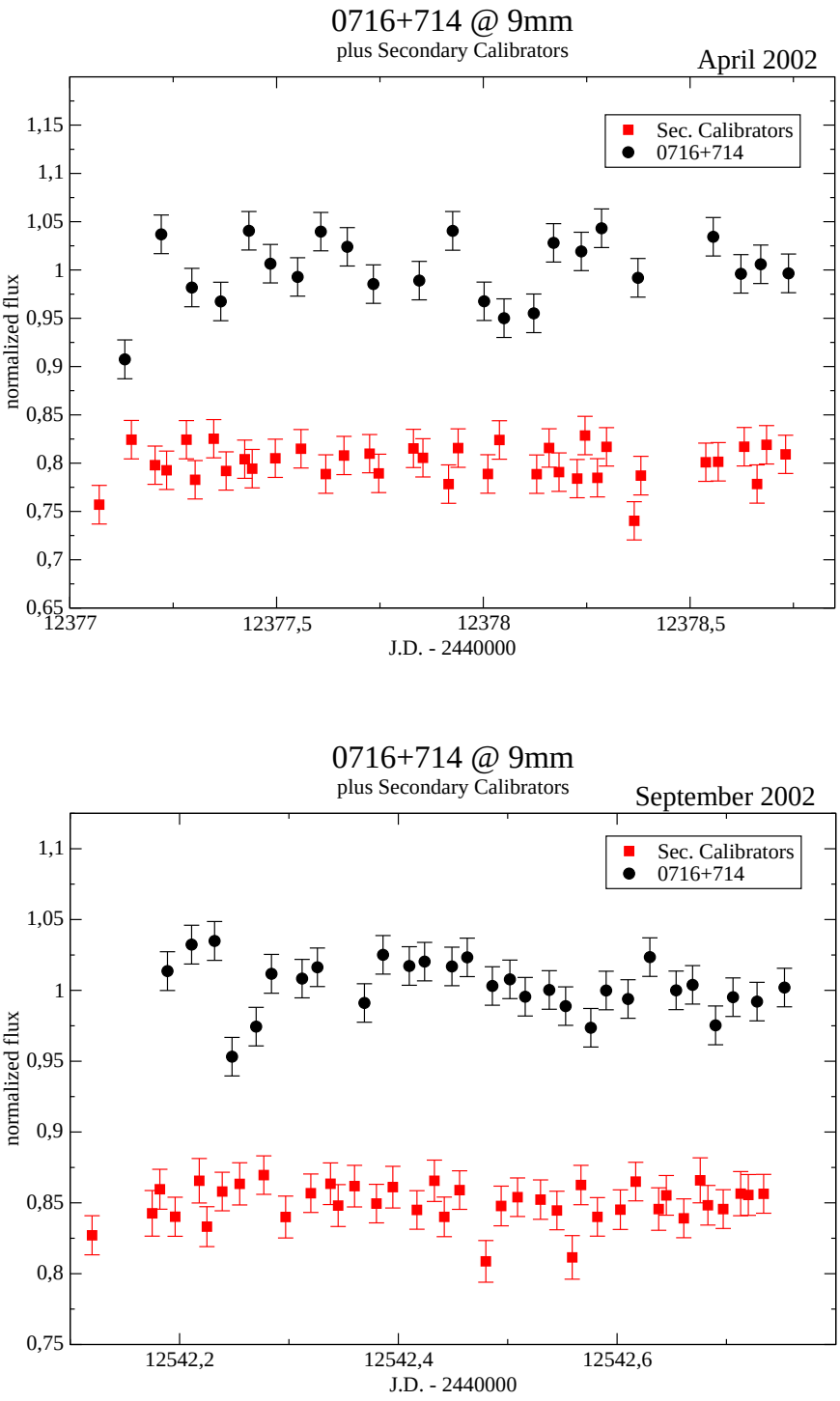

FIGURE 6.10— **Top:** Final light curve of 0716+714 obtained from the first observing run in April 2002 (black). The calibrator scans are superimposed in red (normalized flux minus 0.2 Jy). **Bottom:** Second session in September 2002 with secondary calibrators superimposed (normalized flux minus 0.15 Jy). Although in both cases the overall "scatter" in the data of 0716+714 is larger compared to the calibrator data, a 3σ-variability is not observed.

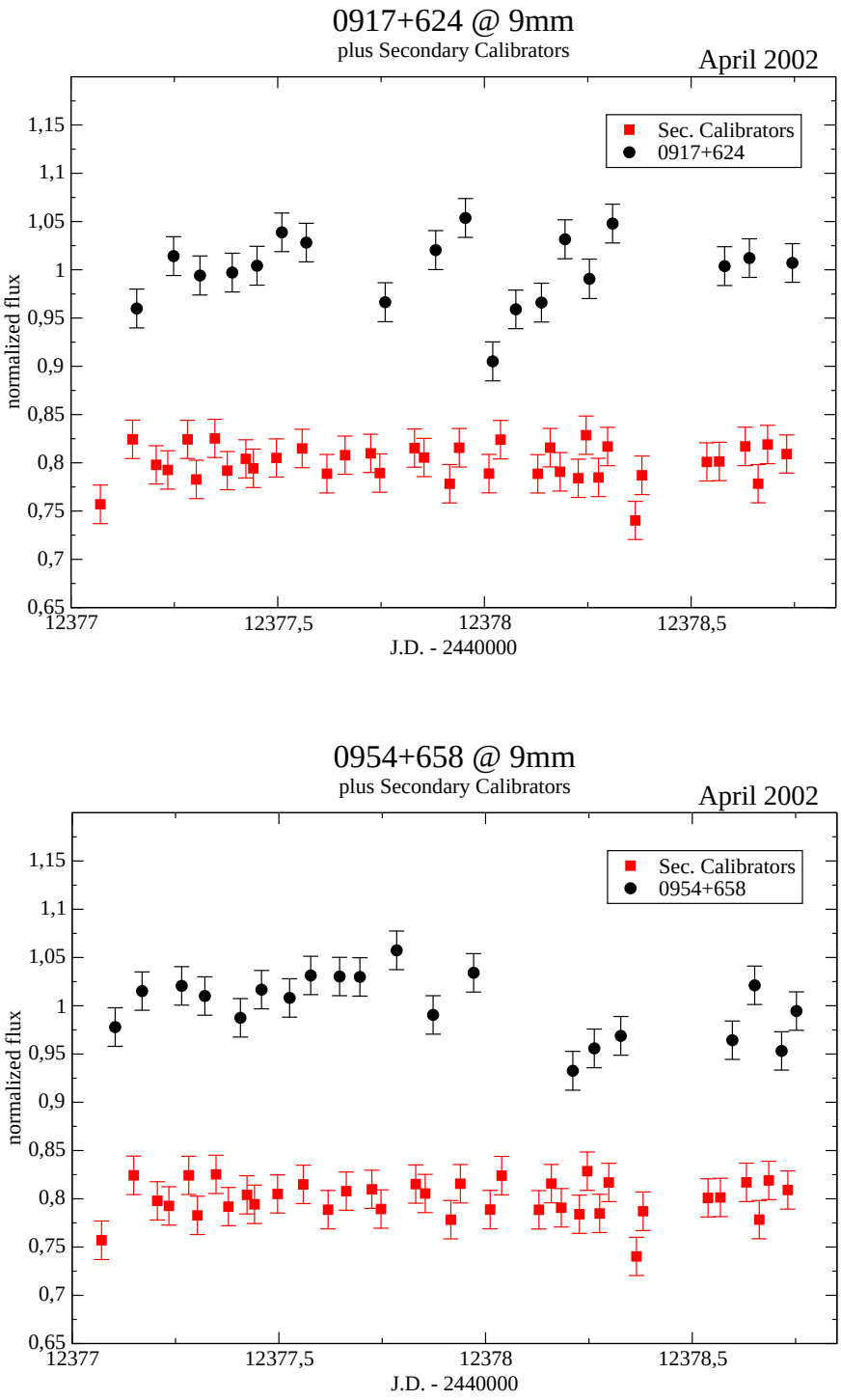

FIGURE 6.11— Final light curves of 0917+624 (top) and 0954+658 (bottom) observed in April 2002 (black) together with the calibrator light curves in red (normalized flux minus 0.2 Jy). Similar to 0716+714, no clear detection of IDV at 32 GHz is visible.

(up to J.D. 2452377.6) 0954+658 appears to be less variable. A χ^2-test without the lowest data point in the light curve (around J.D. 2452378.2) yields again a value below the significance level for variability.

6.3 Discussion and Conclusions

Even though no significant variations at 32 GHz were detected in the observations presented here, some conclusions can be drawn:

(i) The new module of the 32 GHz-receiver with its improved performance compared to the old Module 1 and the combination of the two cosine-total power signals allows to reduce the individual measurement errors to $\sim \pm 2\,\%$ (old module: $\sim \pm 3.5\,\%$). However, excellent weather conditions are still essential, since the scatter seen in the calibrator light curves is of the order 4–5 %. This allows only variations larger than 12−15 % to be clearly detected on a $3\,\sigma$-level.

(ii) The results obtained for 0716+714 at earlier times (September 1998, Figure 6.2) with peak-to-peak variations of 20 % and the strong increase of m towards higher frequencies could not be confirmed.

A possible explanation are intrinsic changes in the source. 0716+714 is known to be highly active on time scales of weeks to month. Outbursts occur in the cm- and mm-regime often with a high degree of correlation and with time delays of a few days to several weeks (Raitieri et al. 2003). This behavior was interpreted in various ways, e.g. homogeneous blobs moving relativistically in the jet at a small viewing angle, perturbance in an inhomogeneous jet traveling down the jet or inhomogeneities in a rotating helical jet. Such structural or geometrical long-term effects could change also the conditions for faster intrinsic variations.

In contrast, the source should exhibit a component of size ~ 0.1 mas scintillating behind a 100–200 pc distant screen when we assume a quenched ISS scenario for the typical modulation indices of $\sim$5–6 % observed at 4.85 GHz. Scaling this source size linear in frequency yields ~ 0.02 mas at 32 GHz and a modulation index of $\sim 1.1\,\%$ at 32 GHz should be expected. This value is comparable to what was found in the second session, where the weather conditions have been much better. Thus, the results presented here are in better agreement with the presence of weak, quenched scattering rather than the presence of an intrinsic contribution as maybe seen in September 1998.

(iii) No strong, significant mm-variations in 0917+624 and 0954+658 could be established. The strongest variations are seen in the former case as low level amplitude changes. If those are real, they are hard to reconcile with the present, extremely quenched variations seen in the cm-regime. As described in Chapter 4, a source size of 0.8 mas at 4.85 GHz for a screen at 100–200 pc is required to quench the scintillations in 0917+624 down to the observed $m \sim 0.5\,\%$. Assuming a linear dependence of the source size with frequency, this yields a size of 0.1 mas at 32 GHz and a modulation index of order $\sim 0.1\,\%$ should be observed. This is not in agreement with the values given here, since one would then expect 0917+624 to show a similar "scatter" as the calibrator sources.

We conclude, that the observations presented here do not show a clear sign of existing intrinsic variations. Whether this is due to the non-existence of an intrinsic up-turn in the m-ν distribution or the insufficient accuracy of our measurements must be answered by new observations with better weather conditions. The high-frequency observations presented here, however, are in better agreement with a quenched ISS scenario (with the exception of 0917+624) rather than the existence of an intrinsic contribution to the IDV pattern.

6.4 Multi-frequency Study of the rapid Scintillator J1819+3845

During our monitoring epoch in April 2003 (Chapter 4), a small gap in the Effelsberg observing schedule of 2.5 hours was used to observe one of the most rapid IDV sources known today. The quasar J1819+3845 has attracted attention due to its fast ($\lesssim 1$ hour) and pronounced ($\sim 300\,\%$) variability pattern

(Dennett-Thorpe & de Bruyn 2000). The detection of (i) an annual cycle in the variability time scale and (ii) a time delay between two distant telescopes favors clearly interstellar scintillation as origin of the variability in this source (see also Chapter 3; Dennett-Thorpe & de Bruyn 2000, 2002). Until now, less is known about its variability characteristics at frequencies higher than 8.5 GHz. Therefore investigations towards higher frequencies are of particular importance to test the ISS explanation for the variability (e.g. its frequency dependence) of J1819+3845. Our short multi-frequency observations (up to 32 GHz) and the subsequent analysis in view of a model for interstellar scintillation are presented in the following.

6.4.1 Observations and Results

Due to the excellent weather conditions during the short run we were able to observe the source simultaneously at higher frequencies: 10.5 and 32 GHz scans were included along with the usual 4.85 GHz observations of the monitoring project. The fast variability cycle in this source (in particular during its "fast period" in the first part of the year) and the additional two observing frequencies reduced the number of observed secondary calibrators to only one. However, the duty cycle was still low with one scan per frequency every ~ 15 min. The standard data reduction procedure was applied as described above.

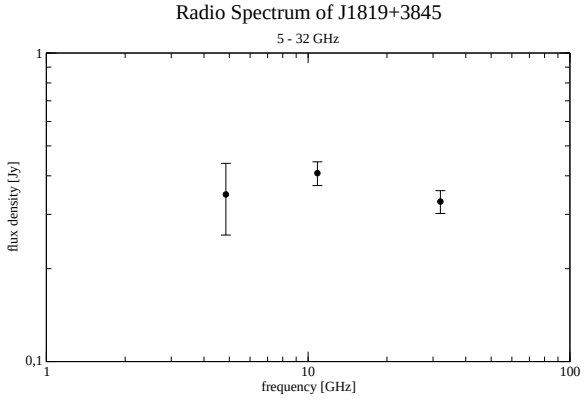

FIGURE 6.12— The radio spectrum of J1819+3845 deduced from our new observations at 4.8, 10.8 and 32 GHz. The spectrum appears to be flat with a spectral index of ~ 0.003 and its peak flux at 10.8 GHz.

The radio spectrum of J1819+3845 was deduced from the data and is shown in Figure 6.12. The source appears to exhibit a flat spectrum with its peak flux near 10 GHz. This is in contrast to previous findings, where a relatively stable, highly inverted spectrum ($\alpha = -0.5$) up to 43 GHz was seen (Dennett-Thorpe & de Bruyn 2000).

Figure 6.13 displays from top to bottom the resulting light curves at 4.8, 10.5 and 32 GHz, respectively. As expected from the low duty cycle, all three light curves are highly undersampled. However, extremely rapid and strong variability is present with peak-to-peak amplitudes reaching up to 110 % ($Y = 78.6$ %) at 4.8 GHz and 50 % ($Y = 25.9$ %) at 10.5 GHz. The deduced modulation indices are given in Table 6.4. In addition, the variations at these two frequencies appear to be correlated over the short observing period. The latter and the variability time scale ($\sim$ 30 minutes) are in good agreement with previous observations performed by the Dutch group (Dennett-Thorpe & de Bruyn 2000) as well as the expectation from the annual modulation model.

The first 32 GHz observations of this source reveal a decrease in flux density from 360 mJy down to 270 mJy over a period of 90 minutes. Such surprisingly high peak-to-peak amplitude of 25 %, however, is mainly based on the last, low data point in the light curve. A more detailed analysis of each subscan of this data point does not show anything unusual. Some doubt due to its accuracy remains, since an influence of the raising Sun during the last period of the experiment can not be ruled out. Consequently, this data point was flagged for the subsequent analysis.

6.4.2 Modeling the Interstellar Scintillation in J1819+3845

The autocorrelation $\rho(\tau)$ of IDV light curves produced by interstellar scintillation can be expressed as integral along the line of sight through the medium (Coles et al. 1987, Beck-

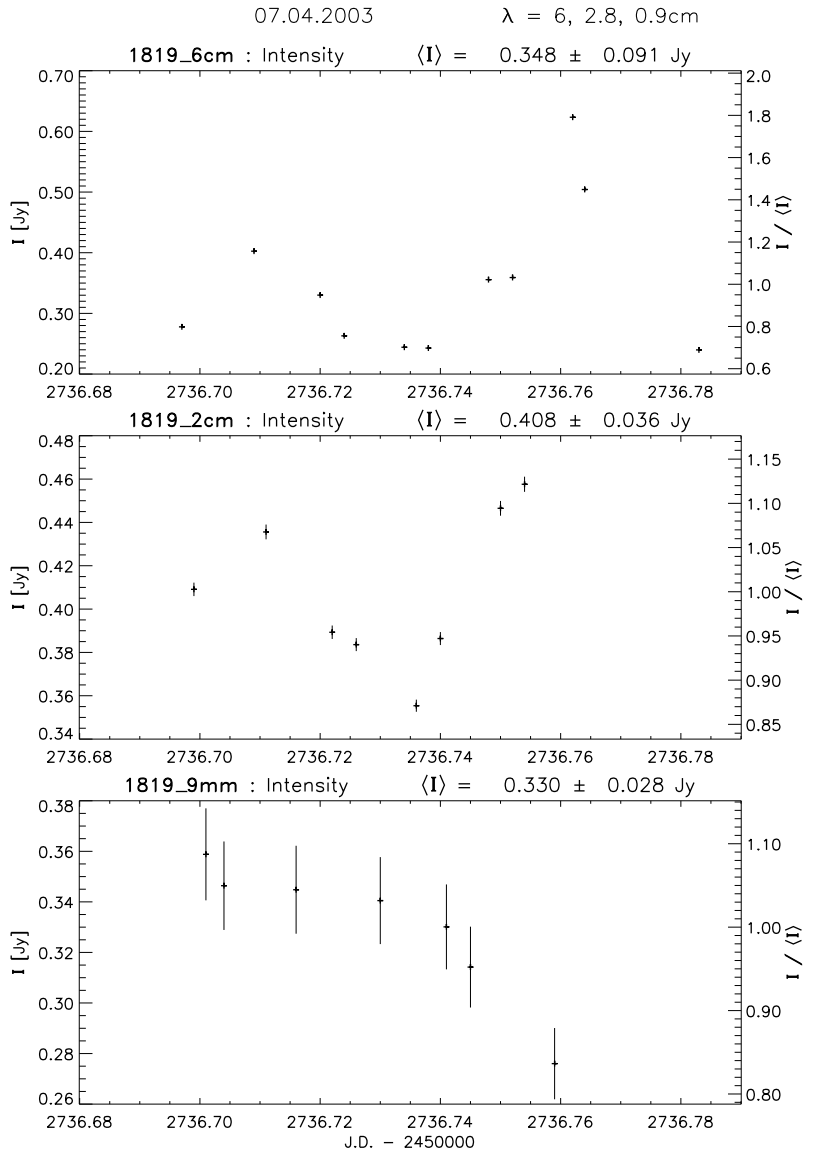

FIGURE 6.13— From top to bottom, final light curves of J1819+3845 at 4.8, 10.5 and 32 GHz, respectively. Note the correlated variability at 4.8 and 10.5 GHz and the high variability amplitudes in all three curves. The last, extremely low data point in the 32 GHz light curve has been flagged, since a possible influence of the raising sun could not be ruled out.

ert et al. 2002). For the two dimensional wave vector $\mathbf{q}$ perpendicular to the line of sight (screen frame) and the vector $\mathbf{x} = \mathbf{v}t$ (observers frame), defined by the relative velocity $\mathbf{v}$ between screen and observer, the autocorrelation function can be written as

$$\rho(\mathbf{x}) = 8\pi r_e^2 \lambda^2 \int_0^D dz \int_{-\infty}^{+\infty} \exp(i\mathbf{xq}) R(\mathbf{q}, z)\, d\mathbf{q}\ , \quad (6.7)$$

where λ is the observing wavelength, D the distance, and r_e the electron radius. The modified power spectrum R($\mathbf{q}$,z) is given by

$$R(\mathbf{q}, z) = \sin^2(\vartheta_q^2) \cdot \Phi(z, q) \cdot |V(\mathbf{q})|^2\ . \quad (6.8)$$

As mentioned in Chapter 2, the spacial power spectrum $\Phi(z, q)$ of electron density fluctuations in the ISM along the line of sight z at wave number q can be described by a power

ν [GHz]	m [%]	θ_F [μas]	θ [μas]
4.8	26.21	26.5	32.0
10.5	8.73	17.9	15.0
32.0	2.33 (8.38)	10.2	5.0

TABLE 6.4— Modulation indices at all three frequencies deduced from the data presented here. In addition, calculated Fresnel angles θ_F and source sizes θ are given. The latter quantities were calculated for a distance of 19 pc and a source size of 32 μas at 5 GHz. The second value of m at 32 GHz includes the last, low data point seen in Figure 6.13.

law,

$$\Phi(z,q) = C_n^2(z) q^{-\beta} \qquad (6.9)$$

between a lower cut-off q_{min} and an upper cut-off q_{max}. For a Kolmogorov spectrum of density irregularities, the power law index β is equal to 11/3. C_n^2 describes the strength of turbulence, while its cumulative effect along the line of sight is given by the scattering measure SM (see equation 3.27). V($\mathbf{q}$) in equation 6.8 represents the visibility of the source surface brightness. Finally, the parameter ϑ_q^2 includes the Fresnel angle $\theta_F = \sqrt{\lambda/2\pi D}$ and is given by $\vartheta_q^2 = \theta_F(qz)/\sqrt{2}$.

Beckert et al. (2002) published an analytical solution for the ACF given in equation 6.7 for different source brightness distributions and different scattering regimes. This enables to compare directly observational quantities with theoretical parameters of the ISM. In particular, observed modulation indices and time scales can be related to the distance of the screen, different kind of scattering (β, C_n^2, SM) and the source size. In the following, this is done with respect to the observations of J1819+3845 presented above.

As shown in Chapter 4, the observed time scale is related to the SF, which itself is given by the ACF as $SF(\tau) = 2[\rho(0) - \rho(\tau)]$. An analysis in view of SFs using equation 6.7 and related ISM parameters is done by Beckert et al. 2002 for the quasar 0917+624. In the case of the light curves presented in Figure 6.13, the time scales (and thus the SFs) are not well defined due to under-sampling and the short observing period (low number of variability cycles). As result, a detailed analysis in this manner was not possible. The modulation index, however, is related to the autocorrelation at zero time lag: $m^2 = \rho(\tau \to 0)$. We will now assume a slab model for the scattering medium with constant C_n^2 at a mean distance D and a circular source model with size θ and constant surface brightness. In this case, Beckert et al. (2002) find for the regime of weak, quenched scattering ($\theta > \theta_F$):

$$m^2 = 2\left(\frac{r_e}{D\theta^2}\right)^2 \lambda^4 (D\theta)^{\beta-2} SM \cdot f_1(\beta) \ . \qquad (6.10)$$

Here, the function $f_1(\beta)$ depends only on β and is of order unity.

Dennett-Thorpe & de Bruyn, 2000 found the modulation index of J1819+3845 to peak around 5 GHz and the time scales to become longer towards higher frequencies. This provides evidence that 5 GHz is the critical frequency ν_{crit} for this source, where refractive, diffractive and Fresnel scales are equal. Using the observed time scales and approximations for a Kolmogorov, thin screen at ν_{crit} (Blandford & Narayan, 1985), they found a screen distance of 19 pc, an upper limit for the source size of $\lesssim 32\,\mu$as, and $C_n^2 = 0.17$ at 5 GHz. Taking these values for D and θ and assuming a linear dependence of source size with frequency, one can compare Fresnel angle and source size at different frequencies. The latter assumption is reasonable for an inhomogeneous synchrotron component, which is flux limited by self-absorption at each frequency. In Table 6.4 the calculated values are given. It turns out, that the Fresnel size of the scattering medium is always larger or comparable to the size of the scintillating component. This is expected for a source which exhibits such large amplitude variations (up to 350 %). Consequently, a weak scattering, point-source scenario for J1819+3845 is more likely than the quenched scattering case presented in equation 6.10. An analytical solution for the ACF in equation 6.7 for this case

yields ($\theta \lesssim \theta_F$):

$$m^2 = 0.025 \left(\frac{D\lambda}{2\pi}\right)^{\frac{\beta-10}{2}} r_e^2 D^4 \lambda^6 \cdot \sin\left(\frac{\pi}{4}\beta\right) SM \cdot f_2(\beta) \ . \quad (6.11)$$

For a Kolmogorov screen with $\beta = 11/3$, the function $f_2(\beta)$ is equal to 6.79. Since the Fresnel size is the relevant scale in this scattering regime, m is now independent of the source size θ.

The statistical error of m (according to Chapter 4) in the case of our short observing period is quite high ($\Delta m \sim 30\,\%$) due to under-sampling and the low number of observed variability cycles. Nevertheless, the values are in agreement with previous, intensive studies of J1819+3845 with the Westerbork telescope, where m was found to be 30.5 % at λ6 cm (Effelsberg: 26.2 %). Hence, we will use our "high frequency" results to perform a first, qualitative comparison of the observed modulation indices with the scattering model presented above. We model the observations with the following assumptions and parameter ranges:

- a slab of 1 pc thickness for the screen with uniform distribution of C_n^2 and mean distance D
- Kolmogorov spectrum of density fluctuations with $\beta = 11/3$
- weak scattering of a point source ($\theta \lesssim \theta_F$)
- range of different distances between 5 and 70 pc
- range of four different values for the strength of turbulence [$m^{-20/3}$] in the screen:
  - $C_n^2 = 10^{-0.77}$ as derived from the variability time scale of J1819+3845 at $\nu_{crit} = 5$ GHz by Dennett-Thorpe & de Bruyn (2000)
  - $C_n^2 \sim 10^{-3}$ as found via pulsar studies of the general ISM by Coles et al. (1987)
  - upper and lower limit $10^{-0.96} < \int_0^d C_n^2(l)dl < 10^{-0.55}$ for the shell material in the model of local scattering deduced from pulsar scintillation (Bhat, Gupta, & Rao 1998).

Bhat, Gupta, & Rao (1998) studied the scattering properties of the local vicinity of the Sun based on pulsar scintillation data. Their best-fit model to the data is characterized by three components: (i) a local shell structure with enhanced scattering properties which can be associated with the wall of the Local Bubble (LB), (ii) an inner cavity and (iii) the outer ISM both with a much lower level of turbulence. We use the upper and lower limits of C_n^2 in their model for the shell structure in the modeling presented here.

6.4.3 Results and Discussion

Figure 6.14 displays the results of our calculations. Panels (a), (b), (c) and (d) correspond to the results obtained for the different values of C_n^2: 0.17, 10^{-3}, $10^{-0.55}$ and $10^{-0.96}$, respectively. The best agreement between model and observations is visible in cases (a), (c) and (d). The "lower turbulence case" of Coles et al. (1987) under-predicts the observed modulation indices for all distances - in the most extreme case by a factor of 10. Panel (a) corresponds to the C_n^2-value calculated by Dennett-Thorpe & de Bruyn (2000) and is in good agreement with our observations. Here, however, a screen distance of only 10 pc is required, a factor of $\sim$2 smaller than suggested by the latter authors. The best agreement is obtained using the upper and lower limits of C_n^2 for the Local Bubble wall (Panels (c) and (d), red curves). In particular, the lower limit of $10^{-0.55}$ yields the best reproduction of the observed modulation indices (nearly 1:1) assuming a screen distance of 15 pc. At this distance, the Fresnel angular size and thus the source size is of the order $\lesssim 30\,\mu$as. The upper limit requires a distance of only 5 pc.

The question remains, if a screen at such small distance of $\sim 5 - 20$ pc can be related to the LB wall, since X-ray, EUV and HI observations suggest a mean LB radius of $\sim$

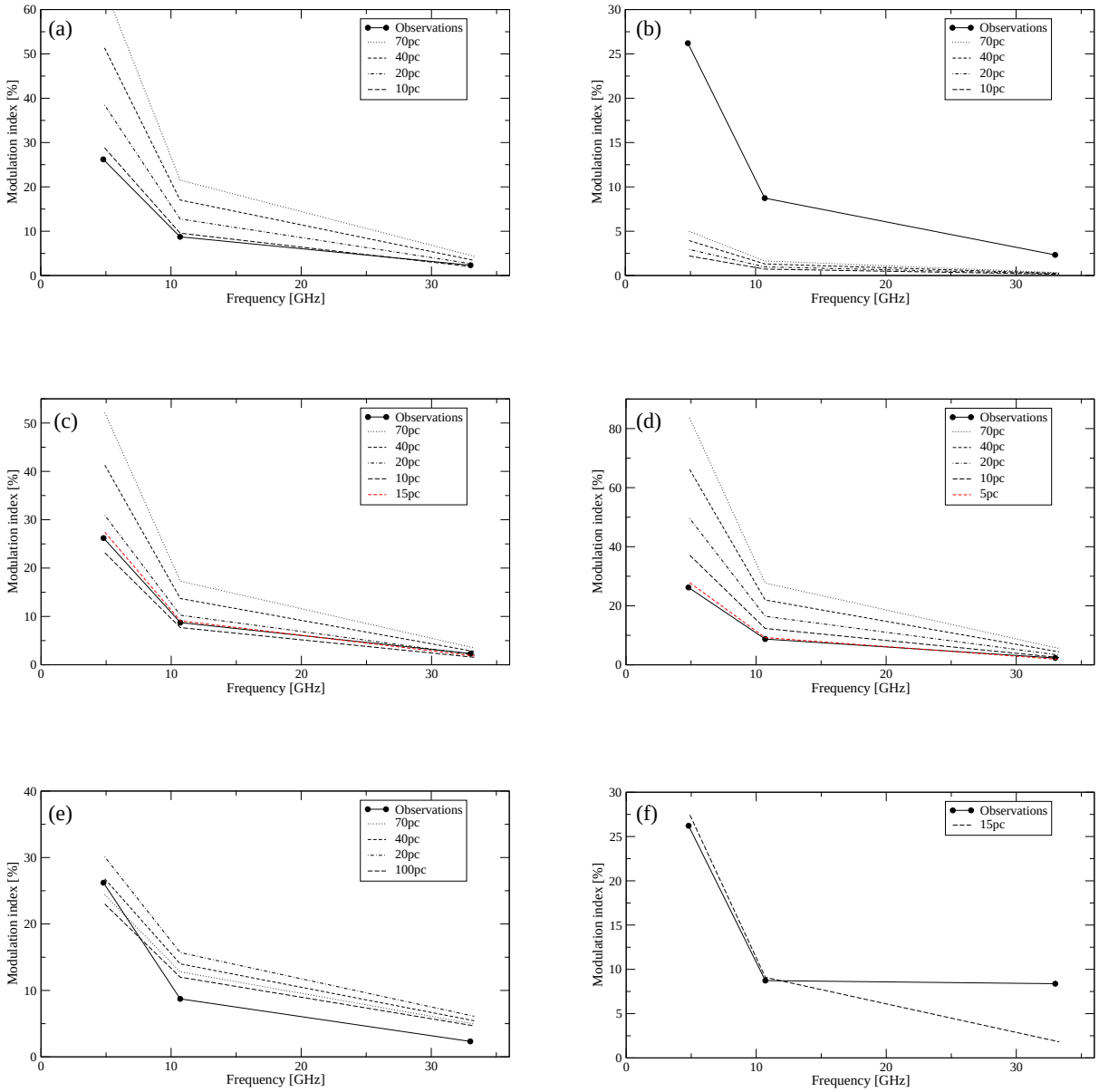

FIGURE 6.14— Results of modeling the scintillations in J1819+3845: The different panels (a)–(d) correspond to the results obtained for unquenched scattering with different values of C_n^2 (see text). Each calculation is done adopting a range of different screen distances. The best agreement is evident in the cases of the upper and lower limit for the LB wall ((c) and (d), red). Panel (e) shows the case of quenched scattering while panel (f) displays the best model with the higher modulation index at 32 GHz superimposed.

75−100 pc around the Sun (e.g. Frisch & York 1983, Snowden et al. 1990 and Warwick et al. 1993). The morphology of the local structure seen at these different wave bands and the shell with enhanced density fluctuations deduced from pulsar scintillation is quite similar. Interestingly, Bhat, Gupta, & Rao (1998) found these structures to be highly asymmetric and the Sun to be located away from the center. In their best-fit model, the shell can be as close as 15 – 25 pc in the direction of $l \sim 0° - 90°$ and $b \sim \pm 30°$. This fits nicely

with the line of sight towards J1819+3845 of $(l, b) = (66.2°, 22.5°)$ and the results presented here.

For comparison, we assumed a scenario, where the scintillations in J1819+3845 are quenched by the source size (equation 6.10) with a size of the scintillating component of 64 μas at 5 GHz. As expected, the results shown in panel (e) of Figure 6.14 are not able to reproduce the observations providing evidence that the point-source assumption for this source is justified.

In Panel (f) of Figure 6.14 the best model (LB wall at 15 pc) is shown, but we overplot here the 32 GHz-modulation index including the last, low data point in the light curve. In this case, m is higher by a factor of $\sim$3.6 at 32 GHz. Thus, a flat rather than steep decrease is seen towards higher frequencies in contrast to the model predictions. This deviation from the scintillation model, if real, is similar to the behavior seen in a few other sources (e.g. 0716+714, Figure 6.1), where even an increase of the strength of the variability with frequency is observed. Such "intrinsic up-turn", as mentioned above, is the most promising sign for an intrinsic contribution to the variability pattern. This would be of particular interest for J1819+3845, since the source is supposed to be the most prominent example of an IDV source where the intraday variations are predominantly caused by scintillation effects.

From the observed light curve and our ISS modeling, we can derive a lower limit on the intrinsic source brightness temperature T_B. Firstly, the average flux density of the scintillating component S_c is not known and has to be constrained. The scintillating component in J1819+3845 can not exhibit more flux than the total average flux density S_{tot} seen in the light curve and can not be negative, thus

$$S_{tot} \geq S_c \geq S_{tot} - S_{min} \ , \qquad (6.12)$$

where S_{min} is the lowest flux value observed in the light curve. Taking the observations at 5 GHz, this yields 110 mJy $\leq S_c \leq$ 350 mJy. Secondly, the size of the scintillating component can be constrained by the results presented above to $\sim 30\,\mu$as. In this case, we obtain an approximate lower limit on the rest-frame brightness temperature of $T_B = 6 \times 10^{12}$ K for $\theta = 30\,\mu$as and $S_c = 110$ mJy at 5 GHz. In order to reduce this value down to the inverse Compton limit of 10^{12} K, relativistic beaming with a Doppler factor of $D \sim 6$ is required. This is in good agreement with VLBI observations of apparent superluminal motion found in flat-spectrum radio cores (Witzel et al. 1988, Marscher et al. 2000, Kellermann et al. 2000). If the source is radiating at the equipartition brightness temperature of $\sim 2 \times 10^{11}$ K rather than at the inverse Compton limit, Doppler boosting with $D \sim 30$ is required.

A further interesting result is the radio spectrum shown in Figure 6.12. Dennett-Thorpe & de Bruyn (2000) suggest the spectral shape of J1819+3845 (0.3-43 GHz) and its relative stability to be an important feature. They attribute the raising spectrum to be caused by synchrotron self-absorption from an isotropic particle distribution producing optically thin emission above ν_{obs}. As seen in Figure 6.12, however, the situation may have changed, since a flat rather than inverted spectrum is observed. Therefore J1819+3845 is possibly not as stable as expected and intrinsic changes during the last years may have changed the conditions in the source. This is supported by the fact that the mean flux density at 5 GHz increased by more than a factor of 2.5 within the last three years. If such flaring behavior is accompanied with the ejection of new jet components, changes in the IDV properties of J1819+3845 should occur in the near future similar to those probably observed in PKS 0405−385 (Kedziora-Chudczer et al. 1998) and 0917+624 (Chapters 4–5, Fuhrmann et al. 2002).

6.4.4 Conclusions

We conclude that the fast and pronounced variability of J1819+3845 seen in our short multi-frequency observations can be modeled by interstellar scintillation in the weak, un-

quenched scattering regime. The best agreement is obtained for a screen exhibiting density fluctuations in the range of $10^{-0.96} \leq C_n \leq 10^{-0.55}$ at a distance of about 15 pc, which we attribute to enhanced turbulence in the nearby LB wall along the line of sight to J1819+3845. The size of the scintillating component of $\theta \sim 30\,\mu$as at 5 GHz yields a brightness temperature of $T_B \simeq 6 \times 10^{12}$ K.

In order to decrease the high statistical error of m and thus, improve the accuracy of the derived parameters, a longer observing run is essential to increase the number of observed variability cycles and improve the sampling rate. In addition, the possible existence of an intrinsic up-turn in the m-ν distribution has to be confirmed by new 32 GHz observations.

Part III: Spectral Line Observations towards IDV Sources

7

Search for the Scattering Screen in Front of IDV Blazar Cores

In this thesis, we started a new observational approach to directly search for the scattering material in the foreground of intraday variables. Until now, only indirect hints for the material do exist and no attempts were performed in order to directly detect the postulated scattering screen. This chapter focuses on the extrinsic part of IDV and outlines the prospects for a direct detection of the material producing IDV in extragalactic radio sources.

The first section gives an overview of the situation and defines a working strategy. The following sections describe a step-by-step procedure in order to identify the required material with emphasis on: (i) the material we are looking for, (ii) the basic components of the interstellar medium, (iii) the local ISM (LISM) and (iv) observational evidence for the material intervening on the line of sight. Finally, we present spectral line observations towards IDV sources along with a statistical analysis of a possible connection between IDV source positions and discrete ISM features.

7.1 Scientific Motivation and Working Hypothesis

As outlined earlier, there is increasing evidence that ISS plays an important role in the rapid variability of IDV sources. Although the overall situation is not yet fully clear, ISS is generally excepted as at least one contribution to the short-term variations.

The presence of scattering material in the Galaxy responsible for ISS of radio sources was suggested since the early days of variability studies (e.g. pulsar scintillation and low-frequency variability of AGN). In particular, Heeschen et al. (1982) already addressed the 'flickering' of compact radio sources to scattering caused by the inhomogeneous structure of the interstellar medium of our Galaxy (Rickett et al. 1984, Heeschen & Rickett 1987). With the advent of variability on much shorter time scales of hours to days it turned out that the postulated screen has to be very close to the Sun, closer than deduced from the flickering of radio sources. As shown in the previous chapters, the ISS modeling depends on several parameters, which have to be assumed or are not known precisely. One of these "free parameters" is the distance to the scattering medium. Furthermore, the properties of the scattering material itself, e.g. the strength of turbulence C_n^2, the turbulence spectrum, velocity of the medium etc. are not precisely determined. Although, for example, the overall distribution of the strength of turbulence in the Galaxy is known form pulsar studies, its value for individual lines of sight is uncertain.

In addition, the characteristic shape of extreme flux density variations seen as extreme scattering events (ESEs) in the multi-frequency light curves of extragalactic radio sources is thought to be caused by the ISM as well. Here, "plasma-lenses" were proposed to be responsible (Fiedler et al. 1987) among other theoretical models (see Walker 2001 for a review). Also this kind of scattering effect

still asks for a final explanation and the detailed mechanism in the ISM has still to be found.

Thus, a clear need is identified for additional information on the scattering regions in front of IDV and ESE sources. Such information could be provided by spectral line observations: a direct detection of the scattering material in front of IDV and ESE sources has the potential to (i) establish a relation between IDV and local structures in the ISM and thus a direct confirmation for the existence of an (at least mostly) extrinsic origin of IDV, (ii) test/check the proposed models for extreme scattering events and (iii) provide better constraints of the physical conditions in the scattering medium (temperatures, densities, velocities, distances etc.) in view of ISS and ESE modeling. The latter can have also impact on the remaining question about an intrinsic contribution to the IDV pattern.

This chapter will firstly develop a strategy for a direct detection of the material. As working hypothesis we address rapid intraday variations in compact radio sources to scattering in the local interstellar medium. The following questions will serve as "working strategy":

1. What tell us the ISS and ESE models about the screen?
2. Which component of the ISM could serve as scattering material?
3. Where is its location in the Galaxy?
4. Do we have already observational evidence for the material?

In the following we will go through this questions step by step.

7.2 What are we looking for?

First, we have to investigate the predictions of the ISS and ESE models for the screen in order to identify the required material in the ISM.

In order to display scintillation, the source size must be of the order of the scattering size of the medium (defined by the first Fresnel zone for weak scattering and the refractive scale for strong scattering). This quantity depends sensitive on the distance to the screen. As outlined earlier, the observed variability time scales provide an estimate for the mean distance to the material. For relative velocities not much larger then $40\,\mathrm{km\,s^{-1}}$ (see Chapter 3) and time scales up to a few days (Typ I sources), we obtain a few 100 pc as upper limit for the distance of the screen. A lower limit can be obtained taking the rapid scintillators into account. Dennett-Thorpe and de Bruyn (2000) deduced a distance of about 25 pc for the highly variable quasar J1819+3845 from annual modulation studies (see Chapter 3). For the other two intra-hour variables PKS 0405−385 and PKS 1257−326 even smaller distances in the range of 3−30 pc were reported (Rickett et al. 2002, Bignall et al. 2003). The small number of highly variable sources observed so far makes it likely to find only a few line of sights in the Galaxy with scattering material so close to the Sun. Thus, we have to search for material mainly between $\sim$30 and a few 100 pc around the Sun with maybe a few line of sights showing material at only a few parsec distance.

The annual modulation study presented in previous chapters can in principle provide additional implications for the medium. If the present inactivity of 0917+624 is indeed caused by dramatic changes in the ISM, the different behavior of the nearby source 0954+658 suggests a very inhomogeneous medium. The latter should then vary at least on angular scales less than a few degrees on the sky. The fitting of seasonal cycles to the IDV data provides evidence that we have to deal with highly anisotropic scattering rather than isotropic inhomogeneities in the plasma (Rickett et al. 2002). The high degree of anisotropy implies well-ordered magnetic fields, which makes a relatively thin scattering layer more likely than an extended medium. In addition, the lack of a clear galactic latitude dependence of IDV compared to e.g. flickering suggests that more discrete, local structures

in the ISM are involved rather than its extended, large scale distribution. The determination of a peculiar velocity of the medium in front of J1819+3845 through time delay measurements supports this idea (Dennett-Thorpe and de Bruyn 2002). In general, the LSR (transverse) velocities of the medium are expected to be low: $\lesssim 30\,\mathrm{km\,s^{-1}}$. Furthermore, the ISS modeling suggests an electron density in the medium of $n_e \simeq 0.1 - 1\,\mathrm{cm^{-3}}$.

Although the relation (if any) between ESE lense structures and the turbulent gas responsible for normal ISS is unclear (e.g. due to the different observational appearance of both), the physical conditions for ESEs appear to be similar. Both, a localized structure in the ISM with a smooth, Gaussian profile of excess electron density ('lens') as well as a large number of electron density fluctuations confined to a localized region in the ISM were discussed in the framework of ESEs. Consequently, ESE sources require also free electrons ($n_e \gtrsim 100\,\mathrm{cm^{-3}}$) intervening on the line of sight with changes in the electron density. Here, however, the medium appears more "clumpy" with a clumpiness on scales ~ 0.4 AU or even one magnitude lower in the case of the extreme ESE observed by Cimó et al. (2002a) in 0954+658.

7.3 Multiphase ISM - Identification of the "Scattering Phase"

Can we identify the required material with an adequate component in the ISM?

There is now substantial evidence that the ISM is best described within the widely accepted model of a multiphase ISM (e.g. McKee & Ostriker 1977, Cox & Reynolds 1987, McKee 1995). The interstellar medium is thought to be highly inhomogeneous, whereas much of the gas is concentrated in both atomic (H I) and molecular clouds which only occupy a small fraction of the total volume. Much of the volume is filled with warmer intercloud gas. The material of the Milky Way seems to exhibit all of the three principal phases and most of the volume in our Galaxy is occupied by: (i) the cold neutral medium (CNM) with a temperature of $T \simeq 10^2$K, (ii) the warm medium ($T \simeq 10^4$K), which has both the warm neutral medium (WNM) and the warm ionized medium (WIM)[1]; and (iii) the hot ionized intercloud medium (HIM) with $T \simeq 10^6$K. Molecular clouds and some transient phases can also be important. The former do not constitute a fourth phase because they are self-gravitating and hence are not in pressure equilibrium with the other phases. The ionized component of the warm phase, the WIM, is found to be an important constituent of the diffuse interstellar medium and probably is related to the ionized surfaces of the warm neutral clouds (WNM).

However, in view of the ionized material required to produce scintillation, a few phases of the ISM can already be excluded. Firstly, the atomar component itself in form of the CNM can not be responsible for ISS. Secondly, the electron densities of the hot ionized medium with $< n_e > \sim 0.003\,\mathrm{cm^{-3}}$ are probably not sufficient to produce regions of enhanced scattering. What remains in view of the multiphase ISM is the warm ionized medium. It exist as "normal" WIM and as so-called ELDWIM (extended low-density warm ionized medium). The former is well known to be associated with the scintillation of pulsars and to produce pulsar dispersion. From this, an averaged smooth volume density of $< n_e > \sim 0.03\,\mathrm{cm^{-3}}$ was derived (e.g. Heiles 1994), while H α emission from such material implies a total emission measure of $\sim 3\,\mathrm{cm^{-6}\,pc}$ and an electron density of the order $0.1\,\mathrm{cm^{-3}}$. The ELDWIM is predominantly found in the Galactic interior (first considered by Mezger 1978), is much brighter than the WIM and is suggested to be the higher density version of the WIM (Heiles et al. 1996). Its connection to star forming regions as ionized envelops of normal H II regions is discussed (e.g. Roshi & Anantharamaiah 2001).

[1]The classification is still under discussion and sometimes used differently in the literature: e.g. more recently, Heiles 2001 discussed an ISM consisting of five gas phases including two kinds of the WIM.

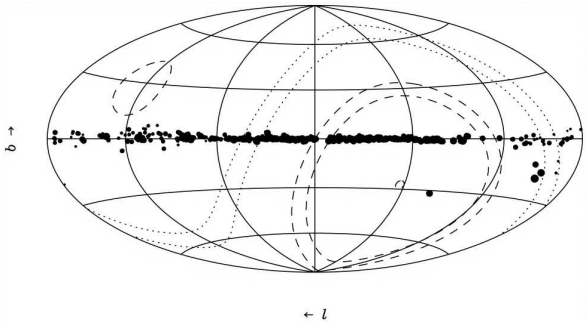

FIGURE 7.1— All-sky catalog of H II regions at 4.85 GHz plotted in an Aitoff projection of the Galaxy (taken from Kuchar & Clark 1997). The sizes of the points are proportional to the source peak flux. Nearly all H II regions are confined to a small range along the galactic plane ($|b| \lesssim 1°$).

In view of the multi-phase ISM, we thus expect the WIM or ELDWIM to be responsible for the scintillation of IDV sources.

7.4 Discrete Structures of the ISM

Besides the different phases of the ISM introduced above, there are additional, mainly well localized structures of the ISM, which could in principle exhibit scattering material.

7.4.1 H II regions

A variety of H II regions is known. They are often formed around young, hot stars by their strong photoionizing radiation. Such highly ionized structures are often embedded in the star forming regions within larger molecular clouds and appear to exist in two different types: (i) ultracompact HII regions with $n_e > 10^4\,\mathrm{cm}^{-3}$ and sizes $\ll 1\,\mathrm{pc}$ and (ii) 'normal' HII regions with electron densities of ~ 1–$1000\,\mathrm{cm}^{-3}$ and sizes of up to a few parsecs. However, these small, ionized structures in star forming regions can be found nearly without exception only in a small latitude range along the Galactic plane ($|b| \lesssim 1°$, see Figure 7.1; e.g. Lockman 1989, Kuchar & Clark 1997). Due to the appearance of IDVs mainly at higher Galactic latitudes ($|b| \gtrsim 10°$), H II regions can be excluded as possible scattering regions.

7.4.2 Molecular Clouds

Half of the gas mass of the Galaxy resides in (giant) molecular clouds, which are the primary sites of star formation and are found to be generally concentrated along the Galactic plane ($|b| \lesssim 10°$). They usually have a small scale height of $\sim 75\,\mathrm{pc}$ from the Galactic plane (e.g. Blitz 1990) and typical distances within $\sim 1\,\mathrm{kpc}$. More interestingly in the context of IDV are the so-called high Galactic latitude molecular clouds (HLCs) due to their proximity to the solar system. This class of (small) molecular clouds are usually distinguished from dense clouds located in the Galactic plane by their low visual extinctions. Up to now, more than 200 HLCs were detected at Galactic latitudes $|\,b\,| \geq 20°$ through dust, H I and CO observations (e.g. Blitz et al. 1984, Magnani et al. 1985). For about 40 HLCs the distance is constrained by the presence or absence of interstellar absorption lines (e.g. sodium, calcium) towards stars located along the line of sight. The average distance to these clouds is 105 pc and the derived cloud sizes are usually smaller than a few parsecs (Magnani et al. 1996). Their scale height from the galactic plane is low, $\sim 90\,\mathrm{pc}$, and thus HLCs are Galactic plane objects. They often appear to be part of larger cloud complexes (e.g. Ursa Major complex), which extend out to a few square degrees on the sky mainly due to their proximity. Although attractive due to the small distances, HLCs itself can not be responsible for interstellar scattering, since ionized material is required.

7.4.3 Photodissociation Regions

There are so-called PhotoDissociation Regions (PDRs, e.g. Hollenbach & Tielens 1997), which in principle could provide ionized material for scattering. The physics and chemistry of such sites in the ISM is determined by the far ultraviolet (FUV) photons ($6\,\mathrm{eV} < h\nu < 13.6\,\mathrm{eV}$) originating from hot nearby stars and/or the overall interstellar radiation field (IRAF). The energy of these photons can be transferred to the ambient gas by photoelectric heating: the FUV photons ionize grains

producing photoelectric electrons, which heat the gas by collisions. Elements like carbon with ionization potentials below 13.6 eV become photoionized by the FUV flux as well and thus C^+ forms efficiently in the outer layers of a PDR, where the FUV radiation is still intense enough.

PDRs form in predominantly neutral regions exposed to an external FUV radiation field, which dominates the heating as well as the chemistry of the gas. Thus, PDRs include most of the atomic gas existing in both, diffuse (H I) clouds (CNM) and in the surfaces of the more opaque molecular clouds. In this context, e.g. the outer layers of the molecular clouds mentioned earlier are PDRs, where the penetrating photons create an atomic H surface layer and deeper inside (with increasing visual extinction A_v) molecular H_2, C^+ ions, and C. In principle, the free electrons produced by the photoionization in PDRs could reflect the scattering material responsible for IDV and/or ESEs. Consequently, the HLCs introduced in the previous section remain "attractive" for the scattering material.

7.4.4 Shells, Bubbles and Radio Loops

A few other, localized (often large) structures of compressed material are known to be part of the ISM extending outwards into the Galactic halo such as H I shells, supershells, "worms" or radio continuum loops (e.g. Heiles 1984). The interaction of such shells or superbubbles with the ambient medium or with other structures of the same kind leads to the formation of interaction zones or walls. Like discussed for the interaction of the radio Loop I and the Local Bubble (Breitschwerdt et al. 1996, 2000), the collision of those is followed by the production of a dense, compressed wall, which is Rayleigh-Taylor unstable. Such instability eats its way through the interaction zone and produces a very turbulent, inhomogeneous region with small bubbles and holes. Such features along the line of sight could be made responsible for the required enhanced scattering material producing ISS and/or ESEs. Indeed, new pulsar studies towards the direction of Loop I ($270° < l < 30°$ and $-40° < b < +80°$) show enhanced levels of scattering. Bhat & Gupta (2002) explain this feature either with their older LB model (as described in Chapter 6) extended by incorporating an additional Loop I shell component or with enhanced scattering in the interaction zone between LB and Loop I.

7.5 The local Vicinity of the Sun

As next step we have to investigate the distribution of the material in the galactic environment of the Sun in order to find an eligible layer for enhanced scattering.

Within the general picture of the ISM, stellar winds produced during star formation evacuate cavities in the molecular clouds in which the stars are born. When subsequent SNe explode in these cavities, violent shock fronts are produced that ram into the surrounding material. Furthermore, they sweep up interstellar gas into supershells, which propagate outwards into the low-density environment. The shocked gas cools and recombines to form "inter-bubble" gas as part of the CNM, and can break up into clouds. Such structures are common in the local vicinity of the Sun. Within the prevailing picture of the local ISM (LISM) as deduced from e.g. X-ray data and high resolution absorption studies towards nearby stars, the LISM ($\sim$ a few 100 pc) is known to contain several major features in the form of clouds, bubbles, supernova shells, star forming regions and H I clouds. The Sun is thought to reside in a great, irregularly shaped void - the hot, low-density ($n_e \sim 0.005\,\mathrm{cm}^{-3}$) X-ray emitting Local Bubble (LB) (e.g. Cox & Reynolds 1987). Snowden et al. (1998) deduced its radial extent from X-ray data to vary between 40 and 130 pc from the Sun (compare Figure 7.2). As outlined in Chapter 6, a similar morphology for the LB wall was found by Bhat, Gupta & Rao (1998) from pulsar studies. Prominent among other features in the LISM, the LB itself is embedded into the interactions of large, often circular structures (compare Figure 7.3),

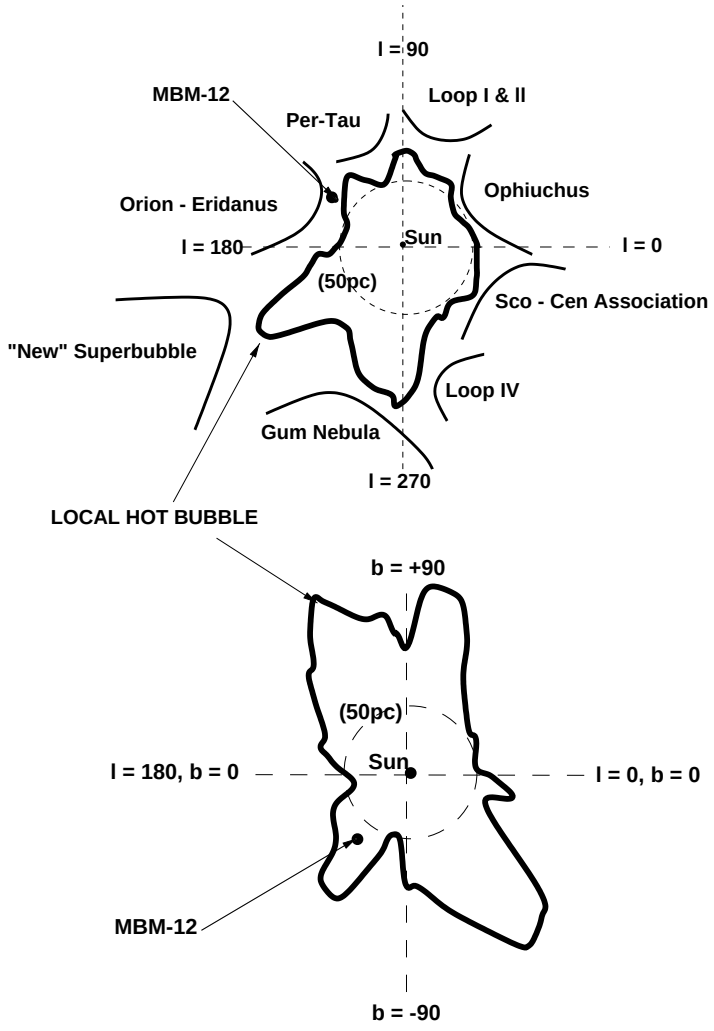

FIGURE 7.2— The approximate extend of the local bubble (thick solid line) deduced from X-ray data by Snowden et al. (1998). **Top:** View from the North Galactic pole. In addition, adjacent bubbles and loop/shell structures are drawn schematically. The position of the HLC MBM-12 at the interface between LB and the Orion-Eridanus bubble is indicated. **Bottom:** View in the Galactic plane.

e.g. the radio Loops I to IV (Haslam, Kahn & Meaburn 1971) and their turbulent interaction zones mentioned earlier. Of these, the Loop I bubble is thought to be an active, expanding super-bubble triggered by star formation in the Sco-Cen star forming region at a distance of $\sim 150\,\mathrm{pc}$ from the Sun.

Furthermore, results from Rosat observations suggest an ongoing interaction between the LB and Loop I. Egger & Aschenbach (1995) found a ring like structure between the two bubbles. The distance to this interaction feature is estimated to be $\sim 70\,\mathrm{pc}$, quite comparable to the distance to the known neutral H I wall ($\sim 40\,\mathrm{pc}$). However, as result of this ongoing interaction, the Sun lies more local inside a warm ($\mathrm{T} \sim 7000\,\mathrm{K}$), diffuse and partially ionized ($n_e \simeq 0.12\,\mathrm{cm}^{-3}$) cloud, the local interstellar cloud (LIC, $\mathrm{d} \sim$ a few pc; Lallement & Berlin 1992). The LIC extends for several parsecs in most directions and is part of the "local fluff" (Frisch 1995). This complex of warm,

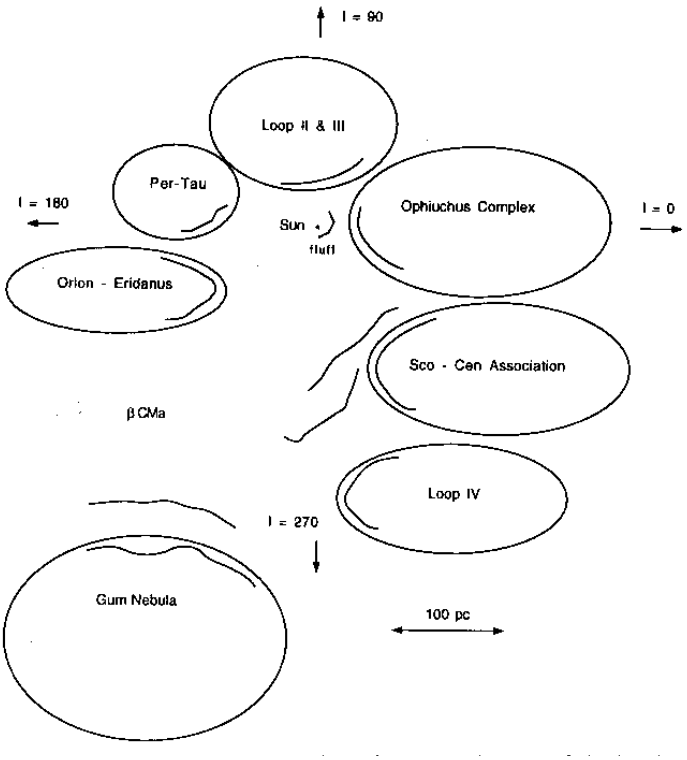

FIGURE 7.3— A schematic picture of the morphology of the local ISM within a few hundred pc (taken from Welsh et al. 1994). Several interacting shells, bubbles and loop structures in the vicinity of the Sun are shown (see text).

nearby clouds or shell-like structures located either insight or at the edge of the LB originated from the Sco-Cen star forming region, since the low-density LB readily permits such material (like shock fronts, shells and superbubbles) to sweep over into our neighborhood ($d \sim 100$ pc).

In addition, the LB is surrounded by other well-known examples of nearby bubbles, star forming regions, and shells of SN remnants (compare Figure 7.3). These features are suitable to either contain or produce "scattering material" within a radius of 100–300 pc, such as the Orion-Eridanus Bubble ($d \sim 100$–150 pc) and the Orion Shell, the Gum Nebula ($d \sim 250$ pc) - a region of ionized hydrogen with the Vela SN remnant inside.

The high latitude molecular clouds introduced in Section 7.4.2 with distances of ~ 100 pc must therefore lie either inside the LB or in the local environment of the LB wall. Since the LB seems not to provide the conditions to form molecular structures, the HLCs are most likely the molecular component of the compressed (CNM) gas in the interaction zones between LB and adjacent bubbles. The position of the closest HLC known so far, MBM-12, is indicated in Figure 7.2 to be at the edge between LB and the Orion-Eridianus bubble (Kuntz, Snowden, & Verter 1997).

Within the picture of the LISM as described here, it appears quite plausible that enhanced scattering material responsible for ESEs and IDV is produced in the turbulent outer shells and/or interface regions of the LB and adjacent bubbles. The origin of the most local screens required for the extreme IDVs remains unclear. Here, the only suitable components are the LIC and the local fluff. The electron density in these clouds is estimated to be of the order $0.1\,\mathrm{cm}^{-3}$ (Wood & Linsky 1997). If the electron density fluctuations Δn_e are proportional to the electron density ($\Delta n_e \propto n_e$;

Rickett 1970), the scattering strength C_n^2 can be assumed to be $C_n^2 \propto n_e^2$. The so derived value of $C_n^2 \sim 0.01$ is at least one magnitude lower than the values incorporated in the ISS modeling of J1819+3845 presented in Chapter 6. Thus, it appears unlikely that the local fluff clouds can sufficiently account for the variability seen in the fast scintillators. Instead, lines of sight passing through the LB wall at its minimum extension from the Sun are more likely (as proposed for J1819+3845 in Chapter 6).

7.6 Observational Evidence for the Material

Finally, we can search in the literature for observational evidence of interstellar material distributed along the line of sight. Present galactic surveys of e.g. dust, H I, H α, CO, radio continuum provide additional information and enable us to search directly for material in each individual source direction. From this we can deduce that IDV sources lie often in regions of enhanced emission, while non-variable sources are often located in regions of less emission or even in "holes". At first, we can search for dust emission towards IDV positions. Dust is an important tracer for CO and often good correlations between IRAS 100 μm data, molecular structures and/or H I emission were found (e.g. de Vries et al. 1987, Heithausen et al. 1993). Taking 100 μm dust maps from the IRAS survey towards IDV positions reveals often enhanced emission of small dust clouds or clumps located close to the line of sight. Figure 7.4 shows an example of a $40^\circ \times 40^\circ$-field containing 12 of our high declination IDV sources. Large scale structures of dust cirrus clouds and filaments are seen in Figure 7.4, which form the so-called North Celestial Pole Loop (e.g. Meyerdierks et al. 1991, Pound & Goodman 1997). The latter is also seen as large H I structure (Heiles & Harbing 1974). The IDV positions within this field are marked by a cross (Figure 7.4, top). All IDV sources appear to be distributed along the large scale loop structure or its fainter filamentary extensions. Zooming into individual IDV positions often reveals enhanced dust emission close to the line of sight, as can be seen in the few examples given at the bottom of Figure 7.4.

The radio Loop III as seen in the radio continuum (Berkhuijsen et al. 1971, Haslam et al. 1982) lies in the same field of view and is shown at the top of Figure 7.5. This large-scale feature extends from the galactic background from (l, b) $\sim (125^\circ, 30^\circ)$ as a half-circle structure northward to (l, b) $\sim (135^\circ, 40^\circ)$ and meets the background near (l, b) $\sim (155^\circ, 30^\circ)$. The IDV positions in this field of Figure 7.5 are superimposed. It turns out that several IDVs are distributed along the Loop III foreground structure. As outlined by Fiedler et al. (1994b), 0954+658 lies behind the continuum loop and, in particular, three high latitude H I shells (a main shell plus two sub-shells) were detected by Hu (1981) to correlate with the positions along Loop III of which one crosses the line of sight to 0954+658. In addition, these shell structures overlap the positions of the IDV sources J0949+6614, 1039+811 and 1150+812 as well.

Several IRAS cirrus clouds are observed to be associated with molecular gas in the form of HLCs, for which the North Celestial Pole Loop shown in Figure 7.4 is a good example. In addition, a correlation was found between HLCs and H I emission and the conclusion was drawn that these clouds probably condensed out of the diffuse CNM (Gir, Blitz, & Magnani 1994). Due to the relatively good correlation between IDV positions and IRAS dust emission it is obvious to search for molecular material in front of IDVs. Here, a large data base of CO cloud detections and CO surveys (e.g. Hartmann, Magnani & Thaddeus, 1998) are available in the literature (see Section 7.8.3). It turns out, that high latitude molecular clouds, cloudlets or cloud complexes close to e.g. 0917+624 and 0954+658 were found (e.g. Magnani & Blitz & Mundy 1985, Matsuhara et al. 1997). Figure 7.5 displays a $\sim 25^\circ \times 40^\circ$ field as part of the IRAS map shown in Figure 7.4. The map is centered

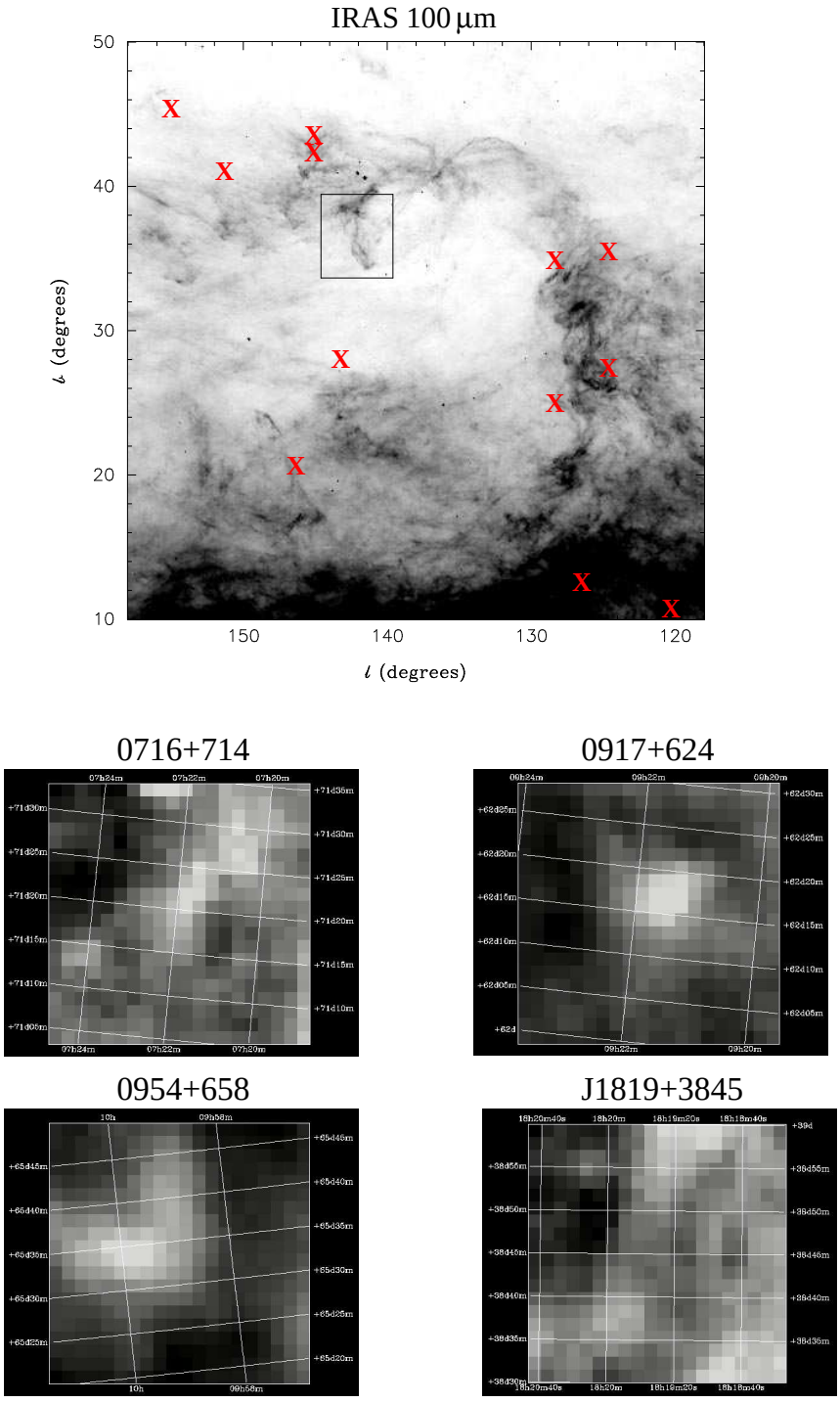

FIGURE 7.4— 100 μm dust maps taken from the IRAS survey of a $40^\circ \times 40^\circ$-field are shown containing 12 of our high declination IDV positions (red crosses, top). These positions often appear to be distributed along the large scale cirrus cloud structures. The position of the Ursa Major clouds as seen in CO is marked with a box (compare Figure 7.5). Individual IDV positions reveal often enhanced dust emission close to the line of sight (bottom).

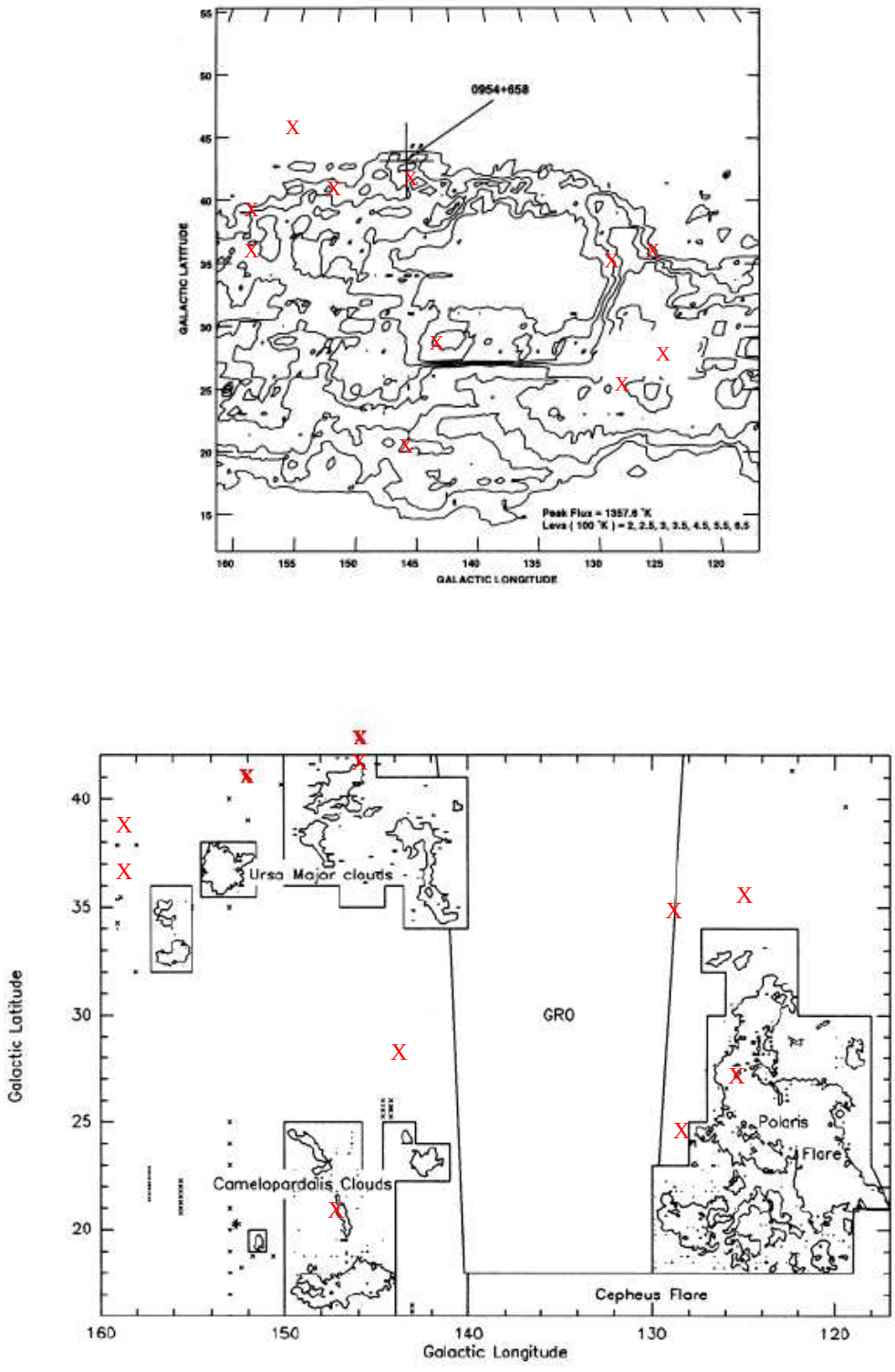

FIGURE 7.5— Radio continuum map containing the radio Loop III is shown at the top (taken from Fiedler et al. 1994) with presently known IDV positions superimposed. The large scale CO map at the bottom exhibits several molecular cloud complexes in the same region of the sky (taken from Heithausen et al. 1993). IDV positions are superimposed as well. In both cases IDV positions often lie behind or close to foreground features (see text).

on the galactic coordinates $(l, b) = (138°, 29°)$ and contains three, large high latitude cloud complexes. The cloud structures detected by the afore mentioned authors are part of the Ursa Major cloud complex (Heithausen et al. 1993), which "hangs down" from the top of the IRAS cirrus clouds in Figure 7.4 (black box). As can be seen, several IDV line of sights lie close to or even behind CO structures. A comparison of a larger number of (high latitude) molecular cloud positions with the positions of IDV sources reveals that often IDVs lie in or near regions of high cloud densities (often within $\leq$ a few degrees). A more statistical analysis of such possible correlation will be presented in Section 7.8.3.

Since free electrons and therefore an ionized medium is required to produce scintillation, surveys showing the distribution of ionized material in the Galaxy (e.g. H α) can provide further informations. The Wisconsin H-Alpha Mapper Northern Sky Survey (WHAM, Haffner et al. 2003) samples the distribution of the WIM in the Galaxy as seen in diffuse H α emission with a resolution of 1°. Here, IDV source positions often lie in "plateau regions".

7.7 Spectral Line Observations towards IDVs

The situation presented above suggests that either the "WIM phase" of the ISM or more discrete features of the local ISM (e.g. HLCs and/or Loop structures) are connected with IDV and/or ESEs. In this section first spectral line observations are presented, which include the attempt to detect both, ionized material as part of the general ISM, as well as discrete ISM structures intervening the line of sight.

7.7.1 Radio Recombination Line Observations

In view of the multi-phase ISM discussed in Section 7.3, we expect the WIM or ELDWIM to be connected with scintillation of extragalactic radio sources. The enhanced electron density in such warm layer ($n_e \sim 1 - 10\,\mathrm{cm}^{-3}$) is maybe large enough to become observable as the emitter of "diffuse recombination lines" at radio frequencies. Such medium was identified through detection of radio recombination lines (RRLs) at several positions free of discrete continuum sources already 30 years ago (e.g. Gottesmann & Gordon 1970), although here mainly towards the galactic plane. This may open the possibility to observe directly the postulated scattering medium in front of IDV sources. As by-product, RRL observations at two different frequencies allow to constrain the physical conditions of the line emitting regions. Consequently, this would provide important parameters (e.g. electron densities) of the ionized medium intervening on the line of sight.

The WHAM-H α survey directly displays the distribution of the warm, ionized ISM and can be used to get an estimation of the local electron densities towards IDV positions (often at higher latitudes). With typical temperature values for the WIM (8000 K) an H α-intensity of 1 Rayleigh corresponds to an emission measure (EM) of $2.25\,\mathrm{cm}^{-6}\mathrm{pc}$ (e.g. Haffner et al. 1998). Assuming the screen as a cylinder of uniform density gas with width L, then the emission measure $\mathrm{EM}\,(\mathrm{cm}^{-6}\mathrm{pc}) = n_e^2 \mathrm{L}$ leads to electron densities of $n_e = 0.3 - 0.9\,\mathrm{cm}^{-3}$ for $L = 20\,\mathrm{pc}$. From the EM-Intensity-Relation one can easily derive EMs and recombination line temperatures T_L for typical linewidths of $30\,\mathrm{km\,s}^{-1}$ using the WHAM-data. The low EMs calculated here lead to low recombination line temperatures of $T_L \lesssim 0.1\,\mathrm{mK}$. Such temperatures are impossible to detect, but one has to note that these EMs derived from the WHAM-intensities in direction of IDV sources are only lower limits, since (i) extinction plays an important rule, (ii) the used intensities are not exactly (due to limitations of the survey) along the line of sight to our sources (often a few degrees away), (iii) the survey is not able to detect such small scale regions due to its resolution. In addition, the detection of such low-density ionized gas was successfully performed via recombination line observations in several surveys (e.g. Lock-

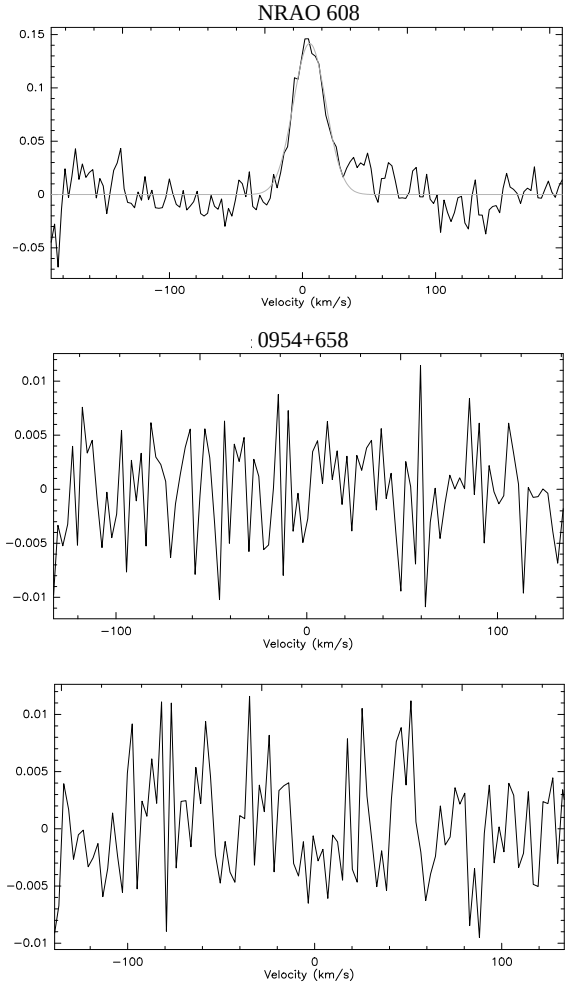

FIGURE 7.6— **Top:** RRL spectrum of NRAO 608 showing a significant detection. In addition, two examples of RRL spectra taken at the position of 0954+658 are shown. Each spectrum has a total integration time of about two hours. Neither the H166α line (**middle**) nor the H167α line (**bottom**) was detected.

man 1976 near 1.4 GHz, Roshi & Anantharamaiah 2000, 2001 near 327 MHz).

Since a low-density ionized medium is expected to be responsible for the scintillation, we observed the hydrogen RRLs H166α and H167α at 1424 MHz and 1399 MHz, respectively. At these lower frequencies RRLs are expected to originate not in normal high-density H II regions due to the effects of continuum opacity, pressure broadening and beam dilution. Hence, observations of low-frequency RRLs are sensitive to relatively low density, larger angular sized ionized regions. The observations were performed with the Effelsberg 100-m telescope in March and July 2002 using the 21 cm prime focus receiver. Due to the large bandwidth of the receiver, both lines could be observed simultaneously. The (old) 1024-channel autocorrelation spectrometer was used in the 4×256 mode, while two IFs (each with a bandwidth of 3.1 MHz) were centered on the H166α-line and the remaining two IFs shifted by −25 MHz. The spectral resolution was 2.6 km^{-1} (12.2 kHz).

Spectra, integrated for 5–10 minutes, were taken towards several IDV positions in both frequency- and position-switch mode. Polynomical baselines were removed and the spectra of both IF's were averaged. To test the system conditions, a few positions of known sources with stronger RRLs were observed (e.g. NRAO 608, W3OH) and significant lines have been detected (Figure 7.6, top). However, in both sessions the observing conditions were strongly effected by radio interference and "bad baselines". Consequently, the overall situation was not optimal to detect weak recombination lines.

Towards all IDV positions observed (0716+714, 0917+624, 0954+658 and J1819+3845) no significant lines were detected to the 3σ limit of our observations. As example, Figure 7.6 (middle, bottom) displays both the H166α and H167α spectra each with a total of two hours of integration at the position of 0954+658.

7.7.2 First CO Observations - A Molecular Cloud in Front of 0954+658?

During the 345 GHz monitoring at the HHT in May 2002 (Chapter 6), we performed a few additional observations: spectral line observations were done towards a few IDV positions in order to search for the nearby screen. Due to the existence of discrete structures like HLCs close to e.g. 0917+624 and 0954+658, we observed the ^{12}CO(2−1) line (230.5 GHz) with the 230 GHz SIS-receiver. Several backends were used simultaneously, including three filterbanks with 1 MHz, 250 kHz, and 62.5 kHz

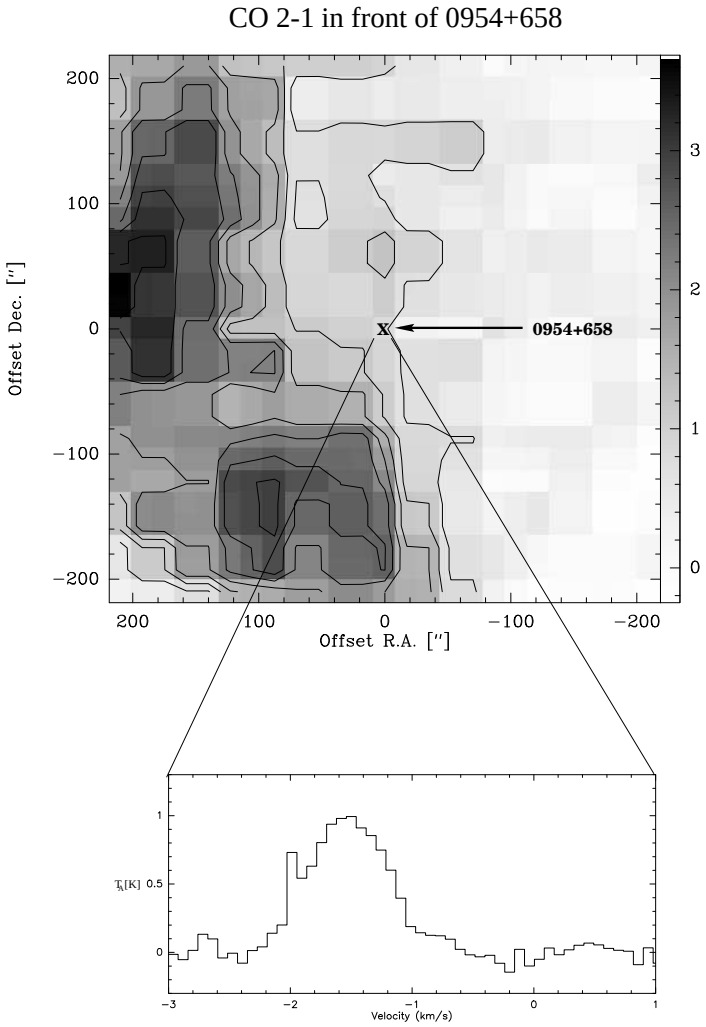

FIGURE 7.7— The detection of a CO cloud in front of the BL Lac object 0954+658 is displayed. **Upper map:** the cloud is located eastern of 0954+658 and extends in the north-south direction with a minimum extension of 440". The position of 0954+658 is marked with a cross. Contour levels are: 20, 30, 40, 50, 60, 70, 80, 90 and 100% of the maximum line emission (lowest contour = 5σ). The IDV source is located behind the outer CO-shell of the cloud. **Lower panel:** Spectrum at the position of 0954+658.

resolutions and an acousto-optical spectrometer (~ 1 MHz resolution). All spectra were taken in position-switch mode and second order baselines were removed. Among spectra taken at the position of 0917+624 and 0716+714 with no significant detection, we were able to detect the CO(2−1)-line in the direction of the BL Lac 0954+658. Subsequently, a $7' \times 7'$ raster map revealed a larger cloud structure extending in the north-south direction. Figure 7.7 displays the final CO map consisting of three coverages with a total observing time of about 15 hours. The map is centered on the position of 0954+658. A CO cloud eastern of the IDV source is seen with a minimum extension of $440''$ in the north-south direction. 0954+658 is located behind the outer western part of the cloud. A Gaussian fit to the line at the position of 0954+658 reveals a line intensity of $T_A = 1.01$ K at a

IDV source	CO detection
0153+744	+
0454+844	+
0602+672	+
0716+714	–
0804+499	–
0917+624	–
0954+556	–
0954+658	+
1039+811	–
1739+522	–
1749+701	–
J1819+3845	–
2007+777	–
J0642+8811	+
2200+420	+

TABLE 7.1— Summary of IDV positions which have been investigated for CO at the HHT and the IRAM 30-m telescope (May and December 2002, top). CO detections are marked with a '+'. A search in the literature for CO cloud detections revealed two further IDV positions with CO intervening on the line of sight (bottom).

LSR velocity of $v = -1.54\,\mathrm{km/s}$.

7.7.3 Follow-up Observations with the IRAM 30 m Telescope

Within another project to search for small-area molecular structures (Heithausen et al. in prep.), a few further IDV source positions were included to search for CO intervening on the line of sight. The observations were conducted in December 2002 with the IRAM 30-m telescope on Pico Veleta using the A and B receivers simulaneously. Both, the ^{12}CO(1−0) and ^{13}CO(2−1) line were detected towards three further IDVs (Type I or II): 0153+744, 0454+844 and 0602+672. This increases our direct CO detections towards IDV sources to four out of a small sample of 13 sources (Table 7.1). While examining the literature for CO detections, two further IDV sources turned out to exhibit CO intervening on the line of sight as well (see below).

7.8 High Latitude Molecular Clouds as Harbour of the Scattering Screen?

The findings presented above lead to the idea that high latitude molecular clouds are generally the harbor of the scattering material producing IDV of extragalactic radio sources. HLCs are attractive as sight for the scattering screen in front of IDVs in several respect. Firstly, as indicated above, these clouds are nearby ($\sim 100\,\mathrm{pc}$) objects and thus are close enough to produce variability on intraday time scales. In particular, the larger HLCs located near 0954+658 and 0917+624 are part of the Ursa Major clouds. The distance to this complex was constrained by Penprase (1993) through optical absorption studies to $100\,\mathrm{pc} < D < 120\,\mathrm{pc}$. Assuming the CO cloud in Figure 7.7 belongs also to this cloud complex, the distance to our detected object should be of the order 100 pc. This fits nicely with the expected distance with regard to the variability time scales observed in 0954+658 (Chapter 4).

Secondly, HLCs are commonly found to be gravitationally unbound and their kinematics are largely dominated by turbulence, which is essential for ISS and ESEs. Matsuhara et al. (1997) detected several similar, small HLC structures close to 0954+658 and the Ursa Major complex. They found the gravitational pressure in the clouds of this region to be orders of magnitude smaller than the turbulent pressure deduced from the velocity width of the CO line. Since the external thermal pressure of the surrounding H I gas is also much smaller, the clouds can not be bound gravitationally or by external thermal pressure. Hence, magnetic and turbulent pressure dominates the dynamics of the clouds.

A further point in this context is the usually low LSR velocity of HLCs deduced from spectral line observations ($|v_{LSR}| \leq 20\,\mathrm{km/s}$). Such velocities are in good agreement with screen (but here transverse) velocities deduced from annual modulation studies (see e.g. Chapters 3–4) and time delay measurements. All this indicates, that HLCs are good candidates for the origin of scattering material

in front of IDVs. However, an ionized component is required to produce ISS and therefore has to be identified in these clouds.

7.8.1 PDRs and C II envelops around HLCs

0954+658 resides behind the outer western shell of the cloud in Figure 7.7. It seems quite plausible to think about an ionized shell or envelop at this position surrounding the cloud and acting as "shield" against the interstellar radiation field (ISRF). Molecular structures can only exist in shielded regions, where the FUV portion of the ISRF has been attenuated and thus photoelectric heating is much weaker compared to atomic regions. In this framework, the shielding occurs within the earlier mentioned PDRs forming the outer layers of molecular clouds. HLCs are so-called (isolated) translucent clouds, which span the range of visual extinctions $A_V \approx 1-5$ mag (van Dishoeck & Black 1988). With increasing depth and visual extinction, layers of H I, H_2, C II and C I do exist. At $A_V \sim 0.5$ mag carbon is mostly ionized, while at $A_V \sim 1$ mag C I becomes the most abundant carbon species (Ingalls 1999). Until this depth, CO photodissoziation dominates over formation, while deeper into the cloud ($A_V \sim 3$ mag) most of the carbon has combined to CO.

Direct evidence of such (low-density) PDRs around the surface of the HLCs in the Ursa Major complex is coming from [C II] emission line observations: The primary cooling process in the CNM and PDRs around the surface of molecular clouds is the 158μm emission (fine-structure) line transition of [C II] (e.g. Ingalls et al. 2002). In addition to their CO observations mentioned earlier, Matsuhara et al. (1997) performed a rocket-borne observation of the [C II] line and FIR continuum along a triangular path crossing several clouds in Ursa Major. The path along spectra were taken is shown in Figure 7.8. The positions of IDVs in the field are indicated. The most interesting position is their beam position three, (l, b)=(145.55°, 43.32°), since

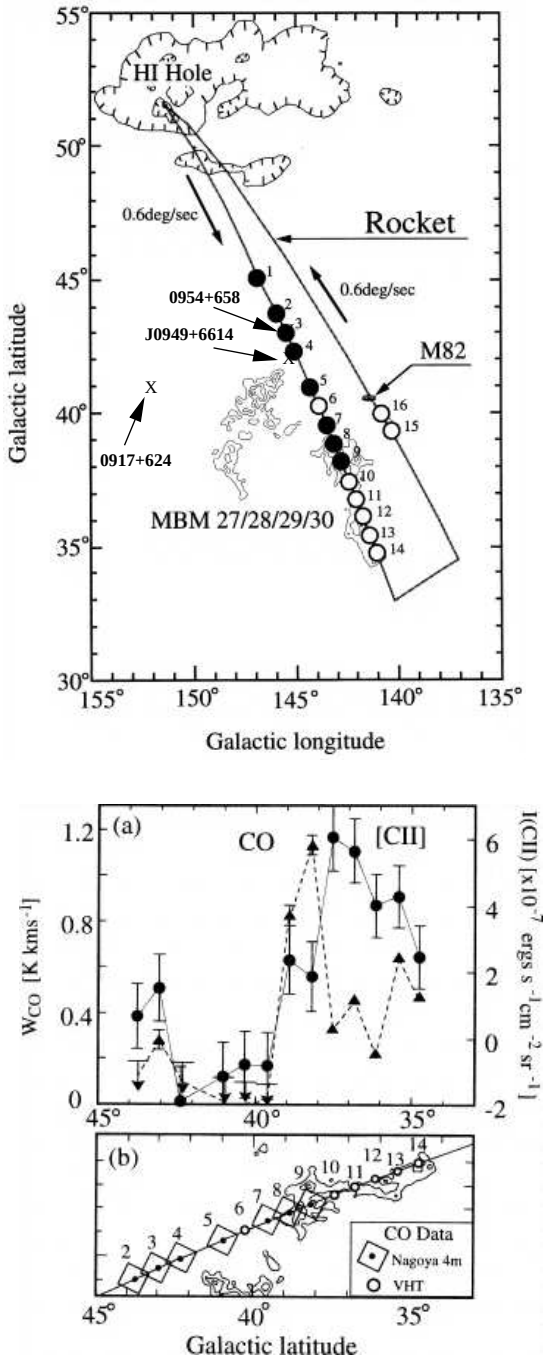

FIGURE 7.8— **Top:** Observation of the [C II] 158 μm emission line performed by Matsuhara et al. (1997) along a triangle path in Ursa Major. IDV source positions are superimposed. Spectra were taken at 16 positions, whereas beam position three covers the line of sight to 0954+658. **Bottom:** The excess [C II] line emission (filled circles) is displayed in panel (a) for beams 2–14, as shown in (b). Beam 3 indeed shows enhanced emission indicating the existance of ionized material in front of 0954+658.

the line of sight to 0954+658, (l, b)=(145.75°, 43.13°) is only 0.28° away. Thus, the position of 0954+658 was within the 36′ beam of their intrument. At the bottom of Figure 7.8 the excess [C II] line intensity along the path between beam position 2 and 14 is displayed. Indeed, beam position three shows excess [C II] emission of about $1.6\times10^{-7}\mathrm{ergs\,s^{-1}cm^{-2}sr^{-1}}$. The strongest emission (beams 8–14) is coming from regions containing the larger CO structures as seen in panel (b).

The authors propose the excess [C II] emission to originate from the PDRs formed around the molecular clouds distributued along the observed region and exclude other possible origins of the emission (e.g. the WIM or shock-compressed H I gas). Consequently, we have direct evidence for the ionized (carbon) material surrounding the detected CO cloud in front of 0954+658. These findings suggest an interpretation of this material and the connected free electrons as origin of the intraday variations seen in 0954+658. Additional support is coming from (i) the small cloud distance which fits to the observed variability time scale, and (ii) the growing picture of molecular clouds as highly inhomogeneous structures on a large range of spatial scales (e.g. Falgarone & Philips 1996, see below), where turbulence most likely plays an important rule (e.g. Falgarone 1996).

7.8.2 ESEs and Molecular Clouds

Furthermore, 0954+658 and the previous findings are of particular interest in the framework of ESEs. This source was the first object in which a variability pattern resembling an ESE was seen (Fiedler et al. 1987). Its interpretation as isolated inhomogeneity (plasma lens) intervening on the line of sight suggests small-scale structures of $\lesssim$0.4 AU in the scattering medium. Interestingly, Walker & Wardle (1998) more recently suggested a new model, where such events are caused by the "photoionized skin" of a cool, neutral AU-size cloud. Here, the ionized material at the surface is expected to be unbound and flow away as evaporated wind. Do such conditions prevail in HLCs and in particular, in the detected cloud of Figure 7.7 ?

Molecular clouds are nowdays believed to be fractal and clumpy in nature containing structures ranging from pc to sub-pc scales (e.g. Falgarone 1998). The 'dense clump model' deduced by Ingalls (1999) from detailed molecular cloud studies describes a HLC embedded in the CNM (HI) of the interface between the LB and adjacent bubbles. The H I/C II envelop surrounds the cloud on scales $\sim$5–10 pc. The HLC as seen in CO has a typical size of $\sim$1 pc and consists of many dense clumps of size $\sim$0.01 pc, which cluster together and contain CO. While the clumps are embedded in an interclump medium (ICM) which consists mostly of H_2 and C I, each clump (except the "shadowed" inner clumps) has its own PDR surface. In addition, there is evidence that the clumping on sub-pc scales extends down to even smaller scales. Absorption line studies towards extragalactic radio sources reveal clump structures on $\lesssim$10 AU (e.g. Marscher et al. 1993). A further interesting point is the occurrence of clump evaporation into the ICM. Ingalls (1999) found the ^{12}CO line across the HLC MBM 12 to be highly structured, since the main Gaussian intensity peaks break into sub-components. As shown in Figure 7.9, Ingalls (1999) explained such "P-Cygni" like shape by an expanding clump along the line of sight. Here, the cooler $\tau = 1$ surface of the optically thick clump is approaching and the warmer interior $\tau = 1$ surface is receding. This provides direct evidence that the CO clumps are expanding (or contracting, if the thermal structure is the reverse of that shown in Figure 7.9) into the surrounding ICM. Therefore it appears likely that the CO and C II gas and the ICM are well mixing and turbulence plays an important role.

Direct evidence for a similar situation in front of 0954+658 is coming from the spectral shape of the CO line across the cloud in Figure 7.7. At the position of 0954+658 a double peak structure of the CO line is seen with the primary component at a velocity of $-1.5\,\mathrm{km\,s^{-1}}$ and weaker secondary

component at a velocity of $-1.9\,\mathrm{km\,s^{-1}}$. This double structure is seen nearly over the entire cloud, while the relative intensity of the two peaks changes. The component separation of $0.4\,\mathrm{km\,s^{-1}}$ suggests an expansion (or contraction) of the gas with $\sim 0.2\,\mathrm{km\,s^{-1}}$ into the umbient medium. This value is comparable to those found by Ingalls (1999) for MBM 12.

Additional support for an ESE connection with CO clouds comes from the ESE source 0333+321 (NRAO 140). The source was earlier found to exhibit CO structures intervening on the line of sight as well (Bania et al. 1991). This increases the number of ESE sources with galactic foreground CO to two. In particular, X-ray absorption studies towards this quasar revealed clump structures of size $\lesssim 1\,\mathrm{AU}$ (Marscher 1988), which is in good agreement with the size of the proposed lens structures responsible for ESEs.

The details of a (possible) physical connection between the detected cloud and the ISS/ESEs in 0954+658 have to be investigated in further detail (which is beyond the scope of this thesis). However, the findings presented here clearly suggest that the scattering processes are likely be produced by the material confined to the detected CO cloud. One could, for example, propose a scenario, where the AU-sized clouds discussed for ESEs by Walker & Wardle (1998) are the same CO clumps as discussed here, and which pass/expand across the compact, milli-arcsecond structure of the background source. The mixture of ICM and C II (and the related free electrons) at the surface of the evaporating CO clumps could than produce a similar electron density profile as proposed by Walker & Wardle.

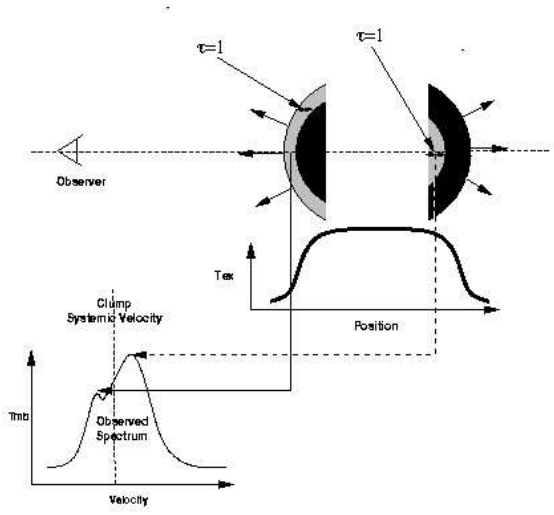

FIGURE 7.9— Model of an expanding clump proposed by Ingalls (1999). The two sides of a clump are separating, while the approaching $\tau = 1$ surface of the CO gas is cooler than the receding, interior $\tau = 1$ surface. The resuling CO spectrum exhibits the structure shown at the bottom left.

VLBI observations of 0954+658 reveal a compact core-jet source with three strong components of sizes 0.1–0.3 mas in the innermost core region (Gabudzda et al. 2000b). Assuming one of these components was focused/defocused during the ESE event in 1981 (e.g. Clegg et al. 1998), a rough comparsion with the previous findings can be done. An angular size of 0.15 mas corresponds to a physical size of $\sim 2\times10^6$ km or 0.02 AU at a distance of 100 pc. Assuming similar (transverse) velocities of the cloud structures as deduced above ($0.2\,\mathrm{km\,s^{-1}}$), such spatial scale could be traversed in about 130 days – in good agreement with the total duration of the ESE event observed in 1981.

7.8.3 A Statistical Approach

In order to identify CO clouds as general origin of the scattering material responsible for ISS, galactic CO surveys provide additional information. Although most of the CO surveys are not sensitive enough to detect smaller molecular structures (as in the case of 0954+658), a more statistical comparsion of known HLC and IDV positions can provide further evidence for a possible connection.

For this reason, we compiled source samples for (i) all IDV source positions known so far and (ii) all HLC positions known from the literature. In addition, two control samples were conducted containing (i) non-IDV (type 0) sources and (ii) random positions on the sky. The list of all known IDV positions was compiled from the work of Heeschen et al. (1987), Quirrenbach (1989), Kraus (1999), Quirren-

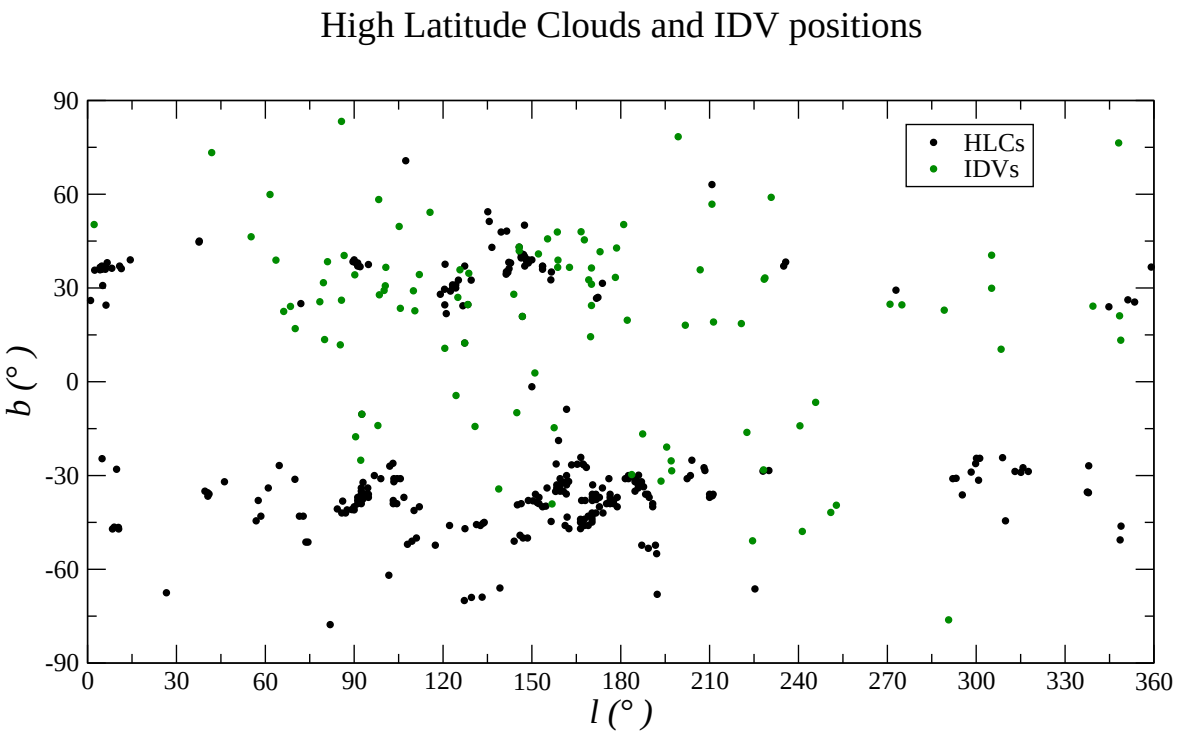

FIGURE 7.10— Galactic distribution of IDVs and HLC positions. Both distributions are rather non-uniform with clustering mainly within the longitude range $l \sim 60° - 210°$. In addition, individual IDV positions or "groups" of IDVs often appear to be close to a cloud, cloud complexes or in regions of higher cloud density.

bach et al. (2000), Kedziora-Chudczer et al. (2001) and Kraus et al. (2003). In addition, the first detections of the Micro-Arcsecond Scintillation-Induced Variability Survey (MASIV, Lovell et al. 2003) were included as well as the new IDV sources presented in Chapter 4. This yields a source list with a total of 101 IDV positions in the nothern and southern galactic hemisphere detected so far. The complete list is given in Appendix D. A total of 293 known HLC positions was extracted from the work of Magnani et al. (1996), Hartmann et al. (1998), Magnani et al. (2000) and Bhatt (2000). The CO detections presented in this thesis were included as well. The sample of 101 non-IDV sources consists of compact (flat-spectrum) sources, which were examined for IDV without significant detection (type 0 sources) in the work of the earlier mentioned authors.

Figure 7.10 diplays the galactic distributions of IDVs with HLC positions superimposed. The HLC distribution is rather non-uniform with clustering in both northern and southern galactic latitudes. As seen from the histograms shown in Figure 7.11, clustering occurs mainly in two longitude and latitude ranges. The HLCs were found mainly at two distinct latitude ranges: $b \sim 15°–45°$ and $b \sim -15°–60°$ with a much higher number of clouds detected at southern latitudes. A further prominent feature is seen in the longitude range $l \sim 90°–210°$, which contains already more than 70 % of the total number of clouds. It appears as an elliptical shell structure extending from the northern to southern hemisphere[2]. Here, the peak cloud density oc-

[2]This structure might be produced by supernovae explosions in the Per-OB association as suggested by Bhatt (2000).

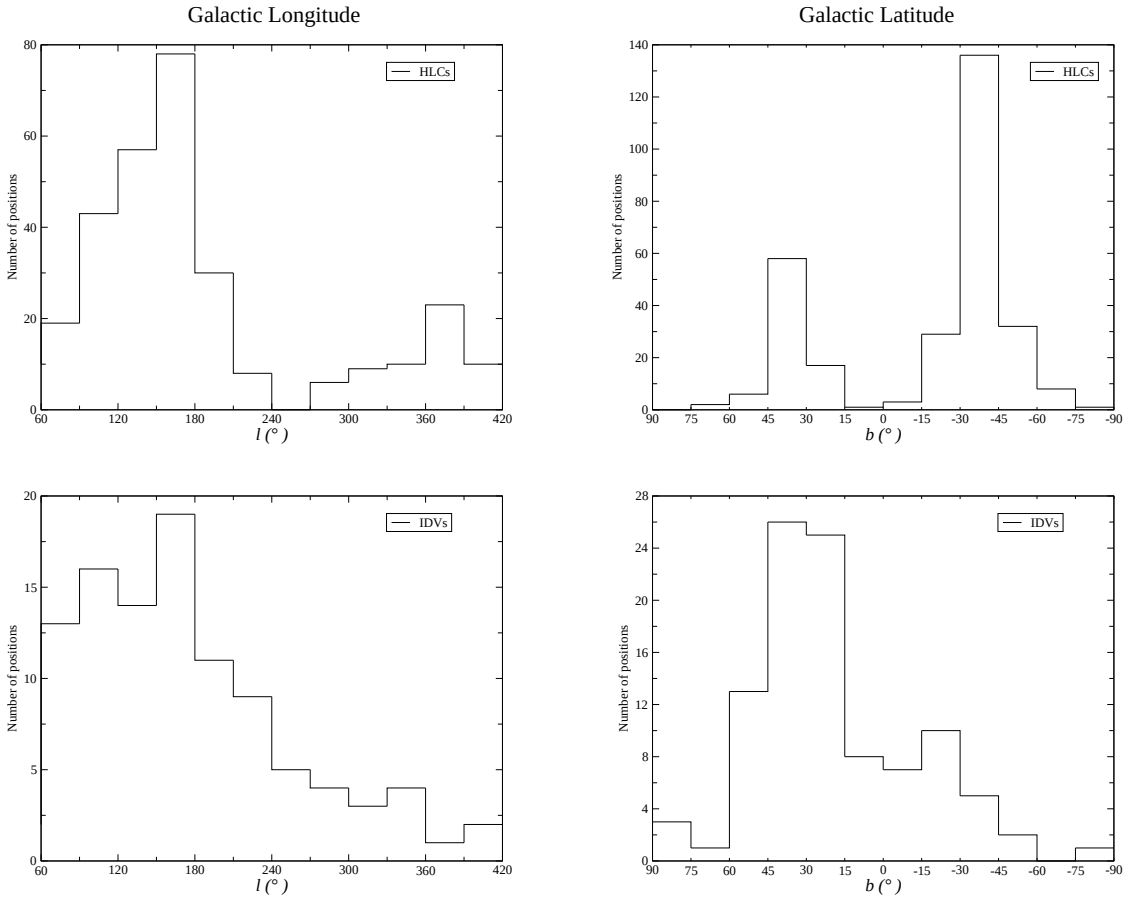

FIGURE 7.11— Histograms showing the distributions of Galactic longitudes (**left**) and Galactic latitudes (**right**) of high latitude molecular clouds (top) and IDV positions (bottom). The clustering seen in both cases is similar (see text).

curs in the range of $l \sim 150°$–$180°$. However, a second "cluster" of HLCs is seen in the longitude range $l \sim 270°$–$60°$, but is relatively poor in population compared to the first region.

The spatial distribution of IDV positions is non-uniform as well. Their clustering occurs mainly in the longitude range $l \sim 60°$–$240°$, similar to the HLCs. This region contains about 80 % of the total number of IDVs and, in particular, the peak in the IDV distribution coincides with the peak in the HLC population ($l \sim 150°$–$180°$). Towards the remaining longitude ranges the number of IDVs decreases and is much lower, similar to what is seen for the HLCs. In addition, IDV sources were detected more often in the northern hemisphere. The peak occures in the latitude range $b \sim 15°$–$45°$, which again coincides with the distribution of the HLCs at northern galactic latitudes. Apart from the overall distribution, individual IDV positions or "groups" of IDVs often appear to be close to a cloud, cloud complexes or in regions of higher cloud density (compare Figure 7.10).

In order to quantify these findings in a more statistical analysis, we examined each of the 101 IDV sources in 0.5°-(circular) bins around their position for the existance of a HLC. The same was done for the control samples (101 type 0 sources and random positions on the sky). While at the top of Figure 7.12 the galactic distributions of the source samples are displayed, the results are summarized in the histograms shown at the bottom. It

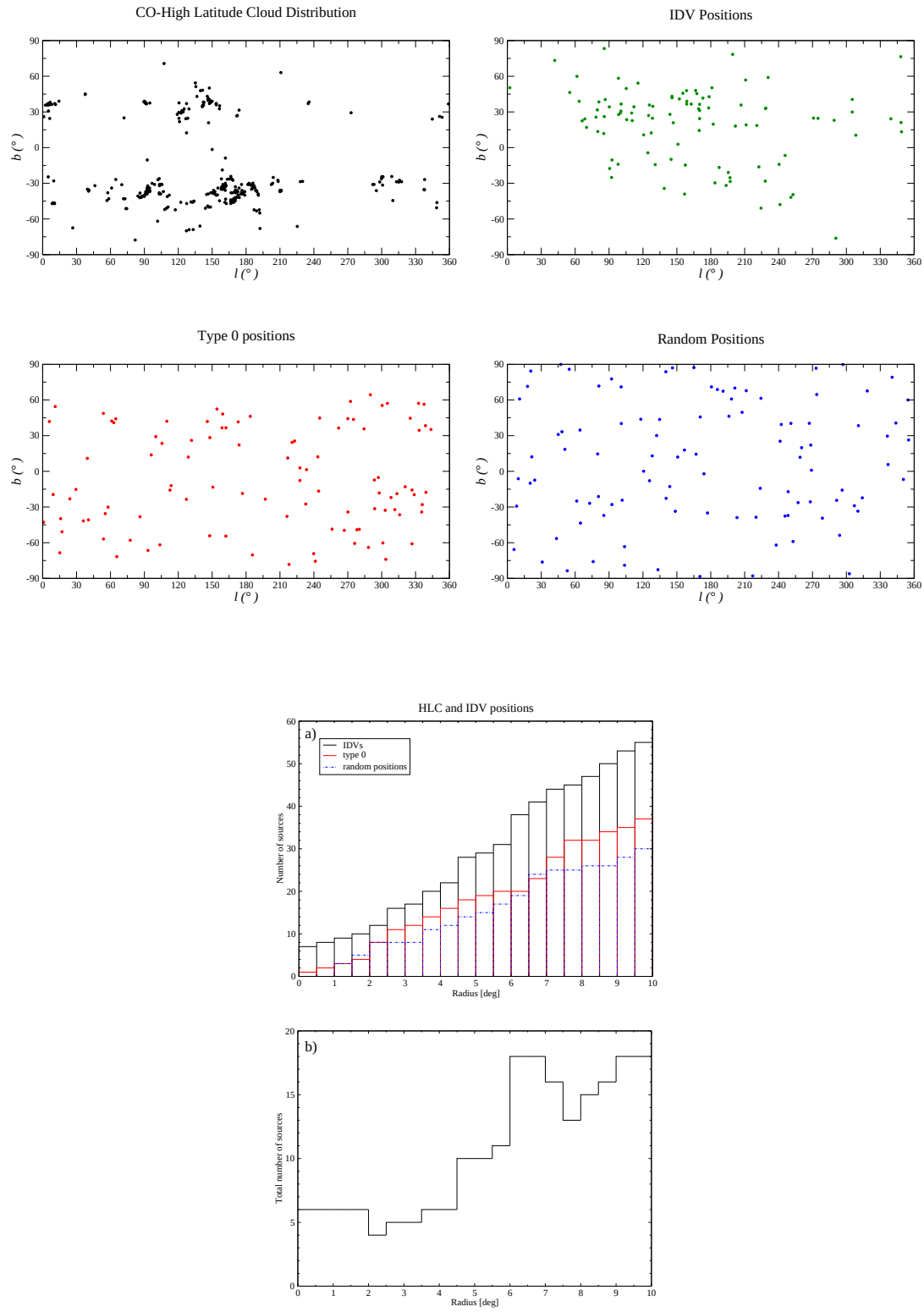

FIGURE 7.12— **Top:** Galactic distributions of the source samples used in the statistical approach presented here. **Bottom:** Results of the analysis (see text).

turns out, that in 55 cases of the 101 IDV positions (54.5 %) we can find at least one HLC (often much more) within a radius of 10° around their position. In comparsion, only 30 random positions (29.7 %) and 37 type 0 sources (36.6 %) have (at least) one HLC located within a radius of 10° around their position. The general behavior of random positions and type 0 sources appears similar. It seems that systematically more IDV sources exhibit a CO cloud within a certain radius than sources of the control samples. This can be seen at the bottom of Figure 7.12, where the results for IDV and type 0 positions are shown in a differential representation. Within a radius of 4.5° the difference in number of IDV sources with a cloud compared to those of type 0 sources keeps about constant at six. This reflects mainly the IDV positions with direct CO detection (compare Table 7.1). Beyond a radius of 4.5°, the difference in number increases in favour of IDV positions to 18 at a radius of 6°. After a decrease and subsequent increase this value is reached again at a radius of 10°.

Statistical investigations of such limited samples are difficult and several biases influence the statistical approach presented here, e.g:

- limited IDV surveys up to now (exception: ATCA survey of Kedziora-Chudczer et al. 2001): small and biased samples, which were restricted to the strongest (flat-spectrum) sources and often limited to certain regions on the sky
- the observation/detection of type 0 sources often occurs in the same regions where IDVs are observed
- type 0 sources can show CO (or more general, scattering material), but are not variable due to larger source sizes
- unevely or less sampled CO survey data towards higher latitudes and certain regions on the sky
- missing (smaller) CO structures due to poor sensitivity and sampling of the CO surveys

However, the observed trend provides evidence that IDV sources are more often found in regions with nearby HLCs. This may support the idea of a possible connection between IDV and HLCs. With the complete, large scale MASIV survey in hand, such statistical investigations can be improved by other statistical methods (e.g. two-point correlation analysis) and will shed further light on the possible link between both classes of objects.

7.9 Connection of IDV and ESE Positions with Radio Loop Structures?

In the same manner as done for the the HLCs, a possible connection of IDV and ESE positions with the radio loop structures can be investigated. The existence of radio spurs and ridges with enhanced continuum emission is well known since decades. Intensive studies since then have shown that these spurs often join to small and large circles, whose centres lie at intermediate latitudes (e.g. Berkhuijsen et al. 1971, Salter 1983). Among the pronounced and well known radio loops I to IV, additional loop structures were deduced from new radio continuum survey data (Reich & Reich 1986). These are known to day as Loop V, Loop VI, and their possible combination into one feature, the Loop V+VI or Loop V+VI′ (e.g. Milogradov-Turin & Urosević 1997, Figure 7.13). The geometry of these ISM structures was found by (least-square) fitting the main ridge lines of their maximum brigthness distribution on the sky (compare Figure 7.13). In the literature, the loop geometry is usually given as the mean center position of the circle in galactic coordinates and its mean radius. Since the loops often deviate strongly from a circle, the exact galactic coordinates of the points on their main ridge lines can not be calculated without the detailed knowledge of the fit parameters. For that reason, the comparsion of source positions and main ridge lines presented here will be more qualitatively.

7.9.1 ESEs and Radio Loops

A possible connection between ESE sources and radio loop structures was investigated already by Romani (1988) and Fiedler et al. (1994a, b). Figure 7.13 displays a reproduction of the plot given in Berkhuijsen et al. (1971) showing the geometry of galactic radio loops. The black crosses mark the measured rigde positions (of peak radio continuum brigthness) used in the fitting procedure of the circles. Superimposed are the new Loop structures (Loop V, V+VI, V+VI$'$) calculated by Milogradov-Turin & Urosević (1997). The red crosses mark the positions of the sources, which so far have shown an ESE. As outlined already by Fiedler et al. (1994b), a possible association of their 9 ESE positions with the foreground Loops I and III is evident. Their detailed statistical analysis with a total of about 200 sources revealed a close correlation between the spatial distribution of their 9 ESE source positions and the radio loop structures. In particular, the fact that 50 % of the source positions lie nearly exactly on the main ridge line of the two galactic structures makes such correlation obvious.

In addition to the nine sources examined so far, a further source, 1741−038, has shown an ESE event (Clegg, Fey, & Fiedler 1996). Its position, (l, b)=(21.6°, 13.1°), is superimposed on Figure 7.13 and again, a good correlation with Loop I is evident. Until now, the ESE source 1611+343 at (l, b)=(55.2°, 46.4°) deviated from a possible connection to the radio loops, since it is located about 25° away from Loop I and more than 30° from Loop III on the sky (Fiedler et al. 1994b). With the advent of the new loop strutures, Loop V and V+VI as plotted in Figure 7.13, also this source appears to be located close to the main ridge line of a radio loop: Loop V+VI. This underlines a possible connection between ESEs and radio loop structures.

7.9.2 IDVs and Radio Loops

Interestingly, 5 out of the 10 ESE sources were observed to exhibit IDV as well. The ESE source 1741−038 at the edge of Loop I is known to show long-term refractive scintillation on a time scale of ∼ 10 days (Hjellming & Narayan 1986) as well. The distance to Loop I is estimated to be ∼ 200 pc (Berkhuijsen et al. 1971), which fits nicely with the observed (longer) variability time scale of this source. Thus, Hjellming & Narayan (1986) suggest the origin of the observed refractive scattering to be Loop I. The remaining 4 ESE sources have not been examined for IDV so far. Thus, at least 60 % of the known ESE sources can be identified also with "normal" interstellar scintillation effects. If indeed the ESEs are the result of enhanced scattering in the galactic loop structures (e.g. in their turbulent 'interaction zones'), the observed IDV in these sources is likely to be produced by the same scattering material.

Already Heeschen et al. (1987) suggested a possible connection of their first IDV sources with local galactic features. Their limited IDV sample of 15 sources was confined to a small region on the sky with $100° \leq l \leq 153°$, $+28° \leq b \leq +41°$ – a region containing complex H I structures and the radio continuum Loop III (Figure 7 in their paper). With the present, much larger number of IDV sources in hand, this possible connection can be re-analysed. Figure 7.14 displays again the geometry of the radio loop structures, now with the 101 IDV positions superimposed. As shown earlier (Figures 7.11 and 7.12), the main clustering of (presently known) IDV positions occurs within the galactic longitude range $60° \lesssim l \lesssim 180°$ and latitude range $-30° \lesssim b \lesssim +60°$. This is the region on the sky, which contains the radio Loop III and the H I structures mentioned earlier. About 60 % of the presently known 101 IDV sources can be found in this region on the sky suggesting a similar conclusion as given by Heeschen et al. (1987). In particular (as outlined in Section 7.6, see also Figure 7.5), several IDV positions are distributed along the Loop III foreground structure or even lie on its main ridge line. The same is true for a few IDV positions distributed along other radio loops: Loop I, Loop II and Loop IV. Taking into account

the new loop structures, Loop V and V+VI, several IDVs previously found in regions of "empty sky" appear to be distributed along or close to these structures. Other prominent ISM features as the Gum nebula, the Orion-Eridanus bubble or the Cygnus loop (indicated as dashed circles in Figure 7.14) cover (at least partly) additional regions with a higher number of IDV positions.

In summary, the re-analysis of a possible connection between IDV positions and galactic foreground features with a much larger number of know IDV sources suggests a similar conclusion as proposed earlier by Heeschen et al. (1987). Due to the afore mentioned problems (limited and biased IDV sample, poor knowledge of the ridge line positions of the loops etc.), a detailed statistical analysis was not possible. Consequently, the possibility of a chance occurence can not be completely ruled out.

7.10 Summary and Conclusions

A new approach was presented, which examined the possibility of a direct detection of the scattering material producing ISS and ESEs in compact, extragalactic radio sources. The clear need for additional information on the scattering regions in view of present ISS and ESE models makes spectral line observations towards these sources "attractive".

In view of the multi-phase ISM, the WIM or ELDWIM is likely to be responsible for the scintillation of IDVs. Furthermore, the structure of the local ISM suggests the turbulent outer shells or interface regions of the LB and adjacent bubbles to provide regions of enhanced scattering. The work presented here provides evidence for more discrete ISM features to be connected with the observed scattering effects: While first RRL observations towards IDVs did not reveal a clear detection, first ^{12}CO(2−1) observations led to the detection of a molecular cloud in front of 0954+658. Several findings suggest a connection between the ISS/ESEs seen in this source and the material confined to the detected cloud structure: (i) the cloud distance of about 100 pc is in good agreement with the expected distance with regard to the ISS time scale observed in Chapter 4, (ii) direct evidence for the existence of a PDR and ionized material along the line of sight to 0954+658 comes from 158μm [C II] emission line observations, (iii) the turbulent, fractal and clumpy nature of HLCs (e.g. the 'dense clump model') provides the physical conditions for ISS and ESEs, (iv) such conditions are supported by the observed "P-Cygny" profiles across the cloud in front of 0954+658. Here, clump evaporation is of particular interest in the framework of the observed ESEs and the new model proposed by Walker & Wardle (1998).

Evidence for a general HLC origin of IDV/ESEs is coming from CO (follow up) observations and CO detections deduced from the literature. Until now, six IDV sources were found to exhibit CO intervening on the line of sight. A more statistical analysis revealed more often IDV positions close to HLCs compared to e.g. non-IDV sources. In addition, IDVs appear to be observed more frequently behind regions of local, (large-scale) ISM structures so far. If indeed the nearby HLCs represent the molecular component of the compressed CNM gas at the interaction zones between LB and adjacent bubbles (e.g. Loop III), one might expect such additional correlation. However, the details of a possible connection between scattering and HLCs have to be investigated further.

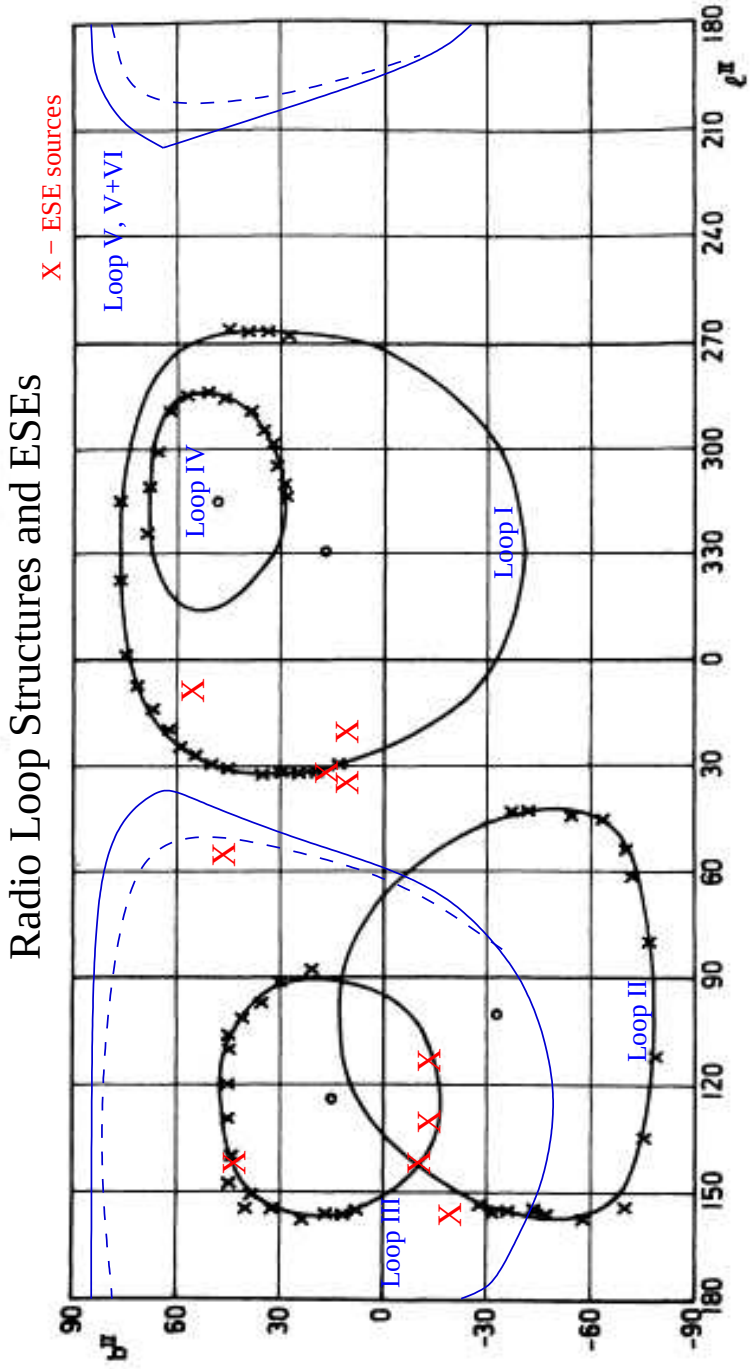

FIGURE 7.13— Galactic geometry of the prominent radio loop structures as shown by Berkhuijsen et al. (1971). Superimposed are the new Loop V, V+VI, V+VI′) determined by Milogradov-Turin & Urosević (1997). The association of ESE source positions and loop structures is evident.

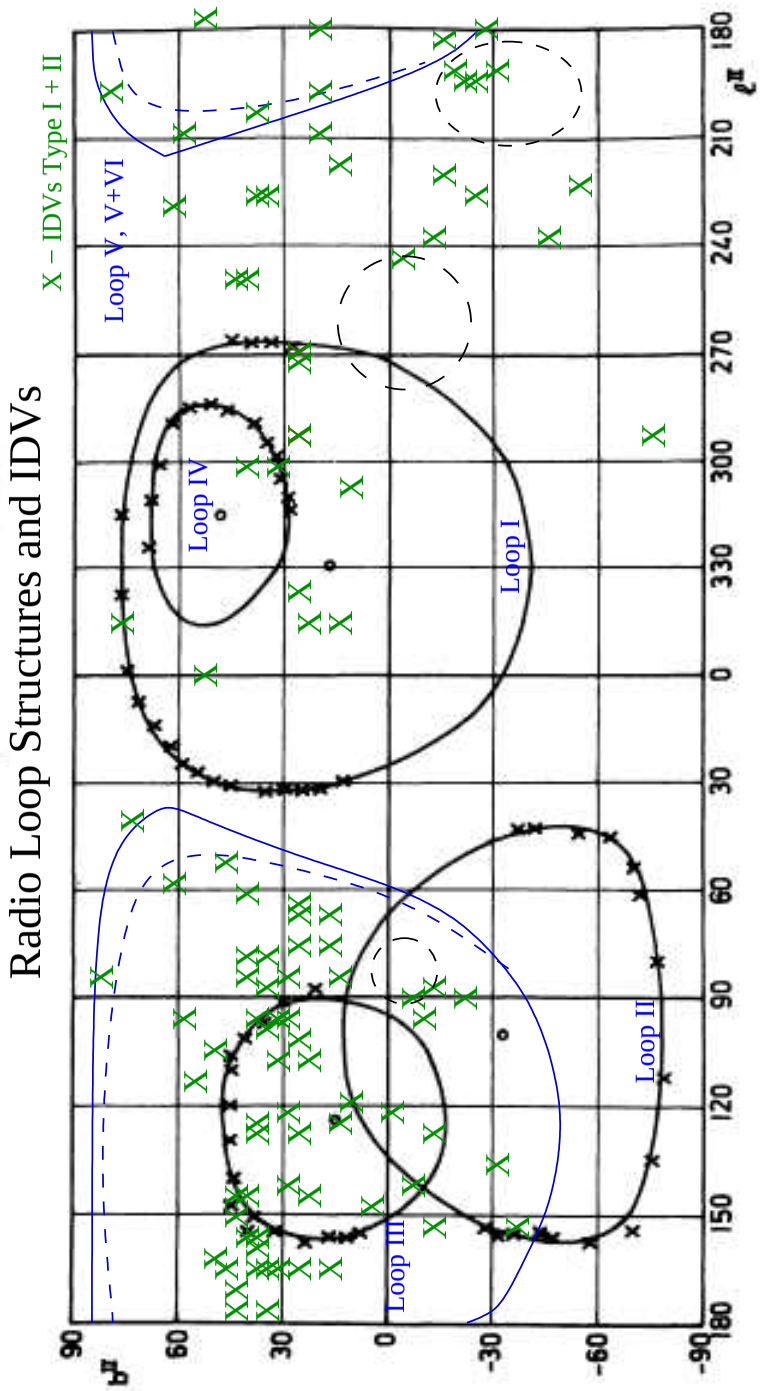

FIGURE 7.14— Same as Figure 7.13, but with all known IDV source positions superimposed. Additional ISM structures are indicated by dashed circles (see text).

8

Summary and Outlook

This thesis is an attempt to shed further light upon the phenomenon of short-term radio variations seen in IDV Blazar cores. To do so, different new observational approaches have been started with particular emphasis on the connected scattering material in the local ISM. The major results which were obtained from each of these approaches are summarized below. Finally, open questions will be discussed and suggestions will be made for future IDV research.

8.1 Detailed Summary of the Results

8.1.1 Seasonal Cycles and Intrinsic Source Evolution

The annual modulation of IDV time scales in the extreme IDV sources recently attracted attention and strongly suggest an ISS origin of the variations seen in these sources. Thus, a larger monitoring project has been started in order to detect similar cycles in "normal" IDV sources. The Effelsberg 4.85 GHz monitoring over a period of more than two years revealed:

- Normal IDV sources are strongly effected by their intrinsic complex structure and long-term activity. The latter can dramatically influence the IDV characteristics of these sources. In turn, this makes the detection of annual cycles and thus the confirmation of an ISS origin of the variations a difficult task.

- The most promising new candidate for a seasonal dependence of the variability time scale is the BL Lac object 0954+658. Here, intrinsic source evolution appears to play a minor rule and the data is in overall agreement with the predictions of the annual modulation model. However, the deduced LSR velocity of the screen in the range of $V_\alpha = -25\,\mathrm{km\,s^{-1}}$ and $V_\delta = 20\,\mathrm{km\,s^{-1}}$ is high.

- The situation appears more complicated for the BL Lac object 0716+714. The variable modulation index and its correlation with other source parameters implies a strong influence of intrinsic source evolution. Consequently, no clear, unambiguous annual cycle in the variability time scale has been detected.

- The seasonal cycle in 0917+624 proposed earlier could not be confirmed. The source has shown a dramatic change in its IDV properties and only extremely quenched variations were observed during the last 2.5 years. The latter strongly contradicts the model predictions for annual modulations. We propose several scenarios in order to explain the unusual behavior of 0917+624. While dramatic changes in the properties of the screen can not be ruled out, intrinsic changes in the (sub-) mas structure of the source (e.g. the ejection of a new jet component and thus temporarily larger angular size) could produce extremely quenched scattering.

- New VLBI observations of this source confirm "the extremely quenched scatter-

ing scenario" for the first period of unusual IDV in September 1998 in contrast to its previous interpretation as a seasonal cycle. A new jet component with an extrapolated ejection date shortly before the present period of low variations could be detected. However, the long-lived 2.5 years non-variability can only be explained by the ejection of further new components. In addition, the non-detection of longer variability time scales between 2000 and 2002 suggests an additional effect of decreasing total flux density contained in the scintillating component.

8.1.2 Search for an Intrinsic Contribution

Due to the frequency dependence of interstellar scintillation, mm- and sub-mm IDV monitoring plays a key-role in present IDV studies. Our attempt to detect an intrinsic contribution to the IDV pattern using high frequency observations revealed:

- none of the three IDV sources observed with Effelsberg at 32 GHz show strong evidence for the existence of intraday variability. In particular, the strong up-turn in the $m-\nu$ distribution of 0716+714 observed in the past could not be confirmed. Instead, our high frequency results are in better agreement with a weak (quenched) scintillation scenario.

- Short multi-frequency observations of the rapid scintillator J1819+3845 could subsequently be explained in terms of ISS. Here, ISS modeling yields the best agreement for weak scattering of a point source ($\sim$ 30 μas at 5 GHz) due to enhanced turbulence in the local bubble wall at a distance of about 15 pc. Due to the changing radio spectrum of the source, we propose intrinsic changes in its radio structure and thus changing variability properties in the near future similar to PKS 0405−385 or 0917+624.

8.1.3 The related Interstellar Medium

We examined the possibility of a direct detection of the scattering medium in the foreground of intraday variables and Extreme Scattering Event (ESE) sources. The clear need for additional information on the scattering material in view of ISS/ESE modeling and a direct confirmation of an extrinsic origin of IDV, outlines the importance of spectral line observations towards these sources. Our main findings can be summarized as follows:

- The investigation of the various components of the (local) ISM identifies the (Extended Low-Density) Warm Ionized Medium (WIM) or more local ($\lesssim$ a few hundred pc), discrete structures to be connected with IDV and ESEs (the Local Bubble wall, adjacent bubble/loop structures and their turbulent interaction zones).

- Observational evidence for the material intervening the line of sight to IDV sources is coming from larger surveys of e.g. dust, CO and the radio continuum. Here, often good correlations are seen between IDV positions and enhanced emission.

- Neither the H166α nor the H167α line could be detected in first radio recombination line observations towards a few IDV sources.

- First ^{12}CO (2−1) observations led to the detection of a high latitude molecular cloud (HLC) in front of 0954+658. The CO spectra across the cloud show a double peak sub-structure suggesting clump evaporation on the line of sight with 0.2 km s^{-1}.

- Several findings suggest as cause for the observed scattering effects (IDV and ESEs) the ionized C II component provided by the photodissociation region surrounding the detected cloud.

- High latitude molecular clouds, which most likely represent the molecular component of the compressed cold neutral gas at the interface regions between the Local Bubble and adjacent bubbles, appear to be generally attractive as scattering regions (e.g. small distance in good agreement with IDV time scales; turbulent, fractal and clumpy nature; ionized material due to photodissociation etc.). Consequently, we propose the possibility of a general HLC origin of IDV and ESEs, which is supported by follow-up CO observations and the results of a more statistical analysis.

8.2 Open Questions and Future Projects

Similar to the previous findings of 0917+624, the annual cycle in 0954+658 proposed here is based upon one data point only. New, more frequent and regularly sampled observations, in particular between the highly interesting period May and October, are essential to confirm this effect.

However, an important conclusion is that the mas/μas structure of an IDV source at the time of observation is important and appears to strongly influence its IDV characteristics. Similar to the episodic IDV seen in PKS 0405+385, the long duty cycle of IDV in 0917+624 (of more than a decade) has stopped at least two times. The present 2.5 years absent of IDV in this source outlines that IDV is not a "steady-state" situation. The VLBI study of the source supports this idea and in particular, suggests a close relation between intrinsic structural changes on VLBI scales, flux density outbursts and the appearance of IDV. Thus, the IDV properties of a radio source are most likely a function of complexity and activity/changes in its inner structure. Several new questions appear which have to be investigated by new IDV and VLBI monitoring of 0917+624 as well as other sources. An important issue one has to address is why intrinsic source evolution often plays a minor role (as seen e.g. in 0716+714 and 0954+658), whereas it can occasionally be dramatic as seen in the extreme case of 0917+624 ? What is the rate of such events ? Can this behavior be related to the kind of object (BL Lac - quasar) ? Are there different mechanisms of creating compact components in these sources ? The amount of source total flux contained in the scintillating component appears to be an important parameter. The compact component has to be bright in order to recognize the source as (ISS induced) IDV source. Compared to the first period of inactivity in 0917+624 (September 1998), this situation may have changed during the present 2.5 years of quiescence since longer variability time scales are not observed. This gives rise to the idea of different formation mechanisms of compact structures in relativistic jets. Long-lived IDV could be produced by components, where their dissipated energy is continously replenished to keep the flux density about constant over longer time periods. On the other hand, short-lived IDV could be the result of more "explosive events" without (or with less) additional energy input after component formation.

Ongoing VLBI, flux density and IDV monitoring projects for 0917+624 and other sources are essential to clarify the situation. Here, the study of the BL Lac 0716+714 may be of particular interest, since this source is known to be one of the most active objects in flux density evolution, IDV as well as on VLBI scales.

A direct access to the ionized (C II) component of the ISM clouds must be addressed to future instruments (e.g. SOFIA). However, carbon radio recombination line observations of PDRs were done in a few cases (e.g. Sorochenko & Tsivilev 2000) and can be combined with [C II] 158 μm emission line observations to constrain the physical conditions in these regions. The general existence of CO clouds in the line of sight to IDV/ESE sources can be tested by new CO observations of a large sample of sources. Such project has been proposed and will be performed in the near

future. Maps with high spatial and velocity resolution (e.g. mm-Interferometry) or molecular absorption line studies as performed by e.g. Lucas & Liszt (1993) can yield further information about the milli-parsec scale structure in these clouds. Using this approach, a possible relation to scattering effects can be investigated in more detail.

Independent of the ISM features connected with interstellar scattering, a "rotation measure survey" towards IDV positions could open direct access to the electron densities of the scattering medium. In addition, interstellar scattering should produce image wander in VLBI images of radio sources which is directly related to physical parameters of the scattering medium (e.g. C_n^2). The astrometric position accuracy of present VLBI phase-referencing techniques of order $\sim 10\,\mu$as may open the possibility to obtain important new constraints on the scattering medium.

If indeed a HLC origin of IDV/ESEs can be established, this would be of great interest also for the study of molecular clouds (e.g. cloud/clump formation and dynamics). For example, rapid extreme scattering events would then imply structures in these clouds on scales ~ 0.04 AU, about two orders of magnitude smaller than presently assumed. Among the appearance of turbulence, the detection of anisotropy in the seasonal cycles of IDVs would consequently imply anisotropic structures in molecular clouds. This would have important implications for the magnetic field configuration in these clouds.

With regard to the "traditional" question of an extrinsic/intrinsic origin of IDV, the overall findings presented in this thesis are in better agreement with an extrinsic explanation. This further supports the importance of ISS. Both, time delay measurements and the detection of annual cycles have proven beyond doubt that the variability in the three extreme IDV sources are due to interstellar scintillation. The situation for normal IDV sources, as studied here, is different, because these methods appear to be limited to the most rapid variable and intrinsically stable sources. Thus, interstellar scintillation is much more difficult to be proven directly for normal IDV sources. Since this is indispensable to establish an ISS origin of IDV in general, other methods have to clarify the situation. Here, spectral line observations may open new possibilities. In addition, new (and improved) high frequency studies have to finally demonstrate whether an intrinsic contribution to the IDV pattern is present or not.

It is hoped that this thesis improves the understanding of IDV in compact Blazar cores in a small way and provides new input for future projects aiming a complete and consistent explanation for this fascinating phenomenon.

Appendices A–C

A

Light Curves obtained during the 4.85 GHz Monitoring

The final total-power light curves of all 28 observing sessions obtained between 2000 and 2002 are given here. The left scale of each plot represents the flux density in Jansky, while the right scale gives the normalized flux. Note that their ranges differ from plot to plot. The header of each light curve consist of source name and the mean value of the flux density plus or minus the rms at the given epoch.

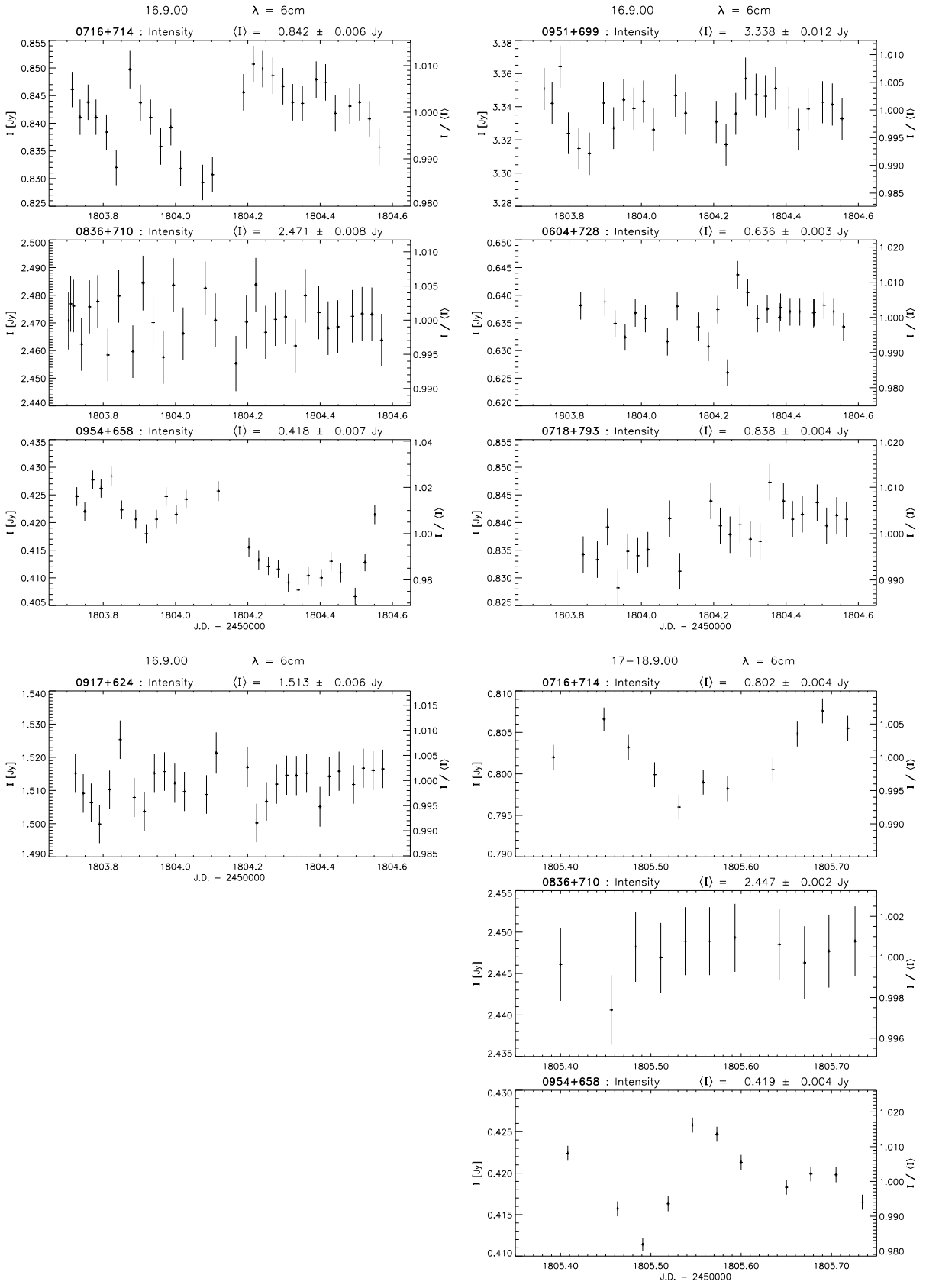

FIGURE A.1— Light curves of epoch 1 and 2: 16. September 2000 and 17-18. September 2000.

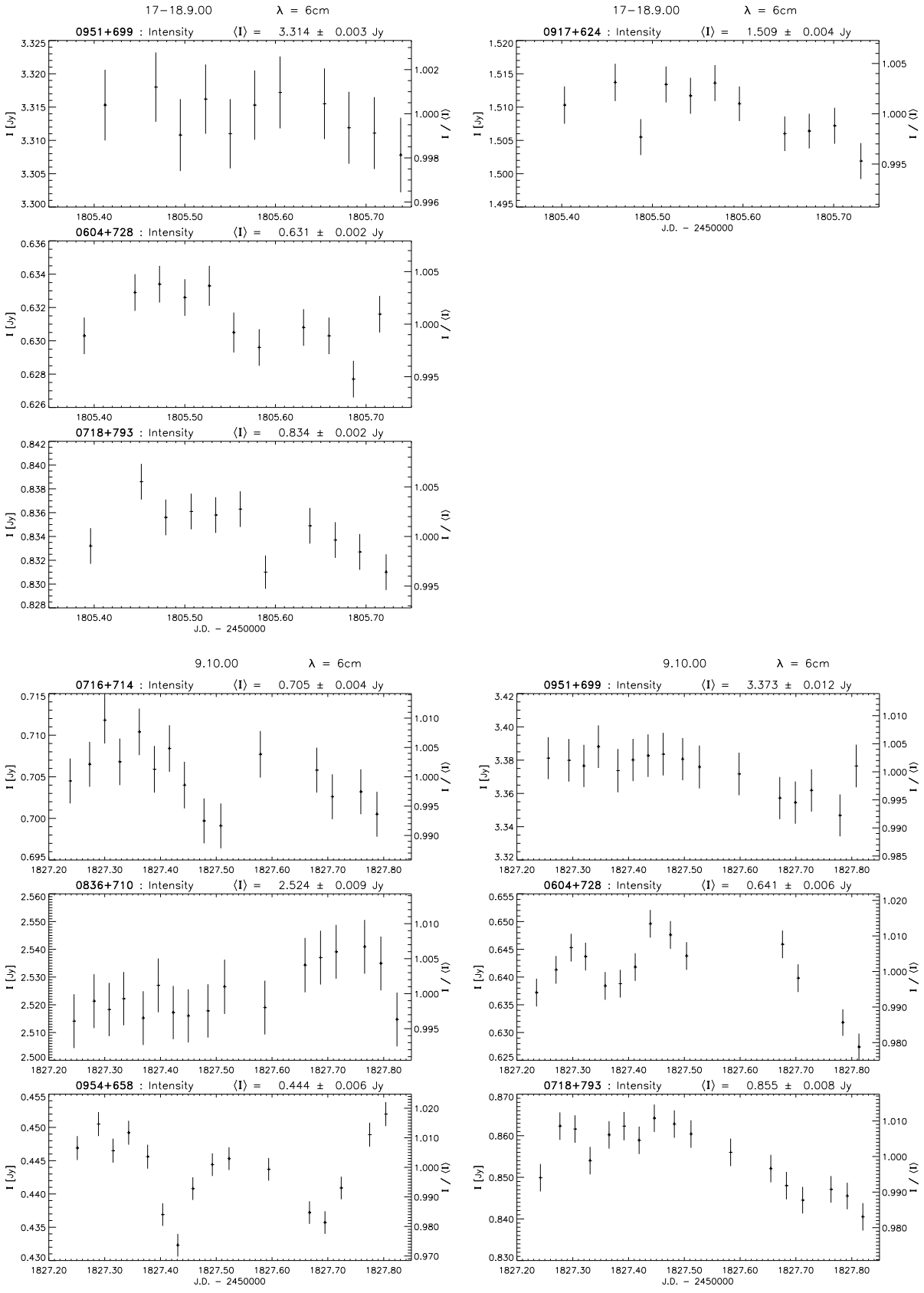

FIGURE A.2— Light curves of epoch 2 (cont.) and 3: 17-18. September 2000 and 9. October 2000

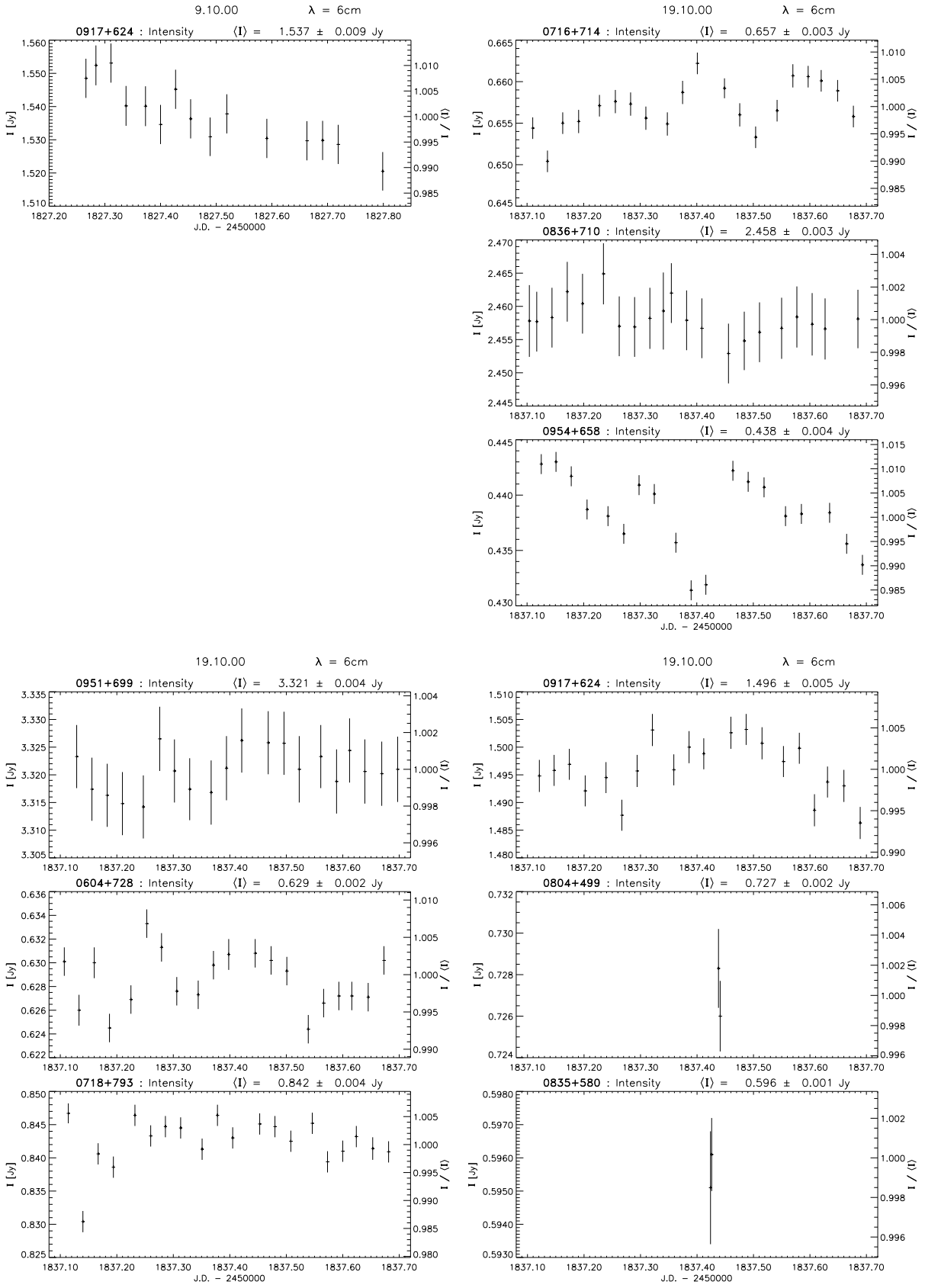

FIGURE A.3— Light curves of epoch 3 (cont.) and 4: 9. October 2000 and 19. October 2000.

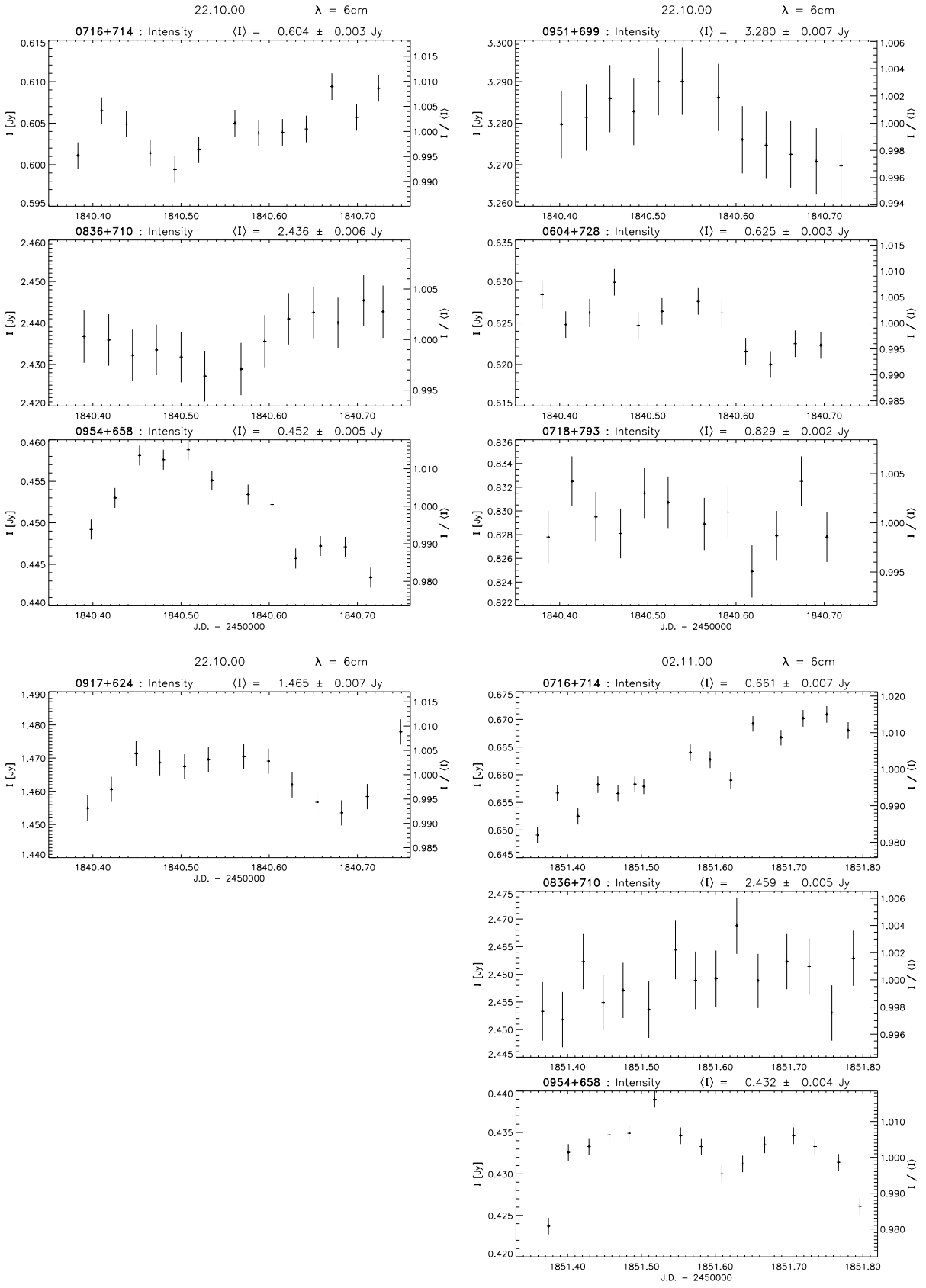

FIGURE A.4— Light curves of epoch 5 and 6: 22. October 2000 and 2. November 2000.

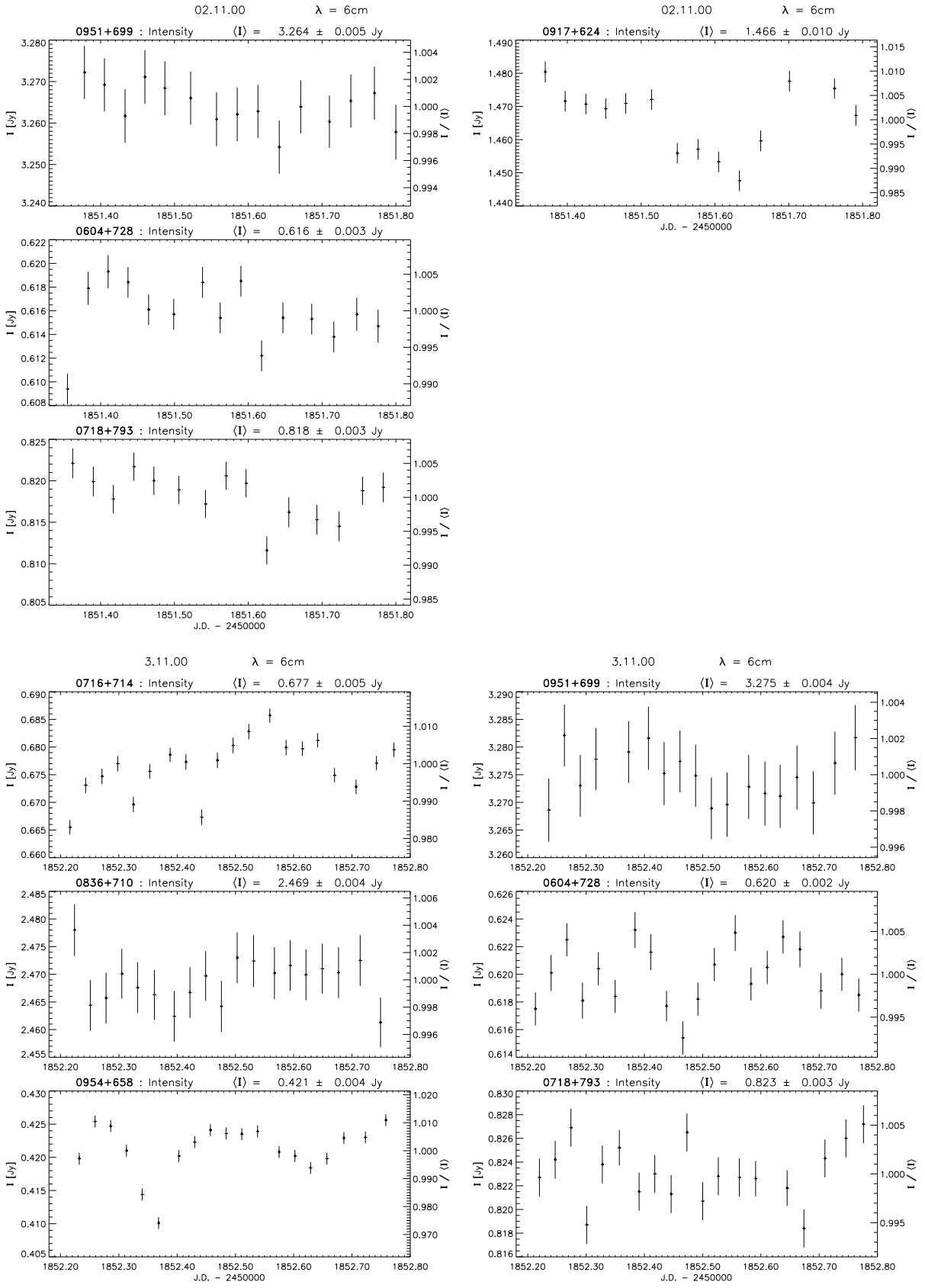

FIGURE A.5— Light curves of epoch 6 (cont.) and 7: 2. November 2000 and 3. November 2000.

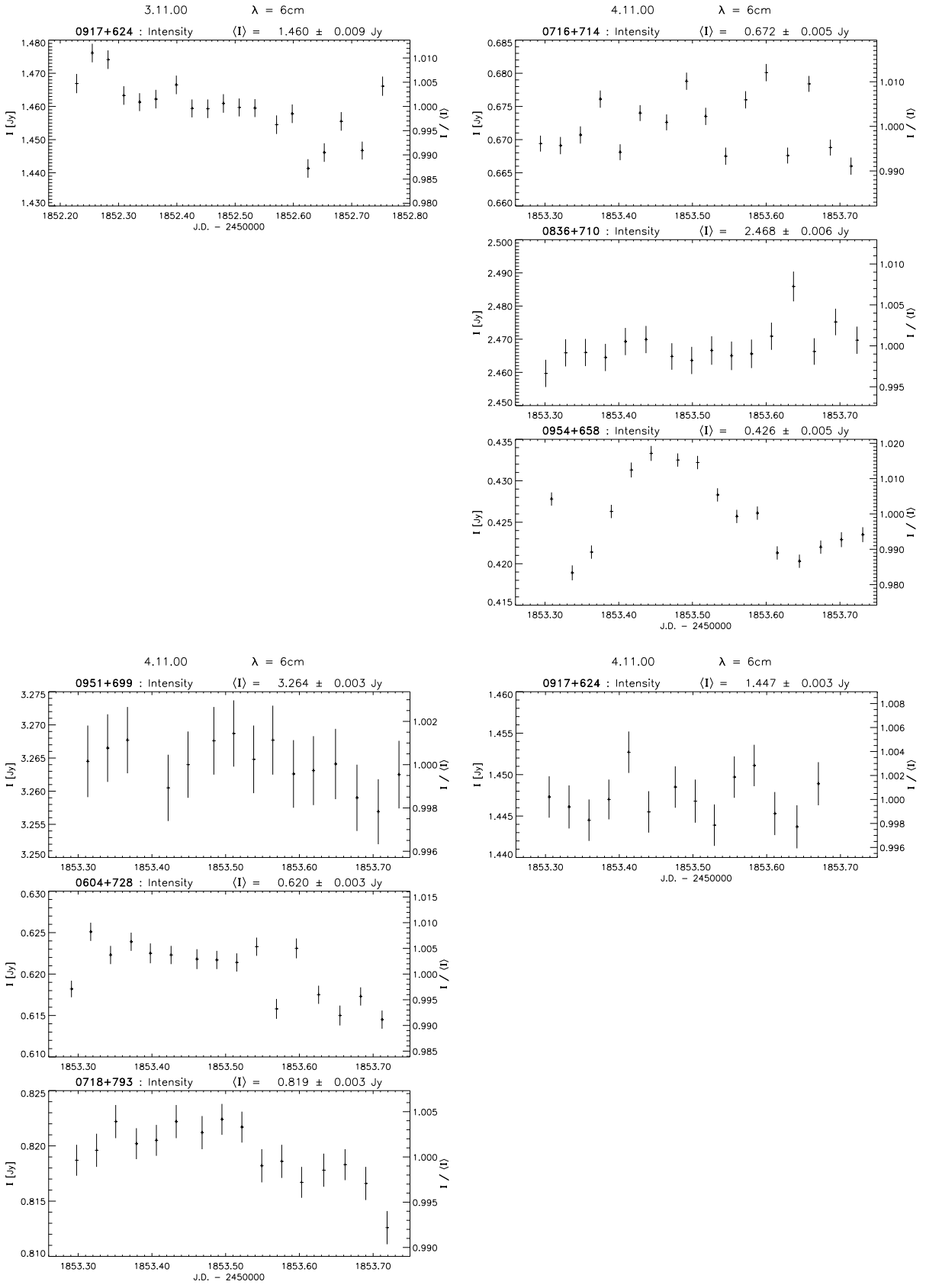

FIGURE A.6— Light curves of epoch 7 (cont.) and 8: 3. November 2000 and 4. November 2000.

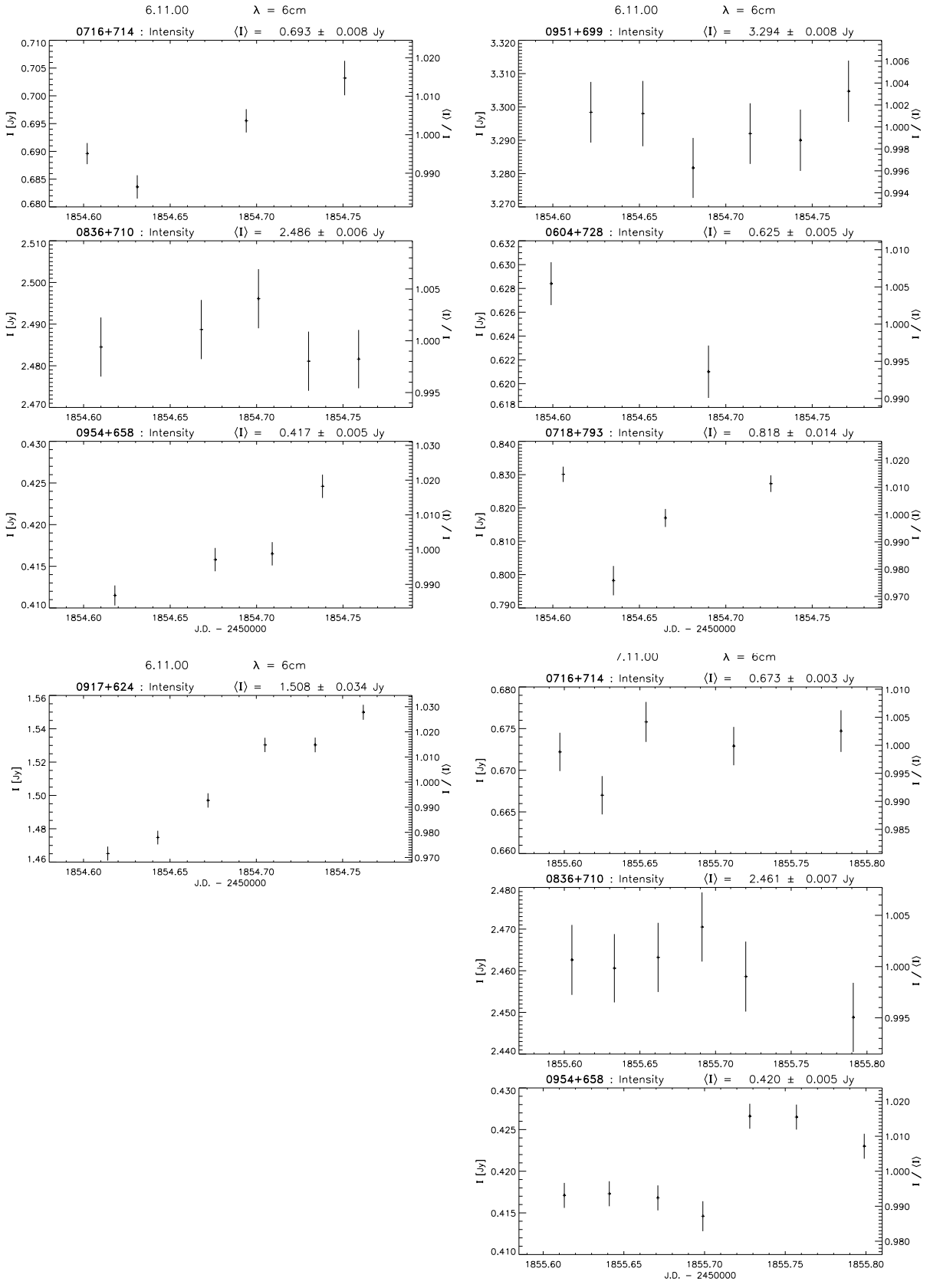

FIGURE A.7— Light curves of epoch 9 and 10: 6. November 2000 and 7. November 2000.

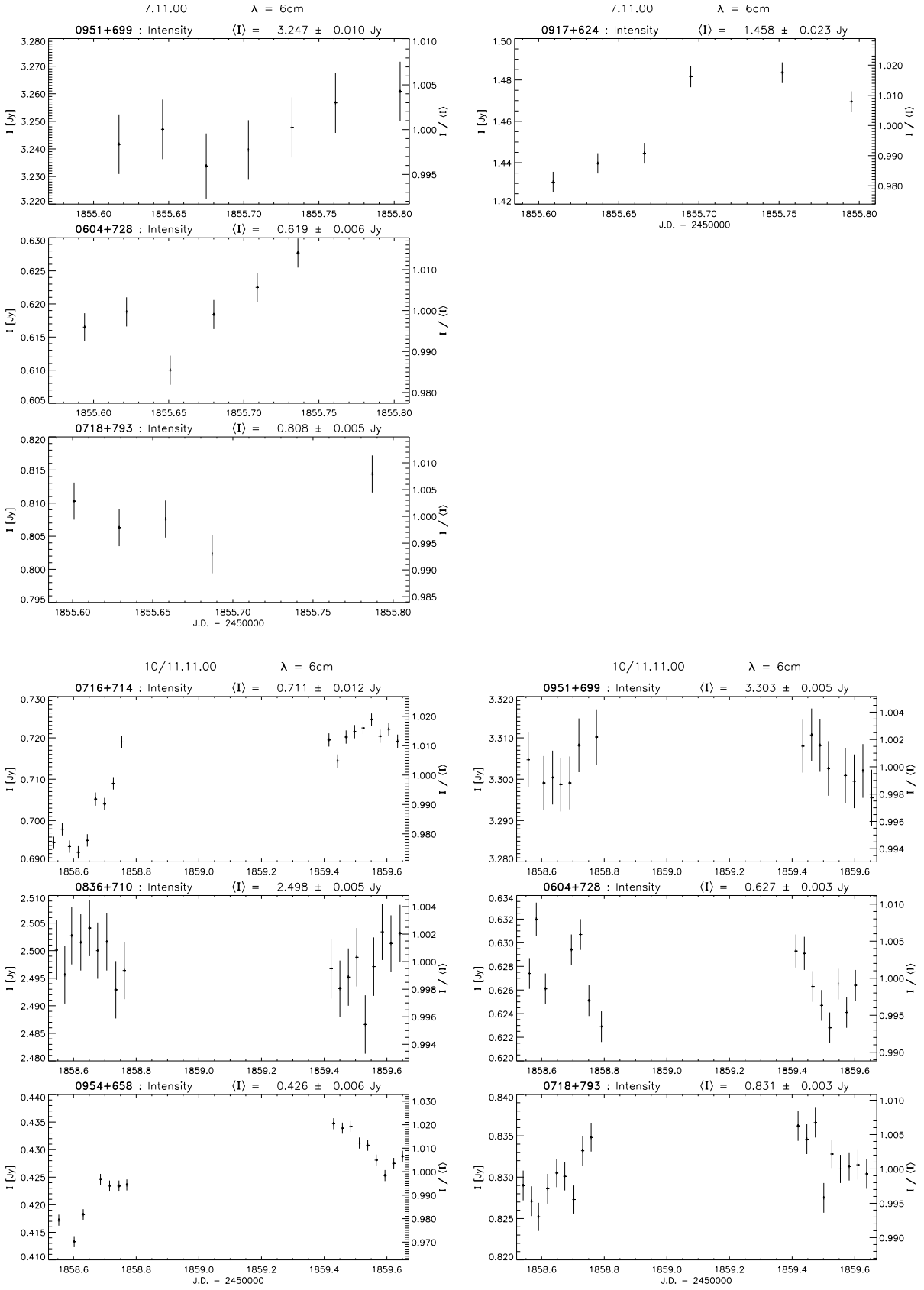

FIGURE A.8— Light curves of epoch 10 (cont.) and 11: 7. November 2000 and 10-11. November 2000.

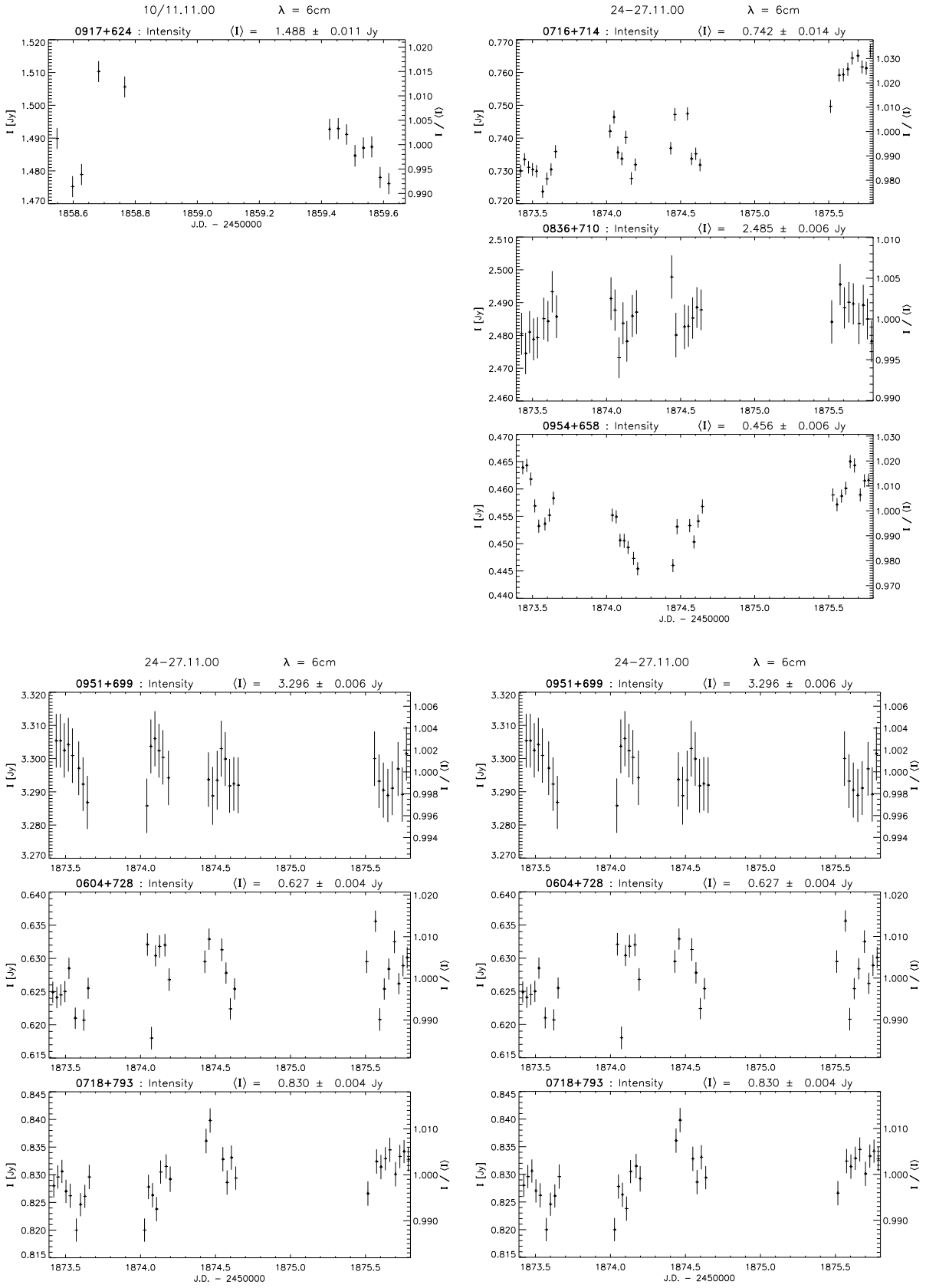

FIGURE A.9— Light curves of epoch 11 (cont.) and 12: 10-11. November 2000 and 24-27. November 2000.

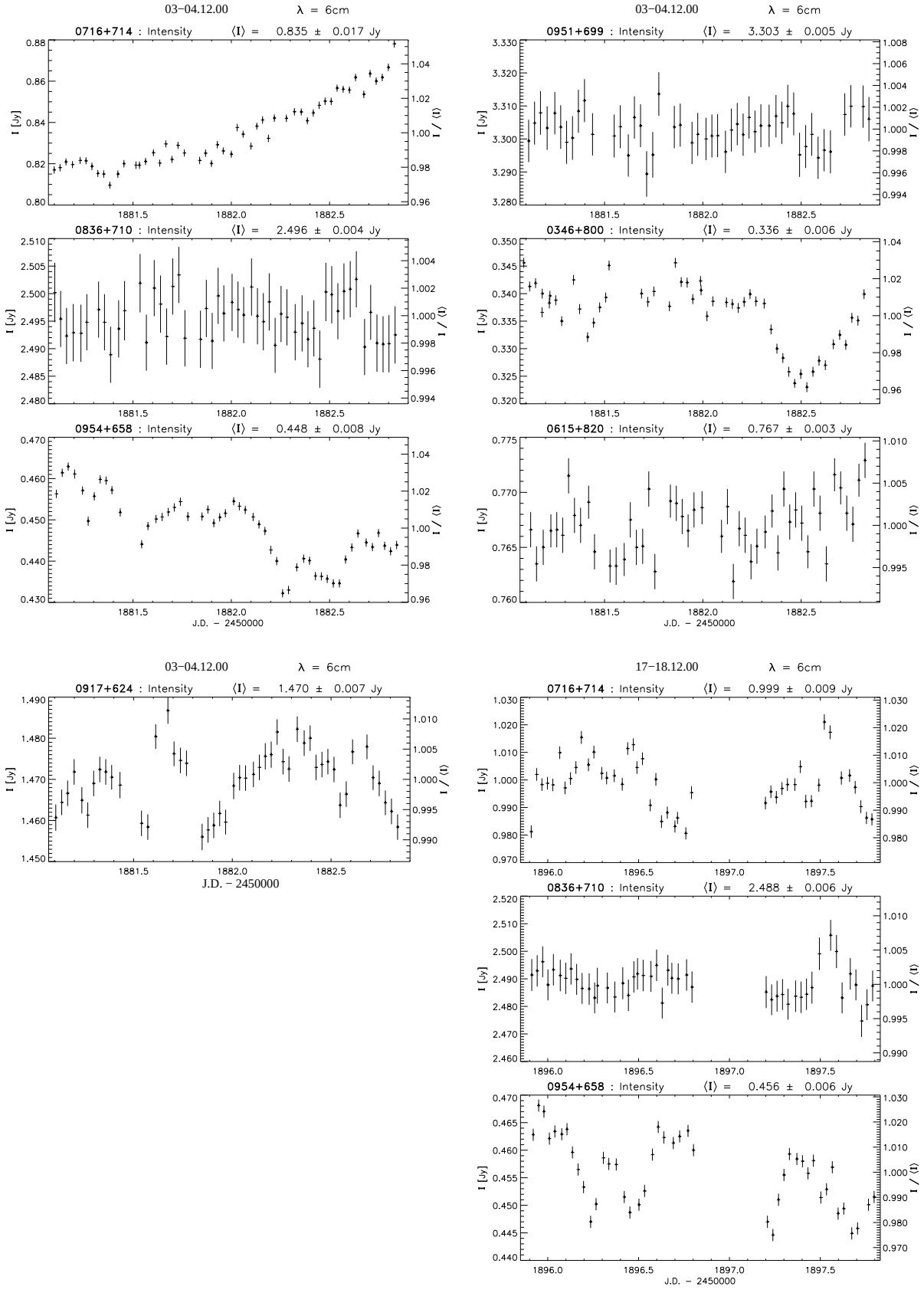

FIGURE A.10— Light curves of epoch 13 and 14: 3-4. December 2000 and 17-18 December 2000.

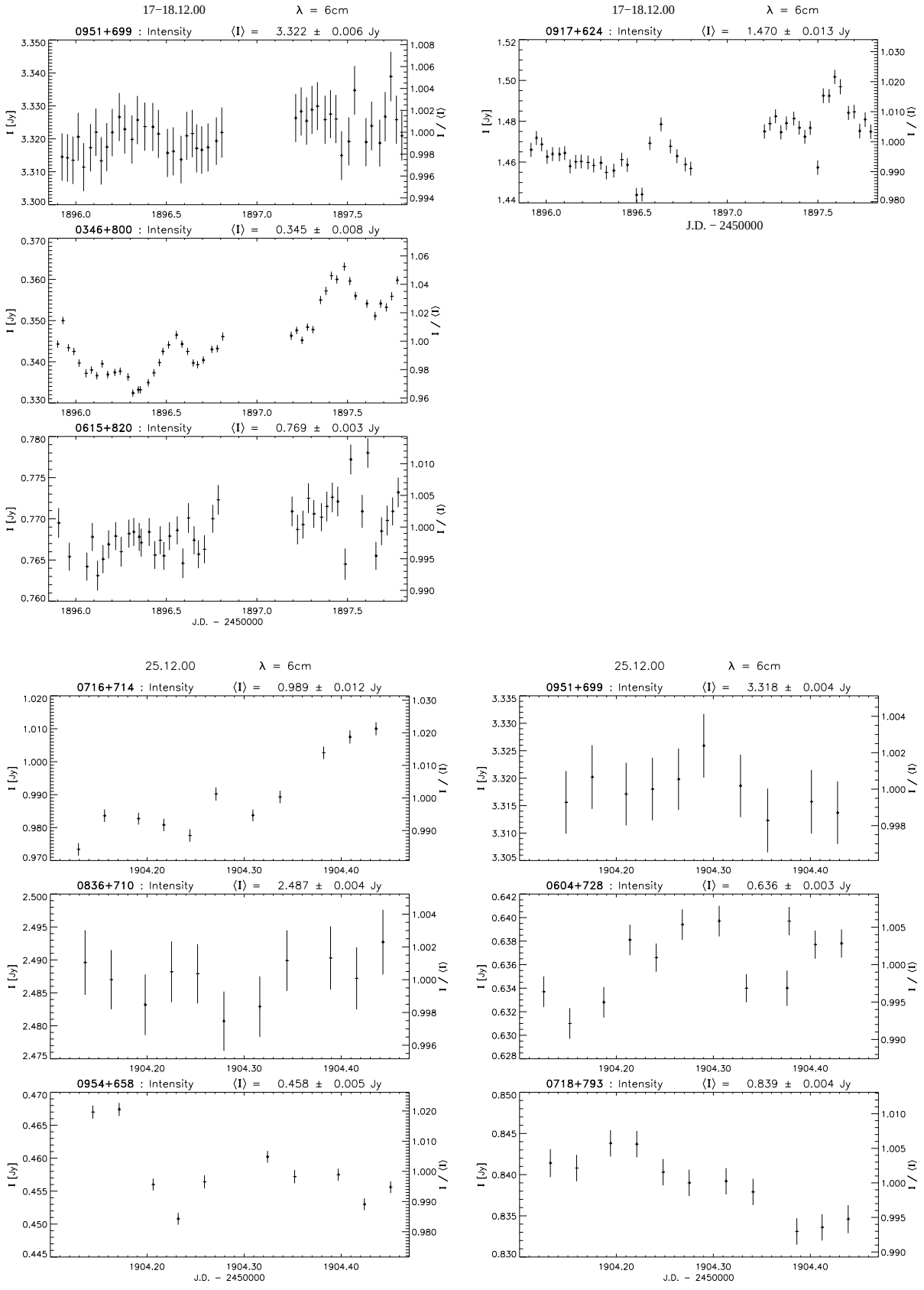

FIGURE A.11— Light curves of epoch 14 (cont.) and 15: 17-18. December 2000 and 25. December 2000.

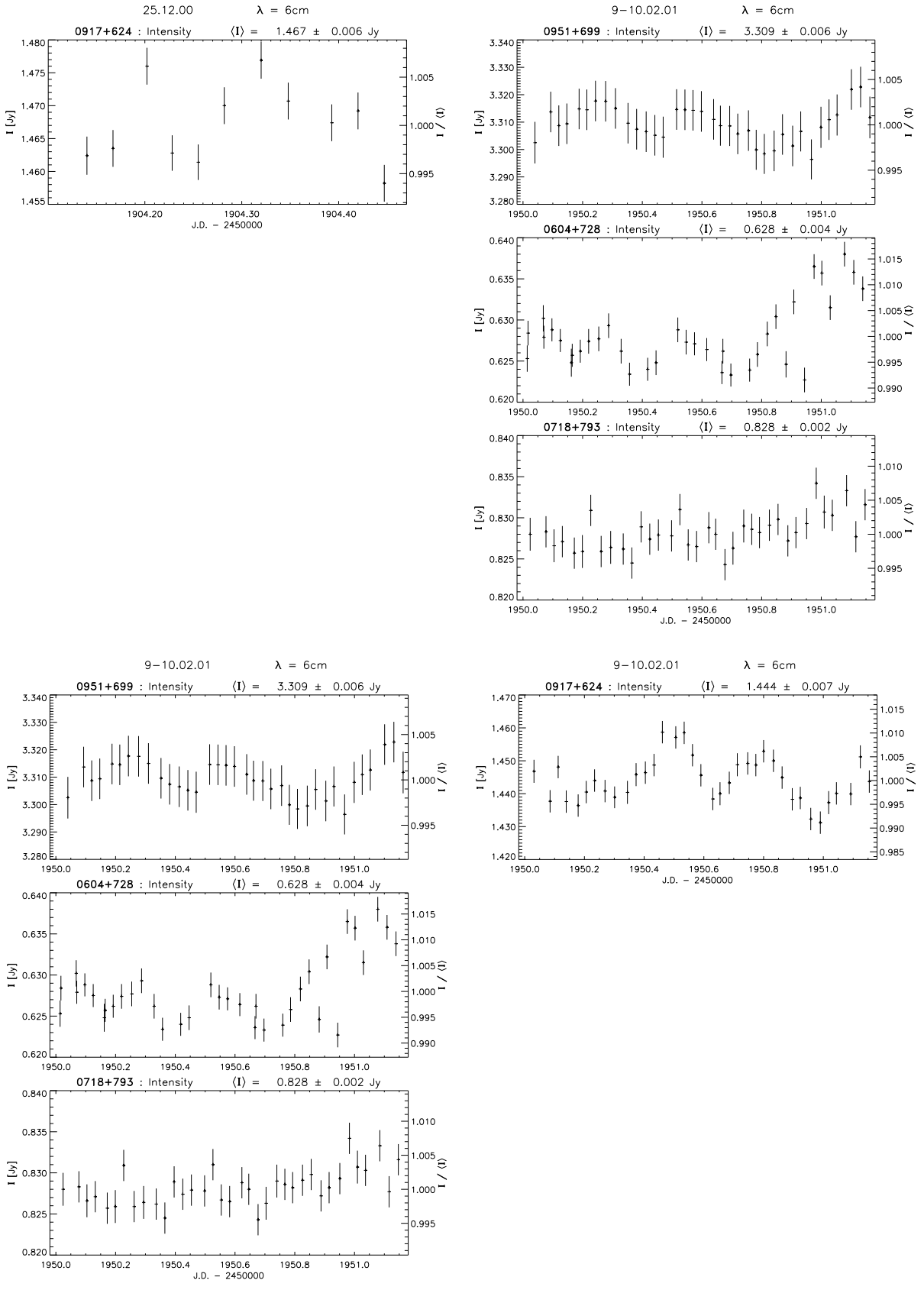

FIGURE A.12— Light curves of epoch 15 (cont.) and 16: 25. December 2000 and 9-10. February 2001.

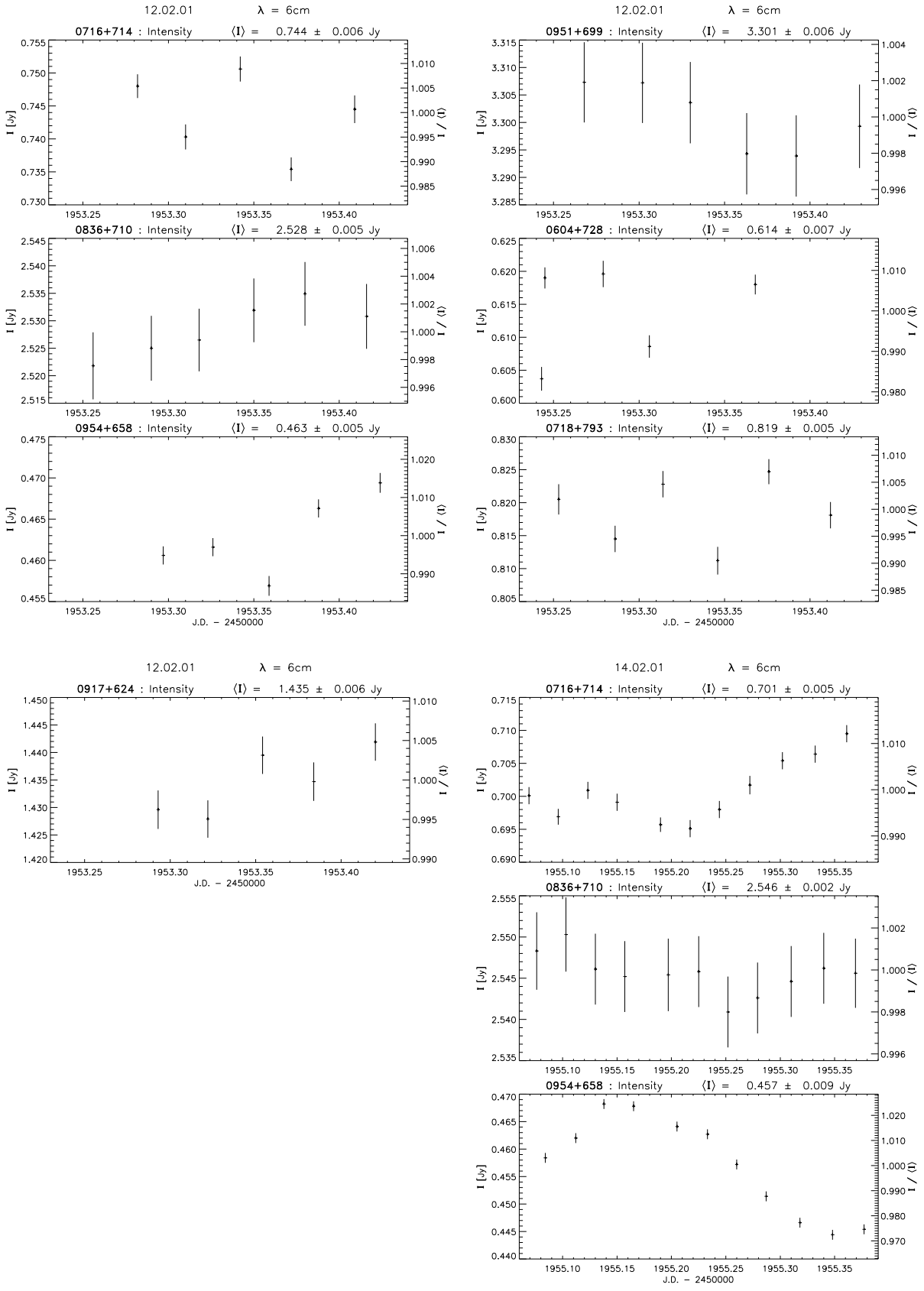

FIGURE A.13— Light curves of epoch 17 and 18: 12. February 2001 and 14. February 2001.

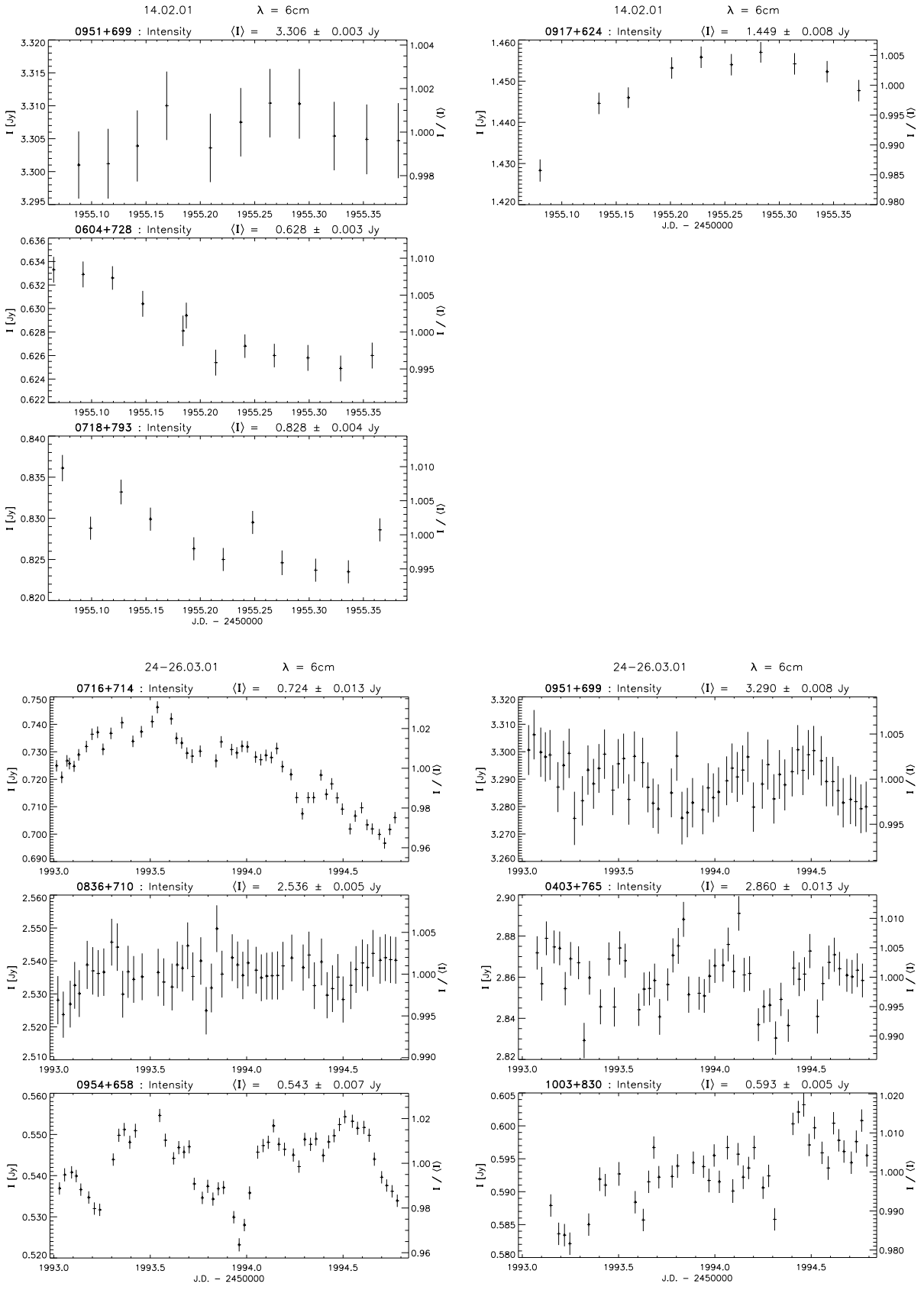

FIGURE A.14— Light curves of epoch 18 (cont.) and 19: 14. February 2001 and 24-26. March 2001.

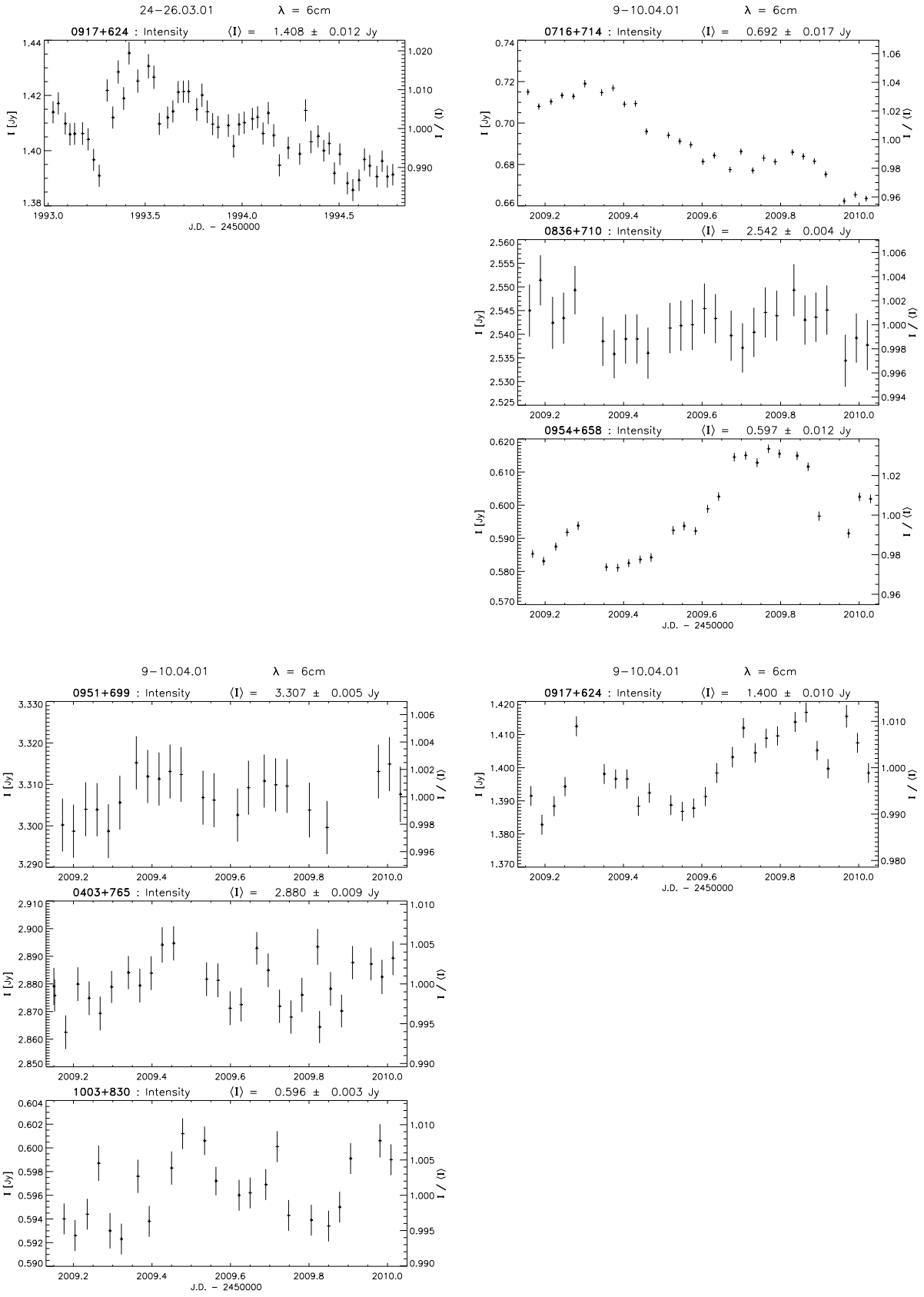

FIGURE A.15— Light curves of epoch 19 (cont.) and 20: 24-26. March 2001 and 9-10. April 2001.

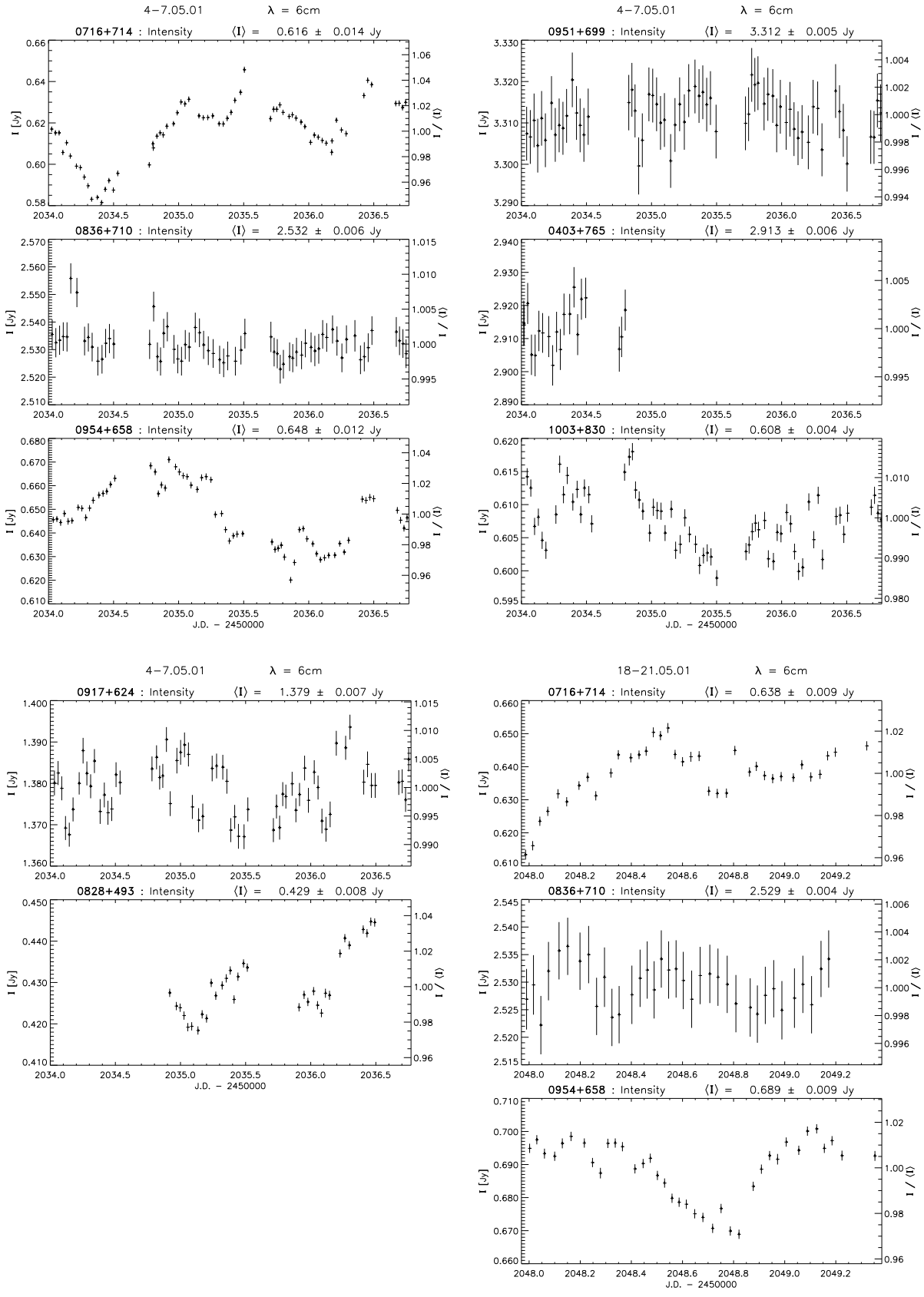

FIGURE A.16— Light curves of epoch 21 and 22: 4-7. May 2001 and 18-21. May 2001.

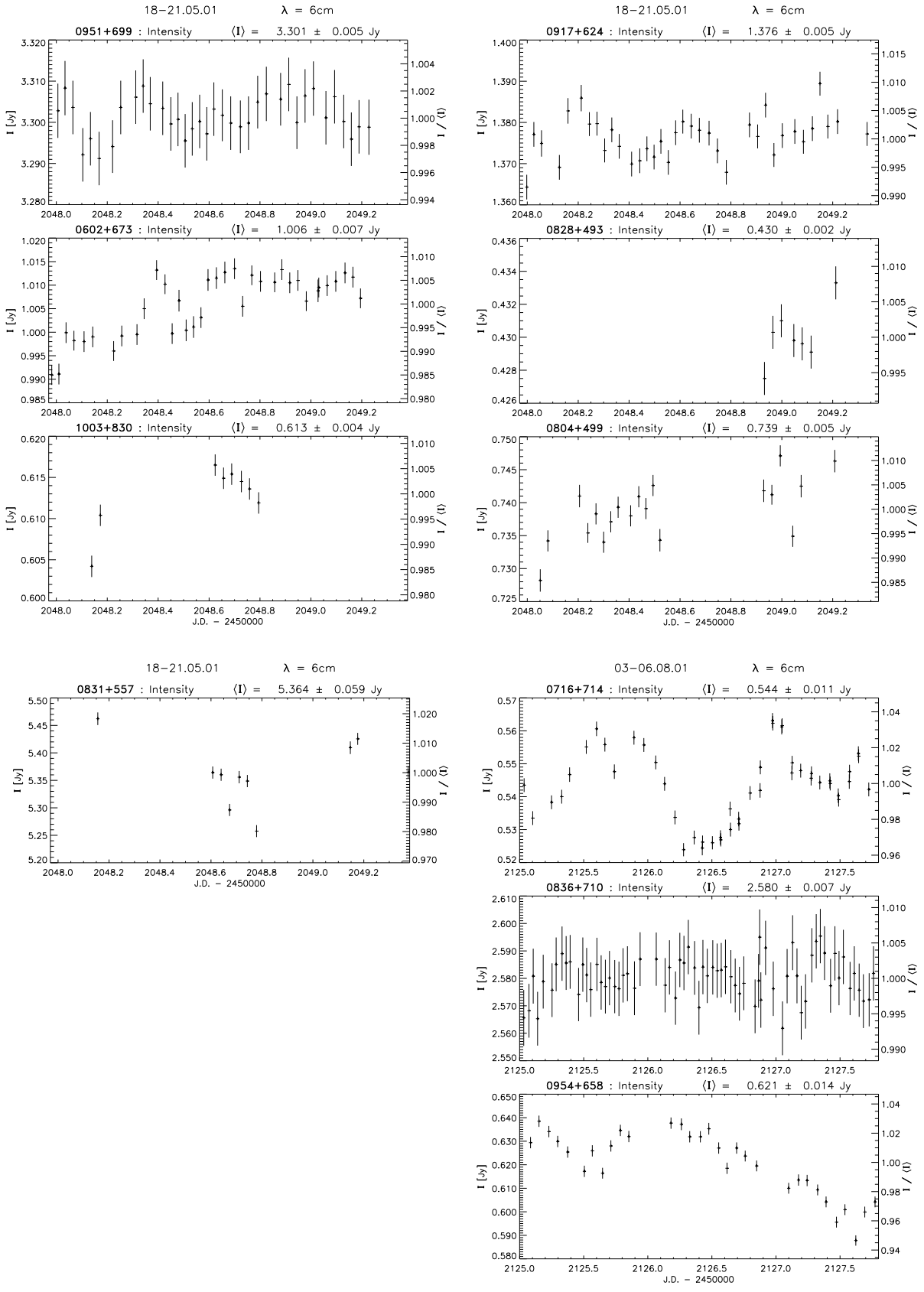

FIGURE A.17— Light curves of epoch 22 (cont.) and 23: 18-21 May 2001 and 3-6. August 2001.

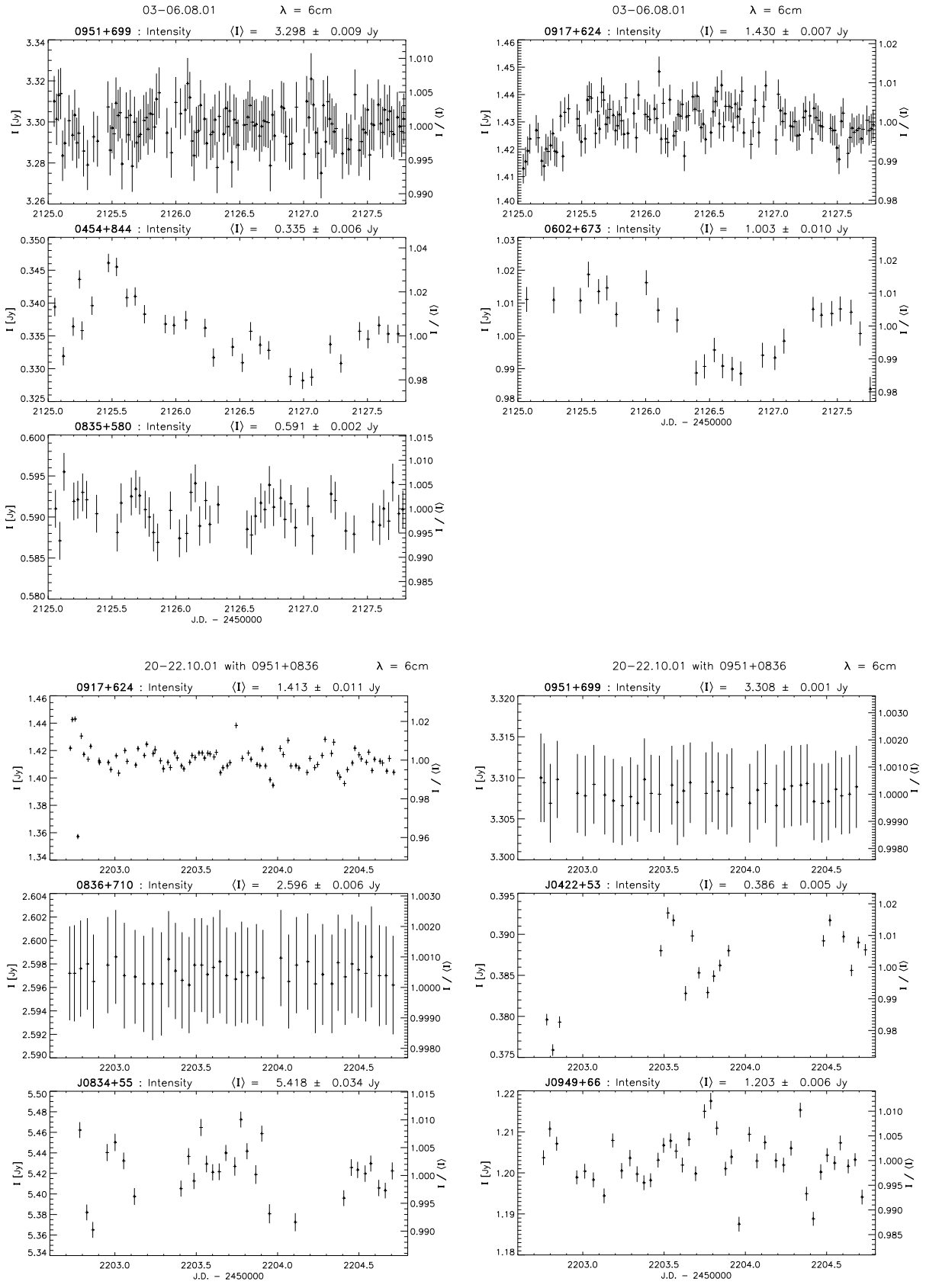

FIGURE A.18— Light curves of epoch 23 (cont.) and 24: 3-6. August 2001 and 20-22. October 2001.

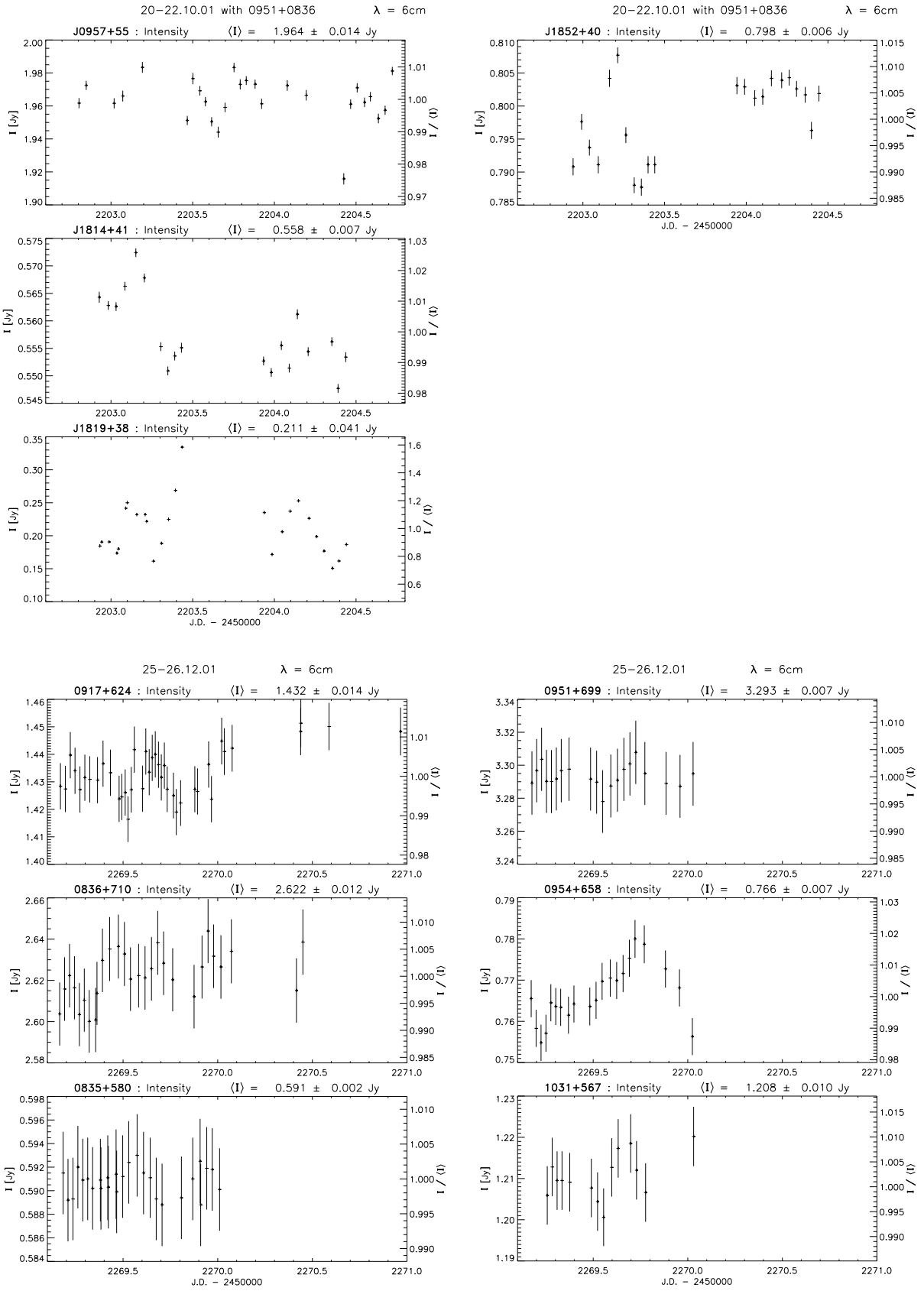

FIGURE A.19— Light curves of epoch 24 (cont.) and 25: 20-22. October 2001 and 25-26. December 2001.

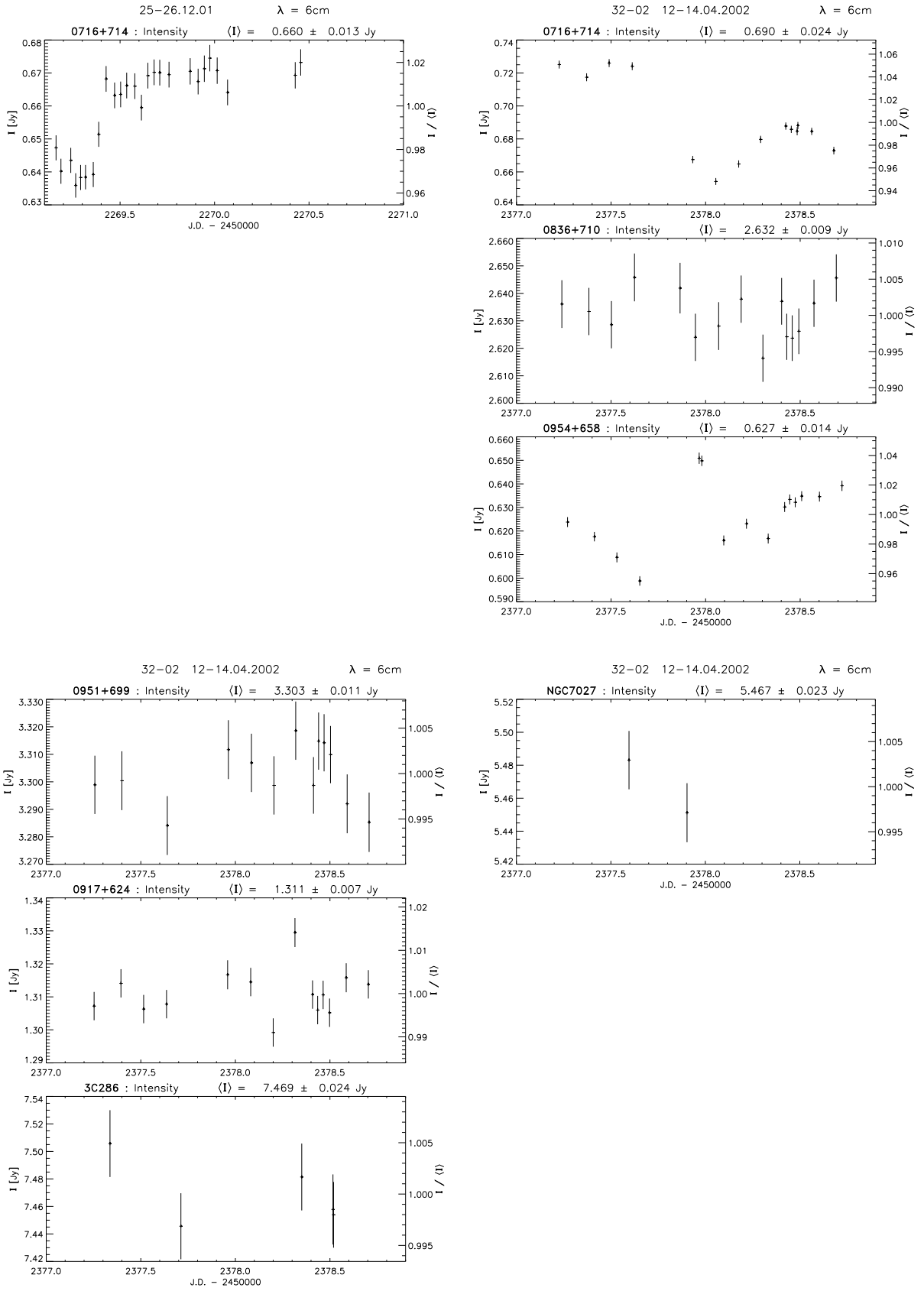

FIGURE A.20— Light curves of epoch 25 (cont.) and 26: 25-26. December 2001 and 12-14. April 2002.

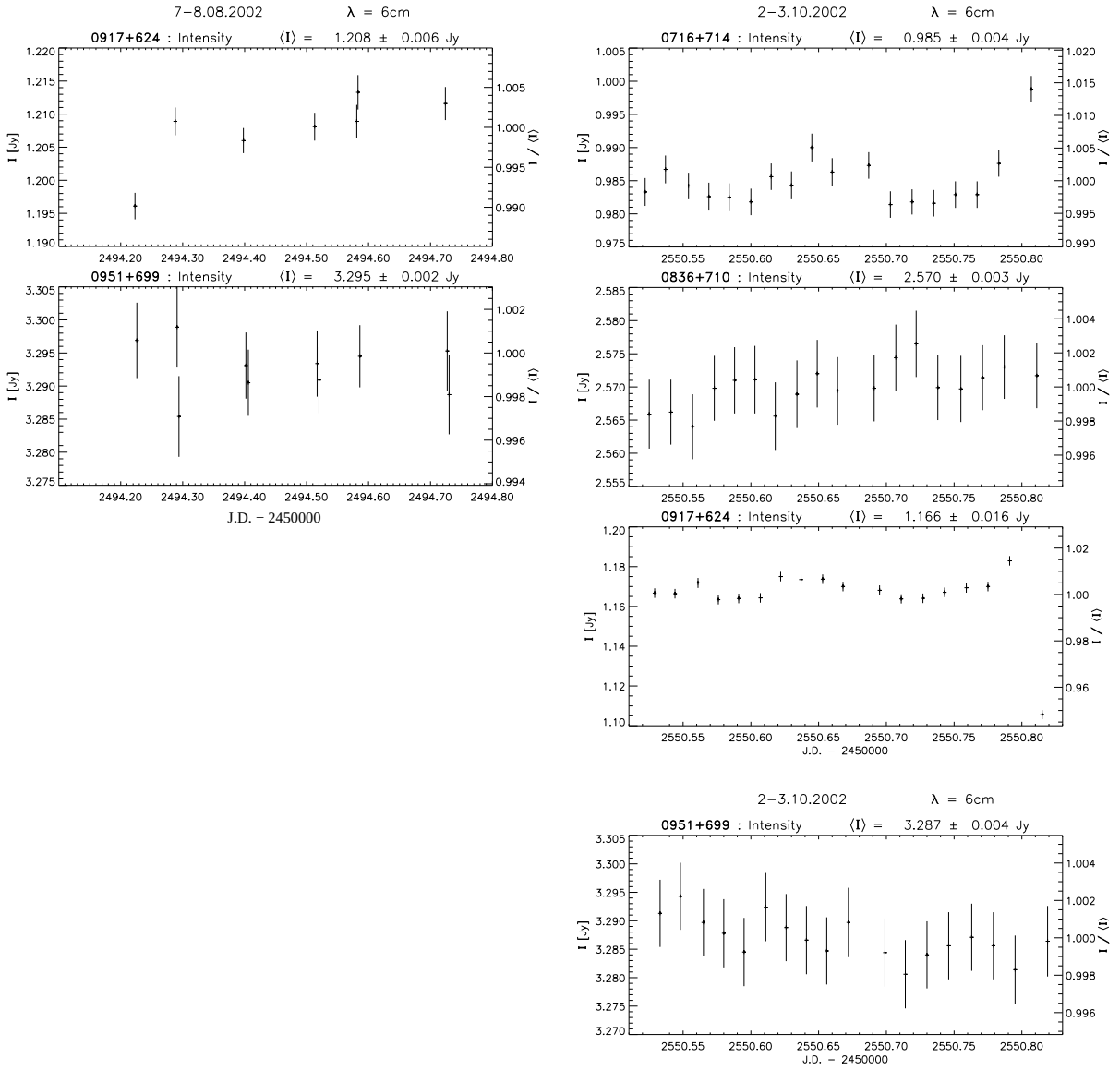

FIGURE A.21— Light curves of epoch 27 and 28: 7-8. August 2002 and 2-3. October 2002.

B

Detailed Results for each Effelsberg Epoch at 4.85 GHz

The following tables summarize the IDV analysis for each of the 28 observing runs between 2000 and 2002 obtained with Effelsberg at 4.85 GHz. The number of scans performed during the run, mean flux density $< S >$ in Jansky, modulation index m [%], variability amplitude Y [%] and the results of the χ^2-test are given for each individual source (target as well as secondary calibrators).

Epoch 1	16. September 2000	T = 24 hrs		$m_0 = 0.4\,\%$			
Source	Scans	S [Jy]	σ [Jy]	m [%]	Y [%]	χ^2	χ^2_r
0604+728	26	0.636	0.003	0.54	1.11	49.266	1.971
0716+714	29	0.842	0.006	0.720	1.78	96.499	3.446
0718+793	24	0.838	0.004	0.53	1.05	42.811	1.861
0836+710	32	2.471	0.008	0.32		21.038	0.679
0917+624	29	1.513	0.006	0.43	0.46	34.041	1.216
0951+699	28	3.338	0.012	0.37		25.914	0.960
0954+658	27	0.418	0.007	1.62	4.72	435.965	16.768

Epoch 2	17 - 18. September 2000	T = 10 hrs		$m_0 = 0.1\,\%$			
Source	Scans	S [Jy]	σ [Jy]	m [%]	Y [%]	χ^2	χ^2_r
0604+728	11	0.631	0.002	0.28	.77	25.244	2.524
0716+714	11	0.802	0.004	0.47	1.36	63.714	6.371
0718+793	11	0.834	0.002	0.28	0.78	25.539	2.554
0836+710	11	2.447	0.002	0.10		3.500	0.350
0917+624	11	1.509	0.004	0.26	.71	21.300	2.130
0951+699	11	3.314	0.003	0.10		3.650	0.365
0954+658	11	0.419	0.004	1.01	3.01	241.158	24.116

Epoch 3	09. October 2000	T = 15 hrs		$m_0 = 0.4\,\%$			
Source	Scans	S [Jy]	σ [Jy]	m [%]	Y [%]	χ^2	χ^2_r
0604+728	14	0.641	0.006	0.94	2.58	79.243	6.096
0716+714	15	0.705	0.004	0.53	1.10	25.752	1.839
0718+793	17	0.855	0.008	0.89	2.41	86.015	5.376
0836+710	17	2.524	0.009	0.37		14.884	0.930
0917+624	15	1.537	0.009	0.61	1.45	36.011	2.572
0951+699	16	3.373	0.012	0.35		13.022	0.868
0954+658	16	0.444	0.006	1.30	3.72	163.814	10.921

Epoch 4	19. October 2000	T = 15 hrs		$m_0 = 0.1\,\%$			
Source	Scans	S [Jy]	σ [Jy]	m [%]	Y [%]	χ^2	χ^2_r
0604+728	20	0.629	0.002	0.38	1.07	72.759	3.829
0716+714	20	0.657	0.003	0.44	1.26	90.206	4.748
0718+793	20	0.842	0.004	0.44	1.27	102.261	5.382
0804+499	2	0.727	0.002	0.22	0.57	0.824	0.824
0835+580	2	0.596	0.001	0.12		0.293	0.293
0836+710	21	2.458	0.003	0.11		6.641	0.332
0917+624	20	1.496	0.005	0.33	0.92	56.155	2.956
0951+699	20	3.321	0.004	0.12		8.520	0.448
0954+658	19	0.438	0.003	0.80	2.37	272.174	15.121

TABLE B.1— Results of the variability analysis for all sources observed between September and October 2000 (Epoch 1 - 4). The number of scans, the mean flux density, the modulation index m, the variability amplitude Y and the results of the χ^2-test are given.

Epoch 5	22. October 2000	T = 10 hrs	$m_0 = 0.2\,\%$				
Source	Scans	S [Jy]	σ [Jy]	m [%]	Y [%]	χ^2	χ^2_r
0604+728	12	0.625	0.003	0.48	1.23	37.476	3.407
0716+714	13	0.604	0.003	0.49	1.30	41.785	3.482
0718+793	12	0.829	0.002	0.27	0.37	12.000	1.091
0836+710	13	2.436	0.006	0.23		9.945	0.829
0917+624	13	1.465	0.007	0.51	1.35	45.785	3.815
0951+699	12	3.280	0.007	0.22		8.878	0.807
0954+658	12	0.452	0.005	1.15	3.36	204.935	18.630

Epoch 6	02. November 2000	T = 15 hrs	m_0 =0.2 %				
Source	Scans	S [Jy]	σ [Jy]	m [%]	Y [%]	χ^2	χ^2_r
0604+728	15	0.616	0.003	0.43	1.14	56.040	4.003
0716+714	15	0.661	0.007	1.01	2.96	293.653	20.975
0718+793	15	0.818	0.003	0.35	0.86	37.839	2.703
0836+710	15	2.459	0.005	0.20		13.026	0.930
0917+624	14	1.466	0.010	0.68	1.94	132.291	10.176
0951+699	15	3.264	0.005	0.15		8.371	0.598
0954+658	15	0.432	0.004	0.86	2.50	192.037	13.717

Epoch 7	03. November 2000	T = 14 hrs	$m_0 = 0.2\,\%$				
Source	Scans	S [Jy]	σ [Jy]	m [%]	Y [%]	χ^2	χ^2_r
0604+728	20	0.620	0.002	0.34	0.89	56.926	2.996
0716+714	20	0.677	0.005	0.75	2.18	268.655	14.140
0718+793	19	0.823	0.003	0.31	0.76	44.886	2.494
0836+710	19	2.469	0.004	0.17		14.552	0.808
0917+624	19	1.460	0.009	0.60	1.73	176.843	9.825
0951+699	18	3.275	0.004	0.14		10.536	0.620
0954+658	19	0.421	0.004	0.91	2.69	329.268	18.293

Epoch 8	04. November 2000	T = 10 hrs	$m_0 = 0.3\,\%$				
Source	Scans	S [Jy]	σ [Jy]	m [%]	Y [%]	χ^2	χ^2_r
0604+728	16	0.620	0.003	0.55	1.47	136.437	9.096
0716+714	16	0.672	0.005	0.67	1.88	193.027	12.868
0718+793	16	0.819	0.003	0.32	0.59	47.192	3.146
0836+710	16	2.468	0.006	0.24		28.266	1.884
0917+624	14	1.447	0.003	0.19		14.898	1.146
0951+699	15	3.264	0.003	0.10		6.492	0.464
0954+658	16	0.426	0.005	1.10	3.21	464.836	30.989

TABLE B.2— Results of the variability analysis for all sources observed between October and November 2000 (Epoch 5 - 8, cont.).

Epoch 9	06. November 2000	T = 5 hrs	$m_0 = 0.2\,\%$				
Source	Scans	S [Jy]	σ [Jy]	m [%]	Y [%]	χ^2	χ^2_r
0604+728	2	0.625	0.005	0.84	2.40	7.054	7.054
0716+714	4	0.693	0.008	1.21	3.55	35.410	11.803
0718+793	4	0.818	0.014	1.77	5.24	61.130	20.377
0836+710	5	2.486	0.006	0.25		3.070	0.768
0917+624	6	1.508	0.034	2.26	6.75	315.989	63.198
0951+699	6	3.294	0.008	0.24		3.860	0.772
0954+658	4	0.417	0.005	1.31	3.86	51.523	17.174

Epoch 10	07. November 2000	T = 5 hrs	m_0 =0.3 %				
Source	Scans	S [Jy]	σ [Jy]	m [%]	Y [%]	χ^2	χ^2_r
0604+728	6	0.619	0.006	0.96	2.73	36.403	7.281
0716+714	5	0.673	0.003	0.51	1.22	8.435	2.109
0718+793	5	0.808	0.005	0.56	1.41	10.113	2.528
0836+710	6	2.461	0.007	0.29		3.654	0.731
0917+624	6	1.458	0.023	1.57	4.61	103.892	20.778
0951+699	7	3.247	0.010	0.29		4.396	0.733
0954+658	7	0.420	0.005	1.19	3.45	62.029	10.338

Epoch 11	10 - 11. November 2000	T = 10 hrs	$m_0 = 0.2\,\%$				
Source	Scans	S [Jy]	σ [Jy]	m [%]	Y [%]	χ^2	χ^2_r
0604+728	15	0.627	0.003	0.44	1.20	60.644	4.332
0716+714	18	0.711	0.012	1.66	4.93	1030.189	60.599
0718+793	18	0.831	0.003	0.39	1.03	58.079	3.416
0836+710	18	2.498	0.005	0.18		13.119	0.772
0917+624	13	1.488	0.011	0.72	2.07	133.287	11.107
0951+699	15	3.303	0.005	0.15		7.525	0.537
0954+658	16	0.426	0.006	1.47	4.38	590.917	39.394

Epoch 12	24 - 27. November 2000	T = 24 hrs	$m_0 = 0.2\,\%$				
Source	Scans	S [Jy]	σ [Jy]	m [%]	Y [%]	χ^2	χ^2_r
0604+728	29	0.627	0.004	0.69	1.94	191.453	6.838
0716+714	31	0.742	0.014	1.82	5.42	1433.516	47.784
0718+793	31	0.830	0.004	0.52	1.41	122.556	4.085
0836+710	32	2.485	0.006	0.23		24.277	0.783
0917+624	29	1.466	0.009	0.65	1.81	174.376	6.228
0951+699	30	3.296	0.006	0.19		16.587	0.572
0954+658	30	0.456	0.006	1.21	3.57	603.164	20.799

TABLE B.3— Results of the variability analysis for all sources observed in November 2000 (Epoch 9 - 12, cont.).

Epoch 13	03 - 04. December 2000		T = 43 hrs		$m_0 = 0.2\,\%$		
Source	Scans	S [Jy]	σ [Jy]	m [%]	Y [%]	χ^2	χ^2_r
0346+800	51	0.336	0.006	1.71	5.10	2095.304	41.906
0615+820	49	0.767	0.003	0.34	0.81	128.943	2.686
0716+714	52	0.835	0.017	2.01	6.01	4607.444	90.342
0836+710	51	2.496	0.004	0.16		29.127	0.583
0917+624	49	1.470	0.007	0.50	1.38	269.549	5.616
0951+699	48	3.303	0.005	0.15		27.963	0.595
0954+658	51	0.448	0.008	1.77	5.29	3125.849	62.517

Epoch 14	17 - 18. December 2000		T = 36 hrs		m_0 =0.2 %		
Source	Scans	S [Jy]	σ [Jy]	m [%]	Y [%]	χ^2	χ^2_r
0346+800	48	0.345	0.008	2.42	7.21	3584.684	76.270
0615+820	44	0.769	0.003	0.42	1.00	139.857	3.252
0716+714	46	0.999	0.009	0.94	2.73	736.668	16.370
0836+710	46	2.488	0.006	0.23		44.624	0.992
0917+624	44	1.470	0.013	0.89	2.56	612.414	14.242
0951+699	45	3.322	0.006	0.18		27.737	0.630
0954+658	44	0.456	0.006	1.38	4.09	1417.213	32.958

Epoch 15	25. December 2000		T = 8 hrs		$m_0 = 0.1\,\%$		
Source	Scans	S [Jy]	σ [Jy]	m [%]	Y [%]	χ^2	χ^2_r
0604+728	12	0.636	0.003	0.47	1.33	59.439	5.404
0716+714	11	0.989	0.012	1.24	3.70	399.733	39.973
0718+793	11	0.839	0.004	0.45	1.26	53.656	5.366
0836+710	11	2.487	0.004	0.15		6.056	0.606
0917+624	11	1.467	0.006	0.41	1.15	47.031	4.703
0951+699	10	3.318	0.004	0.12		3.978	0.442
0954+658	10	0.458	0.005	1.18	3.52	286.422	31.825

Epoch 16	09 - 10. February 2001		T = 27 hrs		$m_0 = 0.2\,\%$		
Source	Scans	S [Jy]	σ [Jy]	m [%]	Y [%]	χ^2	χ^2_r
0604+728	36	0.628	0.004	0.64	1.81	252.469	7.213
0716+714	36	0.780	0.007	0.86	2.52	473.136	13.518
0718+793	36	0.828	0.002	0.27	0.54	47.407	1.354
0836+710	36	2.539	0.005	0.19		23.584	0.674
0917+624	36	1.444	0.007	0.47	1.29	141.206	4.034
0951+699	36	3.309	0.006	0.19		25.447	0.727
0954+658	36	0.441	0.007	1.55	4.60	1344.981	38.428

TABLE B.4— Results of the variability analysis for all sources observed between December 2000 and February 2001 (Epoch 13 - 16, cont.).

Epoch 17	12. February 2001	T = 5 hrs	$m_0 = 0.2\,\%$				
Source	Scans	S [Jy]	σ [Jy]	m [%]	Y [%]	χ^2	χ^2_r
0604+728	5	0.614	0.007	1.17	3.47	67.671	16.918
0716+714	5	0.744	0.006	0.82	2.37	43.520	10.880
0718+793	6	0.819	0.005	0.62	1.77	32.066	6.413
0836+710	6	2.528	0.005	0.19		3.395	0.679
0917+624	5	1.435	0.006	0.42	1.12	12.600	3.150
0951+699	6	3.301	0.006	0.18		3.381	0.676
0954+658	5	0.463	0.005	1.06	3.13	69.655	17.414

Epoch 18	14. February 2001	T = 7 hrs	m_0 =0.1 %				
Source	Scans	S [Jy]	σ [Jy]	m [%]	Y [%]	χ^2	χ^2_r
0604+728	12	0.628	0.003	0.50	1.47	94.576	8.598
0716+714	11	0.701	0.005	0.66	1.95	134.205	13.421
0718+793	11	0.828	0.004	0.49	1.42	72.283	7.228
0836+710	11	2.546	0.002	0.10		3.196	0.320
0917+624	10	1.449	0.008	0.59	1.73	92.014	10.224
0951+699	11	3.306	0.003	0.10		4.275	0.427
0954+658	11	0.457	0.009	1.94	5.80	968.752	96.875

Epoch 19	24. - 26. March 2001	T = 43 hrs	$m_0 = 0.2\,\%$				
Source	Scans	S [Jy]	σ [Jy]	m [%]	Y [%]	χ^2	χ^2_r
0403+765	54	2.860	0.013	0.46	1.19	136.169	2.569
0604+728	3	0.627	0.004	0.56	1.52	7.663	3.831
0716+714	53	0.724	0.013	1.73	5.14	1916.732	36.860
0718+793	3	0.815	0.001	0.15		0.522	0.261
0836+710	55	2.536	0.005	0.20		27.942	0.517
0917+624	56	1.408	0.012	0.83	2.39	459.503	8.355
0951+699	57	3.290	0.008	0.24		41.088	0.734
0954+658	54	0.543	0.007	1.38	4.07	1214.126	22.908
1003+830	43	0.593	0.005	0.86	2.47	370.353	8.818

Epoch 20	09 - 10. April 2001	T = 22 hrs	$m_0 = 0.2\,\%$				
Source	Scans	S [Jy]	σ [Jy]	m [%]	Y [%]	χ^2	χ^2_r
0403+765	29	2.880	0.009	0.31	0.70	59.118	2.111
0716+714	28	0.692	0.017	2.52	7.54	3594.911	133.145
0836+710	27	2.542	0.004	0.17		16.525	0.636
0917+624	27	1.400	0.010	0.71	2.05	286.143	11.006
0951+699	23	3.307	0.005	0.16		14.362	0.653
0954+658	26	0.597	0.012	2.08	6.20	2393.637	95.745
1003+830	23	0.596	0.003	0.48	1.30	103.099	4.686

TABLE B.5— Results of the variability analysis for all sources observed between February and April 2001 (Epoch 17 - 20, cont.).

Epoch 21	04.-07. May 2001	T = 65 hrs	$m_0 = 0.2\,\%$				
Source	Scans	S [Jy]	σ [Jy]	m [%]	Y [%]	χ^2	χ^2_r
0403+765	20	2.913	0.006	0.22		20.909	1.100
0716+714	67	0.616	0.014	2.35	7.03	7984.958	120.984
0828+493	33	0.429	0.008	1.77	5.27	1846.683	57.709
0836+710	65	2.532	0.006	0.22		72.865	1.139
0917+624	65	1.379	0.007	0.47	1.24	311.315	4.864
0951+699	64	3.312	0.005	0.15		37.530	0.596
0954+658	65	0.648	0.012	1.92	5.71	5436.137	84.940
1003+830	65	0.608	0.004	0.71	2.03	718.119	11.221

Epoch 22	18.-21. May 2001	T = 34 hrs	m_0 =0.2 %				
Source	Scans	S [Jy]	σ [Jy]	m [%]	Y [%]	χ^2	χ^2_r
0602+673	36	1.006	0.007	0.65	1.86	316.892	9.054
0716+714	37	0.638	0.009	1.33	3.95	1265.268	35.146
0804+499	19	0.739	0.005	0.63	1.78	141.630	7.868
0828+493	7	0.430	0.002	0.42	1.09	19.189	3.198
0831+557	10	5.364	0.059	1.11	3.26	256.218	28.469
0836+710	36	2.529	0.004	0.15		17.624	0.504
0917+624	36	1.376	0.005	0.37	0.94	101.891	2.911
0951+699	36	3.301	0.005	0.14		18.107	0.517
0954+658	38	0.689	0.009	1.32	3.91	1548.281	41.845
1003+830	8	0.613	0.004	0.64	1.83	64.376	9.197

Epoch 23	03.-06. August 2001	T = 67 hrs	$m_0 = 0.3\,\%$				
Source	Scans	S [Jy]	σ [Jy]	m [%]	Y [%]	χ^2	χ^2_r
0454+844	31	0.336	0.005	1.35	3.95	327.711	10.924
0602+673	26	1.003	0.010	1.00	2.85	175.072	7.003
0716+714	47	0.544	0.011	2.03	6.02	1232.609	26.796
0835+580	50	0.591	0.002	0.35	0.57	40.311	0.823
0836+710	69	2.580	0.007	0.28		37.657	0.554
0917+624	130	1.430	0.007	0.47	1.08	195.981	1.519
0951+699	127	3.298	0.009	0.28		67.617	0.537
0954+658	31	0.621	0.014	2.21	6.58	1047.446	34.915

Epoch 24	20-22. October 2001	T = 49 hrs	$m_0 = 0.03\,\%$				
Source	Scans	S [Jy]	σ [Jy]	m [%]	Y [%]	χ^2	χ^2_r
0836+710	43	2.597	0.001	0.03		1.253	0.030
0917+624	85	1.413	0.011	0.75	2.26	2330.044	27.739
0951+699	39	3.308	0.001	0.03		1.567	0.041
J0422+53	19	0.386	0.005	1.18	3.55	756.967	42.054
J0834+55	30	5.422	0.027	0.50	1.48	323.580	11.158
J0949+66	42	1.203	0.006	0.52	1.57	511.001	12.463
J0957+55	27	1.964	0.014	0.71	2.12	516.675	19.872
J1814+41	19	0.558	0.007	1.21	3.64	1251.354	69.520
J1819+38	26	0.211	0.041	19.44	58.32		
J1852+40	22	0.798	0.006	0.77	2.31	511.687	24.366

TABLE B.6— Results of the variability analysis for all sources observed between May and October 2001 (Epoch 21 - 24, cont.).

Epoch 25	25.- 26. December 2001		T = 23 hrs		$m_0 = 0.5\,\%$		
Source	Scans	S [Jy]	σ [Jy]	m [%]	Y [%]	χ^2	χ^2_r
0716+714	26	0.660	0.013	1.98	5.76	293.451	11.738
0835+580	27	0.591	0.001	0.20		2.837	0.109
0836+710	28	2.622	0.012	0.46		16.539	0.613
0917+624	39	1.433	0.009	0.61	1.05	40.399	1.063
0951+699	20	3.293	0.007	0.20		2.249	0.118
0954+658	21	0.766	0.007	0.91	2.28	47.641	2.382
1031+567	14	1.210	0.006	0.46	.00	7.941	0.611

Epoch 26	12.- 14. April 2002		T = 37 hrs		m_0 =0.3 %		
Source	Scans	S [Jy]	σ [Jy]	m [%]	Y [%]	χ^2	χ^2_r
0716+714	14	0.690	0.024	3.44	10.28	1392.278	107.098
0836+710	15	2.632	0.009	0.33		14.381	1.027
0917+624	14	1.311	0.007	0.55	1.27	35.387	2.722
0951+699	13	3.303	0.011	0.34		13.257	1.105
0954+658	15	0.627	0.014	2.29	6.80	636.288	45.449

Epoch 27	07.- 08. August 2002		T = 14 hrs		$m_0 = 0.1\,\%$		
Source	Scans	S [Jy]	σ [Jy]	m [%]	Y [%]	χ^2	χ^2_r
0917+624	7	1.208	0.006	0.46	1.31	41.746	6.958
0951+699	10	3.293	0.004	0.12		4.134	0.459

Epoch 28	03. October 2002		T = 7 hrs		$m_0 = 0.1\,\%$		
Source	Scans	S [Jy]	σ [Jy]	m [%]	Y [%]	χ^2	χ^2_r
0716+714	18	0.985	0.004	0.43	1.23	74.783	4.399
0836+710	18	2.570	0.003	0.12		6.831	0.402
0917+624	18	1.166	0.016	1.35	4.05	789.397	46.435
0951+699	18	3.287	0.004	0.11		6.295	0.370

TABLE B.7— Results of the variability analysis for all sources observed between December 2001 and October 2002 (Epoch 25 - 28, cont.).

C

IDV Source List

An up-to-date (November 2003) source list of known type I and type II - IDV sources is given. The list with a total of 101 entries was conducted in the framework of the statistical analysis presented in Chapter 7.

Complete list of known IDV sources

Source	α_{2000}	δ_{2000}	α_{1950}	δ_{1950}	$l_{II}[^\circ]$	$b_{II}[^\circ]$
0016+731	00h19m45.7863s	+73d27m30.017s	00h16m54.1934s	+73d10m51.359s	120.64	10.73
0059+581	01h02m45.7623s	+58d24m11.136s	00h59m43.4736s	+58d08m04.751s	124.42	–4.44
0104–408	01h06m45.1079s	–40d34m19.959s	01h04m27.5774s	–40d50m21.698s	290.67	–76.19
0133+476	01h36m58.5947s	+47d51m29.100s	01h33m55.1073s	+47d36m12.765s	130.79	–14.32
0147+2631	01h50m02.86s	+26d46m28.2s	01h47m13.80s	+26d31m36.6s	138.79	–34.29
0153+744	01h57m34.9648s	+74d42m43.230s	01h53m04.3293s	+74d28m05.580s	127.34	12.41
PKS 0235+164	02h38m38.9301s	+16d36m59.275s	02h35m52.6341s	+16d24m03.920s	156.77	–39.11
0300+470	03h03m35.2422s	+47d16m16.275s	03h00m10.1131s	+47d04m33.606s	144.99	–9.86
0340+3612	03h43m28.9524s	+36d22m12.430s	03h40m14.7894s	+36d12m44.379s	157.53	–14.69
PKS 0346–279	03h48m38.136s	–27d49m13.21s	03h46m34.030s	–27d58m20.70s	224.53	–50.91
PKS 0405–385	04h06m59.0352s	–38d26m28.039s	04h05m12.0258s	–38d34m26.122s	241.29	–47.89
0408+0835	04h11m33.8575s	+08d43m11.408s	04h08m51.0882s	+08d35m29.452s	183.67	–29.73
PKS 0422+004	04h24m46.8420s	+00d36m06.329s	04h22m12.5176s	+00d29m16.647s	193.59	–31.78
J0422+5345	04h22m25.3s	+53d45m54s	04h18m29.1s	+53d38m52s	151.04	2.83
0437–454	04h39m00.8547s	–45d22m22.562s	04h37m30.6642s	–45d28m12.687s	250.85	–41.76
0440–003	04h42m38.6607s	–00d17m43.418s	04h40m05.2928s	–00d23m20.601s	197.20	–28.46
0450–469	04h51m53.35s	–46d53m19.3s	04h50m27.90s	–46d58m16.0s	252.78	–39.49
0450+0123	04h53m02.2386s	+01d28m35.625s	04h50m26.8943s	+01d23m41.511s	197.00	–25.32
0454+844	05h08m42.3633s	+84d32m04.544s	04h54m57.1349s	+84d27m52.954s	128.35	24.66
0459+135	05h02m33.2195s	+13d38m10.958s	04h59m43.8443s	+13d33m56.389s	187.41	–16.75
0502+049	05h05m23.1847s	+04d59m42.725s	05h02m43.8145s	+04d55m40.507s	195.48	–20.86
0528–250	05h30m07.9627s	–25d03m29.898s	05h28m05.2117s	–25d05m44.666s	228.30	–28.24
0602+67	06h07m52.6716s	+67d20m55.409s	06h02m38.8678s	+67d21m18.499s	146.80	20.86
0607–157	06h09m40.9494s	–15d42m40.671s	06h07m25.9826s	–15d42m03.328s	222.61	–16.18
0621+4441	06h25m18.2653s	+44d40m01.626s	06h21m38.8058s	+44d41m44.104s	169.77	14.39
J0642+8811	06h42m06.134s	+88d11m55.01s	06h04m00.726s	+88d13m36.01s	124.95	27.04
PKS 0646–306	06h48m14.0964s	–30d44m19.658s	06h46m19.2128s	–30d40m54.448s	240.54	–14.11
0711+356	07h14m24.8174s	+35d34m39.796s	07h11m05.6001s	+35d39m52.587s	182.22	19.74
0716+4743	07h20m21.4977s	+47d37m44.124s	07h16m38.6652s	+47d43m20.696s	170.14	24.35
0716+714	07h21m53.4484s	+71d20m36.363s	07h16m13.0061s	+71d26m15.256s	143.98	28.02
PKS 0728–320	07h30m38.31s	–32d08m21.2s	07h28m43.30s	–32d01m59.0s	245.80	–6.56
0735+178	07h38m07.3937s	+17d42m18.998s	07h35m14.1294s	+17d49m09.291s	201.85	18.07
0754+100	07h57m06.6429s	+09d56m34.852s	07h54m22.5826s	+10d04m39.741s	211.31	19.06
0756+4902	08h00m34.36s	+48d54m23.7s	07h56m53.91s	+49d02m39.9s	170.11	31.16
0804+499	08h08m39.6662s	+49d50m36.530s	08h04m58.3932s	+49d59m23.138s	169.16	32.56
PKS 0808+019	08h11m26.7073s	+01d46m52.221s	08h08m51.1407s	+01d55m51.262s	220.71	18.57
0814+425	08h18m15.9996s	+42d22m45.415s	08h14m51.6680s	+42d32m07.787s	178.23	33.40
0828+493	08h32m23.2167s	+49d13m21.038s	08h28m47.9655s	+49d23m33.092s	170.14	36.38
0833+585	08h37m21.0s	+58d24.6m	08h33m22s	+58d35.0m	158.67	36.60
J0834+5513	08h34m40.6s	+55d13m59s	08h30m51.0s	+55d24m18s	162.65	36.55
0850+581	08h54m41.9963s	+57d57m29.939s	08h50m50.1504s	+58d08m55.758s	158.79	38.93
0851+202	08h54m48.8749s	+20d06m30.641s	08h51m57.2541s	+20d17m58.491s	206.81	35.82
0859+470	09h03m03.9901s	+46d51m04.137s	08h59m39.9831s	+47d02m56.889s	173.04	41.56
0906+430	09h09m26.52s	+42d42m28.1s	09h06m10.53s	+42d54m40.4s	178.58	42.82
J0914+0245	09h14m37.9134s	+02d45m59.246s	09h12m01.9428s	+02d58m27.932s	228.35	32.82
0914+0255	09h16m41.4s	+02d43m00s	09h14m05.5s	+02d55m35s	228.72	33.23
0917+624	09h21m36.2311s	+62d15m52.180s	09h17m40.2985s	+62d28m38.738s	152.20	40.99
J0929+5013	09h29m15.4402s	+50d13m35.990s	09h25m51.9736s	+50d26m44.405s	167.66	45.42
0942+5034	09h46m15.70s	+50d20m02.8s	09h42m56.90s	+50d33m55.0s	166.57	48.03
0945+408	09h48m55.3381s	+40d39m44.587s	09h45m50.0787s	+40d53m43.471s	180.99	50.28

continued on next page

continued from previous page

Source	α_{2000}	δ_{2000}	α_{1950}	δ_{1950}	$l_{II}[^\circ]$	$b_{II}[^\circ]$
J0949+5819	09h49m41.5s	+58d19m06s	09h46m08.5s	+58d33m06s	155.35	45.73
J0949+6614	09h49m12.1651s	+66d14m59.587s	09h45m14.8430s	+66d28m58.078s	145.67	41.94
0954+556	09h57m38.1825s	+55d22m57.733s	09h54m14.3525s	+55d37m16.457s	158.60	47.93
0954+658	09h58m47.2451s	+65d33m54.818s	09h54m57.8379s	+65d48m15.656s	145.75	43.13
1022+2347	10h24m53.63s	+23d32m34.0s	10h22m07.91s	+23d47m48.6s	210.83	56.81
PKS 1034–293	10h37m16.0797s	–29d34m02.812s	10h34m55.8356s	–29d18m26.874s	270.95	24.85
1039+811	10h44m23.0626s	+80d54m39.443s	10h39m27.7453s	+81d10m23.782s	128.74	34.74
1047+1445	10h49m46.7s	+14d30m00s	10h47m07.6s	+14d45m54s	230.79	59.01
PKS 1048–313	10h51m04.7775s	–31d38m14.306s	10h48m43.3658s	–31d22m18.462s	274.93	24.61
PKS 1144–379	11h47m01.3706s	–38d12m11.022s	11h44m30.8624s	–37d55m30.531s	289.24	22.95
1150+812	11h53m12.4993s	+80d58m29.154s	11h50m23.4860s	+81d15m10.408s	125.72	35.84
1156+2931	11h59m31.8339s	+29d14m43.827s	11h56m57.7910s	+29d31m25.874s	199.41	78.37
PKS 1256–220	12h58m54.475s	–22d19m31.33s	12h56m13.940s	–22d03m20.40s	305.20	40.51
PKS 1257–326	13h00m42.4s	–32d53m12s	12h57m57.6s	–32d37m03s	305.18	29.94
1308+326	13h10m28.6638s	+32d20m43.783s	13h08m07.5645s	+32d36m40.353s	85.70	83.35
J1326–5206	13h26m18.8s	–52d06m24s	13h23m14.1s	–51d50m49s	308.36	10.40
1326+6237	13h28m40.0s	+62d21m41s	13h26m54.2s	+62d37m10s	115.56	54.23
1329+1727	13h31m33.47s	+17d12m49.8s	13h29m07.72s	+17d28m15.0s	348.08	76.43
1404+286	14h07m00.3944s	+28d27m14.690s	14h04m45.6213s	+28d41m29.358s	41.86	73.25
1418+546	14h19m46.5974s	+54d23m14.787s	14h18m06.1985s	+54d36m58.157s	98.30	58.31
1435+638	14h36m45.8021s	+63d36m37.866s	14h35m37.2491s	+63d49m35.974s	105.17	49.73
PKS 1502+036	15h05m06.4771s	+03d26m30.813s	15h02m35.6731s	+03d38m07.493s	2.23	50.25
1504+377	15h06m09.5299s	+37d30m51.132s	15h04m12.9628s	+37d42m23.412s	61.65	59.90
PKS 1519–273	15h22m36.68s	–27d43m28.6s	15h19m36.00s	–27d32m48.0s	339.44	24.23
PKS 1556–245	15h59m41.416s	–24d42m39.36s	15h56m41.220s	–24d34m11.30s	348.40	21.11
J1610+7809	16h10m50.626s	+78d09m00.58s	16h13m02.030s	+78d16m35.66s	111.97	34.34
1611+343	16h13m41.0642s	+34d12m47.908s	16h11m47.9210s	+34d20m19.882s	55.15	46.38
PKS 1622–297	16h26m06.0208s	–29d51m26.970s	16h22m57.2466s	–29d44m41.358s	348.82	13.32
1637+574	16h38m13.4563s	+57d20m23.978s	16h37m17.4367s	+57d26m15.810s	86.64	40.36
1642+690	16h42m07.8485s	+68d56m39.756s	16h42m18.0774s	+69d02m13.288s	100.71	36.62
1652+398	16h53m52.2167s	+39d45m36.609s	16h52m11.7373s	+39d50m25.191s	63.60	38.86
J1656+5321	16h56m39.6252s	+53d21m48.763s	16h55m32.3288s	+53d26m24.461s	81.04	38.38
1722+6108	17h22m48.62s	+61d04m56.2s	17h22m14.26s	+61d07m39.3s	90.17	34.16
1739+522	17h40m36.9778s	+52d11m43.407s	17h39m29.0173s	+52d13m10.447s	79.57	31.75
1749+701	17h48m32.8401s	+70d05m50.768s	17h49m03.4099s	+70d06m39.669s	100.53	30.72
1803+784	18h00m45.6839s	+78d28m04.018s	18h03m39.2265s	+78d27m54.310s	110.04	29.07
1807+698	18h06m50.590s	+69d49m28.10s	18h07m18.473s	+69d48m57.14s	100.13	29.17
J1814+4113	18h14m22.7062s	+41d13m05.608s	18h12m47.3255s	+41d12m06.186s	68.52	24.09
1817+5015	18h18m30.5192s	+50d17m19.743s	18h17m16.8964s	+50d16m01.524s	78.41	25.61
J1819+3845	18h19m27.1s	+38d45m08s	18h17m46.8s	+38d43m47s	66.25	22.46
J1821+6818	18h21m59.4931s	+68d18m43.015s	18h22m12.7767s	+68d17m06.501s	98.46	27.77
1823+568	18h24m07.0683s	+56d51m01.490s	18h23m14.9668s	+56d49m18.067s	85.74	26.08
J1852+4019	18h52m30.3725s	+40d19m06.608s	18h50m51.7856s	+40d15m22.481s	70.07	16.97
1928+738	19h27m48.4951s	+73d58m01.569s	19h28m49.3806s	+73d51m44.934s	105.63	23.54
1929+4737	19h31m15.7s	+47d43m31s	19h29m49.6s	+47d37m05s	79.97	13.53
1954+513	19h55m42.7382s	+51d31m48.546s	19h54m22.4856s	+51d23m46.376s	85.30	11.76
2007+777	20h05m30.9298s	+77d52m43.137s	20h07m20.4000s	+77d43m58.000s	110.46	22.73
2200+420	22h02m43.2913s	+42d16m39.979s	22h00m39.3723s	+42d02m08.495s	92.59	–10.44
2214+350	22h16m20.0099s	+35d18m14.180s	22h14m07.0204s	+35d03m14.994s	90.50	–17.62
2234+4201	22h37m04.0s	+42d16m45s	22h34m51.9s	+42d01m10s	97.98	–13.99
2239+2939	22h42m15.3s	+29d55m18s	22h39m54.5s	+29d39m35s	92.17	–25.12

Bibliography

Bibliography

Altenhoff, W. J., Baars, J. W. M., Wink, J. E., and Downes, D.: 1987, *A&A* **184**, 381

Armstrong, J. W., Rickett, B. J., and Spangler, S. R.: 1995, *ApJ* **443**, 209

Baars, J. W. M., Genzel, R., Pauliny-Toth, I. I. K., and Witzel, A.: 1977, *A&A* **61**, 99

Bach, U., Krichbaum, T. P., Ros, E., Britzen, S., Witzel, A., and Zensus, J. A.: 2002, in *Proceedings of the 6th EVN Symposium*, p. 119

Baker, D. N., Borovsky, J. E., Benford, G., and Eilek, J. A.: 1988, *ApJ* **326**, 110

Bania, T. M., Marscher, A. P., and Barvainis, R.: 1991, *AJ* **101**, 2147

Barnothy, J. M.: 1965, *AJ* **70**, 666

Beckert, T., Fuhrmann, L., Cimò, G., Krichbaum, T. P., Witzel, A., and Zensus, J. A.: 2002a, in *Proceedings of the 6th EVN Symposium*, p. 79

Beckert, T., Krichbaum, T. P., Cimò, G., Fuhrmann, L., Kraus, A., Witzel, A., and Zensus, J. A.: 2002b, *Publications of the Astronomical Society of Australia* **19**, 55

Begelman, M. C., Rees, M. J., and Sikora, M.: 1994, *ApJ* **429**, L57

Benford, G.: 1985, in *IAU Symp. 107: Unstable Current Systems and Plasma Instabilities in Astrophysics*, pp 131–138

Benford, G.: 1992, *ApJ* **391**, L59

Bennett, C. L., Halpern, M., Hinshaw, G., Jarosik, N., Kogut, A., Limon, M., Meyer, S. S., Page, L., Spergel, D. N., Tucker, G. S., Wollack, E., Wright, E. L., Barnes, C., Greason, M. R., Hill, R. S., Komatsu, E., Nolta, M. R., Odegard, N., Peiris, H. V., Verde, L., and Weiland, J. L.: 2003, *ApJS* **148**, 1

Berkhuijsen, E. M., Haslam, C. G. T., and Salter, C. J.: 1971, *A&A* **14**, 252

Bevington, P. R. and Robinson, D. K.: 1992, *Data reduction and error analysis for the physical sciences*, New York: McGraw-Hill, —c1992, 2nd ed.

Bhat, N. D. R. and Gupta, Y.: 2002, *ApJ* **567**, 342

Bhat, N. D. R., Gupta, Y., and Rao, A. P.: 1998, *ApJ* **500**, 262

Bhatt, H. C.: 2000, *A&A* **362**, 715

Biermann, P., Duerbeck, H., Eckart, A., Fricke, K., Johnston, K. J., Kühr, H., Liebert, J., Pauliny-Toth, I. I. K., Schleicher, H., Stockman, H., Strittmatter, P. A., and Witzel, A.: 1981, *ApJ* **247**, L53

Biggs, A. D., Browne, I. W. A., and Wilkinson, P. N.: 2001, *MNRAS* **323**, 995

Bignall, H. E., Jauncey, D. L., Lovell, J. E. J., Tzioumis, A. K., Kedziora-Chudczer, L., Macquart, J.-P., Tingay, S. J., Rayner, D. P., and Clay, R. W.: 2003, *ApJ* **585**, 653

Blandford, R. and Narayan, R.: 1985, *MNRAS* **213**, 591

Blandford, R. D. and Königl, A.: 1979, *ApJ* **232**, 34

Blandford, R. D., McKee, C. F., and Rees, M. J.: 1977, *Nature* **267**, 211

Blitz, L.: 1990, in *ASP Conf. Ser. 12: The Evolution of the Interstellar Medium*, pp 273–289

Blitz, L., Magnani, L., and Mundy, L.: 1984, *ApJ* **282**, L9

Bolton, J. G., Stanley, G. J., and Slee, O. B.: 1949, *Nature* **164**, 101
Bondi, M., Padrielli, L., Gregorini, L., Mantovani, F., Shapirovskaya, N., and Spangler, S. R.: 1994, *A&A* **287**, 390
Bondi, M., Padrielli, L., Shapirovskaya, N. Y., and Spangler, S. R.: 1992, *Bulletin of the American Astronomical Society* **24**, 763
Born, M. and Wolf, E.: 1980, *Principles of optics. Electromagnetic theory of propagation, interference and diffraction of light*, Oxford: Pergamon Press, 1980, 6th corrected ed.
Breitschwerdt, D., Egger, R., Freyberg, M. J., Frisch, P. C., and Vallerga, J. V.: 1996, *Space Science Reviews* **78**, 183
Breitschwerdt, D., Freyberg, M. J., and Egger, R.: 2000, *A&A* **361**, 303
Camenzind, M. and Krockenberger, M.: 1992, *A&A* **255**, 59
Chandran, B. D. G. and Backer, D. C.: 2002, *ApJ* **576**, 176
Cimò, G.: 2003, *Ph.D. Thesis, University of Bonn*
Cimò, G., Beckert, T., Krichbaum, T. P., Fuhrmann, L., Kraus, A., Witzel, A., and Zensus, J. A.: 2002a, *Publications of the Astronomical Society of Australia* **19**, 10
Cimò, G., Fuhrmann, L., Krichbaum, T. P., Beckert, T., Kraus, A., Witzel, A., and Zensus, J. A.: 2002b, in *Proceedings of the 6th EVN Symposium*, p. 69
Clegg, A. W., Fey, A. L., and Fiedler, R. L.: 1996, *ApJ* **457**, L23+
Clegg, A. W., Fey, A. L., and Lazio, T. J. W.: 1998, *ApJ* **496**, 253
Codes, J. M., Ananthakrishnan, S., and Dennison, B.: 1984, *Nature* **309**, 689
Coles, W. A., Rickett, B. J., Codona, J. L., and Frehlich, R. G.: 1987, *ApJ* **315**, 666
Cordes, J. M.: 1986, *ApJ* **311**, 183
Cox, D. P. and Reynolds, R. J.: 1987, *ARA&A* **25**, 303
de Vries, H. W., Thaddeus, P., and Heithausen, A.: 1987, *ApJ* **319**, 723
Dennett-Thorpe, J. and de Bruyn, A. G.: 2000, *ApJ* **529**, L65
Dennett-Thorpe, J. and de Bruyn, A. G.: 2002, *Nature* **415**, 57
Dennett-Thorpe, J. and de Bruyn, A. G.: 2003, *A&A* **404**, 113
Dent, W. A.: 1965, *AJ* **70**, 672
Desai, K. M. and Fey, A. L.: 2001, *ApJS* **133**, 395
Desai, K. M., Gwinn, C. R., and Diamond, P. J.: 1994, *Nature* **372**, 754
Edelson, R. A. and Krolik, J. H.: 1988, *ApJ* **333**, 646
Egger, R. J. and Aschenbach, B.: 1995, *A&A* **294**, L25
Falgarone, E.: 1996, in *IAU Symp. 170: CO: Twenty-Five Years of Millimeter-Wave Spectroscopy*, p. 119
Falgarone, E.: 1998, *Lecture Notes in Physics, Berlin Springer Verlag* **506**, 251
Falgarone, E. and Phillips, T. G.: 1996, *ApJ* **472**, 191
Fanti, C., Fanti, R., Ficarra, A., Gregorini, L., Mantovani, F., and Padrielli, L.: 1983, *A&A* **118**, 171
Fiedler, R., Dennison, B., Johnston, K. J., Waltman, E. B., and Simon, R. S.: 1994a, *ApJ* **430**, 581
Fiedler, R., Pauls, T., Johnston, K. J., and Dennison, B.: 1994b, *ApJ* **430**, 595
Fiedler, R. L., Dennison, B., Johnston, K. J., and Hewish, A.: 1987, *Nature* **326**, 675
Fomalont, E.: 1981, *NEWSLETTER. NRAO NO. 3, P. 3, 1981* **3**, 3
Frisch, P. C.: 1995, *Space Science Reviews* **72**, 499
Frisch, P. C. and York, D. G.: 1983, *ApJ* **271**, L59
Fuhrmann, L., Krichbaum, T. P., Cimò, G., Beckert, T., Kraus, A., Witzel, A., Zensus, J. A., QIAN, S. J., and Rickett, B. J.: 2002, *Publications of the Astronomical Society of Australia* **19**, 64

Gabuzda, D. C., Kochenov, P. Y., Cawthorne, T. V., and Kollgaard, R. I.: 2000a, *MNRAS* **313**, 627

Gabuzda, D. C., Kochenov, P. Y., Kollgaard, R. I., and Cawthorne, T. V.: 2000b, *MNRAS* **315**, 229

Gilmore, G. F. and Zeilik, M.: 2000, in *Allen's Astrophysical Quantities, ed. A. N. Cox (New York: Springer-Verlag)*, p. 471

Gir, B., Blitz, L., and Magnani, L.: 1994, *ApJ* **434**, 162

Goodman, J.: 1997, *New Astronomy* **2**, 449

Gopal-Krishna and Subramanian, K.: 1991, *Nature* **349**, 766

Gopal-Krishna and Wiita, P. J.: 1992, *A&A* **259**, 109

Gottesman, S. T. and Gordon, M. A.: 1970, *ApJ* **162**, L93+

Haffner, L. M., Reynolds, R. J., and Tufte, S. L.: 1998, *ApJ* **501**, L83+

Haffner, L. M., Reynolds, R. J., Tufte, S. L., Madsen, G. J., Jaehnig, K. P., and Percival, J. W.: 2003, *ApJS* **149**, 405

Hartmann, D., Magnani, L., and Thaddeus, P.: 1998, *ApJ* **492**, 205

Haslam, C. G. T., Kahn, F. D., and Meaburn, J.: 1971, *A&A* **12**, 388

Haslam, C. G. T., Stoffel, H., Salter, C. J., and Wilson, W. E.: 1982, *A&AS* **47**, 1

Heeschen, D. S.: 1984, *AJ* **89**, 1111

Heeschen, D. S., Krichbaum, T., Schalinski, C. J., and Witzel, A.: 1987, *AJ* **94**, 1493

Heeschen, D. S. and Rickett, B. J.: 1987, *AJ* **93**, 589

Heiles, C.: 1984, *ApJS* **55**, 585

Heiles, C.: 1994, in *ASP Conf. Ser. 66: Physics of the Gaseous and Stellar Disks of the Galaxy*, p. 249

Heiles, C.: 2001, in *ASP Conf. Ser. 231: Tetons 4: Galactic Structure, Stars and the Interstellar Medium*, p. 294

Heiles, C. and Habing, H. J.: 1974, *A&AS* **14**, 1

Heiles, C., Koo, B., Levenson, N. A., and Reach, W. T.: 1996, *ApJ* **462**, 326

Heithausen, A., Stacy, J. G., de Vries, H. W., Mebold, U., and Thaddeus, P.: 1993, *A&A* **268**, 265

Hey, J. S.: 1946, *Nature* **157**, 47

Hjellming, R. M. and Narayan, R.: 1986, *ApJ* **310**, 768

Hollenbach, D. J. and Tielens, A. G. G. M.: 1997, *ARA&A* **35**, 179

Hu, E. M.: 1981, *ApJ* **248**, 119

Hughes, P. A., Aller, H. D., and Aller, M. F.: 1989a, *ApJ* **341**, 54

Hughes, P. A., Aller, H. D., and Aller, M. F.: 1989b, *ApJ* **341**, 68

Ingalls, J. G.: 1999, *Ph.D. Thesis, University of Boston*

Ingalls, J. G., Reach, W. T., and Bania, T. M.: 2002, *ApJ* **579**, 289

Jauncey, D. L., Kedziora-Chudczer, L. L., Lovell, J. E. J., Nicolson, G. D., Perley, R. A., Reynolds, J. E., Tzioumis, A. K., and Wieringa, M. H.: 2000, in *Astrophysical Phenomena Revealed by Space VLBI, Proceedings of the VSOP Symposium, held at the Institute of Space and astronautical Science, Sagamihara, Kanagawa, Japan, January 19 - 21, 2000, Eds.: H. Hirabayashi, P.G. Edwards, and D.W. Murphy, Published by the Institute of Space and Astronautical Science, p. 147-150.*, pp 147–150

Jauncey, D. L. and Macquart, J.-P.: 2001, *A&A* **370**, L9

Kühr, H., Pauliny-Toth, I. I. K., Witzel, A., and Schmidt, J.: 1981a, *AJ* **86**, 854

Kühr, H., Witzel, A., Pauliny-Toth, I. I. K., and Nauber, U.: 1981b, *A&AS* **45**, 367

Kedziora-Chudczer, L., Jauncey, D. L., Wieringa, M., Reynolds, J. E., Tzioumis, A. K., Nicolson, G. D., and Walker, M. A.: 1998, *Bulletin of the American Astronomical Society* **30**, 903

Kedziora-Chudczer, L., Jauncey, D. L., Wieringa, M. H., Walker, M. A., Nicolson, G. D., Reynolds, J. E., and Tzioumis, A. K.: 1997, *ApJ* **490**, L9+

Kedziora-Chudczer, L. L., Jauncey, D. L., Wieringa, M. H., Tzioumis, A. K., and Reynolds, J. E.: 2001, *MNRAS* **325**, 1411

Kellermann, K. I.: 2002, *Publications of the Astronomical Society of Australia* **19**, 77

Kellermann, K. I. and Pauliny-Toth, I. I. K.: 1969, *ApJ* **155**, L71+

Kellermann, K. I., Vermeulen, R. C., Zensus, J. A., and Cohen, M. H.: 2000, in *Astrophysical Phenomena Revealed by Space VLBI, Proceedings of the VSOP Symposium, held at the Institute of Space and astronautical Science, Sagamihara, Kanagawa, Japan, January 19 - 21, 2000, Eds.: H. Hirabayashi, P.G. Edwards, and D.W. Murphy, Published by the Institute of Space and Astronautical Science, p. 159-166.*, pp 159–166

Königl, A. and Choudhuri, A. R.: 1985, *ApJ* **289**, 188

Kraus, A.: 1997, *Ph.D. Thesis, University of Bonn*

Kraus, A., Krichbaum, T. P., Wegner, R., Witzel, A., Cimò, G., Quirrenbach, A., Britzen, S., Fuhrmann, L., Lobanov, A. P., Naundorf, C. E., Otterbein, K., Peng, B., Risse, M., Ros, E., and Zensus, J. A.: 2003, *A&A* **401**, 161

Kraus, A., Witzel, A., Krichbaum, T. P., Lobanov, A. P., Peng, B., and Ros, E.: 1999, *A&A* **352**, L107

Krichbaum, T. P., Jin, C., Kraus, A., Witzel, A., and Zensus, J. A.: 2000, in *Astrophysical Phenomena Revealed by Space VLBI, Proceedings of the VSOP Symposium, held at the Institute of Space and astronautical Science, Sagamihara, Kanagawa, Japan, January 19 - 21, 2000, Eds.: H. Hirabayashi, P.G. Edwards, and D.W. Murphy, Published by the Institute of Space and Astronautical Science, p. 133-142.*, pp 133–142

Krichbaum, T. P., Kraus, A., Fuhrmann, L., Cimò, G., and Witzel, A.: 2002, *Publications of the Astronomical Society of Australia* **19**, 14

Krichbaum, T. P., Quirrenbach, A., and Witzel, A.: 1992, in *Variability of Blazars, Eds. E. Valtaoja and M. Valtonen, Cambridge University Press*, pp 331–345

Kuchar, T. A. and Clark, F. O.: 1997, *ApJ* **488**, 224

Kuntz, K. D., Snowden, S. L., and Verter, F.: 1997, *ApJ* **484**, 245

Lallement, R. and Berlin, P.: 1992, *A&A* **266**, 479

Lambert, H. C. and Rickett, B. J.: 2000, *ApJ* **531**, 883

Lang, K. R.: 1974, *Astrophysical formulae: A compendium for the physicist and astrophysicist*, New York, Springer-Verlag New York, Inc., 1974. 760 p.

Lesch, H. and Pohl, M.: 1992, *A&A* **254**, 29

Lockman, F. J.: 1976, *ApJ* **209**, 429

Lockman, F. J.: 1989, *ApJS* **71**, 469

Lovell, J. E. J., Jauncey, D. L., Bignall, H. E., Kedziora-Chudczer, L., Macquart, J.-P., Rickett, B. J., and Tzioumis, A. K.: 2003, *AJ* **126**, 1699

Lucas, R. and Liszt, H. S.: 1993, *A&A* **276**, L33+

Macquart, J.-P., Kedziora-Chudczer, L., Rayner, D. P., and Jauncey, D. L.: 2000, *ApJ* **538**, 623

Magnani, L., Blitz, L., and Mundy, L.: 1985, *ApJ* **295**, 402

Magnani, L., Hartmann, D., Holcomb, S. L., Smith, L. E., and Thaddeus, P.: 2000, *ApJ* **535**, 167

Magnani, L., Hartmann, D., and Speck, B. G.: 1996, *ApJS* **106**, 447

Marscher, A. P.: 1988, *ApJ* **334**, 552

Marscher, A. P.: 1992, in *Testing the AGN Paradigm*, pp 377–385

Marscher, A. P. and Bloom, S. D.: 1992, in *The Compton Observatory Science Workshop*, pp 346–353

Marscher, A. P. and Gear, W. K.: 1985, *ApJ* **298**, 114

Marscher, A. P., Gear, W. K., and Travis, J. P.: 1992, in *Variability of Blazars*, p. 85

Marscher, A. P., Marchenko-Jorstad, S. G., Mattox, J. R., Wehrle, A. E., and Aller, M. F.: 2000, in *Astrophysical Phenomena Revealed by Space VLBI, Proceedings of the VSOP Symposium, held at the Institute of Space and astronautical Science, Sagamihara, Kanagawa, Japan, January 19 - 21, 2000, Eds.: H. Hirabayashi, P.G. Edwards, and D.W. Murphy, Published by the Institute of Space and Astronautical Science, p. 39-46.*, pp 39–46

Marscher, A. P., Moore, E. M., and Bania, T. M.: 1993, *ApJ* **419**, L101+

Matsuhara, H., Tanaka, M., Yonekura, Y., Fukui, Y., Kawada, M., and Bock, J. J.: 1997, *ApJ* **490**, 744

Matthews, T. A. and Sandage, A. R.: 1963, *ApJ* **138**, 30

McKee, C. F.: 1995, in *ASP Conf. Ser. 80: The Physics of the Interstellar Medium and Intergalactic Medium*, p. 292

McKee, C. F. and Ostriker, J. P.: 1977, *ApJ* **218**, 148

Meyerdierks, H., Heithausen, A., and Reif, K.: 1991, *A&A* **245**, 247

Mezger, P. O.: 1978, *A&A* **70**, 565

Milogradov-Turin, J. and Urosevic, D.: 1997, *Bulletin de l'Observatoire Astronomique de Belgrade* **155**, 41

Narayan, R.: 1992, *ApJ* **394**, 261

Ott, M., Witzel, A., Quirrenbach, A., Krichbaum, T. P., Standke, K. J., Schalinski, C. J., and Hummel, C. A.: 1994, *A&A* **284**, 331

Otterbein, K., Krichbaum, T. P., Kraus, A., Lobanov, A. P., Witzel, A., Wagner, S. J., and Zensus, J. A.: 1998, *A&A* **334**, 489

Pen, U.: 1999, *ApJS* **120**, 49

Penprase, B. E.: 1993, *ApJS* **88**, 433

Pound, M. W. and Goodman, A. A.: 1997, *ApJ* **482**, 334

Qian, S.: 1995, *Chinese Astronomy and Astrophysics* **19**, 69

Qian, S., Li, X., Wegner, R., Witzel, A., and Krichbaum, T. P.: 1996, *Chinese Astronomy and Astrophysics* **20**, 15

Qian, S. and Zhang, X.: 2001, *Chinese Journal of Astronony and Astrophysics* **1**, 133

Qian, S. J., Kraus, A., Witzel, A., Krichbaum, T. P., and Zensus, J. A.: 2000, *A&A* **357**, 84

Qian, S. J., Quirrenbach, A., Witzel, A., Krichbaum, T. P., Hummel, C. A., and Zensus, J. A.: 1991, *A&A* **241**, 15

Qian, S. J., Witzel, A., Kraus, A., Krichbaum, T. P., and Zensus, J. A.: 2001, *A&A* **367**, 770

Quirrenbach, A.: 1989, *Ph.D. Thesis, University of Bonn*

Quirrenbach, A., Kraus, A., Witzel, A., Zensus, J. A., Peng, B., Risse, M., Krichbaum, T. P., Wegner, R., and Naundorf, C. E.: 2000, *A&AS* **141**, 221

Quirrenbach, A., Witzel, A., Kirchbaum, T. P., Hummel, C. A., Wegner, R., Schalinski, C. J., Ott, M., Alberdi, A., and Rioja, M.: 1992, *A&A* **258**, 279

Quirrenbach, A., Witzel, A., Qian, S. J., Krichbaum, T., Hummel, C. A., and Alberdi, A.: 1989, *A&A* **226**, L1

Quirrenbach, A., Witzel, A., Wagner, S., Sanchez-Pons, F., Krichbaum, T. P., Wegner, R., Anton, K., Erkens, U., Haehnelt, M., Zensus, J. A., and Johnston, K. J.: 1991, *ApJ* **372**, L71

Raiteri, C. M., Villata, M., Tosti, G., Nesci, R., Massaro, E., Aller, M. F., Aller, H. D., Teräsranta, H., Kurtanidze, O. M., Nikolashvili, M. G., Ibrahimov, M. A., Papadakis, I. E., Krichbaum, T. P., Kraus, A., Witzel, A., Ungerechts, H., Lisenfeld, U., Bach, U., Cimò, G., Ciprini, S., Fuhrmann, L., Kimeridze, G. N., Lanteri, L., Maesano, M., Montagni, F., Nucciarelli, G., and Ostorero, L.: 2003, *A&A* **402**, 151

Readhead, A. C. S.: 1994, *ApJ* **426**, 51
Rees, M. J.: 1967, *MNRAS* **135**, 345
Reich, P. and Reich, W.: 1986, *A&AS* **63**, 205
Rickett, B. J.: 1970, *MNRAS* **150**, 67
Rickett, B. J.: 1986, *ApJ* **307**, 564
Rickett, B. J.: 1990, *ARA&A* **28**, 561
Rickett, B. J., Coles, W. A., and Bourgois, G.: 1984, *A&A* **134**, 390
Rickett, B. J., Kedziora-Chudczer, L., and Jauncey, D. L.: 2002, *ApJ* **581**, 103
Rickett, B. J., Quirrenbach, A., Wegner, R., Krichbaum, T. P., and Witzel, A.: 1995, *A&A* **293**, 479
Rickett, B. J., Witzel, A., Kraus, A., Krichbaum, T. P., and Qian, S. J.: 2001, *ApJ* **550**, L11
Roberts, D. H., Kollgaard, R. I., Brown, L. F., Gabuzda, D. C., and Wardle, J. F. C.: 1990, *ApJ* **360**, 408
Rohlfs, K. and Wilson, T. L.: 1996, *Tools of Radio Astronomy*, Tools of Radio Astronomy, XVI, 423 pp. 127 figs., 20 tabs.. Springer-Verlag Berlin Heidelberg New York. Also Astronomy and Astrophysics Library
Romani, R. W.: 1988, in *AIP Conf. Proc. 174: Radio Wave Scattering in the Interstellar Medium*, pp 156–162
Roshi, D. A. and Anantharamaiah, K. R.: 2000, *ApJ* **535**, 231
Roshi, D. A. and Anantharamaiah, K. R.: 2001, *ApJ* **557**, 226
Rybicki, G. B. and Lightman, A. P.: 1979, *Radiative processes in astrophysics*, New York, Wiley-Interscience, 1979. 393 p.
Ryle, M., Hine, G., Shakeshaft, J., and Caswell, J. L.: 1978, *Nature* **276**, 571
Salter, C. J.: 1983, *Bulletin of the Astronomical Society of India* **11**, 1
Schmidt, M.: 1963, *Nature* **197**, 1040
Shapirovskaia, N. I.: 1978, *AZh* **55**, 953
Sholomitsky, G. B.: 1965, *Informational Bulletin on Variable Stars* **83**, 1
Sieber, W.: 1982, *A&A* **113**, 311
Simonetti, J. H., Cordes, J. M., and Heeschen, D. S.: 1985, *ApJ* **296**, 46
Slysh, V. I.: 1992, *ApJ* **391**, 453
Snowden, S. L., Cox, D. P., McCammon, D., and Sanders, W. T.: 1990, *ApJ* **354**, 211
Snowden, S. L., Egger, R., Finkbeiner, D. P., Freyberg, M. J., and Plucinsky, P. P.: 1998, *ApJ* **493**, 715
Sorochenko, R. L. and Tsivilev, A. P.: 2000, *Astronomy Reports* **44**, 426
Spada, M., Salvati, M., and Pacini, F.: 1999, *ApJ* **511**, 136
Standke, K. J., Quirrenbach, A., Krichbaum, T. P., Witzel, A., Otterbein, K., Alef, W., Eckart, A., Alberdi, A., Marcaide, J. M., Ros, E., Lesch, H., Steffen, W., Kraus, A., and Zensus, J. A.: 1996, *A&A* **306**, 27
Stickel, M., Fried, J. W., and Kühr, H.: 1993, *A&AS* **98**, 393
Taylor, J. H. and Cordes, J. M.: 1993, *ApJ* **411**, 674
Taylor, J. R.: 1982, in *An Introduction to Error Analysis, Mill Valley, CA, USA: University Science Book*
Urry, C. M. and Padovani, P.: 1995, *PASP* **107**, 803
Valtaoja, E., Haarala, S., Lehto, H., Valtaoja, L., Valtonen, M., Moiseev, I. G., Nesterov, N. S., Salonen, E., Terasranta, H., Urpo, S., and Tiuri, M.: 1988, *A&A* **203**, 1
Valtaoja, E., Terasranta, H., Urpo, S., Nesterov, N. S., Lainela, M., and Valtonen, M.: 1992, *A&A* **254**, 71
van Dishoeck, E. F. and Black, J. H.: 1988, *ApJ* **334**, 771

Wagner, S. J.: 1998, in *ASP Conf. Ser. 144: IAU Colloq. 164: Radio Emission from Galactic and Extragalactic Compact Sources*, p. 257

Wagner, S. J. and Witzel, A.: 1995, *ARA&A* **33**, 163

Wagner, S. J., Witzel, A., Heidt, J., Krichbaum, T. P., Qian, S. J., Quirrenbach, A., Wegner, R., Aller, H., Aller, M., Anton, K., Appenzeller, I., Eckart, A., Kraus, A., Naundorf, C., Kneer, R., Steffen, W., and Zensus, A.: 1996, *AJ* **111**, 2187

Wagner, S. J., Witzel, A., Krichbaum, T. P., Wegner, R., Quirrenbach, A., Anton, K., Erkens, U., Khanna, R., and Zensus, A.: 1993, *A&A* **271**, 344

Walker, M. and Wardle, M.: 1998, *ApJ* **498**, L125+

Walker, M. A.: 1998, *MNRAS* **294**, 307

Walker, M. A.: 2001, *Ap&SS* **278**, 149

Wambsganss, J., Schneider, P., Quirrenbach, A., and Witzel, A.: 1989, *A&A* **224**, L9

Wardle, J. F. C., Homan, D. C., Ojha, R., and Roberts, D. H.: 1998, *Nature* **395**, 457

Warwick, R. S., Barber, C. R., Hodgkin, S. T., and Pye, J. P.: 1993, *MNRAS* **262**, 289

Welsh, B. Y., Craig, N., Vedder, P. W., and Vallerga, J. V.: 1994, *ApJ* **437**, 638

Witzel, A.: 1990, in *Parsec-scale radio jets, Eds. J.A. Zensus and T.J. Pearson, Cambridge Univ. Press*, p. 206

Witzel, A., Heeschen, D. S., Schalinski, C., and Krichbaum, T.: 1986, *Mitteilungen der Astronomischen Gesellschaft Hamburg* **65**, 239

Witzel, A., Schalinski, C. J., Johnston, K. J., Biermann, P. L., Krichbaum, T. P., Hummel, C. A., and Eckart, A.: 1988, *A&A* **206**, 245

Wood, B. E. and Linsky, J. L.: 1997, *ApJ* **474**, L39+

Danksagung/Acknowledgements

Danksagung/Acknowledgements

An dieser Stelle möchte ich mich herzlich bei allen bedanken, die mir in den letzten Jahren tatkräftig zur Seite standen und mich bei dieser Dissertation unterstützt haben. Nur durch sie war es mir möglich diese Arbeit anzufertigen.

Insbesondere geht mein Dank an

- den Direktor der VLBI-Gruppe des Max-Planck-Instituts für Radioastronomie, Dr. J.A. Zensus, für die Möglichkeit diese Arbeit in seiner Gruppe anzufertigen, sowie für die finanzielle Unterstützung.

- Herrn Dr. Arno Witzel. Ihm gebührt mein ganz besonderer Dank. Seine wissenschaftliche und organisatorische Kompetenz haben maßgeblich zu dieser Arbeit beigetragen. Seine Anregungen, Tipps und die interessanten Diskussionen mit ihm – auch nicht-astronomischer Natur – haben ein Klima geschaffen in dem ich gerne und mit großer Freude diese Arbeit anfertigen konnte. Durch ihn erfuhr ich die Bedeutung und Wichtigkeit eines "Doktorvaters".

- Dr. Thomas P. Krichbaum. Ihm möchte ich in ganz besonderem Maße danken. Seine fachliche Anleitung, Geduld, seine wertvollen Ideen, Anregungen und Hilfestellungen, ebenso wie die fruchtvollen Diskussionen und die angenehme Arbeitsatmosphäre haben diese Arbeit erst ermöglicht. Danke Thomas!

- Dr. Alexander Kraus. Ihm möchte ich besonders danken für seine Aufofperungsbereitschaft, Tipps, Anregungen und Unterstützung bei zahlreichen Messkampagnen, wichtigen wissenschaftlichen Diskussionen und Fragestellungen.

- my italian friend Giuseppe Cimò: Thanks for your help during all stages of my work, the fruitful scientific and non-scientific discussions and the real!!! Pasta at an altitude of 3186 m (place of nowhere). It was a great time!

- die Herren Prof. Dr. U. Klein und Priv.-Doz. Dr. W.K. Huchtmeier für die Übernahme des Referats bzw. Koreferats. Herrn Huchtmeier möchte ich desweiteren für seine Unterstützung und Hilfsbereitschaft danken, die mir meine "ersten Schritte" in die Spektroskopie wesentlich erleichterten.

- Dr. Thomas Beckert für die gute Zusammenarbeit, seine Tipps und anschaulichen Erklärungen zur Theorie, sowie für seine "analytischen Lösungen zum Modulationsindex".

- Dr. B.J. Rickett for kindly providing the model predictions of an anisotropic ISS scenario as well as Prof. S.J. Qian for his advice concerning the annual modulation model.

- das Team am Radioteleskop Effelsberg, insbesondere an die Operateure für die Ermöglichung eines reibungslosen und unterhaltsamen Beobachtungsbetriebes während mehr als 700 Stunden Meßzeit und die Versorgung mit ca. 73 Liter Kaffee während der letzten Jahre.
- Herrn Dr. Andreas Heithausen für die Suche nach neuen CO-Wolken vor IDV-Quellen.
- Dr. Jens Klare für die freundschaftliche Atmosphäre, unser Philosophieren über "Gott und die Welt" und die außerbetrieblichen Aktivitäten.
- die Doktoranden der VLBI Gruppe. Insbesondere danke ich Simone Friedrichs, Violetta Impellizzeri und Matthias Kadler für das besondere Flair, viele interessante Gespräche und das gute Büroklima.
- an alle Mitglieder der VLBI Gruppe für die lehrreiche Arbeitsatmosphäre und diverse Hilfestellungen. Stellvertretend seien hier erwähnt: Dr. Andrei Lobanov, Dr. Eduardo Ros, Dr. Walter Alef und Dr. Richard W. Porcas.
- meine Freunde, insbesondere an die "Handballjungs" – die 1. Mannschaft der SpVgg Lülsdorf – für viele spannende und interessante Handballpiele und die festlichen Aktivitäten.
- meine Familie in Düsseldorf für die unermüdliche moralische und finanzielle Unterstützung, sowie stetige Ermunterung und Rückhalt während des gesamten Studiums. Ohne Euch wäre das nicht möglich gewesen. Danke!
- Zu guter Letzt möchte ich meinem eigentlichen Stern am Himmel – Dir Katrin – für alles danken, insbesondere für Deine unendliche Unterstützung und Deine Liebe.

Lebenslauf/Curriculum Vitae

Persönliche Details:

Name	:	Lars Fuhrmann
Geburtsort	:	Duisburg, Nordrhein-Westfalen
Familienstand	:	ledig
Nationalität	:	deutsch

Schulische und universitäre Ausbildung:

- August 1979 – Mai 1992: Grundschule und Gymnasium (Abtei-Gymnasium, Duisburg). Abschluß: Abitur
- Oktober 1992 – Oktober 1993: Zivildienst im Altenheim 'Morian-Stift', Duisburg
- Oktober 1993 – Oktober 1999: Studium der Physik und Astronomie an der Universität Bonn
- Juli 1998 – Oktober 1999: Anfertigung der Diplomarbeit am *Radioastromomischen Institut der Universität Bonn*. Titel der Diplomarbeit: "Multifrequenzanalyse an Riesenradiogalaxien"; Wissenschaftliche Hilfskraft
- März 1999 – Juni 1999: Auslandsstudienaufenthalt als ERASMUS-Student am *Istituto di Radioastronomia del CNR*, Bologna, Italien.
- Oktober 1999 – Abschluß: "Diplom in Physik"
- seit November 1999: Anfertigung vorliegender Dissertation und wissenschaftlicher Mitarbeiter am *Max-Planck-Institut für Radioastronomie* (MPIfR), Bonn. Titel der Doktorarbeit: **"Investigations of Intraday Variable Blazar Cores and the Connected Interstellar Medium"**.
- seit April 2002: Student in der *International Max-Planck Research School*.